The Essential Elements of a Model for Localized Corrosion Systems with Complex Geometries:

From Prediction to Mitigation Strategies

A Dissertation

Presented to the Faculty of the School of Engineering and Applied Science

University of Virginia

In partial fulfillment

of the requirements for the degree

Doctor of Philosophy in Material Science and Engineering

By

Rebecca Skelton Marshall

July 18th, 2022

APPROVAL SHEET

This Dissertation
is submitted in partial fulfillment of the requirements for the degree of
Doctor of Philosophy

Rebecca Skelton Marshall

Author Signature

This Dissertation has been read and approved by the examining committee:

Advisor: Dr. Robert G. Kelly

Chair Committee Member: Dr. James M. Fitz-Gerald

Committee Member: Dr. John R. Scully

Committee Member: Dr. B. Jill Venton

Committee Member: Dr. Fritz Friedersdorf

Accepted for the School of Engineering and Applied Sciences:

Jennifer L. West, School of Engineering and Applied Science
August 2022

Abstract

In the presence of an electrolyte and an electrochemical potential difference, galvanic corrosion can occur, increasing the corrosion rate on the more-active material and decreasing the corrosion rate on the more-noble material. Although galvanic corrosion is generally considered an isolated mechanism on its own, it often induces other localized corrosion events. For example, micro-galvanic couples between active intermetallic precipitates and the more-noble matrix of a given alloy can initiate and accelerate pitting corrosion. Similarly, macro-galvanic couples between dissimilar materials in a crevice geometry can have a large enough driving force to induce crevice corrosion which would not have been present if the crevice former was inert.

In modern structures, neither scenario above is avoidable. Alloying elements are added within a material to achieve an optimization of mechanical properties, leaving the substrate susceptible to pitting via the electrochemical potential differences between the precipitates and matrix. Furthermore, precipitate-strengthened aluminum alloys require mechanical joining, rather than welding, which introduces dissimilar materials into electrical contact. A common form of mechanical joining uses fasteners, which can create an occluded region between the fastener shaft and fastener hole. The geometry of both a cylindrical fastener hole and a hemispherical surface pit can act as a stress concentrator, increasing the probability for crack initiation and propagation. Therefore, both macro- and micro-galvanic induced localized corrosion events are extremely relevant in terms of the structural stability and lifetime of a component. This work takes a mixed experimental and computational approach of validation, prediction, and finally mitigation of galvanic-induced localized corrosion in three sections: 1) galvanic-induced crevice corrosion, 2) pitting corrosion, 3) computational methodologies to accommodate complex systems. The effect of geometry, environmental factors (chloride concentration and water layer thickness), and material selection were investigated in each section, and limitations within each simulated scenario were discussed.

Validation of a finite element method (FEM) model assuming the Laplace equation was first conducted through comparison with literature and in-house experimental panels for a SS316/Ti-6Al-4V/AA7075 fastener/panel galvanic couple. The computational and experimental results determined that in fastener-in-panel systems, severe galvanic-induced crevice corrosion occurred within the fastener hole, independent of the visible surface corrosion damage. Therefore, two main strategies were determined to mitigate corrosion damage within the susceptible fastener hole region, 1) to lower the overall galvanic current, possible through the application of a sol-gel coating or less-noble fastener, 2) to concentrate the majority of current on the surface of the panel, rather than the occluded fastener hole, which may be achieved through controlled surface defects, bulk WL, and a raised fastener head. A machine learning algorithm was also created through the resulting FEM data to predict under which conditions, environmental and geometric, the majority of current would occur in a creviced region, with the goal to understand and prevent problematic scenarios.

The work on macro-galvanic couples was extended to account for, and mitigate, stress corrosion cracking. A materials selection framework was created, combining linear elastic fracture mechanics (LEFM) and FEM, to limit scenarios in which high crack growth rates or high corrosion rates may occur. The potential distributions predicted through the FEM, specifically in the highest-stress region, were used to optimize scenarios which fell in the base of the “U”-shaped crack growth rate dependence on potential. Current density distributions and the total current in the system were then used to further narrow down the material selection scenarios.

In terms of micro-galvanic coupling, pitting of SS316 was investigated with the same computational approach as above. The stability of a given pit was determined through the critical pit stability product $(i \cdot x)_{crit}$ and the repassivation potential (E_{rp}), for a variety of pit geometries, finite cathode sizes, and water layer thicknesses. In all tested conditions, E_{rp} predicted a higher stability of pits to continue growing than $(i \cdot x)_{crit}$, leading to the consideration that the conventionally measured value of E_{rp} may be too conservative. Pulling upon two recent pitting framework developed in literature, an equation was proposed to calculate E_{rp} based on the transition potential (E_T), the critical percent saturation (f), and the anodic $E - \log(i)$ Tafel relationship of the pit base (b_a). Utilizing data from literature on SS316, consistent values of E_{rp} were determined which were approximately 70 to 120 mV more electropositive than convention.

An accumulation of the macro- and micro-galvanic coupling work was conducted by simulating a SS316/AA7050 couple which was experiencing localized pitting events on the inhomogeneous AA7050 surface. It was determined that to best correlate the simulated results with the experimental scanning vibrating electrode technique (SVET), the experimental boundary conditions needed to account for both anodic and cathodic deviations from generic bulk conditions. Although FEM was not able to account for individual pitting events, as the location, size, and distribution of the activated regions would be needed as input parameters, the *average* current density distribution and total current magnitude showed good comparison between the computational and experimental data, once the boundary conditions were modified.

Acknowledgements

To fully capture the gratitude that I have for those who have helped me along this journey, written words cannot suffice. However, there are those which deserve special recognition. First, I would like to thank my advisor, Prof. Rob G. Kelly, who took a chance on someone who walked into his office out of the blue and didn't know the first thing about corrosion. The number of hours that Prof. Kelly pours into his students' lives to help them develop professionally and personally is immeasurable. The words written in this document are a direct result of, and can be completely attributed to, Prof. Kelly's encouragement and guidance throughout this process. Moreover, the valuable life advice, often in the form of a catchy phrase, such as frogs in hot water, will be carried with me throughout the remainder of my life.

I would also like to thank my committee members, Prof. Jim Fitz-Gerald, Prof. John Scully, Prof. Jill Venton, and Dr. Fritz Friedersdorf. I appreciate your patience, in advance, of reading this document and appreciate the valuable advice that you have given to me along this process. In addition, every faculty member who I have had the pleasure of interacting with at UVa, either through classes, collaborations, or through friendly bumps in the hallways, has been the epitome of kindness, with their readiness to help students and to lend advice. One of the reasons which I have loved volunteering at recruitment weekend is that I can honestly tell new students about the joys of our department and our faculty, knowing that it is not an understatement or exaggeration in the least.

A large contribution to the inviting atmosphere of the Material Science Department is the hard work of our admin and staff. Specifically, Kim Fitzhugh-Higgins, Kari Werres, Tonya Reynolds, Richard White, Joe Thompson, and Ig Jakovac have all made an incredibly positive impact on my graduate career.

Although it is a joy to convene at departmental events and talk with all of the colleagues in the department, specific people deserve special recognition. My office mates, Qiyuan Lin, Lee Kendall, Pedro Atz-Dick, Carolina Moraes (Atz-Dick), and a former office mater, Gilbert Chao Liu. Our discussions, on and off the topic of research, have always been something to look forward to when coming into the office, not to mention helpful, in terms of learning everyone's research and getting a fresh perspective on my own.

Friends and family are truly what helped me through these past few years, and of that, I will be incredibly grateful forever. There are many of whom I could name, and many photos with fond memories to which I could show, but to those who have in comradery distracted me from the worst through hikes, games, movies, and wine nights (to name a few), you all know who you are, and I am so grateful for you (Luke, Meg, Will, Katie, Jonathan, Pedro, Carolina, Anna, Victor, Bryan, Cecilia, and Libby – You all are awesome, amazing people!).

My family is my rock, and of that, a true gemstone. Through thick and thin, I can always count on their honest opinion and caring hearts.

Lastly, my husband, Timothy, has been my best friend and unwavering supporter. Through his encouragement, loving support, adventurous spirit, and shoot-for-the-sky ideas, I am who I am today. Throughout all his actions, he continuously pointed me towards loving and glorifying God; a reminder of the bigger picture when I was (often) lost in research, and needed it the most.

To God be the glory.

“As we conquer peak after peak, we see in front of us regions full of interest and beauty, but we do not see our goal, we do not see the horizon; in the distance tower still higher peaks, which will yield to those who ascend them still wider prospects, and deepen the feeling, the truth of which is emphasized by every advance in science, that ‘Great are the Works of the Lord’.”

J. J. Thompson

Bibliography

Publications resulting from this dissertation are listed below,

1. **R. Skelton Marshall,** R. G. Kelly, A. Goff, & C. Sprinkle. (2019). Galvanic Corrosion Between Coated Al Alloy Plate and Stainless Steel Fasteners, Part 1: FEM Model Development and Validation. *Corrosion, 75*(12), 1461–1473.
2. **R. Skelton Marshall,** A. Goff, C. Sprinkle, A. Britos, & R. G. Kelly. (2020). Estimating the Throwing Power of SS316 When Coupled with AA7075 Through Finite Element Modeling. *Corrosion*, *76*(5), 476–484.
3. **R. Skelton Marshall,** K. A. Define, R. S. Rosner, A. Goff, C. Sprinkle, P. V. Balachandran, & R. G. Kelly. (2022). Galvanic Corrosion Between Coated Al Alloy Plate and Stainless Steel Fasteners, Part 2: Application of FEM and Machine Learning to Study Galvanic Current Distributions. *(Submitted to Corrosion)*
4. **R. Skelton Marshall,** R. M. Katona, M. A. Melia, & R. G. Kelly. (2022). Pit Stability Predictions of Additively Manufactured SS316 Surfaces Using Finite Element Analysis. *Journal of The Electrochemical Society*, *169*(2), 021506
5. ***R. Skelton Marshall,** A. Shehi, R. M. Katona, M. A. Melia, R. G. Kelly. (2022). Perspective – An Alternative Calculation of the Repassivation Potential, to Represent Less Conservative and More Realistic Values. *Journal of The Electrochemical Society, (To be submitted to the Journal of the Electrochemical Society, Perspective)*

6. *Z. D. Harris, **R. S. Marshall,** J. T. Burns, R. G. Kelly. (2022). Coupling Fracture Mechanics Experiments and Electrochemical Modeling to Mitigate Environment-Assisted Cracking in Engineering Components, *(to be submitted)*

7. ***R. Skelton Marshall,** Z. D. Harris, M. K. Small, K. L. Brunner, J. T. Burns, & R. G. Kelly. (2022). A Materials Selection Framework for Fastener-in-Panel Geometries Using FEM and LEFM, to Mitigate Coating Degradation and Hydrogen Embrittlement, *(to be submitted)*

8. U.-E., Charles-Granville[=], **R. Skelton Marshall[=],** C. V. Moraes[=], C. F. Glover, J. R. Scully, & R. G. Kelly. (2022). Application of Finite Element Modeling to Macro-Galvanic Coupling of AA7050 and SS316: Validation Using the Scanning Vibrating Electrode Technique. *Journal of The Electrochemical Society*, *169*(031502), 1–14.

*To be submitted to a peer-reviewed journal

[=] denotes equal authorship

Table of Contents

List of Figures

List of Tables

List of Symbols

AA	Aluminum alloy
b_a	Anodic Tafel slope (in log base-10-scale)
C_i	Concentration of each species, i
D, $\mathrm{D_{cath}}$	Cathode diameter
D_i	Diffusivity of each species, i
$\mathrm{E_{base}}$	FEM-calculated electrode potential at pit base
$\mathrm{E_{edge}}$	FEM-calculated electrode potential at cathode edge
$\mathrm{E_{mouth}}$	FEM-calculated electrode potential at pit mouth
$\mathrm{E_{OCP}^{cath}}$	Open circuit potential of cathode
E_{rp}	Repassivation potential
E_T	Transition potential
FEM	Finite element method
f	Degree of critical pit solution saturation required to maintain stable propagation
HER	Hydrogen evolution reaction
I_{LC}	Anodic current demand
$I_{\mathrm{c}}^{\mathrm{ext}}$	Ideal cathodic current capacity
I_{crit}	Critical current which satisfies the pit stability product in a given scenario
I_{FEM}	FEM-calculated current
i	Current density
i_{lim}	Diffusion limited current density
$(i{\cdot}x)_{\mathrm{crit}}$	1-D pit stability product at critical salt film saturation
$(i{\cdot}x)_{\mathrm{sf}}$	1-D pit stability product at 100% salt film saturation
$\left(\frac{I}{r}\right)_{\mathrm{crit}}$	3-D hemispherical pit stability product at critical salt film saturation
$\left(\frac{I}{r}\right)_{\mathrm{sf}}$	3-D hemispherical pit stability product at 100% salt film saturation
LD	Loading density
N_i	Ionic flux of species, i
OCP	Open circuit potential
ORR	Oxygen reduction reaction
PDS	Potentiodynamic scan
r	Pit mouth radius
r_{crit}	Critical pit radius when a stability criterion is satisfied
RH	Relative humidity

r_{max}	The maximum pit radius derived from the maximum pit model
R_{sol}	Solution resistance
SA_a, SA_c	Surface area of the anode, and cathode, respectively
SEM	Scanning electron microscopy
S_{length}	Scribe length
S_{width}	Scribe width
SS	Stainless steel
SVET	Scanning vibrating electrode technique
u_i	Mobility of each species, i
V_{SCE}	Electrode potential measured in reference to a saturated calomel electrode
v	Fluid velocity
WL	Water layer thickness
x	1-D pit depth
ZRA	Zero-resistance ammeter
Z, n	Number of electrons transferred
β_a	Anodic Tafel slope (in natural log-scale)
β_c	Cathodic Tafel slope (in natural log-scale)
δ_{nc}	Natural convection boundary layer thickness
κ, σ	Electrolyte conductivity
Φ	Electrolyte potential
Φ_{sol}	Ohmic potential drop due to solution resistance

Summary of Significant Findings

- Galvanic-induced crevice corrosion can cause significant damage within a fastener hole, and the amount of damage can be predicted computationally despite simplifying assumptions of the Laplace equation, so long as an external cathodic surface is present to act as the main driving force for corrosion
- The galvanic coupling of noble fasteners to a structural panel is significant up to a certain radius, denoted as the throwing power, the value of which *decreases* with 1) decreasing water layer thickness (WL), 2) less bulk-exposed cathodic surface areas (*i.e.*, fastener geometry), and 3) slower cathodic kinetics (*i.e.*, fastener material type)
- The distribution of corrosion damage is also dependent on the three parameters described above as well as external surface defects, with thinner WL, countersunk fasteners, and small scribe dimensions concentrating the majority of damage in the highest-stress region, the occluded fastener hole
- A combined computational methodology of the finite element method (FEM) and machine learning has been developed to generalize the parameters above and predict when the majority of corrosion damage will occur within a creviced region and how the majority of corrosion damage can be pulled to the more-visible surface regions of the panel
- Going one step beyond the maximum pit model, described in the literature, FEM was used with more realistic assumptions and estimated that the maximum pit may be conservative by a factor of two in its calculations of the maximum pit radius
- The FEM model determined that the surface area of a pit may be the most important geometric factor in causing repassivation, rather than the shape of the pit

- A novel calculation of the repassivation potential was developed based on the recent pitting frameworks in literature, in which a less-conservative value could be determined through easily-measured parameters such as the Tafel slope and transition potential
- A methodology has been developed to combine FEM and linear elastic fracture mechanics (LEFM) for coating and material selection processes, with selective plating and bare Ti-6Al-4V fasteners found to engineer the potential into the low-crack growth rate region while maintaining low galvanic currents within the system
- FEM was used in conjunction with the experimental scanning vibrating electrode technique (SVET) to determine the relationship of the electrolyte current density as a function of distance in the electrolyte, as well as quantifying the underestimation obtained by the SVET and highlighting the sensitivity of boundary conditions within the FEM
- It was determined that with representative boundary conditions, the Laplacian model could accurately predict the total current and average current density distribution of an actively pitting surface, although it was *impossible* for the model to capture the individual “hot spots” of current due to the localized pitting, with the present assumptions

Chapter 1: Introduction

Aerospace structures are often geometrically complex and contain dissimilar alloys in ionic contact through a thin atmospheric electrolyte[1–3]. The selected dissimilar materials are often used to optimize the mechanical properties of the structure; however, localized corrosion can be accelerated by these materials through macro-galvanic couples, with damage propagating discretely until cracking and failure occur. Engineering alloys have heterogeneous microstructures, often by design. However, the heterogeneities can lead to highly localized micro-galvanic couples as well. Within this work, macro- and micro-scale galvanic couples are considered through the localized corrosion processes of crevice and pitting corrosion, respectively. Finite element method (FEM) modeling is first experimentally validated, and then used to predict the potential and current density distributions of the localized corrosion processes, through a variety of geometric and environmental conditions. Experimental boundary conditions are input into the respective model, to simulate a realistic system.

1.1 Background

Finite Element Method (FEM) Modeling

Electrochemical processes can be highly complex and interdependent, requiring the use of many advanced experimental and computational techniques in order to understand their behavior. Even in the most-simplistic scenario of a small, planar galvanic couple under full immersion conditions, the equipotential lines and current density vectors can only be qualitatively plotted, unless one solves a set complex differential equations simultaneously[4]. The galvanic coupled potential (E_{gal}) and galvanic coupled current density (i_{gal}) can then be predicted based on the individual polarization behavior of the isolated materials via Mixed Potential Theory[5] (Figure

1.1). That is, for a single material, the corrosion potential (E_{corr}) and corrosion current density (i_{corr}) can be estimated through the Tafel extrapolation of the experimentally-determined polarization behavior, as shown in Figure 1.1(a). The usefulness of Mixed Potential Theory is that it states that the *individual* polarization behavior of two materials can be plotted together to determine the electrochemical parameters of the *couple*, that is, the two materials if they were in electrolyte contact. This theory generally considers the cathode surface area to be equal to that of the anodic surface area (a 1:1 ratio), elsewise the respective polarization behaviors need to be scaled to account for the surface area differences[6].

Through the electrochemical parameters of the galvanic couple, it can be seen that the corrosion current density of the more active material (as the anode, mat, a) is *increased* to i_{gal} while the corrosion current density of the more noble material (as the cathode, mat, n) is *decreased* (Figure 1.1(b)). This observation serves as the foundational basis for galvanic corrosion[2,5].

However, as complexities arise, either through multifaceted geometries or atmospheric environments, simple calculations of corrosion parameters through Mixed Potential Theory are no longer possible. Therefore, the utilization of computational techniques has become popular, as the complex electrochemical processes can be solved in an iterative manner through numerical modeling[7,8].

The accuracy of the computational results is critically dependent on the boundary conditions used. Recently, the use of experimentally-determined boundary conditions have been used as inputs, rather than reliance on assumed Butler-Volmer or Tafel expressions, creating a model which is not purely theoretical in nature[9–11].

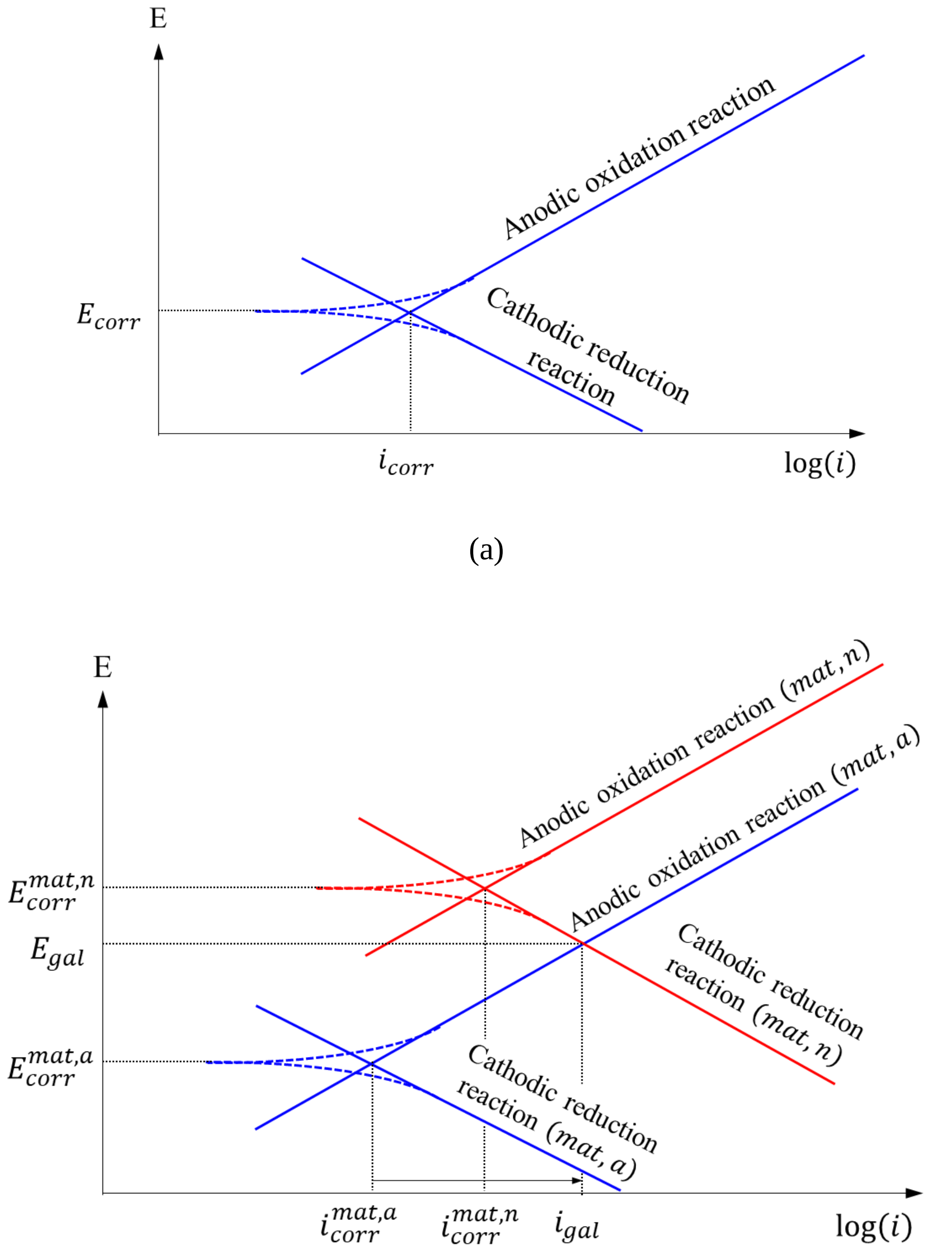

(a)

(b)

Figure 1.1: (a) Schematic of the Tafel extrapolation (solid lines) and resulting polarization curve (dashed lines) on a single material, with electrochemical potential and current density parameters on the individual material noted. (b) Mixed Potential Theory schematic on a more active material (blue lines, mat, a) with Tafel extrapolation and a more noble material (red lines, mat, n) with Tafel extrapolation, indicating the increased corrosion rate on the more active material. Note that the notation, E_{OCP}, E_{corr} = the open circuit potential (or corrosion potential), $i_{gal}, i_{couple}, i_{corr}^{couple}$ = the galvanic corrosion current density, and $E_{gal}, E_{couple}, E_{corr}^{couple}$ = the galvanic coupled potential are all equivalent

It is important to note that through these methods a solution to the governing equations is *approximated* based on a tolerance factor determining what level of residual error is acceptable. That is, an approximate numerical solution to “12” could be “12.0001” or “11.89”, based on the tolerance factor. Throughout the present work in all simulations, a tolerance of 0.1% was held constant.

Specifically, numerical computations utilizing the finite element method (FEM) have become popular, due to their ability to handle macro-scale geometries[7]. The basis of this method involves the establishment of a modeling domain, representing a conductive electrolyte in the context of electrochemistry, to which a meshing algorithm is applied to create a finite number of elements[7]. The mesh consists of triangular or quadrilateral elements, with a node at each vertex. The governing equation is then solved at each node through input parameters and boundary conditions, and then the results are interpolated along the vertices and elements.

Derivation of the Laplace equation

The governing equation must contain a balance between accuracy in the system and computational difficulty. As this equation will be solved at each node, the computational time can increase exponentially with new variables introduced. Therefore, simplifying assumptions are most often utilized to reduce the computational cost while still capturing the overarching themes and reactions occurring in the model. This methodology also applies to the mesh. As an example, an infinite number of points exist along a single straight line and solving an infinite number of equations would therefore capture the behavior of the line. However, only two points are truly needed, which largely simplifies the number of equations needed but still captures the behavior of the line; for a triangle, instead, three points are needed and two points would be an *oversimplification*. Refinement of the mesh and addressing which assumptions of the governing equation are *too* simple require local knowledge of the system being studied and often experimental work to confirm the computational assumptions.

With that being said, in electrochemical computations, foundational work has been conducted in literature toward experimentally validating the Laplace equation, which includes simplifying assumptions [12–21]. Below, the Laplace equation will be derived to highlight and understand each specific assumption before moving forward with the computational work.

The most common equation governing the electrochemical behavior of ions in dilute solutions involves the Nernst-Planck equation (Eq. 1.1), which describes the three modes of mass transport[4,22,23].

$$N_i = -D_i \nabla C_i - F z_i u_i C_i \nabla \Phi + v C_i \qquad 1.1$$

where N_i is the ionic flux of each species, D_i is the diffusivity of each species, C_i is the concentration of each species, F is Faraday's constant, z_i is the charge of each species, u_i is the mobility of each species, Φ is the electrolyte potential, and v is the fluid velocity. The del operator (∇) denotes the partial derivation over the spatial domain, $\frac{\partial}{\partial x} + \frac{\partial}{\partial y} + \frac{\partial}{\partial z}$.

The Nernst-Planck equation is composed of three different mass transport mechanisms; the first term (diffusion) is governed by concentration gradients, the second term (migration) is governed by potential gradients, and the final term (convection) is governed by the bulk fluid velocity.

In a closed-system, electroneutrality is generally assumed as charge must be conserved.

$$\sum z_i C_i = 0 \tag{1.2}$$

That is, the each negatively charged species (anions), such as Cl^-, and each positively charged species (cations), such as metal ions (M^{n+}) or Na^+, must balance. This conservation of charge in the electrolyte is not always the case in local regions close to the electrode surface. Note that the most general form of an electrochemical solution does not assume electroneutrality, but instead utilizes Poisson's equation (Eq. 1.3) to solve for charge neutrality[4]. The reactions in Poisson's equation occur on a nm-length or below scale, increasing the computational difficulty.

$$\nabla^2 \Phi = -\frac{F}{\epsilon} \sum z_i C_i \tag{1.3}$$

where ϵ is the dielectric constant. However, the assumption of electroneutrality (Eq. 1.2) is a good approximation for macro-scale geometries.

The current density (i) in the system can also be defined as the summation of ionic flux of each species multiplied by their respective charge.

$$i = F \sum z_i N_i \tag{1.4}$$

These first three equations (Eq. 1.1, Eq. 1.2, and Eq. 1.4) can be used to derive a form of Ohms law. First, through combining Eq. 1.1 and Eq. 1.4,

$$i = F \sum z_i [-D_i \nabla C_i - F z_i u_i C_i \nabla \Phi + v C_i] \tag{1.5}$$

And further simplifying,

$$i = -F \sum z_i D_i \nabla C_i - F^2 \sum z_i^2 u_i C_i \nabla \Phi + F v \sum z_i C_i \tag{1.6}$$

From the electroneutrality Eq. 1.2, the last term in 1.6 (defining the influence of convection mass-transport on the current density) must be zero, which physically means that if all charges are balanced, then an external bulk velocity moving the charges around will not impact the current density.

$$i = -F\sum z_i D_i \nabla C_i - F^2 \sum z_i^2 u_i C_i \nabla \Phi \qquad 1.7$$

There are two conditions for which the influence of diffusion on the current density (that is, the first term in Eq. 1.1 and Eq. 1.7) also falls out: 1) if the concentration gradients within the electrolyte are zero or near-zero ($\nabla C_i = 0$), as could occur through high concentrations of a supporting electrolyte (such as Na^+ and Cl^-) which act to homogenize the solution, or 2) if the potential gradient is much greater than the concentration gradient ($\nabla \Phi \gg \nabla C_i$), as could occur during a galvanic couple with a high potential driving force between the anode and cathode. Therefore, within systems assuming either of the two scenarios described above, the current density relationship can further be simplified,

$$i = -F^2 \sum z_i^2 u_i C_i \nabla \Phi \qquad 1.8$$

The above relationship is an expression of Ohms law, relating i directly with Φ, more clearly seen through defining the conductivity of the solution (κ),

$$\kappa = F^2 \sum z_i^2 u_i C_i \qquad 1.9$$

Combining Eq. 1.8 and Eq. 1.9,

$$i = -\kappa \nabla \Phi \qquad 1.10$$

The conservation of mass must also be satisfied to progress through the derivation of the Laplace equation. As the charge is carried by ions in an electrolyte, the mass-balance throughout the closed system is mandated through,

$$\frac{\partial C_i}{\partial t} = -\nabla \cdot N_i + R_i \tag{1.11}$$

where t is the time, and R_i is the production rate of species in the bulk. Generally, $R_i = 0$, as ions are not created in the *bulk* electrolyte, but rather on the electrode surface. Multiplying both sides of the Eq. 1.11 by the sum of charges on each species $(\sum z_i)$,

$$\sum z_i \left(\frac{\partial C_i}{\partial t}\right) = \sum z_i (-\nabla \cdot N_i) \tag{1.12}$$

And further simplifying,

$$\frac{\partial}{\partial t}(\sum z_i C_i) = -\nabla \cdot \sum z_i N_i \tag{1.13}$$

From the assumed electroneutrality in the system of Eq. 1.2, we can see that the left term of Eq. 1.13 is equal to zero, thereby mandating that the right term of Eq. 1.13 is also zero.

$$\nabla \cdot \sum (z_i N_i) = 0 \tag{1.14}$$

Applying the del operator to both sides of the Eq. 1.4,

$$\nabla \cdot i = F\big(\nabla \cdot \sum (z_i N_i)\big) \tag{1.15}$$

Therefore, Eq. 1.14 and Eq. 1.15 can be combined to represent a form of the conservation of charge,

$$\nabla \cdot i = 0 \tag{1.16}$$

That is, the dot product of the del operator, denoting the *divergence*, of the current density vector is zero. A divergence of zero indicates that there is no outward or inward flux in a closed system, resulting in a *net flux* of zero.

To continue the derivation towards the Laplace equation, the del operator can again be applied to both sides of Eq. 1.10, which results in,

$$\nabla \cdot i = \nabla \cdot (-\kappa \nabla \Phi) \qquad 1.17$$

Simplifying, with the use of charge conservation, Eq. 1.16,

$$\kappa \nabla^2 \Phi = 0 \qquad 1.18$$

Therefore, the Laplace equation is derived,

$$\nabla^2 \Phi = 0 \qquad 1.19$$

And lastly, due to the previous assumption of negligible concentration gradients, the conductivity must be a constant value,

$$\kappa = const. \qquad 1.20$$

Therefore, to derive the Laplace equation, four main equations are needed, Eq. 1.1 (Nernst-Planck equation), Eq. 1.2 (electroneutrality assumption), Eq. 1.4 (current density definition), and Eq. 1.11 (conservation of mass). In addition, four important equations were derived, Eq. 1.10 (a form of Ohms law), Eq. 1.16 (a form of conservation of charge), Eq. 1.20 (constant conductivity), and Eq. 1.19 (Laplace equation).

The purpose of the derivations above are to clearly identify what assumptions and limitations are implicit when using the Laplace equation as the governing system over the computational domain. Therefore, it can be determined that three main assumptions are necessary when using the Laplace equation, and from those assumptions two further limitations result from the derivation. The first three assumptions are 1) a dilute solution, to use the Nernst-Planck equation (Eq. 1.1), 2) electroneutrality (Eq. 1.2) and negligible concentration gradients ($\nabla C_i \cong 0$), whereas the resulting limitations from these assumptions were a form of the conservation of charge (Eq. 1.16) and constant conductivity (Eq. 1.20).

Note that the diffusivity and migration transport of *minor* species can be tracked, as long as a supporting electrolyte is present to maintain a constant concentration (*i.e.*, with no global concentration gradients). In such cases, the mobility of each species is simplified via the Nernst-Einstein relationship (Eq. 1.21), in which the diffusivity and mobility are assumed to be equivalent. Additionally, this assumption is only strictly valid in dilute solutions. Moraes *et al.*, offers a thorough discussion on when the transport of these minor species may be useful, or even necessary, through comparing various models including or excluding the transport of minor species[24].

$$u_i = \frac{D_i}{RT} \tag{1.21}$$

The Laplace equation is therefore a useful simplification to solving the full Nernst-Planck equation and requires much fewer computational resources. The natural question, then, would be in which systems are the inherent assumptions above valid, thereby determining when the simplifications of the Laplace equation can be utilized. This question is non-trivial, but significant progress in the field has been made through experimental validation of the Laplace equation for various systems[12–21]. Specifically, Murer *et al.*, conducted simulations of a planar pure Al/Al4%Cu alloy galvanic couple utilizing both the Laplace equation and the full Nernst-

Planck, and compared the solutions from both methods with the experimental scanning vibrating electrode technique (SVET)[12]. The Laplace equation seemed to better capture the experimentally determined magnitudes of current, with the caveat that the boundary conditions are correct.

In addition, Liu *et al.,* created a thorough investigation of a Laplacian-based FEM model[23,25–27], with experimental validation conducted on planar stainless steel (SS)/Zn galvanic couple through optical profilometry[13]. Galvanic couples with SS304/AA7050 in a fastener/panel design were also simulated with the Laplace equation, but computational results were never validated in this geometrically-complex design[27].

Snihirova *et al.,* also created a countersunk fastener/panel FEM model, although utilizing a simplified Nernst-Planck equation with only diffusion and migration terms, through a Ti-6Al-4V/AA2024 galvanic couple with electrolyte only assumed to be over the surface[28]. That is, no electrolyte was within the fastener hole. Experimental validation took place through comparisons with the SVET-derived current density and concentration of oxygen. However, it was not determined if the diffusion mass-transport term could be ignored in the system (and therefore, assume the Laplace equation) and solution within the occluded region of the fastener hole was not investigated.

Note that FEM computations on fastener geometries have not only been conducted in the field of electrochemistry, but also in the interdisciplinary field of stress corrosion cracking (SCC). Specifically, work conducted by Harrison *et al.,*[29–32] and Lo *et al.,*[33] focus on using FEM on a fastener-hole geometry to predict the stress fields and crack propagation, if a corrosion pit or intergranular corrosion is already present. That is, simulating a terminal scenario in which severe corrosion in the stress-concentrating area acts to initiate cracking, with the goal of understanding the crack propagation to failure. However, as no consideration was given to the corrosion process itself, let alone to any galvanic coupling effects of a noble fastener or any surface corrosion, mitigation techniques to prevent the mechanical failure were impossible.

Crevice and Galvanic Corrosion

Crevice corrosion, which occurs within an occluded region between two faying surfaces, either of the same material or with one inert crevice former, has been well studied in literature on aluminum alloys and stainless steels[34–43]. The limited mass transport associated with the occluded crevice region leads to an accumulation of aggressive species; as an example, the aluminum hydrolysis (Eq. 1.22) produces H^+ ions, which correspondingly lowers the pH.

$$4\mathrm{Al}^{3+} + 12\mathrm{H_2O} \rightarrow 4\mathrm{Al(OH)_3} + 12\mathrm{H}^+ \qquad 1.22$$

In bulk conditions, the H^+ ions are consumed via the cathodic oxygen reduction reaction (ORR) (Eq. 1.23) and hydrogen evolution reaction (HER) (Eq. 1.24) in acidic conditions, which both correspondingly increases the pH to balance out the system.

$$\mathrm{O_2} + 4\mathrm{H}^+ + 4\mathrm{e}^- \rightarrow 2\mathrm{H_2O} \qquad 1.23$$

$$2\mathrm{H}^+ + 2\mathrm{e}^- \rightarrow \mathrm{H_2(g)} \qquad 1.24$$

However, in occluded regions with cathodic reactions occurring on an external surface, the pH inside of the crevice is lowered while the pH outside of the crevice is increased. In addition, the mass-transport of species is constrained in the crevice, as opposed to being facilitated in bulk conditions, and diffusion of the aggressive species outside of the pit is limited. Decreasing pH values further accelerates the breakdown of the natural passive oxide on aluminum, Al_2O_3, as seen in the Pourbaix diagram of Figure 1.2, assuming thermodynamic equilibrium.

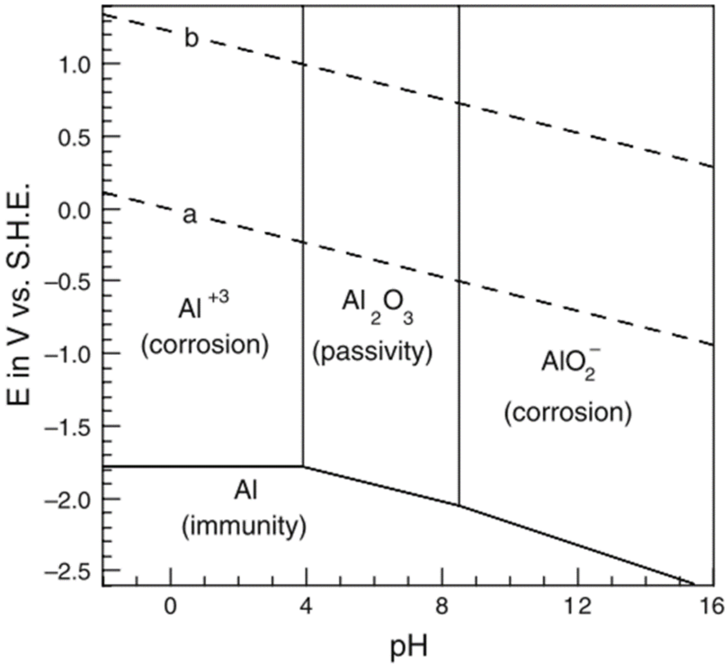

Figure 1.2: Pourbaix diagram of aluminum[22,44]

These conditions described above lead to the often-hidden crevice corrosion, which can produce more corrosion damage than would be expected from the bulk solution, due to the aggressive local conditions. Therefore, considerable work has focused on determining under which conditions the aggressive species will accumulate and that crevice corrosion will occur. Broadly speaking, Oldfield & Sutton proposed that ten different variables may affect crevice corrosion: the crevice geometry (gap and length), the total geometry of the sample, the crevice solution composition, the bulk solution composition, the bulk solution environment, mass transport, the electrochemical reactions, the passive film characteristics, the alloy composition, and the crevice type[45]. In addition, under a given environment on a specific material, a geometric scaling law (Eq. 1.25) was determined to be necessary to create a critical crevice solution (CCS) and initiate any crevice attack as the geometry was scaled to larger or smaller values[38,42,43].

$$\frac{x^2}{g} = const \tag{1.25}$$

where x is the critical distance into the crevice at which the corrosion will initiate and g is the crevice gap or the height between the base panel and crevice former.

As stated previously, crevice corrosion denotes the accumulation of aggressive solution within a single material or when an inert crevice former is in contact with the material of interest. However, often in modern structures, multiple materials are in electrochemical contact through a conducting electrolyte, leading to the possible addition of galvanic corrosion. This form of corrosion, often studied in planar geometries as a simplification to more-complex systems, provides a driving force for higher corrosion rates on the more active material through cathodic reactions occurring on a more-noble material[5].

Complex fastener/panel designs incorporate both the occluded crevice features within the fastener hole, and the driving force for accelerated corrosion on the anode through the noble fastener and active panel. Experimental work has therefore determined that severe corrosion is a result from these systems. Specifically, through using the zero-resistance ammeter (ZRA) technique, Feng *et al.,*[1,46–49], Wang *et al.,*[50,51], Boerstler *et al.,*[52–54], and Jokar *et al.,*[55], have conducted a thorough investigation on the galvanic current flowing through each fastener (in a multi-fastener system). Although the occluded region of the fastener was present, any contributions were attempted to be removed via electrochemically isolating the crevice with plastic tape and therefore were not investigated as a part of the works above.

Utilizing a μm-scale version of a fastener and panel, through a SS316 pin inserted into an AA7050 cylinder, Rafla *et al.,* was able to isolate corrosion that was *only* within the creviced region[56–59]. In addition, Rafla *et al.,* was able to conduct a larger-scale replica (mm-scale) of a

SS316/AA7050 fastener/panel cross-section using a coupled microelectrode array (CMEA), which allowed for electrochemical monitoring of both the surface and crevice as a function of time[60]. It was determined that anodic charge within the fastener/panel cross-section was 3.5 times greater than that on a planar electrode geometry, highlighting the importance that the crevice may play on the overall system[60]. Although hugely successful in advancing the field towards the realistic fastener geometries and cyclic wet/dry atmospheric conditions, an experimental limitation of the CMEA is the uneven potential distribution and possible edge-effects of each wire electrode. In addition, due to the complexity of the CMEA setup, testing a variety of geometric or environmental parameters through this method could be extremely tedious and non-cost effective.

Lastly, corrosion within a realistic fastener hole was observed by Young & Payer[61] and Moran *et al.*,[62] through cross-sectional metallographic analysis. The countersunk fastener was Cd-plated SS and was inserted into either an AA2024 or AA7075 panel, with a mechanism proposed to explain the corrosion initiation with both alloys and within the fastener hole geometry[61,62]. Fissures up to 2 mm in length were observed and indicated as SCC, although no external stress was applied on the panel, and statistical corrosion events were documented[61,62]. Although severe corrosion within the countersunk fastener hole was observed, the post-metallographic analysis was destructive and not practical to monitor the health of existing structures. In addition, the statistical damage metrics were only conducted on the countersunk portion of the fastener hole, and the total damage within the remainder of the fastener hole or on the surface of the panel were not considered.

Therefore, crevice corrosion and galvanic corrosion can clearly coincide in the same system, although none of the works above have addressed this issue. Of particular note is that no one has previously determined if the crevice in their system would corrode *without* the presence of the more-noble fastener material. In such cases, the term galvanic-*induced* crevice corrosion would describe the process of crevice corrosion being initiated *only* through the increased driving force due to the galvanic couple. This term has been coined in this work and will be used going forward. However, the severe corrosion from these geometries could not solely be attributed to galvanic effects, as seen through the difference in planar vs. creviced CMEA designs by Rafla *et al.,*[60], leading to the conclusion of a combined galvanic- and crevice-effect.

Pitting Corrosion

Pitting corrosion is an autocatalytic phenomenon which occurs in three phases: 1) initiation, 2) metastable pit growth, 3) stable pit growth[63–66]. Initiation may appear stochastic, but that is only due to the many possible nucleation sites on a given surface, such as surface inclusions, surface roughness features, or chemical inhomogeneities within the solution[67–72]. Once stable growth occurs, the pit can take a number of shapes depending on the mechanisms at hand, including an undercutting phenomenon inducing a “lacy cover” appearance on the surface of the sample[73–75]. However, once initiated and before stable growth occurs, the metastable pit is at a precipice at which it can continue towards stable growth or repassivate (*i.e.,* cease growing). What parameters or local environmental conditions which result in a metastable pit repassivating, as opposed to undergoing stable growth, have been a popular topic of research since the 1960’s as controlling (or even, understanding) repassivation could aid to the maintenance of all structures built with pitting-susceptible materials, such as stainless steels and aluminum alloys[66,76–82]. Two conventional pit stability thresholds have been proposed in literature, Galvele’s pit stability product $(i \cdot x)$[77,78,83] and the repassivation potential $\left(E_{rp}\right)$[76]. Although both representing the lower limit of pitting, these two thresholds have never *directly* been compared. Srinivasan &

Kelly *indirectly* compared these thresholds through calculated the experimental time to repassivation (via E_{rp}) and the theoretical time for the pit to dilute to a critical concentration (via $(i \cdot x)$)[84]. Through unifying these values (*i.e.,* at the point when both times were equal), a critical fraction of salt film saturation was determined to be 50%[84].

Note also that 1-D pitting occurs through an accumulation of aggressive species much in the same way as crevice corrosion, with the base of the pit actively corroding rather than the surface of the crevice, which would be analogous to the pit walls. Such 1-D pits have been popular to determine pitting mechanisms, as individual parameters could be isolated, although not necessarily representing the complexity of 3-D pit geometries and pit interactions in bulk samples. Experimental and computational work have been used to investigate different aspects of single pits, such as the salt film growth at the base of the pit[85–90], the passive oxide film at the top of the pit[91–93], as well as the effects of electrochemical pitting parameters[94–96].

One numerical method was developed to represent the maximum radius at which a single pit could theoretically grow when surrounded by an idealized flat cathodic surface. This numerical model, denoted as the maximum pit model, was able to bound the problem of pitting; that is, even if stable pit growth was to occur, the worst-case scenario would be a pit of the calculated maximum size [97–101]. Extensions of this model predicted the maximum radius for different environments (*i.e.,* solution concentrations, solution composition, WL) and accounted for precipitation reactions[100]. The premise of this model balanced the demand for current from the anode (calculated through $(i \cdot x)$) and the cathodic current capacity (calculated through E_{rp}) to determine the maximum radius at which a pit to grow. However, throughout these calculations the potential and current distributions along the length of the cathode were not considered, as a mathematical simplification. Due to pits generally being on the order of µm-scale and the external cathode diameters being on the order of cm-scale, the cathode:anode surface area is generally extremely large, which would lead to high levels of ohmic potential drop across the surface[6].

Two recent pitting frameworks have been proposed to address pitting mechanisms and repassivation theories. The first, from Srinivasan *et al.,*[84,102–104] utilized computational and experimental 1-D pit scans to measure both $(i \cdot x)$ and E_{rp} in the same experiment and proposed a critical pH (pH_{crit}) to initiate repassivation, based on the work from Okada *et al.,*[91,92]. The second framework, from a series of papers by Li, Scully, and Frankel, introduces new pitting threshold parameters to measure in 1-D and 3-D bulk scans, and propose a diffusion limited current density at a critical fraction of salt film saturation[63,86,105–108]. Multiple works have already begun measuring these new pitting thresholds[85,109,110]. Both new pitting frameworks have contributed to advance the field of localized corrosion. However, the lower threshold for pitting still remains problematic, as the first framework offered no experimental validation for the pH_{crit}, only theoretical Tafel predictions, and the second framework's equivalent lower threshold to E_{rp} (E_{crit}) is difficult to observe and measure based on its dependence on scan rate and pit depth[86,104].

1.2 Objectives

The overall objective of this work was to investigate localized corrosion (crevice and pitting corrosion) through a FEM perspective, with the goal of predicting and mitigating geometric and environmental parameters which would put the given system at risk for severe corrosion or mechanical failure (Figure 1.3).

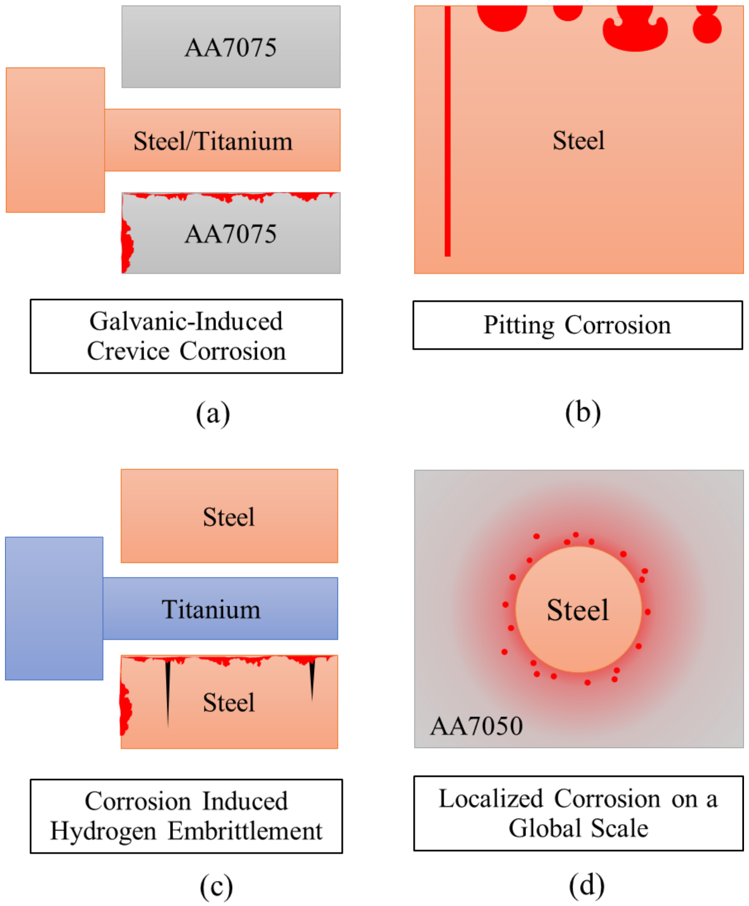

Figure 1.3: A schematic overview of the three main sections and goals presented in this work, (a) Section 1: Galvanic-Induced Crevice Corrosion, (b) Section 2: Pitting Corrosion, (c) and (d) Section 3: Computational Methodologies to Accommodate Complex Systems. Red areas indicate schematics of the corrosion location and morphology studied.

Specifically, the present work in Section 1 built off of the foundational literature described above through creating a FEM model which uses the Laplace equation on a complex realistic-scale SS316/AA7075 or Ti-6Al-4V/AA7075 fastener/panel geometry with electrolyte within the occluded regions of the fastener hole (Figure 1.3(a)). Experimental validation on this complex geometry was conducted through macro-scale cross-sectional metallographic analysis, and through comparison with current densities measured in literature through a ZRA. Specific limitations determined through this work were addressed, such as when the Laplace equation assumptions hold and under which conditions the assumptions breakdown.

Section 2 of this work assumed that a single pit on SS316 has already initiated, but has not yet reached stable growth, to computationally investigate the repassivation effects. Multiple pit shapes, sizes, cathode sizes, and environmental conditions were investigated, with the resulting potential and current density distributions used to quantify the repassivation behavior (Figure 1.3(b)). Both $(i \cdot x)$ and E_{rp} were tested as stability parameters and were compared. A unified description of pitting literature and a less-conservative calculation of E_{rp} was proposed.

Lastly, in Section 3 of this work the computational methodology developed in both Sections 1 and 2 was extended to account for more complex processes, such as incorporating pitting hot spots in an occluded region and accounting for globally pitted surfaces (Figure 1.3(c) and (d)). The first two chapters in this section combine FEM with fracture mechanics, with the goal of mitigating SCC through both lowering the crack growth rate and through lowering the corrosion rate, in a variety of environmental conditions (Figure 1.3(c)). The last chapter focuses on validating a computational model which can account for global pitting events on AA7050, induced via the galvanic coupling with SS316, not through capturing the local hot spots but through capturing the overall average current density and current behavior of the actively corroding surface (Figure 1.3(d)).

Three reoccurring words in the present text which encompass the methodology of this work are **validation, prediction,** and **mitigation**. Experimental electrochemical techniques, from metallographic analysis to ZRA to SVET, were used to **validate** the computational model in this work. That is, experimental and computational results were compared; if similar values and trends were seen between the computational predictions and experimental observations, then the model was considered validated. **Prediction** was conducted with the validated model, in which either the geometry or environment (corresponding often to a change in the boundary conditions) were varied, but the overall assumptions within the model stayed constant. After determining the severity of the corrosion under investigation, mitigation was found to be needed. **Mitigation** techniques varied from cathodic surface coatings and surface treatments, to sacrificial coatings and surface defect geometries to pull the majority of current out of high-stress areas.

Lastly, this work also provided full transparency in the area of limitations in the sections described above. Limitations are therefore specified within each section, and act as a transition to the future-work section, described in Chapter 10. The goal of the transparency in this work is that it will lead to future investigations, as this work was built on the investigation of so many others.

Below is an overview of the respective objectives on each section of the work.

<u>Section 1: Galvanic-Induced Crevice Corrosion</u>

- Develop and experimentally validate a computational model capable of capturing the corrosion behavior of a complex galvanic couple in a fastener/panel design
- Use the validated computational model described above to investigate corrosion within the fastener hole, to determine the underlying mechanism and possible mitigation strategies
- Discuss limitations to the Laplacian model, with specific examples in which the assumptions are not valid

<u>Section 2: Pitting Corrosion</u>

- Use finite element method (FEM) modeling to investigate the autocatalytic nature of pitting, with a focus on the thresholds determining if a pit will repassivate or reach stable growth
- Determine the impact of pit geometry, cathode size, water layer thickness, and NaCl molarity variations on the stability of a single pit
- Unify multiple pitting theories and parameters described in literature and suggest a less-conservative calculation of the repassivation potential $\left(E_{rp}\right)$ in the context of $(i \cdot x)$

Section 3: Computational Methodologies to Accommodate Complex Systems

- Combine FEM and linear elastic fracture mechanics (LEFM) techniques to develop a framework to mitigate stress corrosion cracking through hydrogen embrittlement (HE) within the fastener hole
- Expand the above methodology to atmospheric conditions, considering two relative humidities (RH) at a constant loading density (LD), and determine mitigation strategies based on which material combinations decrease HE cracking susceptibility
- Build a computational model which is able to incorporate the local corrosion of pitting on a macro-scale surface, in contrast to focusing on a single pit

1.3 References

1. Feng, Z., and G.S. Frankel, *Corrosion* 70 (2014): pp. 95–106.

2. Compton, K.G., A. Mendizza, and W.W. Bradley, *Corrosion* 11 (1955): pp. 35–44, http://corrosionjournal.org/doi/abs/10.5006/0010-9312-11.9.35.

3. Benavides, S., ed., *Corrosion Control in the Aerospace Industry* (Woodhead Publishing, 2009).
4. Newman, J., and K.E. Thomas-Alyea, *Electrochemical Systems*, Third Edit (Wiley-Interscience, 2004).
5. Oldfield, J.W., *ASTM Special Technical Publication* STP (1988): pp. 5–22.
6. Mansfeld, F., *Corrosion* 27 (1971): pp. 436–442.
7. Munn, R.S., and O.F. Devereux, *Corrosion* 47 (1991): pp. 618–634.
8. Helle, H.P.E., G.H.M. Beek, and J.T. Ligtelijn, *Corrosion* 37 (1981): pp. 522–530.
9. King, A.D., J.S. Lee, and J.R. Scully, *J Electrochem Soc* 163 (2016): pp. 342–356.
10. Tattersall, C., "Modeling and Analysis of Geometrically Complex Corrosion," University of Virginia, 2018.
11. Turner, M.E., "Finite Element Modeling of Galvanic Corrosion of Metals," Masters of Engineering, Rensselaer Polytechnic Institute, 2012.
12. Murer, N., R. Oltra, B. Vuillemin, and O. Néel, *Corrosion Science* 52 (2010): pp. 130–139, http://dx.doi.org/10.1016/j.corsci.2009.08.051.
13. Liu, C., G.W. Kubacki, and R.G. Kelly, *Corrosion Journal* 75 (2019): pp. 465–473.
14. Murer, N., N.A. Missert, and R.G. Buchheit, *Journal of The Electrochemical Society* 159 (2012): p. C265, http://jes.ecsdl.org/cgi/doi/10.1149/2.102206jes.
15. Thébault, F., B. Vuillemin, R. Oltra, C. Allely, and K. Ogle, *Electrochimica Acta* 82 (2012): pp. 349–355, http://dx.doi.org/10.1016/j.electacta.2012.04.068.
16. Thébault, F., B. Vuillemin, R. Oltra, C. Allely, and K. Ogle, *Corrosion Science* 53 (2011): pp. 201–207.

17. Deshpande, K.B., *Corrosion Science* 52 (2010): pp. 3514–3522.

18. Thébault, F., B. Vuillemin, R. Oltra, K. Ogle, and C. Allely, *Electrochimica Acta* 53 (2008): pp. 5226–5234.

19. Haque, Z., B.A. Clark, and R.S. Lillard, *Corrosion* 74 (2018): pp. 903–913.

20. Kramer, P., T. Curtin, M. Merrill, M. Kim, F. Friedersdorf, and R. Adey, "Atmospheric Corrosion Measurements to Improve Understanding of Galvanic Corrosion of Aircraft," in NACE International: CORROSION (2018), pp. 1–11.

21. Adey, R., A. Peratta, J. Baynham, and T. Curtin, "Predicting Cumulative Galvanic Corrosion Damage in Aircraft Structures," in North Atlantic Treaty Organization Science and Technology Organization (2018), pp. 1–14.

22. McCafferty, E., *Introduction to Corrosion Science* (Springer, 2010).

23. Liu, C., and R.G. Kelly, *Corrosion Journal* 75 (2019): pp. 1285–1299.

24. Moraes, C. v., R.J. Santucci, J.R. Scully, and R.G. Kelly, *Journal of The Electrochemical Society* 168 (2021): p. 051505.

25. Liu, C., and R.G. Kelly, *The Electrochemical Society Interface* 23 (2014): pp. 47–51.

26. Liu, C., J. Srinivasan, and R.G. Kelly, *J Electrochem Soc* 164 (2017): pp. C845–C855, http://jes.ecsdl.org/lookup/doi/10.1149/2.1641713jes.

27. Liu, C., V.N. Rafla, J.R. Scully, and R.G. Kelly, "Mathematical Modeling of Potential and Current Distributions for Atmospheric Corrosion of Galvanic Coupling in Airframe Components," in NACE International: CORROSION (2015), pp. 1–11.

28. Snihirova, D., D. Höche, S. Lamaka, Z. Mir, T. Hack, and M.L. Zheludkevich, *Corrosion Science* 157 (2019): pp. 70–78, https://doi.org/10.1016/j.corsci.2019.04.036.

29. Harrison, T.J., "Intergranular Corrosion Protocol Development for 7075-T651 Extrusion," in 28th International Congress of the Aeronautical Sciences (2012), pp. 1–7.

30. Harrison, T.J., B.R. Crawford, G. Clark, and M. Brandt, *Advanced Materials Research* 891–892 (2014): pp. 242–247, https://www.scientific.net/AMR.891-892.242.

31. Harrison, T.J., B.R. Crawford, M. Brandt, and G. Clark, *Computational Materials Science* 84 (2014): pp. 74–82, http://dx.doi.org/10.1016/j.commatsci.2013.11.033.

32. Harrison, T.J., B.R. Crawford, C. Loader, G. Clark, and M. Brandt, *International Journal of Fatigue* 82 (2016): pp. 700–707, http://dx.doi.org/10.1016/j.ijfatigue.2015.09.028.

33. Lo, M., R. Jones, A. Bowler, M. Dorman, and D. Edwards, *Fatigue and Fracture of Engineering Materials and Structures* 40 (2017): pp. 1664–1675.

34. Alavi, A., and R.A. Cottis, *Corrosion Science* 27 (1987): pp. 443–451.

35. Sharland, S.M., *Corrosion Science* 27 (1987): pp. 289–323.

36. Sharland, S.M., and P.W. Tasker, *Corrosion Science* 28 (1988): pp. 603–620.

37. Sharland, S.M., C.P. Jackson, and A.J. Diver, *Corrosion Science* 29 (1989): pp. 1149–1166.

38. Vankeerberghen, M., *Corrosion* 60 (2004): pp. 707–717.

39. Rosenfeld, I.L., and I.K. Marshakov, *Corrosion* 20 (1964): pp. 115–125.

40. Laycock, N.J., J. Stewart, and R.C. Newman, *Corrosion Science* 39 (1997): pp. 1791–1809.

41. Alkire, R., and T. Tomasson, *Electrochemical Society Extended Abstracts* 132 (1985): pp. 1027–1031.

42. Lee, J.S., M.L. Reed, and R.G. Kelly, *Journal of The Electrochemical Society* 151 (2004): pp. B423–B433.

43. Kelly, R.G., and J. Lee, *Localized Corrosion: Crevice Corrosion*, Encyclopedia of Interfacial Chemistry (Elsevier, 2018), http://dx.doi.org/10.1016/B978-0-12-409547-2.13420-1.

44. Deltombe, E., and M. Pourbaix, *Corrosion* 14 (1958): pp. 16–20.

45. Oldfield, J.W., and W.H. Sutton, *British Corrosion Journal* 15 (1980): pp. 31–34.

46. Feng, Z., "Galvanic Corrosion of Coated Al Alloy Panels with More Noble Fasteners," The Ohio State University, 2015.

47. Feng, Z., G.S. Frankel, and C.A. Matzdorf, *J Electrochem Soc* 161 (2014): pp. 42–49, http://jes.ecsdl.org/cgi/doi/10.1149/2.059401jes.

48. Feng, Z., J. Boerstler, G.S. Frankel, and C.A. Matzdorf, *Corrosion* 71 (2015): pp. 771–783.

49. Feng, Z., G.S. Frankel, W.H. Abbott, and C.A. Matzdorf, *Corrosion* 72 (2016): pp. 342–355.

50. Wang, S., and G.S. Frankel, *Corrosion* 74 (2018): pp. 444–456.

51. Wang, S., J. Boerstler, and G.S. Frankel, *Corrosion* 74 (2018): pp. 499–508.

52. Boerstler, J.T., "Corrosion Degradation of Coated Aluminum Alloy Systems through Galvanic Interactions," The Ohio State University, 2018.

53. Boerstler, J.T., M. Jokar, and G.S. Frankel, *Corrosion Engineering, Science and Technology* (2020): pp. 1–14, https://doi.org/10.1080/1478422X.2020.1740856.

54. Boerstler, J.T., M. Jokar, and G.S. Frankel, *Corrosion Engineering, Science and Technology* (2020): pp. 1–13, https://doi.org/10.1080/1478422X.2020.1732113.

55. Jokar, M., and G.S. Frankel, *Materials and Corrosion* (2022).

56. Rafla, V., A. Davenport, and J.R. Scully, *Corrosion Communications* 71 (2015): pp. 1171–1176.

57. Rafla, V.N., A.D. King, S. Glanvill, A. Davenport, and J.R. Scully, *Corrosion* 74 (2018): pp. 5–23.

58. Rafla, V.N., and J.R. Scully, *Corrosion* 75 (2019): pp. 587–603.

59. Rafla, V., A. Davenport, and J.R. Scully, *Corrosion, Poster Award Research Letters* 71 (2015): pp. 1300–1303.

60. Rafla, V.N., and J.R. Scully, *Corrosion Journal* 75 (2019): pp. 12–28.

61. Young, P.S., and J.H. Payer, *Corrosion* 71 (2015): pp. 1278–1293.

62. Moran, A., J. Jennings, H. Nee, S. Pearson, B. Clark, and R.S. Lillard, *Corrosion Journal* 75 (2019): pp. 484–498.

63. Frankel, G.S., T. Li, and J.R. Scully, *J Electrochem Soc* 164 (2017): pp. C180–C181.

64. Kreider, K.L., J.M. Mckinnon, C.B. Clemons, R.S. Lillard, and G.W. Young, *Corrosion Science* 179 (2021): p. 109086.

65. Frankel, G.S., *Journal of The Electrochemical Society* 145 (1998): pp. 2186–2198.

66. Pistorius, P.C., and G.T. Burstein, *Phil. Trans. R. Soc. Lond A* (1992): pp. 531–559.

67. Moayed, M.H., N.J. Laycock, and R.C. Newman, *Corrosion Science* 45 (2003): pp. 1203–1216.

68. Zhang, T., D. Wang, Y. Shao, G. Meng, and F. Wang, *Corrosion Science* 58 (2012): pp. 202–210, http://dx.doi.org/10.1016/j.corsci.2012.01.026.

69. Budiansky, N.D., L. Organ, J.L. Hudson, and J.R. Scully, *J Electrochem Soc* 152 (2005): pp. B152–B160.

70. Harwell, A., M.D. Division, and E.O.X. Ora, *J Electrochem Soc* 132 (1985): pp. 1796–1804.

71. Shibata, T., *Corrosion* 52 (1996): pp. 813–830, http://meridian.allenpress.com/corrosion/article-pdf/52/11/813/1532784/1_3292074.pdf.

72. Williams, D.E., C. Westcott, and M. Fleischmann, *J Electrochem Soc* 132 (1985): pp. 1804–1811.

73. Ghahari, M., D. Krouse, N. Laycock, T. Rayment, C. Padovani, M. Stampanoni, F. Marone, R. Mokso, and A.J. Davenport, *Corrosion Science* 100 (2015): pp. 23–35, http://dx.doi.org/10.1016/j.corsci.2015.06.023.

74. Jafarzadeh, S., Z. Chen, J. Zhao, and F. Bobaru, *Corrosion Science* 150 (2019): pp. 17–31, https://doi.org/10.1016/j.corsci.2019.01.006.

75. Wang, K., M. Salasi, and M. Iannuzzi, *J Electrochem Soc* 168 (2021): p. 041502.

76. Pourbaix, M., L. Klimzack-Mathieiu, C. Mertens, J. Meunier, C. Vanleugenhaghe, L. de Munck, J. Laureys, L. Neelemans, and M. Warzee, *Corrosion Science* 3 (1963): pp. 239–259.

77. Galvele, J.R., *Corrosion Science* 47 (2005): pp. 3053–3067.

78. Galvele, J.R., *J Electrochem Soc* 123 (1976): pp. 464–474.

79. Newman, R., *The Electrochemical Society Interface* 19 (2010): pp. 33–38.

80. Szklarska-Smialowska, Z., *Corrosion Science* 41 (1999): pp. 1743–1767.

81. Schwenk, W., *Corrosion* 20 (1964): pp. 129t–139t.

82. Pride, S.T., J.R. Scully, and J.L. Hudson, *J Electrochem Soc* 141 (1994): pp. 3028–3040.

83. Newman, R.C., M.A.A. Ajjawi, H. Ezuber, and S. Turgoose, *Corrosion Science* 28 (1988): pp. 471–477.

84. Srinivasan, J., and R.G. Kelly, *J Electrochem Soc* 163 (2016): pp. C759–C767.

85. Tavassolian, R., M.H. Moayed, and M. Mirjalili, *J Electrochem Soc* 168 (2021): p. 111505.

86. Li, T., J.R. Scully, and G.S. Frankel, *J Electrochem Soc* 166 (2019): pp. C3341–C3354.

87. Sun, X., J. Srinivasan, R.G. Kelly, and R. Duddu, *Corrosion Science* 179 (2021): p. 109130, https://doi.org/10.1016/j.corsci.2020.109130.

88. Gaudet, G.T., W.T. Mo, T.A. Hatton, J.W. Tester, J. Tilly, H.S. Isaacs, and R.C. Newman, *AIChE Journal* 32 (1986): pp. 949–958.

89. Hakkarainen, T., "Factors Determining the Dissolution Rate in Pitting Corrosion of Stainless Steels," in Electrochemical Methods in Corrosion Research, ed. M. Duprat (Trans Tech Publications Ltd, 1986), pp. 81–90.

90. Hakkarainen, T., "Electrochemical Conditions inside Growing Corrosion Pits in Stainless Steel," in NACE: Advances in Localized Corrosion, eds. H.S. Isaacs, U. Bertocci, J. Kruger, and S. Smialowska (1990), pp. 277–282.

91. Okada, T., *J Electrochem Soc* 131 (1984): pp. 241–247.

92. Okada, T., *J Electrochem Soc* 131 (1984): pp. 1026–1032.

93. Anderko, A., N. Sridhar, and D.S. Dunn, *Corrosion Science* 46 (2004): pp. 1583–1612.

94. Laycock, N.J., and S.P. White, *J Electrochem Soc* 148 (2001): pp. B264–B275.

95. Laycock, N.J., and R.C. Newman, *Corrosion Science* 39 (1997): pp. 1771–1790.

96. Nyby, C., X. Guo, J.E. Saal, S.-C. Chien, A.Y. Gerard, H. Ke, T. Li, P. Lu, C. Oberdorfer, S. Sahu, S. Li, C.D. Taylor, W. Windl, J.R. Scully, and G.S. Frankel, *Sci Data* 8 (2021): pp. 1–11.

97. Chen, Z.Y., and R.G. Kelly, *J Electrochem Soc* 157 (2009): pp. 69–78.

98. Chen, Z.Y., F. Cui, and R.G. Kelly, *J Electrochem Soc* 155 (2008): pp. 360–368.

99. Katona, R.M., J. Carpenter, E.J. Schindelholz, and R.G. Kelly, *J Electrochem Soc* 166 (2019): pp. C3364–C3375.

100. Katona, R.M., A.W. Knight, E.J. Schindelholz, C.R. Bryan, R.F. Schaller, and R.G. Kelly, *Electrochimica Acta* 370 (2021): p. 137696, https://doi.org/10.1016/j.electacta.2020.137696.

101. Woldemedhin, M.T., M.E. Shedd, and R.G. Kelly, *J Electrochem Soc* 161 (2014): pp. E3216–E3224.

102. Srinivasan, J., C. Liu, and R.G. Kelly, *J Electrochem Soc* 163 (2016): pp. C694–C703.

103. Srinivasan, J., and R.G. Kelly, *J Electrochem Soc* 163 (2016): pp. C768–C777.

104. Srinivasan, J., and R.G. Kelly, *Corrosion* 73 (2017): pp. 613–633.

105. Li, T., J.R. Scully, and G.S. Frankel, *J Electrochem Soc* 165 (2018): pp. C484–C491.

106. Li, T., J.R. Scully, and G.S. Frankel, *J Electrochem Soc* 165 (2018): pp. C762–C770.

107. Li, T., J.R. Scully, and G.S. Frankel, *J Electrochem Soc* 166 (2019): pp. C115–C124.

108. Li, T., J. Wu, and G.S. Frankel, *Corrosion Science* 182 (2021): p. 109277, https://doi.org/10.1016/j.corsci.2021.109277.

109. Wang, K., M. Salasi, and M. Iannuzzi, *J Electrochem Soc* 168 (2021): p. 121504.

110. Wang, K., M. Salasi, S. Bakhtiari, and M. Iannuzzi, *J Electrochem Soc* 168 (2021): p. 061506.

Galvanic-Induced Crevice Corrosion

Summary

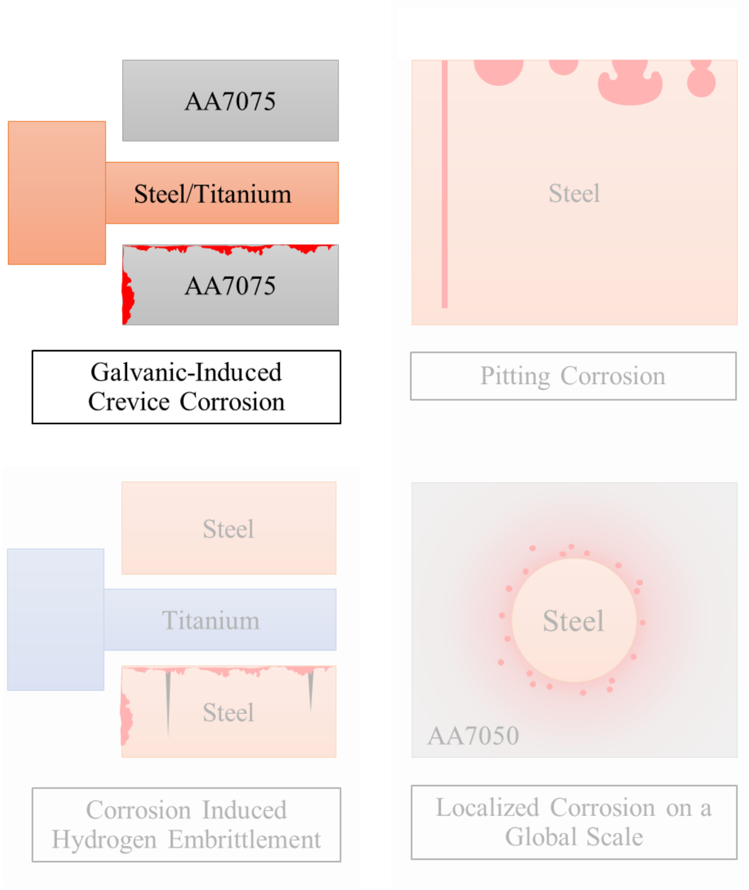

In this first section of this dissertation, a Laplacian-based FEM, machine learning techniques, and cross-sectional metallographic analysis were used to investigate various geometric and environmental effects which may impact galvanic-induced crevice corrosion in a fastener/panel design. Chapter 2 first focuses on the experimental **validation** of the Laplacian model, and confirmation of the galvanic-induced localized corrosion behavior under salt spray conditions (B117), which constitute a representative bulk water layer thickness (WL) for the cathodic kinetics over the surface of the sample. Note that "bulk WL" conditions herein represent a finite

WL (~ 800 µm to $4{,}000$ µm) which are greater than the natural convection boundary layer thickness (δ_{nc}), thereby not influencing the cathodic kinetics, but are *not* representing an infinite full-immersion WL, as the ohmic solution resistance may still have a contribution, albeit small. It was determined that the presence and size of an external cathodic surface area are the main driving force for galvanic-induced crevice corrosion, and are necessary when using Laplacian based models, as occluded cathodic surface reactions mitigate the current density through production of hydroxyl and consumption of H^+ which is not accounted for through the Laplace equation.

Chapters 3 and 4 then take the validated model and **predict** the current distributions under a variety of conditions. Specifically, Chapter 3 evaluates the throwing power (*i.e.*, galvanic coupling distance) of a raised and countersunk fastener in bulk conditions, with three different cathodic materials considered. It was determined that a raised SS316 fastener can significantly couple with an AA7075 panel (increasing the corrosion rate by 50%) up to distances of two inches from the fastener. Countersunk fasteners have a lower throwing power in terms of distance, but instead concentrate the majority of current into the fastener hole.

Chapter 4 focuses on predicting the magnitude and distribution of current within the occluded fastener hole, investigating both representative-bulk WL and atmospheric WL, with the goal to mitigate corrosion within the high-stress regions to enhance structural lifetime. In a bulk WL, the scribe dimensions (that is, external defects) were more influential on controlling the current distributions whereas in atmospheric conditions, the WL dictated the magnitude of current and pushed the majority of corrosion damage into the creviced fastener hole regions. An open-source machine learning algorithm was built using the FEM computational results, to create an accessible framework which can predict when the majority of current will occur within a creviced or bulk region, depending on the WL and external defect dimensions. Additional **mitigation** techniques, investigated in all three chapters, included the application of a barrier sol-gel to the cathodic surfaces to limit the overall cathodic kinetics on those surfaces. The sol-gel coating on the noble fasteners was able to mitigate the total anodic charge within a fastener assembly by 84% after 504 hrs exposure to a continuous 0.9 M NaCl salt fog. In addition, applying the sol-gel coating to SS316 fasteners was able to decrease the throwing power below that of a bare Ti-6Al-4V fastener.

Publications resulting from this section of the work:

- **R. Skelton Marshall,** R. G. Kelly, A. Goff, & C. Sprinkle. (2019). Galvanic Corrosion Between Coated Al Alloy Plate and Stainless Steel Fasteners, Part 1: FEM Model Development and Validation. *Corrosion*, *75*(12), 1461–1473.
- **R. Skelton Marshall,** A. Goff, C. Sprinkle, A. Britos, & R. G. Kelly. (2020). Estimating the Throwing Power of SS316 When Coupled with AA7075 Through Finite Element Modeling. *Corrosion*, *76*(5), 476–484.
- **R. Skelton Marshall,** K. A. Define, R. S. Rosner, A. Goff, C. Sprinkle, P. V. Balachandran, & R. G. Kelly. (2022). Galvanic Corrosion Between Coated Al Alloy Plate and Stainless Steel Fasteners, Part 2: Application of FEM and Machine Learning to Study Galvanic Current Distributions. *(Submitted to Corrosion)*

Chapter 2: Galvanic Corrosion Between Coated Al Alloy Plate and Stainless Steel Fasteners, Part 1: FEM Model Development and Validation[+]

Rebecca Skelton Marshall[*], Rob G. Kelly[*], Adam Goff[**], Charles Sprinkle[**]

*University of Virginia, 395 McCormick Rd, Charlottesville VA 22903

**Luna Innovations, Inc., 706 Forest St. Suite A, Charlottesville VA 22903

Authorship contributions: R. Skelton Marshall (formal analysis, computational work, experimental cross-sectional analysis, optical analysis, and writing – original draft), A. Goff (experimental polarization behavior, and writing – review & editing), C. Sprinkle (experimental polarization behavior, and writing – review & editing)

[+] Note that the vast majority of this work has been published, but Figure 2.2, Figure 2.13, Figure 2.17, Figure 2.18, and Figure 2.19 all represent unpublished data

2.1 Abstract

Aerospace structures often involve dissimilar materials to optimize structural performance and cost. These materials can then lead to the formation of galvanic couples when moisture is present. Specifically, noble metal fasteners (such as SS316) are often used in aluminum alloy load-bearing structures, which can lead to accelerated, localized corrosion attack of the aluminum alloy due to the cathodic current supplied by the SS316 fastener. This localized attack is difficult to predict, and tests are often expensive, so modeling of these galvanic couples could be of great utility. The work reported here focuses on the galvanic coupling between fasteners installed in a panel test assembly, and the resultant corrosion damage down the fastener holes.

This arrangement is a common assembly geometry in aerospace applications. A specific sol-gel coating was applied to the fasteners, to determine its effectiveness on mitigating galvanic corrosion; bare fasteners were also tested, to investigate a worst-case scenario. Geometric constraints in the model were made to match those of an experimental test panel, which was exposed to ASTM B117 salt fog for 504 hrs. The electrochemical boundary conditions were generated in solutions appropriate to the material and environment to which it would be exposed. Anodic charge passed during exposure was calculated from image analyses of the corrosion damage in the experimental test, and the results were compared with the model. It was determined that Laplacian based model provides a very good first approximation for predicting the damage within the fastener hole, when a large external cathodic surface area is present. Validation was provided by both experimental results generated in this study as well as comparison to results in the literature that used similar, but not identical, conditions.

2.2 Introduction

Aluminum alloys are commonly used in aerospace structures, with AA7075-T6 specifically used in the fuselage and frames due to its high strength:weight[1]. Due to microstructural constraints, however, AA7075-T6 cannot be welded, and components must be joined together mechanically[2]. Most often, more noble fasteners are utilized, as they supply adequate mechanical properties. If both the fastener and panel are painted with a coating which has no defects, the assembly would experience no corrosion. Problems arise when defects in the coating are present, either developed during service or from installation, which allow pathways for an aqueous solution to interact with the metals. This intrusion of solution can initiate the onset of galvanic corrosion. Repairs to aircraft sometimes lead to the installation of bare, noble metal fasteners[3], which can further exacerbate the galvanic corrosion. Dry installation (i.e., without the inclusion of sealant in the hole) represents a worst-case scenario for this panel/fastener design with respect to corrosion susceptibility, but has been known to occur in-service.

Experimental measurements of localized corrosion damage can be time-consuming in terms of sample construction, testing duration, and post-test optical profilometry and cross-sectional metallography. Having a validated computational model allows focusing of experiments in the most important parts of parameter space (explored more in Part 2 (Chapter 4)). Therefore, finite element modeling has become a common approach to study the effects of galvanic coupling, through the utilization of both the Laplace equation[4–12], and the Nernst-Planck equation[4,13–16]. A thorough discussion on both approaches was recently published by Liu *et al.*[17], however this work will only focus on a Laplacian-based model.

Much computational research has been done on the galvanic coupling of dissimilar metals in simple geometries[4–6,9,14,18]. However, less computational work has been conducted on more complex geometries, such as panel/fastener assemblies[8,11,12,19,20], which are more common in real-life situations and are known to trap water in crevices between the dissimilar metals[21,22].

The complex geometry of structural components in the aircraft increases the difficulty in both experimental measurement and modeling of the galvanic couple. The fastener shaft and hole form an occluded cell with the panel, which leads to local changes in chemistry and thus electrochemical behavior. The occluded geometry also requires complex ohmic drop considerations. Previous experimental work has focused on the external surface corrosion of a scribed fastener/panel assembly[3,23,24], however, fastener holes are known to be the location of most crack initiation, due to the stress concentration that occurs there. Corrosion damage, which is known to serve as an initiation site for fatigue cracks[25–28], can severely impact the fatigue life of the aircraft if it occurs in a fastener hole where it is very difficult to detect without disassembly[28,29].

The present work aims to develop a validated modeling strategy for galvanic corrosion in complex geometries, particularly within a fastener hole. The main goals were to quantitatively evaluate damage within the fastener holes of corroded panels, and then comparing the experimental results to model predictions. The effects of applying a sol-gel coating to the noble fastener, with the goal of mitigate corrosion damage, were also investigated. Specifically, the computational portion of this research evaluated the galvanic corrosion current within fastener holes containing bare noble metal fasteners. The model was also used to create calculations that could be compared to measurements of the galvanic current during corrosion via zero resistance ammeters, as reported by Feng *et al.*,[23,30], Wang *et al.*,[31] and Boerstler[24]. Lastly, experimental crevice samples were created to investigate possible limitations of using the Laplace equation in computational work.

In order to evaluate the corrosion in the complex geometry described above, an accelerated galvanic corrosion test plate designed by Matzdorf *et al.*[3] was used. Referred to in this document as the "NAVAIR test panel", it consisted of cathodic fasteners and hardware assembled in a coated aluminum plate. Scribes were placed on the surface of the coated aluminum plate to simulate defects in the coating.

To mitigate the galvanic coupling occurring inside of the fastener hole, a specific sol-gel coating was applied to the cathodic fasteners. The rationale for coating the cathode is based on simple electrochemical theory. The conservation of electric charge requires that the total anodic current, I_a, must equal the total cathodic current, I_c. Utilizing this relation, one can see that the cathode surface area (SA_c) to anode surface area (SA_a) ratio (SA_c: SA_a) becomes extremely important when trying to decrease the amount of anodic current density in a system (see Eq. 2.1).

$$\sum i_a SA_a = \sum i_c SA_c \tag{2.1}$$

where i_a is the anodic current density and i_c is the cathodic current density. If the cathodic surface area decreases, then the anodic dissolution current density must decrease (for a constant anode surface area). Conversely, if the anodic surface area decreases, then the anodic dissolution current density will increase. Such considerations are important when assessing coating schemes in galvanic couples. If the anode is coated, any area exposed by defects will experience a very high current density, making the local dissolution worse than if there was no coating at all. Conversely, if the cathode is coated, any defect in the coating will only increase the dissolution of the anode by an amount proportional to the exposed area, and the galvanic attack will never be worse than if no coating was applied. If perfect coatings existed, there would be no difference between coating the anode vs coating the cathode. As this is not the case, coating the cathode is the more robust means of minimizing the effects of a galvanic couple. Any surface treatment on the cathode would act in the same way as a coating, limiting the amount of cathodic current available to galvanically couple.

2.3 Methods

The work reported here involved both experimental and computational methods.

Accelerated Testing

An accelerated corrosion test panel configuration designed by NAVAIR[3] was utilized (see Figure *2.1*). This panel has been used in previous literature to study the effects of galvanic coupling between dissimilar fasteners assembled in a panel[3,19,23,31,32]. Around each of the lower two fastener holes, two scribes were made through the coating in the aluminum plate to assess the effects of coating defects on the corrosion morphology. The panels were 3” x 6” x 0.25”, with four fasteners on one half and four fasteners on the other half. 10-32 threaded SS316 and 10-32 threaded Ti-6Al-4V fasteners were offset from each other in two horizontal rows. SS316 washers with an outer diameter of 0.75” were placed under the SS316 fasteners and Ti-6Al-4V washers with an outer diameter of 0.5” were placed under the Ti-6Al-4V fasteners. All bolts were torqued to 100 in oz. Further details of the NAVAIR plates can be found elsewhere[3,23,32].

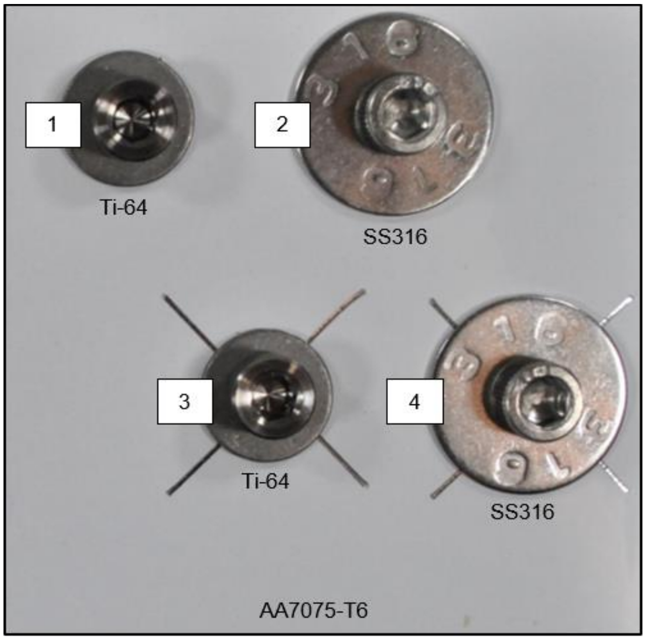

Figure 2.1: AA7075 NAVAIR galvanic test panel assembly with bare SS316 and Ti-6Al-4V fasteners; numbers represent different simulated real-life scenarios

These panels were constructed from a AA7075-T651 (UNS A97075) plate (6 mm), with two SS316 (UNS S31600) fasteners and two Ti-6Al-4V (UNS R56400) fasteners installed[3,19,23,31]. AA7075-T6 and SS316 are both commonly used alloys in aircraft design, for structure and fasteners, respectively. Ti-6Al-4V fasteners are more noble than SS316 fasteners, and they are generally much more expensive. Both fasteners were assembled in the same panel, to make testing most efficient. The combination of this panel design and alloys is consistent with literature.

For the current work, the AA7075-T6 panel was coated front and back with a Surtec 650V pretreatment, and a 44GN072 chromate-containing primer (MIL-PRF 85582). Along the front and edges of the panel, a 03W127A topcoat (MIL-PRF 85285) was applied. In the first panel, all fasteners were uncoated (*i.e.*, bare) and were thus dry installed. This represented a worst-case scenario for a repair to aircraft, making it most susceptible to corrosion. It is important to note that the interior of the holes in the present work was also intentionally not coated.

Overall, there were four “real life” scenarios that the experimental panel attempted to emulate (Figure *2.1*).

I. A section of an aircraft with bare Ti-6Al-4V fasteners, dry installed in a panel with no coating defects (best-case for minimal galvanic corrosion)

II. A section of an aircraft with bare SS316 fasteners, dry installed in a panel with no coating defects (better case)

III. A section of an aircraft with bare Ti-6Al-4V fasteners, dry installed in a panel which contains a surface defect modeled by a scribe in the coating (bad case)

IV. A section of an aircraft with bare SS316 fasteners, dry installed in a panel which contains a surface defect modeled by a scribe in the coating (worst case)

A second NAVAIR panel was tested with both types of fasteners spray coated with a protective sol-gel coating, rather than being assembled bare. These fasteners were still dry-installed. The sol-gel was approximately 5 – 10 µm thick. The goal of applying this sol-gel was to limit cathodic current availability and thus limit the anodic dissolution of the AA7075-T6 panel. This sol-gel coated fastener panel was made to be compared with the four bare fastener scenarios above, to determine the effect of the sol-gel. Information regarding the sol-gel formulation can be obtained from Luna Labs USA, LLC.[1]. An additional test was conducted in which all of the fasteners were nylon in order to assess the contribution of crevice corrosion to the damage in the fastener holes.

The panels were exposed to ASTM B117[33] continuous salt spray for 504 hours (21 days). This testing environment is very common for evaluating the effects of corrosion damage within a galvanic couple[3,18,22,23,31,32,34]. Although this test is known to be much more aggressive than most service conditions, and cannot predict specimen lifetimes[34], it has become a standard and results from it can be gathered and compared with other data from the literature. This test consists of a continuous vertical spray of 5% NaCl salt water, which creates a fog over the samples mounted at a 15° tilt, while the temperature and humidity remain constant[33].

Once the plates were removed from the testing environment, they were chemically stripped of the primer and coating, and the hardware was removed. Metallographic analysis was conducted by cutting the plate cross-sectionally through the center of the holes. The cross-sectioned samples containing the exposed holes were polished to a 3-micron mirror finish and imaged using a Hirox RH 8800 optical microscope and a scanning electron microscope (SEM).

After the samples were imaged, a MATLAB algorithm developed specifically for the depth analysis of cross-sectional corrosion damage[19] was used to quantify the results. The algorithm first converts the optical image into a binary image and extracts the outline of the sample based

---

[1] Email: goffa@lunainc.com

on a gray tolerance factor. Next, the algorithm plots the corroded surface of the sample as a function of distance. The profile of corrosion damage was used to calculate the approximate total volume of corrosion damage within the hole, by assuming that the damage exposed in the four cross-sections made was the same throughout the entire hole.

Zero Resistance Ammeter Technique

Crevice samples were also conducted and assembled. SS316 and AA7075 rectangular coupons, 38 mm by 12.7 mm, were cut using an 8-inch precision wet cut-off saw with continuous anti-corrosion coolant. Samples were then polished down to 1200 grit mirror finish, rinsed with water, and dried with pressurized air. Three scenarios were assembled, following the schematic of Figure 2.2. In all scenarios, an electrically-insulating polymide tape (McMaster-Carr Super-Thin Masking Tape for Electronics) of 38.1 µm thick and 0.25 in (6350 µm) wide was used to maintain a gap between the AA7075/SS316 coupons, simulating the gap between the macro-scale fastener and panel. The tape was placed on both short sides of the coupons, to allow for solution ingress in both long-sides. Specific surface areas on each scenario are indicated in **Table 2.1**, where SA^{i} represents the exposed interior (creviced) surface areas and SA^{ex} represents the exposed exterior (bulk) surface areas.

Table 2.1: Description of exposed surfaces areas to the solution on the creviced samples

	SA^{i}_{SS316} [mm^2]	SA^{ex}_{SS316} [mm^2]	SA^{i}_{AA7075} [mm^2]	SA^{ex}_{AA7075} [mm^2]
Scenario 1	321.31	321.31	321.31	321.31
Scenario 2	321.31	-	321.31	-

Scenario 3	-	321.31	321.31	-

Samples were connected to conducting Ni-wires with Cu-tape. Only controlled surface areas were exposed to the solution while all remaining surfaces were masked off with insulating beeswax. Tape was loosely used to bind the SS316 coupon onto the AA7075 coupon, with no pressure applied to limit interference with the carefully controlled gap. Assembled samples were then placed in a cylindrical beaker and exposed to full-immersion 0.9 M NaCl solution for 20 hrs or 40 hrs.

The zero resistance ammeter (ZRA) was conducted via a connection to each wire on the sample, through Bio-Logic Multichannel Potentiostat (Bio-Logic SAS,Claix, France) running EC-Lab (Version 11.27) software. The coupled potential and total cathodic and anodic current were measured on the SS316 and AA7075 surfaces, respectively, with measurements taken every 15 seconds. The measured current was normalized by the exposed areas in **Table 2.1** to calculate the average current densities. SEM was utilized to conduct post-exposure analysis of the AA7075 surface on scenarios 2 and 3.

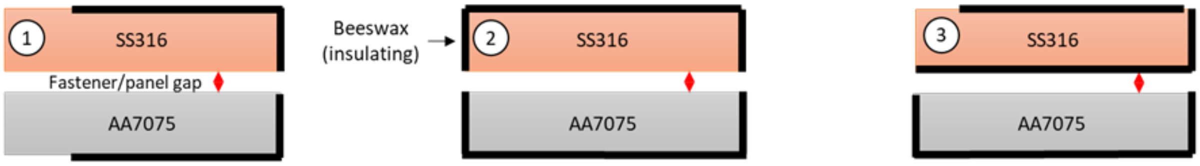

(a) (b) (c)

Figure 2.2: Crevice samples exposed to 0.9 M NaCl full-immersion conditions; (a) scenario 1, with interior and exterior SS316 and AA7075 surface areas active; (b) scenario 2, with only interior SS316 and AA7075 surface areas active; (c) scenario 3, exterior SS316 and interior AA7075 surface areas active

2.3.3. Finite Element Method Modeling

The modeling software used was COMSOL Multiphysics© (version 5.3a). A secondary current distribution model was used to calculate the total interface current on each surface in the NAVAIR panel. The three main pillars of this type of modeling are the assumptions used, the boundary conditions implemented, and the geometry built.

There were four main assumptions in the model which were made intentionally to reduce the computational expense. First, the system was assumed to be in steady state conditions over the entire testing period. This assumption has been previously made in finite element models[4,6,10,12,18,26,35]. The current distribution was calculated in the model and was converted to anodic charge to compare with experimental data. Rather than multiplying the current by the total amount of time which the experimental samples were exposed to the testing environment (504 hours in our case), a four-day "initiation" period for corrosion was accounted for. That initiation period came from an approximation from previous data found in literature, where steady state corrosion appeared after four days in B117, as measured by a zero-resistance ammeter[23,24,30,31]. Since both the experimental panels and testing environment in this literature were similar to the current study, the same initiation time was used. Including this initiation period of corrosion helped make the "steady state" assumption in the model more accurate.

The second assumption made was that migration of charged ions was the main mass transport mechanism, and therefore diffusion and convection could be ignored. In utilizing this assumption, the more general Nernst-Planck equation becomes the Laplace equation, which only takes into account the migration of ions. This simplification has been shown to give a good approximation of current densities in galvanic couples, and significantly decreases the computational time required for each simulation[8,10,12,13,18,36].

The presence of a perfectly insulating coating system on the panel, with zero flux, was the third assumption in the model. This assumption meant that actively corroding AA7075-T6 was only considered to occur within the fastener holes and in the scribes on the surface. Note that the model cannot account for undercutting of the coating because of this assumption. At short exposure times, this assumption is valid, as the cathodic current will take the path of least resistance which is generally towards the initially bare AA7075-T6. However, at long exposure times, the aggressive solution is known to undercut surface coating and cause corrosion outside of the scribes.

The solution in the model was selected to represent the continuous salt spray environment to which the experimental panels were subjected. Therefore, the fourth assumption was that the water layer thickness in B117 was 4,000 µm. Multiple water layer thicknesses were considered, but previous work determined that a thickness of 4,000 µm most accurately represented a constant salt spray environment[37,38]. Recent literature has also determined that all water layers above the natural convection boundary layer of 800 µm behave as bulk immersion, with minimal change in the total current under these conditions[36]. This result indicates that although the water layer thickness in B117 testing has never experimentally been confirmed, as long as it is greater than 800 µm, the value input into the model does not change the overall results significantly. Therefore, a 4,000 µm water layer thickness was used in the model, along with a solution conductivity of 6 S/m[19].

The boundary conditions input into the model were experimentally-derived via potentiodynamic scans of bare AA7075-T651, SS316, and Ti-6Al-4V. The experimental set up utilized a 250 mL glass corrosion flat cell with a 1 cm^2 working electrode area and a 5 mL Luggin well. Platinum mesh was used as the counter electrode. Quiescent curves were generated in bulk 5 wt% NaCl

(0.9 M NaCl) at 35°C (as used in B117 testing)[33], without any addition of gas to the solution. Deaerated curves were generated in the same environmental conditions as above, with research grade nitrogen bubbled in the solution at about 50 cc/min. The scan rate for the quiescent tests was 0.1 mV/sec, while the scan rate for the deaerated tests was 5 mV/sec. For all tests, the starting potential was held for 1 hr, before scanning. Once the open circuit potential (OCP) was reached, another 1 hr hold was initiated, before continuing to the end of the scan. The solution was not agitated through stirring for any of the tests described above.

The AA7075-T6 quiescent polarization curve was generated after the sample was held at an initial potential of -0.3V_{SCE} to activate localized corrosion on the aluminum, and then was scanned downwards in potential until reaching -1.2 V_{SCE}. The potential range of the scan was aimed to encompass both the cathodic and anodic reactions on the AA7075-T6 surface. In this test, the solution at the surface of the AA7075-T6 was assumed to best represent the aggressive solution that develops in the occluded region of the hole during the B117 testing.

Deaerated cathodic SS316 and Ti-6Al-4V curves were generated, to represent the change in chemistry within the fastener hole. These curves were input into the model as boundary conditions for the occluded fastener surfaces. Quiescent cathodic SS316 and Ti-6Al-4V curves were generated to represent the surface of the fasteners. These curves were input into the model as boundary conditions for all fastener surfaces outside of the occluded region. The anodic behavior of these two alloys was not of particular interest in the current research and therefore was not tested.

The geometry in the model was constructed in COMSOL with the dimensions specified to match that of the experimental panels. The average gaps between the washers, fasteners, and panel were determined by metallographic analyses of an identically prepared plate assembly that had not been exposed to the corrosion chamber (see Figure *2.3*). To represent the “dry installation” of the fasteners, the surfaces of the fastener holes were considered to be bare aluminum.

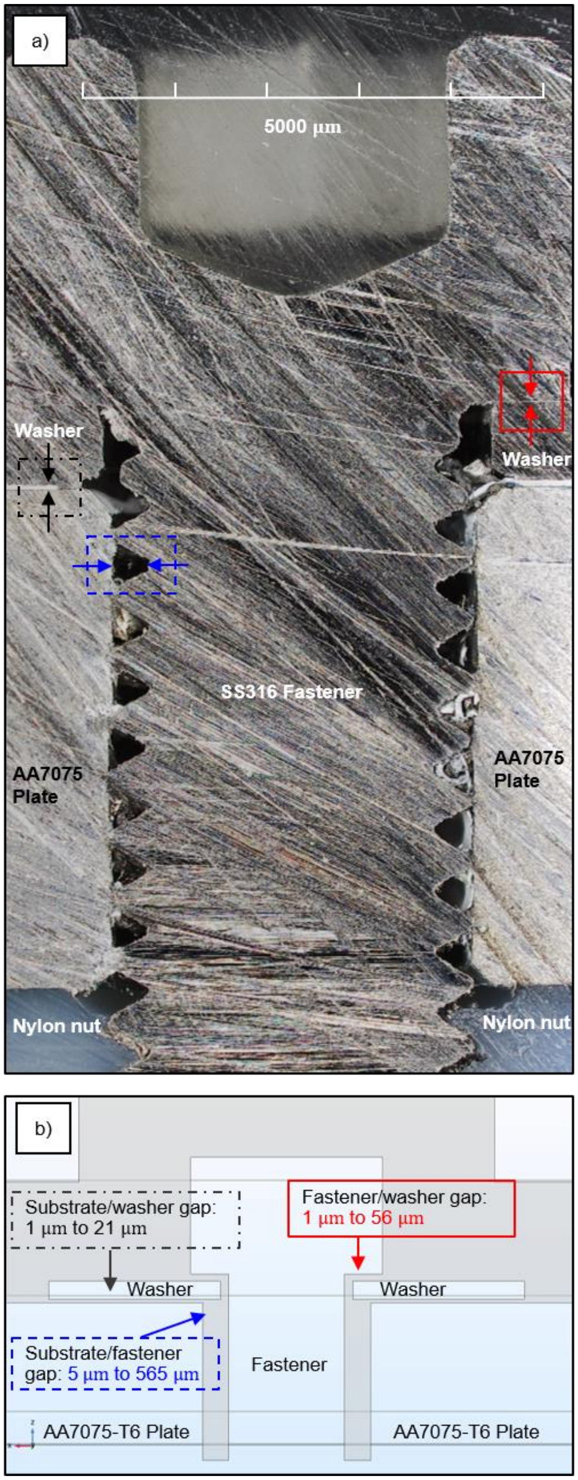

Figure 2.3: (a) Cross-sectional analysis of assembled NAVAIR panel to assess gaps in the system; (b) gaps input into computational geometry

The model was used to calculate the total anodic current (TAC), and both the net current and net current density at all positions where the aluminum metal was bare. The net current results were quantitatively related to the experimental data set by converting the current to charge using Faraday's law for alloys assuming a 408 hr period of active localized corrosion. False-color net current density plots were used to qualitatively see the current distributions and were compared with experimental data.

In all cases, the total anodic and cathodic currents of the entire panel were compared to verify that the conservation of charge was being observed. Throughout all of the calculations, the percent difference between those values never rose above 0.7%. The error tolerance level, for the current in the electrolyte, was set to 0.1%. The model was extended to several sets of experimental data found in the literature[23,24,30,31]. These studies also used the NAVAIR panel, albeit with some differences in the geometry and required boundary conditions.

In addition to the simulations of the NAVAIR panel, the small-scale crevice geometry, representing the fastener hole, was also simulated. The geometry was built identical to the experimental set up described in Figure 2.2. The Laplace equation, boundary conditions, and all other assumptions from the model described above remained constant, unless otherwise noted.

2.4 Results

B117 Exposure Results

Upon removal of the panels after 504 hours exposure to the test chamber, corrosion damage was easily visible on the NAVAIR panel with the bare fasteners. After the surface coating was stripped off and the hardware was removed, further corrosion damage became visible (Figure 2.4(a) and (b)). The majority of the damage appeared to be in the scribes. It is important to note that the surface surrounding the top left hole (which contained a bare Ti-6Al-4V fastener) received local damage where the coating blistered likely due to a defect during installation. In the top right hole (which contained a bare SS316 fastener), there was no visible damage because the coating did not blister at that location. When comparing the scribes surrounding the two different fasteners, it can be seen that the scribes closest to the SS316 fastener (including those portions of the scribes on the Ti-6Al-4V fastener hole) suffered more severe damage. The damage in these scribes appeared to be localized at the tips, outside of the washers. We denoted these as corrosion "bulbs".

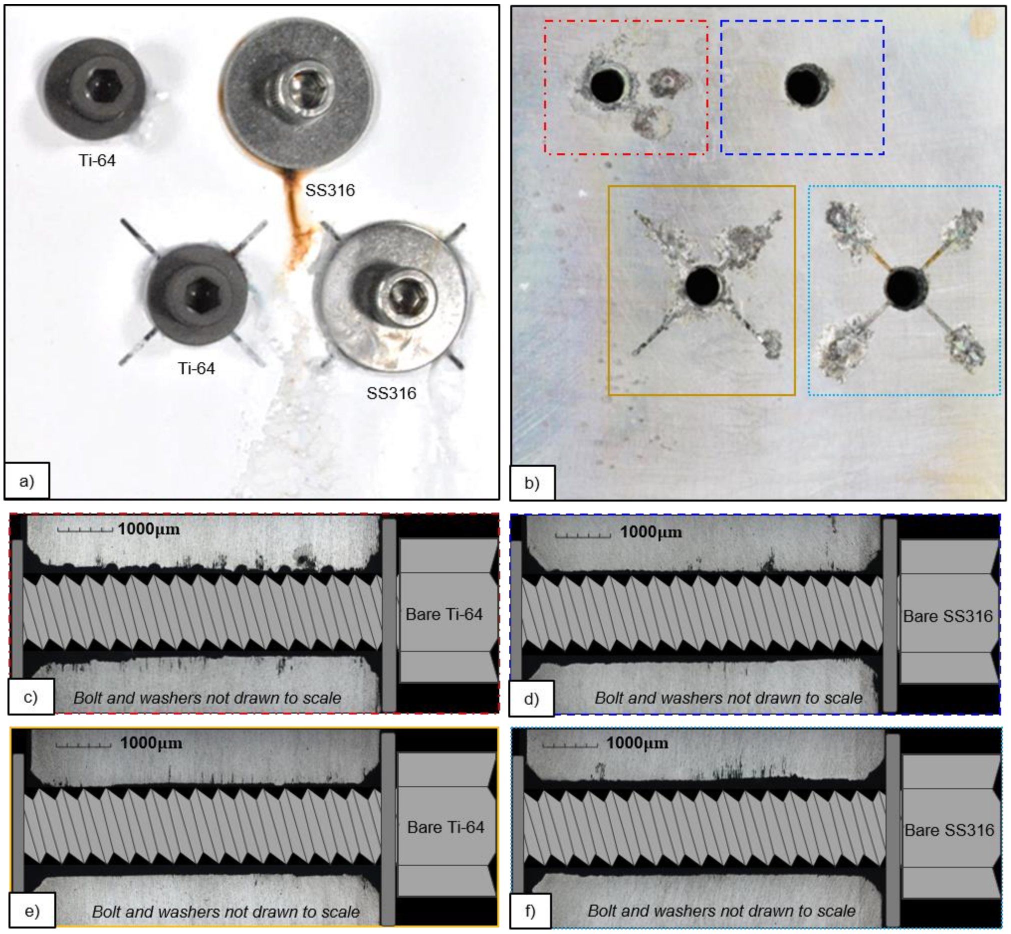

Figure 2.4: Cross-sections of fastener holes in AA7075 plate (a) after 504 hours exposure to ASTM B117; (b) surface of panel after hardware and coatings were stripped off, dashed boxes represent each the location of each respective cross-section; (c) bare Ti-64 fastener hole without scribes; (d) bare SS316 fastener hole without scribes; (e) bare Ti-64 fastener hole with scribes; (f) bare SS316 fastener hole with scribes

Down-hole analysis was conducted through metallographic cross-sectioning of the panels. Large amounts of intergranular corrosion (IGC) was seen within the bare fastener holes (Figure 2.4(c) – (f)). The top right hole (which contained a bare SS316 fastener but no intentional coating defect) had deep pits and one IGC fissure reaching 2 mm in length (Figure 2.5). This fastener hole showed no surface appearance of damage. This indicated that although the surface coating did not appear to be damaged, electrolyte was still able to enter the fastener hole and form an aggressive occluded cell.

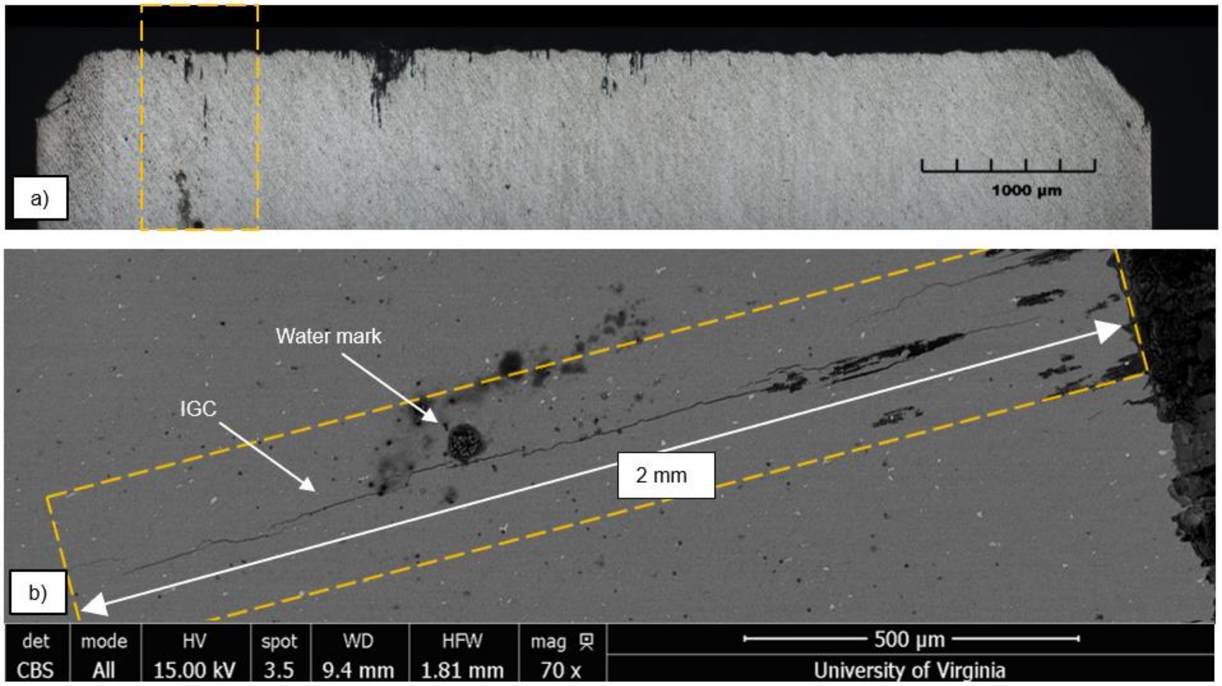

Figure 2.5: Micrograph of 2 mm fissure observed in AA7075 hole with scribes containing bare SS316 fastener after exposure to B117 for 504 hours; taken with (a) optical microscopy, and (b) CBS Scanning Electron Microscopy

The top left hole (which contained a bare Ti-6Al-4V fastener and no intentional coating defect) appeared to suffer mechanical damage, as can be seen by the systematic hemispheres of damage (Figure 2.4(c)). It is unknown whether this mechanical damage helped initiate the surface coating failure. In all of the data presented in this research, mechanical damage was accounted for and filtered out. Significant exfoliation of the AA7075-T6 plate was observed on the surface under the Ti-6Al-4V washer (Figure 2.6). This type of corrosion is known to appear on AA7075-T6 in particular[39,40].

The cross-sectioned images of the bare fastener holes were input into an algorithm to quantify the corrosion damage. The amount of anodic coulombic charge that must have been present for the given mass loss was calculated. The results showed that the damage down all of the bare fastener holes was nearly equivalent, independent of fastener type (Ti-6Al-4V or SS316) or surface defects (scribes or no scribes). This equivalence was in spite of the fact that that the SS316 fastener produced more cathodic current than the Ti-6Al-4V fastener.

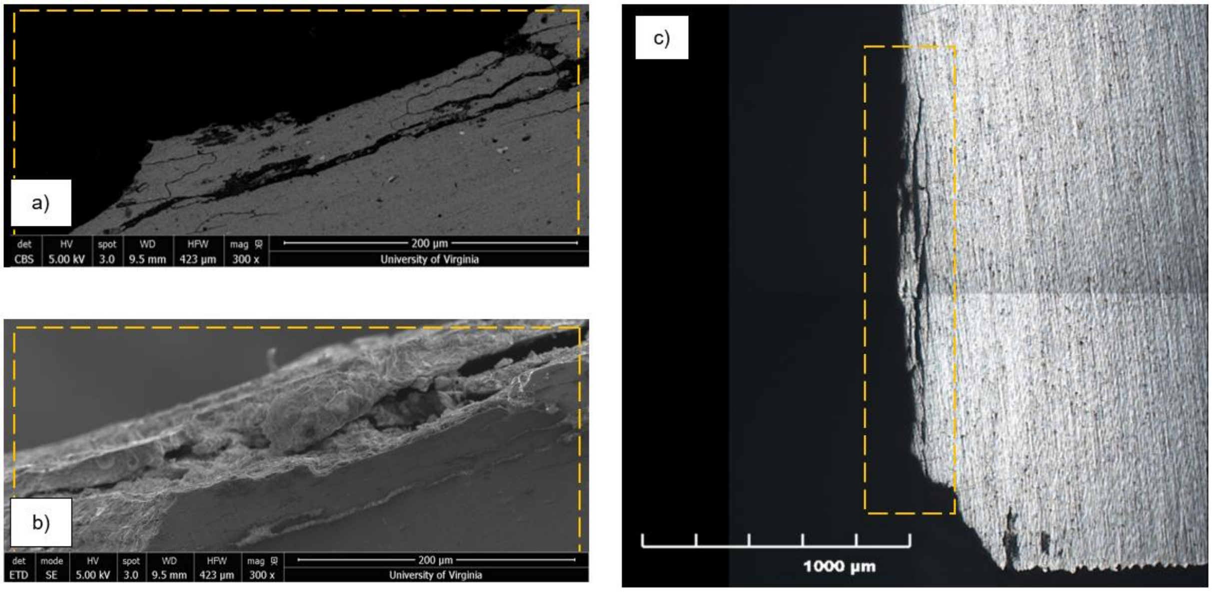

Figure 2.6: Exfoliation of AA7075 surface observed near hole with no scribes containing bare Ti-6Al-4V after exposure to B117 for 504 hours; taken with (a) CBS Scanning Electron Microscopy, (b) SE Scanning Electron Microscopy, and (c) optical microscopy

The surface damage on the NAVAIR panel containing sol-gel coated fasteners, after 504 hours exposure to the test chamber, was much more limited than that of the bare fasteners panel. Small amounts of discoloration in the scribes were observed, but the surfaces with no scribe contained no corrosion attack (Figure 2.7(a) and (b)). The panel containing sol-gel coated fasteners was cross-sectioned, as was conducted for the bare fastener panel, to observe damage inside of the fastener holes. It was seen that there was no corrosion damage down either of the fastener holes with no intentional scribe defects (Figure 2.7(c) – (d)). However, there was a small amount of IGC observed down both of the fastener holes with surface scribed defects (Figure 2.7(e) – (f)). This damage within the holes was independent of the fastener type but was dependent on the surface defect.

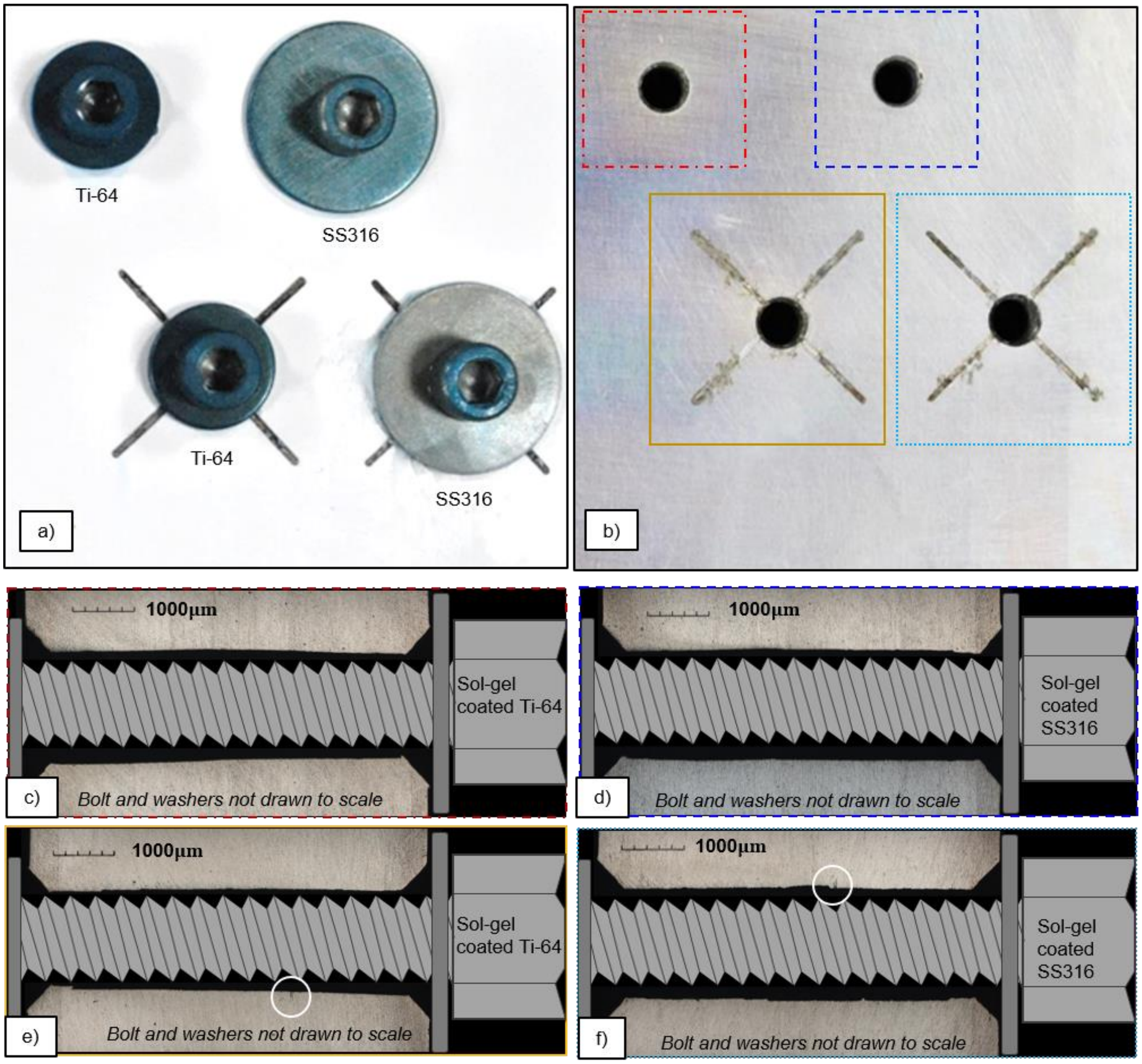

Figure 2.7: Cross-sections of sol-gel coated fastener holes in AA7075 plate (a) after 504 hours exposure to ASTM B117; (b) surface of panel after hardware and coatings were stripped off, dashed boxes represent each the location of each respective cross-section; (c) sol-gel coated Ti-64 fastener hole without scribes; (d) sol-gel coated SS316 fastener hole without scribes; (e) sol-gel coated Ti-64 fastener hole with scribes; (f) sol-gel coated SS316 fastener hole with scribes

Modeled Secondary Current Distribution Results

The model was assembled with the assumptions, boundary conditions, and geometry described above. Figure 2.8 indicates all of the polarization curves which were used in the present model, and the respective surfaces in the model to which they were assigned. False-color current density plots were generated for a qualitative comparison to the surface appearance of the NAVAIR panels (Figure 2.9). Only the active AA7075-T6 surfaces are shown on the plot for convenience, although all fasteners have negative cathodic current in the system. The false color plot showed the peak current density on the tip of the scribes outside of the washers.

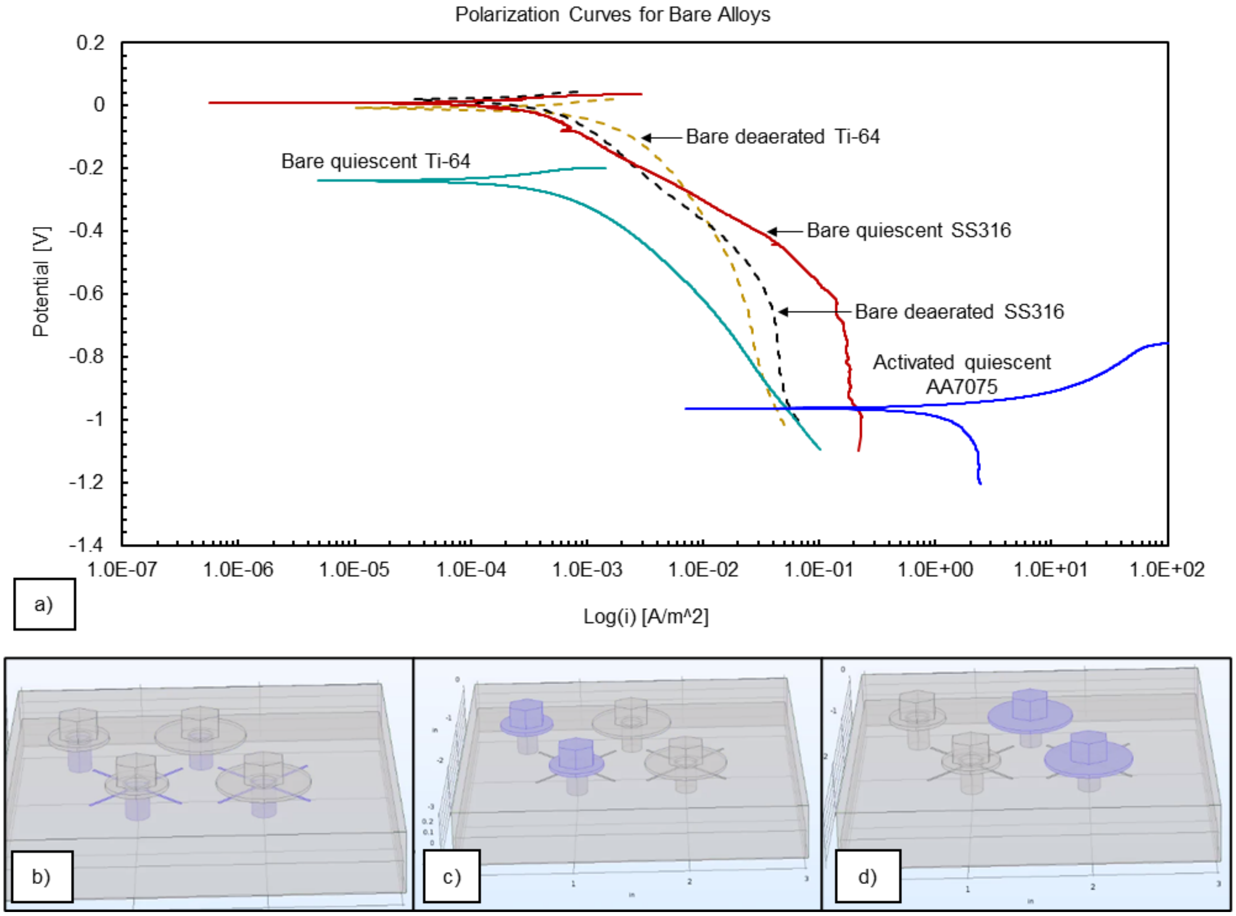

Figure 2.8: (a) Polarization curves for quiescent (solid lines) and deaerated (dashed lines) cathodic and anodic alloys; surfaces in blue represent (b) bare AA7075-T6 (all blue surfaces used the activated AA7075 polarization curve as a boundary condition); (c) Ti-6Al-4V fasteners and washers; (d) SS316 fasteners and washers; Note: for both (c) and (d), deaerated polarization curves were used as cathodic boundary conditions for the fastener shafts, while the washers and head of the fasteners used the quiescent polarization curves as boundary conditions

To quantify the damage, the current density was integrated over the bare AA7075-T6 surface area to obtain the average current. This summation was conducted for each bare AA7075-T6 fastener hole individually. These results were then converted to columbic charge considering a four-day initiation period, *i.e.,* it was assumed that after four days, the corrosion initiated and immediately propagated at steady state for the remaining seventeen days. The length of this initiation period came from literature with similar experimental test parameters as our own[23,24,30,31].

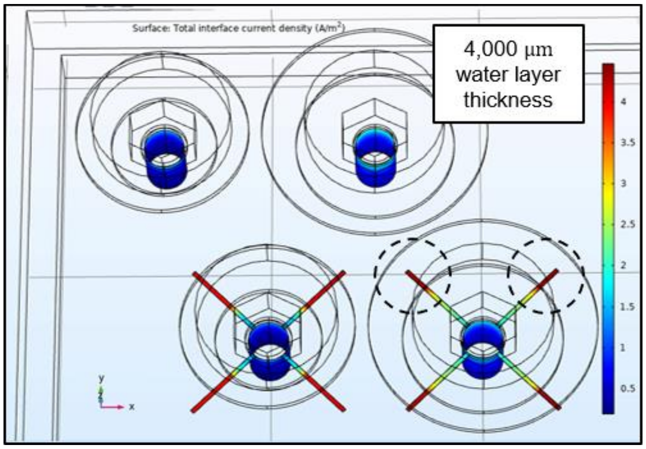

Figure 2.9: False-color current density plot of exposed AA7075 substrate under 4,000 µm water layer thickness with active Ti-64 fastener and active SS316 fastener installed; dashed circles highlight the peak current density at tip of scribes, qualitatively agreeing with experimental data

Investigation of Damage Down Ti-6Al-4V Fastener Hole

To follow up on the experimental results observed, three tests were conducted to determine why the holes containing bare Ti-6Al-4V fasteners were experiencing severe corrosion. As it is known that Ti-6Al-4V creates a less strong galvanic couple than SS316[23,31,32], these results were intriguing. An experimental test was conducted to investigate the possibility of crevice corrosion in the NAVAIR panel. Two modeling tests were conducted to evaluate the level of interactions between the SS316 and Ti-6Al-4V fasteners.

The goal of the experimental test was to determine whether the damage observed in the hole containing Ti-6Al-4V fasteners was due to crevice corrosion of the AA7075-T6 in the occluded cell, independent of the nature of the fastener. Nylon fasteners and hardware of the same dimensions as the SS316 and Ti-6Al-4V fasteners and hardware were installed in the AA7075-T6 NAVAIR panel, providing similar occluded regions but without any galvanic interactions. The test panel was exposed to the same test conditions as described above (504 hours in B117). Metallographic analysis showed a complete lack of corrosion damage (see Figure 2.10), demonstrating that AA7075 crevice corrosion was not contributing damage to this test assembly, and that the increased driving force for corrosion provided by the *galvanic* interactions must be necessary. This form of corrosion was then considered to be galvanic-*induced* crevice corrosion.

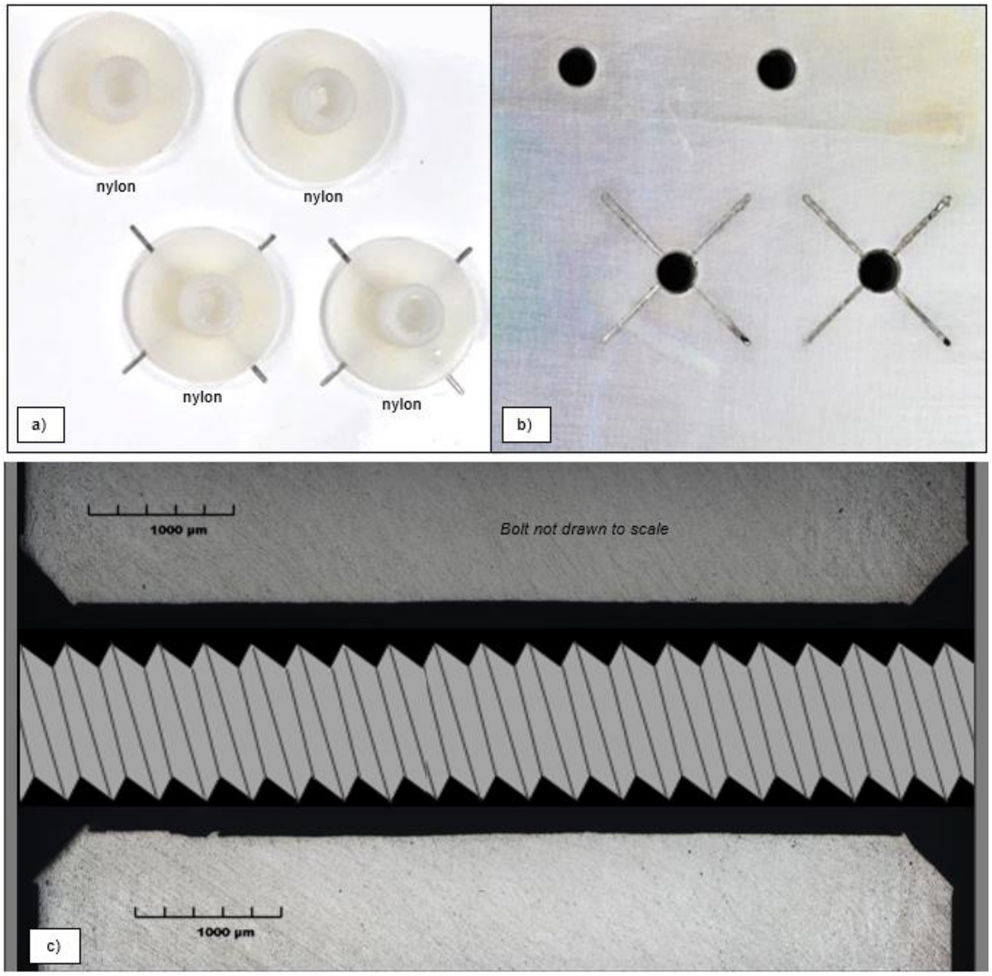

Figure 2.10: (a) Nylon fasteners assembled in AA7075 NAVAIR plate 504 hours exposure to ASTM B117; (b) hardware and coatings stripped off of panel; (c) no corrosion visible in cross-section of fastener hole

The first modeling test was conducted to determine the level of cathodic current which the Ti-6Al-4V fastener was contributing towards the galvanic couple. Ti-6Al-4V boundaries were set to have zero flux while the geometry and remaining boundary conditions stayed the same. In this case, the only galvanic current that could occur would be due to the SS316 fasteners. The model showed that the scribes surrounding the inert Ti-6Al-4V fastener experienced nearly the same amount of current density as before being inert. This supported the proposal that the SS316 fasteners must be communicating with the Ti-6Al-4V holes via the water layer, and that the contribution of the Ti-6Al-4V fasteners was almost negligible (Figure 2.11). Interactions between fasteners in the NAVAIR configuration have been observed in previous work[3,19,32]. However, this finding shows that the Ti-6Al-4V fasteners are not contributing a significant amount to the corrosion of the aluminum but are just hiding the true extent of damage caused by the SS316 fasteners down the fastener holes.

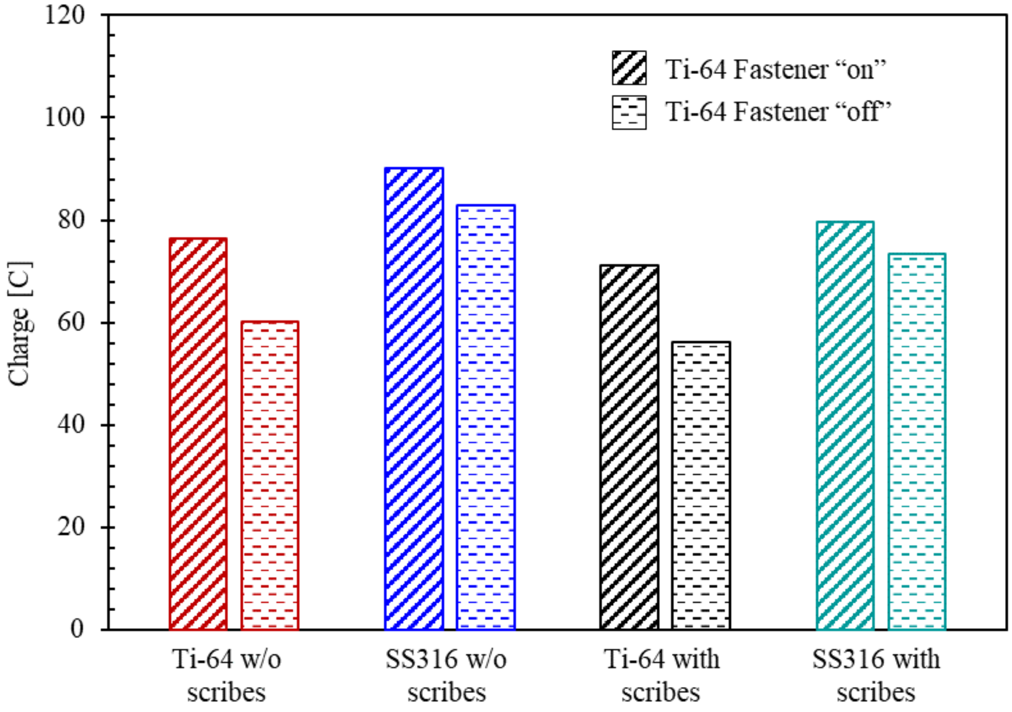

Figure 2.11: Total current within the fastener holes, with Ti-64 surfaces active vs non-active

The second modeling test was conducted to verify the theory of the SS316 fastener galvanically coupling with bare AA7075-T6 surrounding the Ti-6Al-4V fastener. Both of the fasteners had active boundary conditions, as well as the AA7075-T6 surfaces. The water layer thickness was changed from 4,000 μm to 800 μm, while all other test parameters remained the same. A water layer thickness of 800 μm is still considered "bulk" electrolyte (as it is at the threshold of the boundary layer thickness)[36], however the migration of ions should feel increased resistance from the 4,000 to 800 μm water layer thickness. The results showed an asymmetry in the scribes surrounding the Ti-6Al-4V fastener (see Figure 2.12). This result indicates that the SS316 fastener is contributing the majority of the galvanic current surrounding the Ti-6Al-4V fastener, however with a thinner water layer, not all surfaces of the bare AA7075-T6 are as easy to couple with.

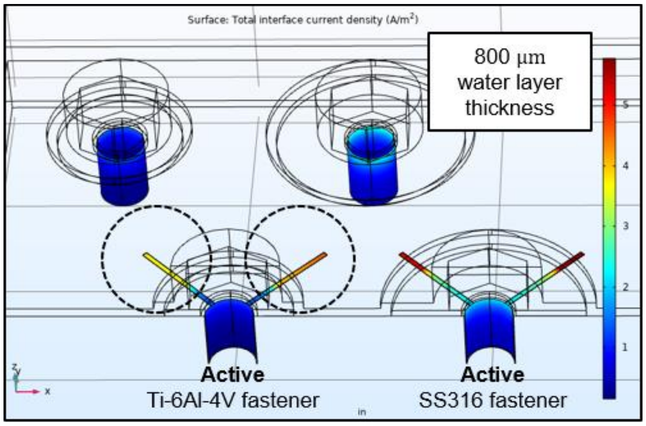

Figure 2.12: False-color current density plot of exposed AA7075 substrate under 800 μm water layer thickness with active Ti-64 fastener and active SS316 fastener installed; dashed circles highlight asymmetry in current distribution on the scribes, indicating interaction between the scribe and SS316 fastener

2.4.4. Measurements on isolated crevice coupons

The goal of the three creviced scenarios was to control the surface area ratios of the SS316 and AA7075 and determine any limitations of the Laplace equation. Each individual scenario maintained the same total cathode:anode surface area ratio (that is, SA_c:SA_a of 1:1); of these total anodic (or cathodic) surface areas, scenarios 2 and 3 were equal, while the total anodic surface area of scenario 1 was double that of scenarios 2 and 3 (**Table 2.1**).

Scenario 1 specifically allowed for both external and internal surface areas to be present on both the SS316 and AA7075 coupons (Figure 2.2). The *external* SA_c: SA_a was 1:1 and the *internal* SA_c: SA_a was 1:1. Scenario 2 only allowed for the *internal* surface areas to be active, both on the SS316 and the AA7075. All external surface areas were all insulated. Scenario 3 maintained the internal anodic surface areas on AA7075, but on the SS316 sample instead isolated the internal surface areas and exposed the *external* surface areas (Figure 2.2).

The resulting anodic current densities during the 20-hr exposure are then shown in Figure 2.13. As charge is conserved, and the total SA_c: SA_a were maintained at 1:1 in all scenarios, the cathodic current density was a negative equivalent of the anodic current density. Scenario 3 had the highest current densities while scenario 2 had the lowest, and all systems seemed to reach steady-state around 7.5 hrs. The overall decrease in the current densities indicated that the system was passive, however, sharp, transient increases in the current density, most clearly seen in scenario 2, highlight breakdown/pitting events. The sharp, small decreases in current density (again, most obvious on scenario 2) which return to a higher current density indicate noise during the measurements.

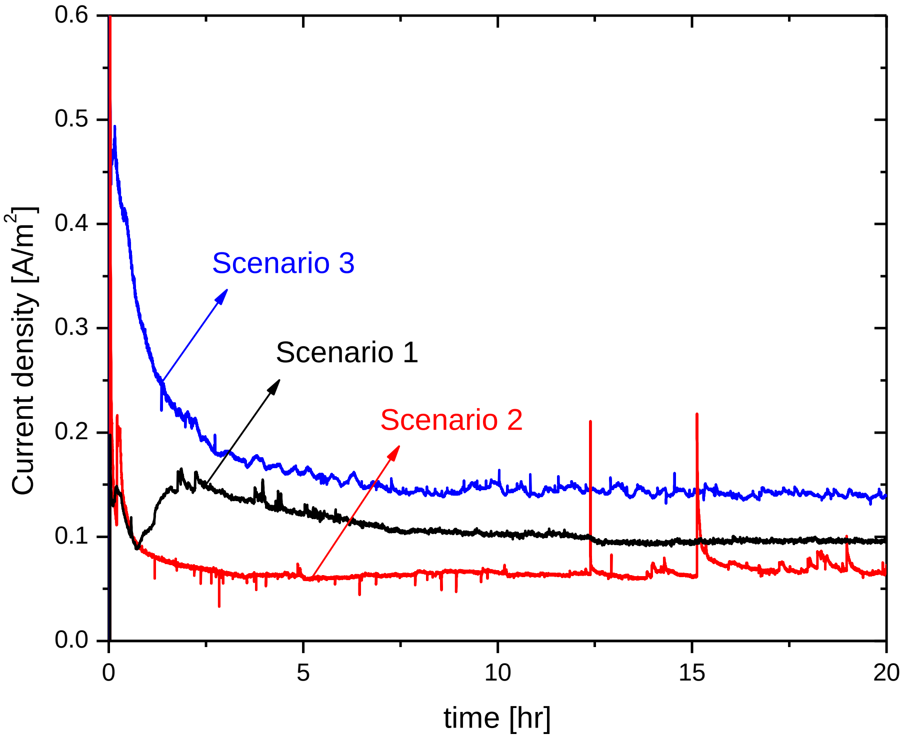

Figure 2.13: ZRA results on the three creviced scenarios, exposed to 5 wt% NaCl (0.9 M NaCl) full-immersion conditions for 20 hrs

2.5 Discussion

From a structural perspective, damage within fastener holes is very important because of the increase to the inherent stress concentration of the hole by the corrosion morphology. Damage on the order of hundreds of microns, as was observed in our samples, could serve as crack initiators if high stress was applied that had a component perpendicular to the corrosion damage or if bending stresses existed. The surface appearance was not a reliable predictor of the corrosion damage down the fastener holes. However, it was seen that with the application of sol-gel on the noble fasteners, the severe corrosion damage down the fastener holes was greatly mitigated. The modeled results agreed qualitatively with the damage distribution on the surface, and quantitatively with the total damage within the fastener holes. The model was able to predict the complex interactions between the SS316 fasteners and the bare AA7075-T6 panel.

2.5.1. Comparison of Damage Down Holes for Bare vs. Sol-gel Coated Fasteners in the NAVAIR Plate

Previous work using similar NAVAIR plates has shown that the SS316 fasteners produce nearly double the cathodic current of the Ti-6Al-4V fasteners[23,31,32]. This result is known to be due to the slow cathodic kinetics on the Ti-6Al-4V surface, although its open circuit potential is higher relative to SS316. Feng *et al.*,[23,32] thus concluded that SS316 fasteners will therefore cause more severe corrosion attack. In theory, an isolated SS316 fastener would cause corrosion attack on the panel which is twice as severe as an isolated Ti-6Al-4V fastener, as indicated by the total current measurements. However, close proximity of fasteners relates to a more realistic situation, as is represented by the NAVAIR panel design. The research presented here indicates that when fasteners are put in this close proximity design, the damage distribution can no longer be predicted by the measured currents on the individual fasteners. It was seen that, although the current from the SS316 fastener was nearly double that of the Ti-6Al-4V fastener (as known from literature), the damage within the fastener holes was all of the same order of magnitude. The measured cathodic current in this configuration is then concluded to be a poor proxy for damage within the fastener hole, which is of more structural importance. It should also be noted that conventional crevice corrosion does not appear to play any role in the damage within the holes as shown by the experiment with the nylon fasteners (Figure 2.10), indicating that the galvanic driving forces must be necessary for corrosion initiation in these scenarios. The SS316 fastener's ability to couple with the AA7075-T6 panel, as a function of distance, is investigated further in Chapter 3.

Figure 2.14 compares the overall damage within the sol-gel fastener holes to that of the bare fastener holes, through anodic charge comparisons. Because the holes with the sol-gel fasteners suffered visible corrosion only on the scribed holes, the damage in the non-scribed holes was not reported on the bar chart and is approximately zero. The error bars represent the minimum and maximum damage seen down the cross-section of the holes. Due to the non-uniform corrosion within the fastener holes (see Figure 2.4), the errors bars could become very large.

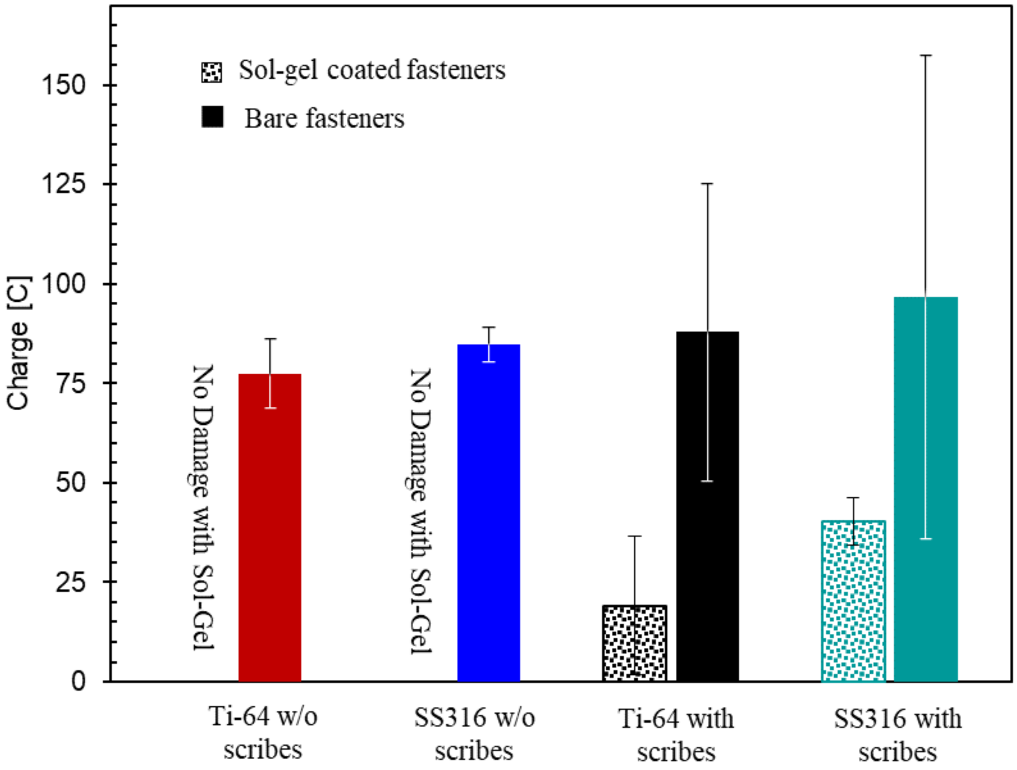

Figure 2.14: Comparison of damage within bare vs sol-gel fastener holes after a 504 hr exposure time to ASTM B117

The sol-gel coating reduced the total anodic charge by a factor of approximately 84% after 504 hours of exposure to the aggressive B117 testing. A statistical analysis of the damage was also performed for the two fastener systems. The maximum depth of corrosion damage within the bare fastener holes ranged from about 280 µm to 370 µm, whereas the maximum depth of corrosion damage within the sol-gel coated fasteners holes ranged from about 180 µm to 200 µm. The area corroded however, differed by one order of magnitude, with the bare fasteners having approximately 0.21 mm^2 and the sol-gel fasteners having approximately 0.069 mm^2 worth of damage. These results show that at least up to 504 hours in the accelerated salt spray chamber, the sol-gel coating limited cathodic current, thereby stifling the galvanic coupling which causes the corrosion initiation and propagation in the present galvanic-induced crevice corrosion.

2.5.2. Comparison Between Model and Experimental Results

The false-color current density plots generated in the model agreed qualitatively with observations of the experimental test panels, where severe bulb-shaped corrosion was seen at the ends of the scribes (see Figure 2.9). The model demonstrates that the end of the scribe is most accessible for the cathodic current and is thus an area of high current density. The current density decreases as one moves under the washer, due to the high solution resistance in that region. Details regarding the current distributions are discussed in Part 2 (Chapter 4).

The results from the model were compared with down-hole experimental data gathered from metallographic analysis[2] (see Figure 2.15). The experimental data of 504 hours of exposure compared well with the computational data for the bare fasteners, supporting the assertion that the use of the simplified model (*i.e.*, one based on the Laplace Equation) works well when the boundary conditions are accurate, representing the electrochemical kinetics in the expected occluded solution, although this observation will be investigated more thoroughly within the

---

[2] Mass loss for samples of this size (6”x3”x0.25” = 12 g) due to localized corrosion is a poor metric as the maximum damage loss observed would represent a mass loss of 0.08%.

creviced scenarios. As observed experimentally, the simulated damage in the four holes with the bare fasteners was similar. The differences in the computational results between Ti-6Al-4V and SS316 is within the error of the cross-sectional methodology.

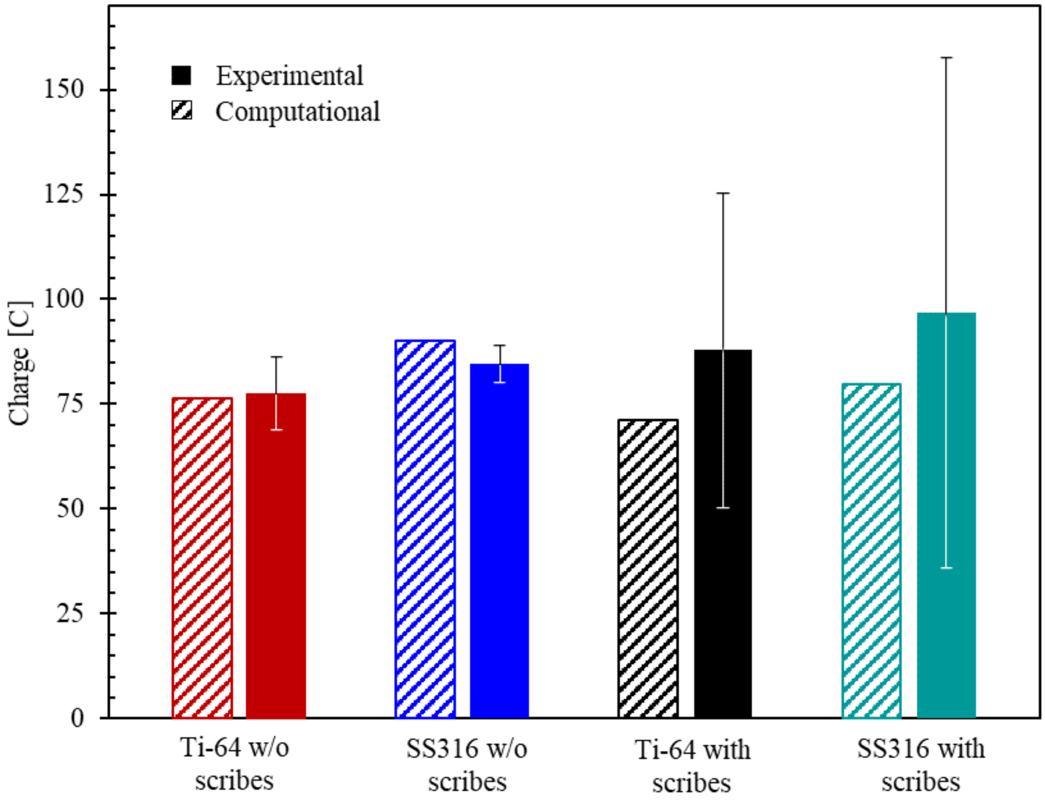

Figure 2.15: Comparison of modeling vs experimental data of charge down fastener hole after 504 hr exposure to B117; solid bars represent experimental data while the striped bars represent computational data, accounting for 4-day initiation period

To further demonstrate the utility of this modeling approach, the geometry was adapted to represent the experimental procedure described in other work. The boundary conditions remained the same as the testing above, however the geometries were changed slightly, along with the arrangement of fasteners. Wang *et al.*, tested two bare SS316 and two bare Ti-6Al-4V fasteners in a single NAVAIR panel[31], similar to the configuration described above, whereas a

Boerstler and Feng *et al.*, tested four bare SS316 fasteners[24,30]. Feng *et al.*, also tested both of the experimental scenarios, with both SS316 and Ti-6Al-4V fasteners[23]. One of the largest differences in the experimental set up was the size of the SS316 washers. The ones used in the literature were much smaller than the ones used in this research, which would affect the total amount of cathodic current available due to the decrease in the cathodic surface area.

The model was run with the new considerations described above and the current density was integrated over all four fasteners, to compare with the experimental data taken with a ZRA. The results are plotted against each other in Figure 2.16. The model is seen to give similar results to the experimental data from literature, during steady state corrosion. Note that the data from Boerstler[19] in Figure 2.16(b) used the NAVAIR plate without scribes, and therefore has a longer corrosion initiation period. However, once steady-state is reached, the galvanic current is similar to the experiments including scribes. The quality of the agreement between the computations and data generated independently is strong evidence of the validity of the modeling approach. However, an additional experimental and computational comparison between the in-house ZRA creviced scenarios will also be considered.

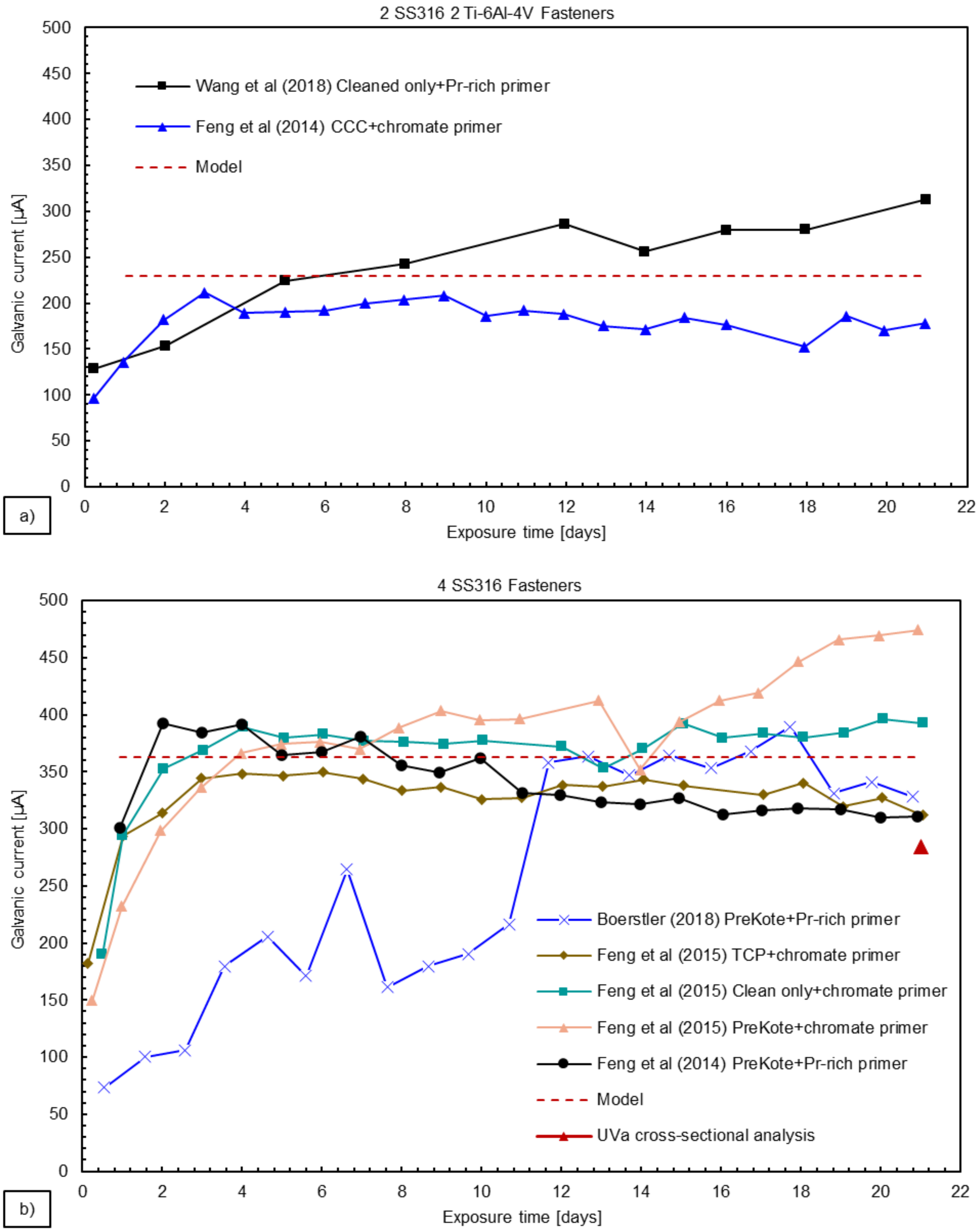

Figure 2.16: Comparison of galvanic current in the system calculated with the model vs. calculated in literature with ZRA; (a) 2 SS316 fasteners and 2 Ti-6Al-4V fasteners installed in

AA7075 panel; (b) 4 SS316 fasteners installed in AA7075 panel; note steady state corrosion begins in both experimental scenarios around 4 days[23,24,30,31]

2.5.3. Shortcomings of the Laplace equation assumptions

All three scenarios of the ZRA creviced geometry resulted in clearly different current densities ($\sim 0.1\ \mathrm{A/m^2}$ variation); as the surface areas were identical, and correspondingly the opportunity for surface reactions was equal, the difference in current must be due to the electrochemical reactions themselves (or interactions thereof) (Figure 2.13). Scenario 1 served as a baseline, with electrochemical reactions able to occur on both external and internal surface areas, analogous to the entire fastener structure which had both externally exposed anodic surface areas (scribes), externally exposed cathodic surface areas (fastener head and washer), as well as anodic and cathodic creviced regions (within the fastener hole).

Scenario 3 forced virtually all of the anodic reactions to occur within the crevice, which led to a drop in pH via an accumulation of H^+ produced through the hydrolysis of aluminum. The cathodic reactions were instead occurring on the bulk exterior surfaces, as in a conventional crevice corrosion system without a dissimilar metal galvanic driving force. As the cathodic oxygen reduction reaction (ORR) and hydrogen evolution reaction (HER) consumed H^+ or produced hydroxyl (OH^-), depending on acidic or basic conditions, the pH over the external surface areas would rise to more basic conditions. The acidic conditions within the crevice break down any passive Al_2O_3 on the aluminum surface, leading to more active areas and more current demand, corresponding to larger corrosion rates[41] (Figure 2.13).

However, scenario 2 represented an isolated crevice, with no external cathodic surface areas. Acidification due to the aluminum hydrolysis still occurred, which acted as an aggressor towards a more-active surface. However, the cathodic reactions were able to consume H^+ and produce OH^- within the crevice, which *mitigated* the aggressive solution by pulling the pH back to near-neutral conditions. Furthermore, the occluded crevice limited the mass transport of O_2 via deaeration, which lowered the cathodic kinetics (as seen in Figure 2.8), further mitigating the corrosion rate. Therefore, the overall current density in the system of scenario 2 was *lower* than that of the baseline scenario 1 (Figure 2.13).

Post-exposure metallographic analysis was conducted on the creviced AA7075 surfaces, to specifically evaluate any differences in corrosion morphology between the lower and upper measured current density extremities of scenarios 2 and 3. The most prevalent form of corrosion present on scenario 2 samples was trenching, due to IGC (Figure *2.17*). Along a surface, precipitates naturally form and cluster around the high-energy grain boundaries, which can lead to preferential attack if the precipitates are anodic to the overall aluminum matrix, as occurs commonly in 5XXX aluminum alloys[42–44]. This preferential attack can surround a grain, as seems to be the case in Figure *2.17*(b), which can lead to grain fall-out.

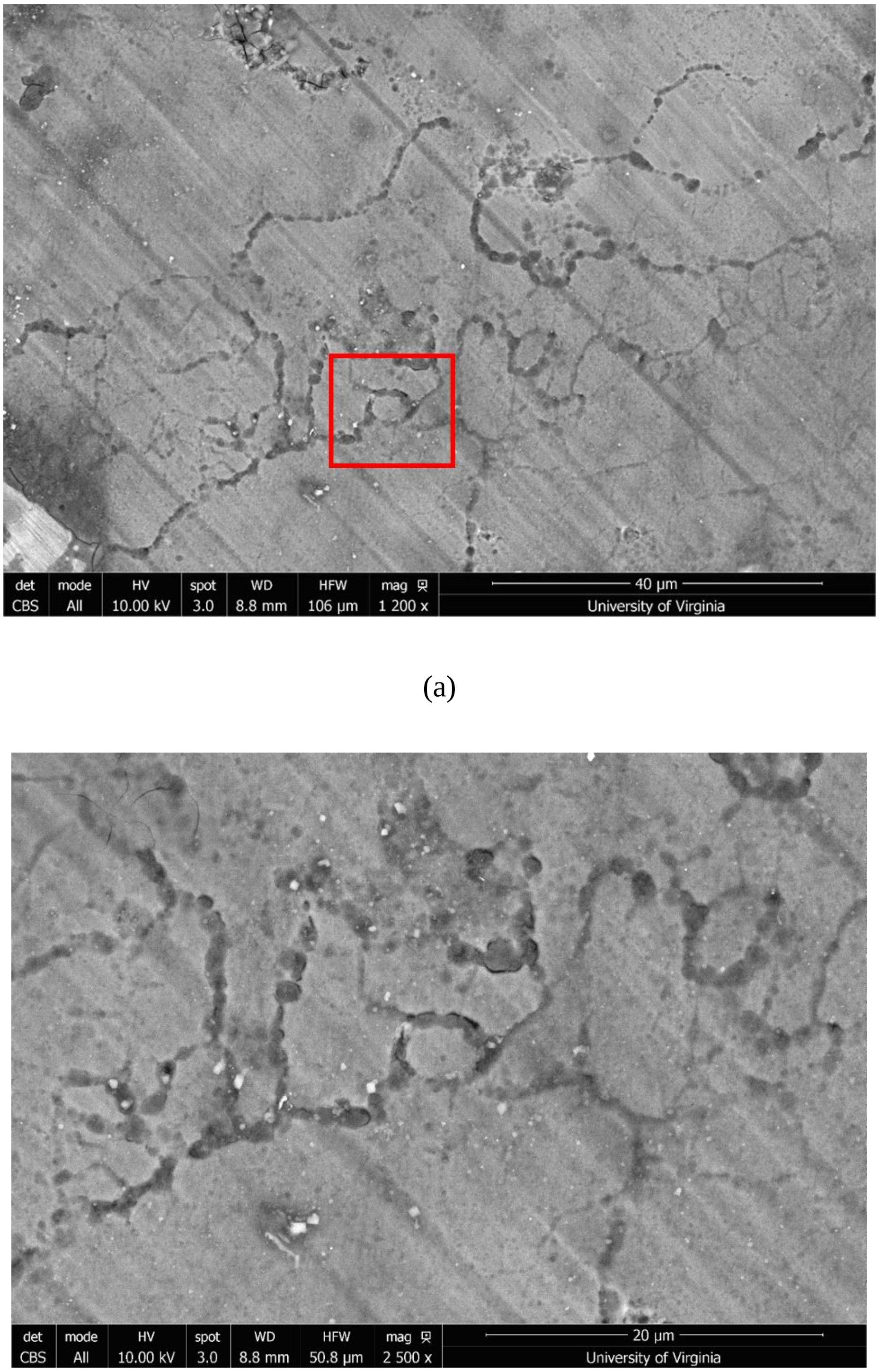

(a)

(b)

Figure 2.17: (a) Backscattered micrographs of sample 2 of the ZRA crevice samples, after the 20 hr exposure to 0.9 M NaCl, (b) a magnified portion focusing on the trenching IGC

The surface morphology of the AA7075 surface in scenario 3 was seen to have areas of more aggressive attack, which may be expected from the increased current densities and breakdown of the AA7075 surface (Figure *2.13*). Three main types of corrosion morphologies were identified. The first was trenching IGC, as seen in the scenario 2 sample (Figure *2.17*) and is highlighted by arrows in Figure *2.18*(a). The second form of attack was the deep coalescence of pitting seen in the center of the micrograph, nearly 20 µm in diameter. The rough surface inside of the corrosion attack again indicates preferential dissolution through micro-galvanic couples within the matrix and precipitates, which could indicate localized dealloying (Figure *2.18*(a)). Lastly, shallow dimple features were observed in certain areas of the creviced surface, magnified in Figure *2.18*(b). These 1 µm to 2 µm diameter features could be considered either metastable pitting events which repassivated, or *general* corrosion. That is, a form of corrosion observed to occur on aluminum alloys which is between pitting and uniform corrosion, as it occurs over a wide area but consists of shallow dimple features[45].

The higher driving force of the third scenario was therefore able to induce not only the susceptible grain boundaries through IGC, but also was able to initiate two additional forms of corrosion.

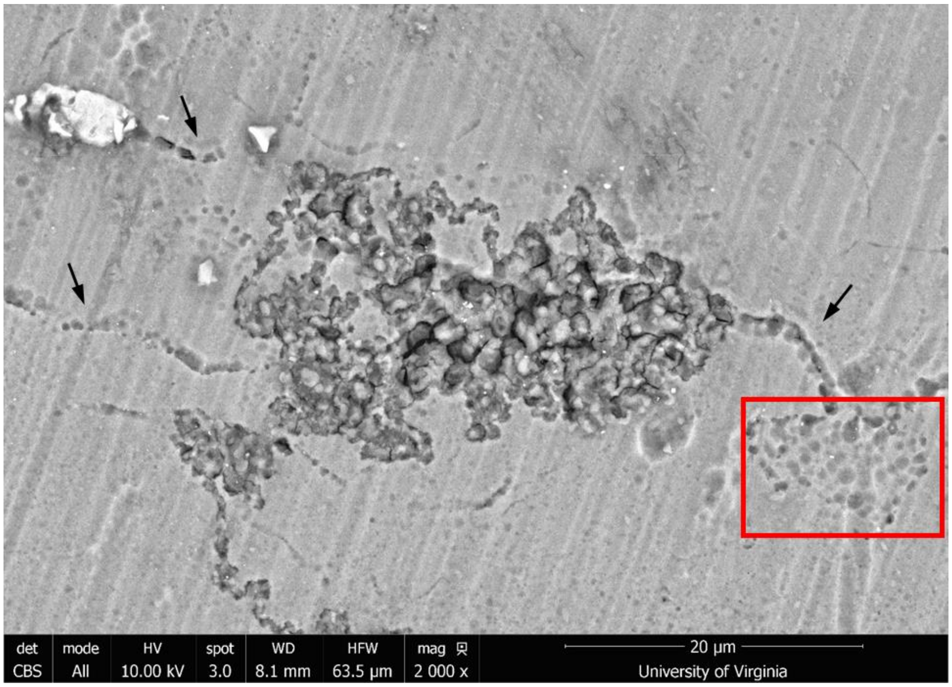
det
CBS
mode
All
HV
10.00 kV
spot
3.0
WD
8.1 mm
HFW
63.5 µm
mag
2 000 x
20 µm
University of Virginia

(a)

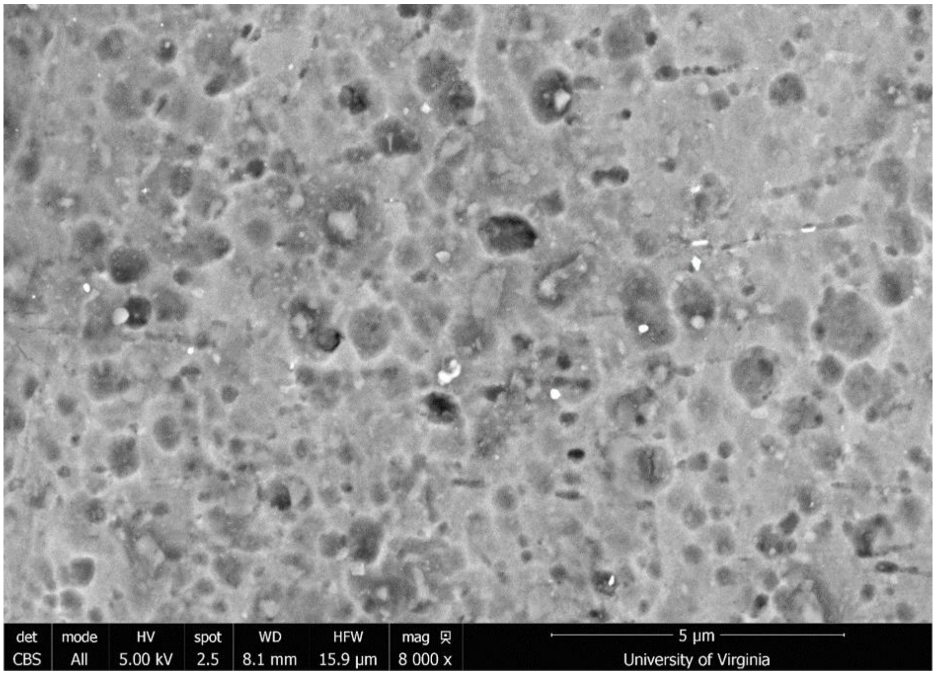
det
CBS
mode
All
HV
5.00 kV
spot
2.5
WD
8.1 mm
HFW
15.9 µm
mag
8 000 x
5 µm
University of Virginia

(b)

Figure 2.18: (a) Backscattered micrographs of sample 3 of the ZRA crevice samples, after the 20 hr exposure to 0.9 M NaCl, (b) a magnified portion focusing on the $\boldsymbol{\mu m}$-sized pits. Arrows in (a) indicate the trenching IGC observed in sample 2.

The computational model was then extended to the small crevice geometry to see if it could account for these subtle but important differences in the corrosion processes while still assuming the simplifications associated with the Laplace equation. The Laplace equation takes into account the ohmic potential drop in solution through accounting for the solution resistance, but does not account for any production or consumption of species. In addition, the diffusion mass-transport mechanism is assumed to be negligible in comparison to the migration mechanism, limiting the model to assume negligible concentration gradients.

The first simulation used only bulk, quiescent boundary conditions for the SS316/AA7075 couple. The surface areas in scenario 1 were double that of scenarios 2 and 3, which allows for more current within the system. However, as the total SA_c: SA_a within each scenario were equal at 1:1, the normalized average current density over the entire anodic and cathodic surfaces were also predicted to be equal within the model (Figure 2.19(a)). The assumptions within the present Laplacian model cannot account for surface reactions which influence the increase and decrease in pH, accounting for the variations in current seen experimentally (Figure 2.19(a)). Therefore, there is no possibility of the *present* model capturing the experimental behavior, which highlights a clear limitation of using the Laplace equation.

Rather than using bulk cathodic polarization as boundary conditions across the entire sample, deaerated SS316 polarization, shown in Figure 2.8, was used as boundary conditions in the creviced regions (Figure 2.19(b)). As scenario 3 had no creviced cathodic surface areas, the computational results did not change from Figure 2.19(a). However, scenarios 1 and 2 decreased in their respective magnitudes of current densities, as expected from the experimental results (Figure 2.19(b)).

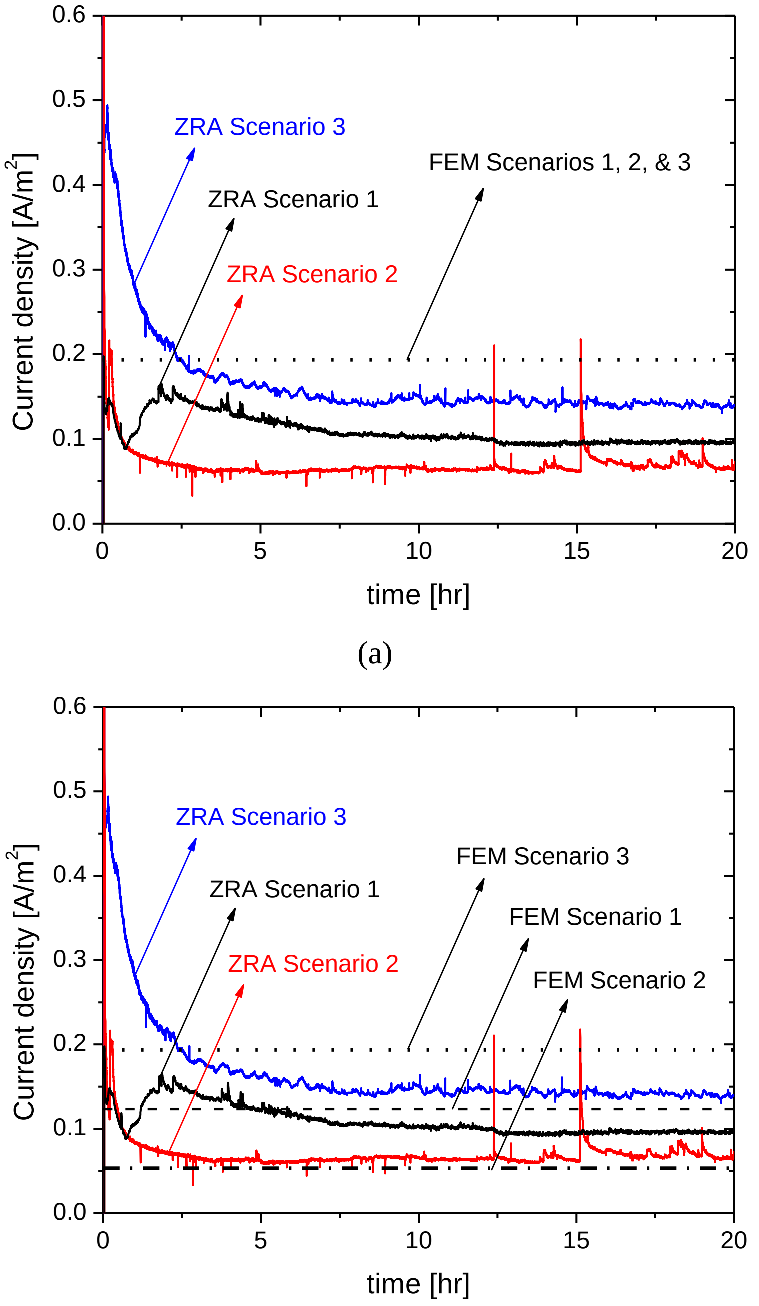

(a)

(b)

Figure 2.19: Experimental ZRA on creviced samples compared with computational results from the Laplacian model; (a) only bulk SS316 boundary conditions used on all cathodic surfaces, and (b) bulk SS316 and deaerated SS316 boundary conditions used on the external and internal surfaces, respectively.

These results point to two important conclusions: 1) the cathodic driving force for galvanic-induced crevice corrosion comes from exterior surface reactions, while *interior* surface reactions actually inhibit corrosion, and 2) evidence that the location of the cathodic reactions taking place is more dominant than purely more surface area to react, which shows a strong limitation of the Laplace equation assumptions, as the Laplace equation only considers geometric effects, unless the boundary conditions are modified.

2.7 Limitations Specific to the Present Work

Although the results produced by the model compared well with experimental data in the majority of scenarios, both in-house and from literature, the approach does have limitations that should be appreciated. The model assumes a perfect coating on the exterior surfaces, and thus as constituted cannot be used to assess the effects of different coatings or surface treatments. Experimentally, clear distinctions have been seen in the literature between coatings containing chromium and non-chromium coatings (Figure 2.16). The steady state assumption in the model also requires that either the initiation period be known or the test is long enough that the initiation time is small.

In addition, assumptions implicate with the Laplace equation were shown to prevent applications of the Laplacian model towards isolated crevices, where the diffusion, production, and consumption of individual species was found to be more important than simply the ohmic potential drop in solution.

To circumvent the specific limitation described above, three options are possible, from the most-thorough to the most approximate solution: 1) solve the entire Nernst-Planck equation, to track each species and account for every complexation reaction which may influence the pH, 2) assume the Laplace equation, but track the *minor* species (such as metal cations) which may have the largest influence on the pH, 3) assume the Laplace equation at steady-state but input boundary conditions representing the aggressive solution (or deaerated conditions) which may be present.

The third circumnavigation tool was utilized in this work through both activation of the AA7075-T6 to better capture the active localized corrosion kinetics and deaeration boundary conditions to account for the mass-transport limitations within the occluded crevice. However, future work is suggested to include the transport of *minor* species in addition to the Laplace assumption, which may result in more accurate approximations within the creviced geometry.

The question is then raised as to why the Laplacian model resulted in values very similar to that of the experimental bulk fastener-in-panel systems presented in this work (Figure *2.15* and Figure *2.16*). The validation of the model is justified through the large external cathodic surface areas of the fastener head and washer, which were shown to provide the bulk cathodic driving-force for the corrosion to occur. That is, the mitigating effects of the deaeration and production of OH^- (or corresponding consumption of H^+) within the crevice were impossible for the Laplace equation to capture, unless the boundary conditions were modified. The acidification of the crevice, on the other hand, was taken into account through the activated AA7075 kinetics use in this work, which captured the breakdown of the passive film.

Therefore, in summary, the electrochemical kinetics chosen as boundary conditions are critical to the results of the model when using the Laplace equation, as highlighted through comparisons with the creviced experimental scenarios. The specific impact of variations to the boundary conditions will be explored further in Chapter 4 and Chapter 9.

2.8 Conclusion

- This work shows the importance of investigating the corrosion damage within fastener holes of galvanic panels. A lack of corrosion damage on the panel surface does not correlate to a lack of damage within the hole. All studies using the NAVAIR galvanic panel or similar designs to assess the performance of coatings should assess damage within the holes.
- Damage within bare and sol-gel coated fastener holes was independent of fastener type due to interactions between the SS316 fasteners and all bare AA7075-T6 surfaces throughout the panel. FEM calculations showed this independence and interaction as well. Crevice corrosion was ruled out as the cause of the damage, and a new mechanism of galvanic-induced crevice corrosion was introduced.
- Application of a specific sol-gel formulation to cathodic fasteners greatly reduced corrosion both within fastener hole and on the surface of the panel by reducing the cathodic current available to drive the anodic dissolution.
- Damage within the fastener holes was reduced by 84% after 504 hours of exposure to B117 with use of sol-gel coated fasteners as opposed to bare fasteners.
- The finite element model developed was shown to give a good approximation of both the charge within the fastener holes, and of total current of fasteners found in literature at times before severe coating degradation. These results indicated that the simplifying assumptions made in the model did not change the system significantly, while a large exterior cathodic surface area was present. Limitations in using the Laplace equation within the finite element model were determined, and suggestions on improvement were provided.

2.9 Acknowledgements

Any opinions, findings and conclusions or recommendations expressed in this material are those of the author(s) and do not necessarily reflect the views of Office of Naval Research. This work is supported by the Office of Naval Research under Contract No. N68335-16-C-0121 (Mr. William Nickerson) through a subcontract with Luna Labs USA, LLC. In addition, support was also provided by the NASA Virginia Space Grant Consortium through a Graduate Research Fellowship. Lastly, the author greatly acknowledges SEM assistance from Dr. Jonathan M. Skelton at the University of Virginia.

2.10 References

1. Wu, S., A.G. Dimakis, S. Sanghavi, F.X. Yu, D. Holtmann-Rice, D. Storcheus, A. Rostamizadeh, and S. Kumar, "Aluminum Alloys for Aerospace Applications," in Aerospace Materials and Material Technologies (2018), pp. 29–52.
2. "Aluminum 7075-T6; 7075-T651," ASM Aerospace Specification Metals Inc (n.d.), http://asm.matweb.com/search/SpecificMaterial.asp?bassnum=ma7075t6 (Jun. 11, 2018).
3. Matzdorf, C.A., W.C. Nickerson, B.C. Rincon Tronconis, G.S. Frankel, L. Li, and R.G. Buchheit, *Corrosion* 69 (2013): pp. 1240–1246.
4. Mizuno, D., and R.G. Kelly, *Corrosion* 69 (2013): pp. 681–692.
5. Liu, C., and R.G. Kelly, *The Electrochemical Society Interface* 23 (2014): pp. 47–51.
6. Turner, M., and E. Gutierrez-miravete, "Modeling Galvanic Corrosion," in COMSOL Conference (Boston, 2013), pp. 1–4.
7. Liu, C., P. Khullar, and R.G. Kelly, *Journal of The Electrochemical Society* 166 (2019): pp. 153–161.

8. Liu, C., V.N. Rafla, J.R. Scully, and R.G. Kelly, “Mathematical Modeling of Potential and Current Distributions for Atmospheric Corrosion of Galvanic Coupling in Airframe Components,” in NACE International: CORROSION (2015), pp. 1–11.

9. King, A.D., J.S. Lee, and J.R. Scully, *J Electrochem Soc* 163 (2016): pp. C342–C356, http://jes.ecsdl.org/lookup/doi/10.1149/2.0171607jes.

10. Kramer, P., T. Curtin, M. Merrill, M. Kim, F. Friedersdorf, and R. Adey, “Atmospheric Corrosion Measurements to Improve Understanding of Galvanic Corrosion of Aircraft,” in NACE International: CORROSION (2018), pp. 1–11.

11. Snihirova, D., D. Höche, S. Lamaka, Z. Mir, T. Hack, and M.L. Zheludkevich, *Corrosion Science* (2019).

12. Adey, R., A. Peratta, J. Baynham, and T. Curtin, “Predicting Cumulative Galvanic Corrosion Damage in Aircraft Structures,” in North Atlantic Treaty Organization Science and Technology Organization (2018), pp. 1–14.

13. Murer, N., R. Oltra, B. Vuillemin, and O. Néel, *Corrosion Science* 52 (2010): pp. 130–139, http://dx.doi.org/10.1016/j.corsci.2009.08.051.

14. Amorim, T.M., C. Allély, and J.P. Caire, “Modelling Coating Lifetime: First Practical Application for Coating Design,” in COMSOL Conference (Hannover, 2008).

15. Murer, N., N.A. Missert, and R.G. Buchheit, *Journal of The Electrochemical Society* 159 (2012): p. C265.

16. Dolgikh, O., H. Simillion, S. V Lamaka, A.C. Bastos, H.B. Xue, M.G. Taryba, A.R. Oliveira, C. Allely, B. Van Den Bossche, K. Van Den Bergh, J. De Strycker, and J. Deconinck, *Materials and Corrosion* 70 (2018): pp. 780–792.

17. Liu, C., and R.G. Kelly, *CORROSION* (2019).

18. Liu, C., G.W. Kubacki, and R.G. Kelly, *Corrosion Journal* 75 (2019): pp. 465–473.

19. Tattersall, C., “Modeling and Analysis of Geometrically Complex Corrosion,” University of Virginia, 2018.

20. Jones, R., M. Lo, D. Peng, A. Bowler, M. Dorman, M. Janardhana, and N.S. Iyyer, *Meccanica* 50 (2015): pp. 517–532.

21. Rafla, V., A. Davenport, and J.R. Scully, *Corrosion, Poster Award Research Letters* 71 (2015): pp. 1300–1303.

22. Moran, A., J. Jennings, H. Nee, S. Pearson, B. Clark, and R.S. Lillard, *Corrosion Journal* 75 (2019): pp. 484–498.

23. Feng, Z., G.S. Frankel, and C.A. Matzdorf, *J Electrochem Soc* 161 (2014): pp. 42–49, http://jes.ecsdl.org/cgi/doi/10.1149/2.059401jes.

24. Boerstler, J.T., “Corrosion Degradation of Coated Aluminum Alloy Systems through Galvanic Interactions,” The Ohio State University, 2018.

25. Burns, J.T., J.M. Larsen, and R.P. Gangloff, *Fatigue & Fracture of Engineering Materials and Structures* 34 (2011): pp. 745–773.

26. Harrison, T.J., B.R. Crawford, G. Clark, and M. Brandt, *Advanced Materials Research* 891–892 (2014): pp. 242–247.

27. Harrison, T.J., B.R. Crawford, M. Brandt, and G. Clark, *Computational Materials Science* 84 (2014): pp. 74–82, http://dx.doi.org/10.1016/j.commatsci.2013.11.033.

28. Cole, G.K., G. Clark, and P.K. Sharp, “The Implications of Corrosion with Respect to Aircraft Structural Integrity” (DSTO Aeronautical and Maritime Research Laboratory, 1997).

29. Lo, M., R. Jones, A. Bowler, M. Dorman, and D. Edwards, *Fatigue and Fracture of Engineering Materials and Structures* 40 (2017): pp. 1664–1675.

30. Feng, Z., J. Boerstler, G.S. Frankel, and C.A. Matzdorf, *Corrosion* 71 (2015): pp. 771–783.

31. Wang, S., J. Boerstler, and G.S. Frankel, *Corrosion* 74 (2018): pp. 499–508.

32. Feng, Z., and G.S. Frankel, *Corrosion* 70 (2014): pp. 95–106.

33. *ASTM B117*, Standard Practice for Operating Salt Spray (Fog) Apparatus (West Conshohocken, PA: ASTM International, 1994).

34. Feng, Z., G.S. Frankel, W.H. Abbott, and C.A. Matzdorf, *Corrosion* 72 (2016): pp. 342–355.

35. Haque, Z., B.A. Clark, and R.S. Lillard, *Corrosion* 74 (2018): pp. 903–913.

36. Liu, C., J. Srinivasan, and R.G. Kelly, *J Electrochem Soc* 164 (2017): pp. C845–C855, http://jes.ecsdl.org/lookup/doi/10.1149/2.1641713jes.

37. Liu, C., "Assessment of the Utility of Laplace ' s Equation for Modeling of Localized Corrosion," 2018.

38. Blohm, L.M., "Galvanic Coupling of AA5XXX-H116 and CDA 706 Utilizing Laboratory, Outdoor, and Accelerated Testing," 2018.

39. El-amoush, A.S., *Materials Chemistry and Physics* 126 (2011): pp. 607–613.

40. Andreatta, F., H. Terryn, and J.H.W. De Wit, *Electrochimica Acta* 49 (2004): pp. 2851–2862.

41. Deltombe, E., and M. Pourbaix, *Corrosion* 14 (1958): pp. 16–20.

42. Mizuno, D., and R. Kelly, *Corrosion* 69 (2013): pp. 681–692, http://www.corrosionjournal.org/doi/abs/10.5006/0812.

43. Mizuno, D., and R. Kelly, *Corrosion* (2013): pp. 580–592, http://www.corrosionjournal.org/doi/abs/10.5006/0812.

44. Steiner, P.J., and J.T. Burns, *Corrosion* 74 (2018): pp. 1117–1131.

45. Ferrer, K.S., and R.G. Kelly, *Corrosion* 58 (2002): pp. 452–459, http://meridian.allenpress.com/corrosion/article-pdf/58/5/452/2003597/1_3277636.pdf.

Chapter 3: Estimating the Throwing Power of SS316 When Coupled with AA7075 Through Finite Element Modeling

Rebecca Skelton Marshall[*], Adam Goff[**], Charles Sprinkle[**], Alejandro Britos[*], Rob G. Kelly[*]

*University of Virginia, 395 McCormick Rd, Charlottesville VA 22903

**Luna Innovations, Inc., 706 Forest St. Suite A, Charlottesville VA 22903

Authorship contributions: R. Skelton Marshall (formal analysis, computational work, and writing – original draft), A. Goff (experimental polarization behavior, and writing – review & editing), C. Sprinkle (experimental polarization behavior, and writing – review & editing), A. Britos (selection computational simulations)

3.1 Abstract

Galvanic corrosion is common in applications involving a fastener and panel assembly. Often, the fastener is made from a more noble metal and the panel is made from a less noble metal, selected for their respective mechanical properties. The ability for the more noble material to galvanically couple to the panel's surface as a function of distance is referenced to as "throwing power", and was the main subject of this research. In this work, SS316 and AA7075 were investigated as the fastener and panel material, respectively. A Ti-6Al-4V fastener and a sol-gel coated SS316 fastener were also considered to determine the impact of different materials on the galvanically driven throwing power. Along with different fastener materials, different fastener geometries were considered as well. Raised fasteners are generally used in tandem with washers, while countersunk fasteners are not in order to remain flush with the surface. The difference

between these two geometries on the throwing power was investigated. It was determined that the SS316 washer was the largest contributor to the galvanic current in the raised fastener assembly, due to its large surface area. At distances of two inches away, the SS316 fastener and washer were able to double the natural corrosion rate of AA7075. A countersunk SS316 fastener, with the same total surface area as that of the raised fastener and washer assembly, was seen to lower the throwing power which forced a large amount of current down the fastener hole. Throughout all of the computational tests, the model relies on the generation of accurate electrochemical kinetics measured in solutions of appropriate composition.

3.2 Introduction

Corrosion due to galvanic coupling of dissimilar materials can be detrimental to aerospace structures. A connecting pathway for ions, in the form of a thin electrolyte layer of saltwater, for example, is all that is required to create a galvanic cell if dissimilar materials are already present. A lack of weldability, due to the precipitate-strengthened nature of the alloy, requires fasteners to join 7XXX series aluminum[1]. Stainless steel is ubiquitous as the fastener material[2], because of its good mechanical properties and corrosion resistance. Therefore, a common location of dissimilar metals in electrical contact is near fasteners on the surface of an aluminum aircraft structures.

The susceptibly of corrosion damage can be increased when complex geometries are involved, because the system can create occluded regions in which the local chemistry can be altered to allow stable localized corrosion to propagate more easily. Specifically, fasteners, by their very nature, involve holes in the structural panel and have been seen to have galvanic corrosion 3.5 times greater than that of a flat panel[3]. The occluded regions created between the fastener and the hole as well as beneath the washer can be sites of damage that are hard to detect. Corrosion damage inside of that geometry can then be of great significance if the structure is under stress due to the stress-concentrating nature of the hole being amplified by any corrosion damage in the hole[4–7].

Because of this complexity, computational models have been of great interest as they can isolate parameters artificially and study their effects individually in ways that cannot be accomplished experimentally. In the current work, a geometry is built in a finite element model to represent a noble fastener mated to an AA7075 structural plate. The current density distribution as a function of defect size in the coated panel around a noble fastener was studied. Intentional defects on the surface coating are a common way to test for worst-case scenarios in a panel assembly[8–12]. The defect, in the form of a scribe, both activates dissolution on the surface of the panel and allows a pathway for solution to enter into the fastener hole.

For any computational model to be useful, accurate and appropriate electrochemical boundary conditions must be used. As seen in the literature, these kinetic descriptions can be established via standard polarization curve measurements[11,13–15]. The main caveat is that they are generated on the appropriate material and in the appropriate solution. The computational model can then account for the ohmic drop that occurs between the cathode and anode, and for polarization resistance at the metal/solution interface, through utilization of the secondary current distribution[13,16,17].

Simplifying assumptions are encompassed in the secondary current distribution model, such as neglecting any concentration gradients in the system. The governing equation can, therefore, be simplified to the Laplacian, as migration is assumed to be the dominant transport term[16].

Applying the entire Nernst-Planck equation is another, more robust, means of conducting FEM through utilization of tertiary current distributions. There are fewer assumptions with this method, and it accounts for migration, convection, and diffusion [14,15,18–22]. Although providing a thorough model, there are a few difficulties with solving this method. First, the reaction rate constants need to be known as an input to the model. These can be measured experimentally, which can be difficult, or in limited cases, found in literature. Second, the computational power can increase exponentially in these systems, as many of the variables have interdependent terms. Several authors in the literature have utilized secondary current distribution assumptions for similar systems to this work, with good comparison to experimental data[11–13,23–25]. Therefore, this work will also use the Laplacian as the governing equation.

King *et al.* utilized a finite element analysis to determine the throwing power of AA2024 and pure Mg, when put in a galvanic couple with each other. This analysis was done to estimate the ability of the Mg-rich primer to provide cathodic protection of a scribe. The Laplace equation was assumed, and experimental potentiodynamic scans were utilized as boundary conditions. The model involved a simplified two-dimensional geometry with only one cathodic surface, and anodic surfaces which stayed stationary with respect to time[11]. This work proposes a similar approach, with a different application and a more complex geometry. The throwing power calculations in this work have the ability to determine the most susceptible region to corrosion damage, based on the radius from the fastener. The geometry is three-dimensional, with 14 cathodic surfaces and an evolving anodic surface (*i.e.* the scribe), leading to a design that can be directly applied in practice.

In previous work, SS316 fasteners were seen to galvanically couple with bare AA7075 at distances of one inch away[23]. The corrosion damage caused by the SS316 fastener was insidious, because it manifested itself inside of a hole containing a Ti-6Al-4V fastener. Knowing the extent to which the SS316 fastener can galvanically couple with bare AA7075 would be an important parameter to the maintenance and design of aerospace structures.

3.3 Methods

Finite Element Modeling

The finite element model built in COMSOL Multiphysics© (version 5.3a) in previous work[23] was used to calculate the current distributions at the scribe tip of the fastener/panel galvanic assembly. This model utilized secondary current distributions, which accounts for both ohmic drop in the solution and interfacial polarization resistivity, but neglects any diffusional mass transport. The underlying assumption was that the migration of ions was the dominant transport mechanism, allowing the Nernst-Planck equation to be simplified to the Laplace equation as the governing equation. The full derivation of the Laplace equation can be seen in a recent review paper on FEM by *Liu et al.*[16].

The model was assumed to be in steady state equilibrium, neglecting any time dependencies. The surface of the AA7075 panel was assumed to have a perfect coating in the model, implying that only surfaces defined as "bare" would be susceptible to damage. In the current model, the bare surfaces on the panel consisted of the "X" scribes on the surface and inside of the fastener hole (Figure *3.1*(b)).

The geometry of the model was made to represent that of a single fastener and washer in a panel, to simulate a realistic common geometry found in aerospace structures (Figure *3.1*(a) and (b)). In all scenarios, the washer was made out of the same material as the fastener. Note that in practice, the fastener and washer would have an insulating coating; however, friction inside of the hole would eventually wear down coating, making a galvanic couple possible[26]. Therefore, bare fasteners and washers are studied in this work, in order to test for a worst-case scenario.

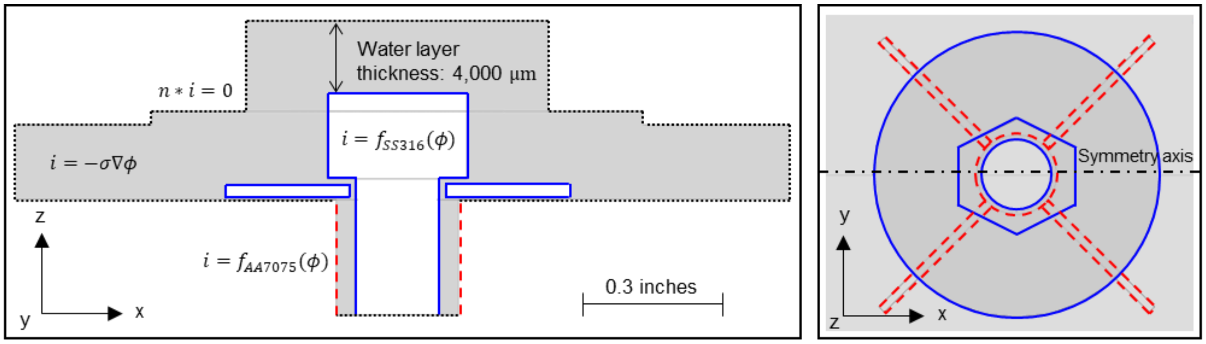

Figure 3.1: Geometry in model of fastener in panel; (a) y-x planar cross-sectional view with boundary conditions labeled; (b) z-x planar aerial view; Red dashed lines indicate AA7075 boundaries, blue solid lines indicate cathodic boundaries (SS316, Ti-6Al-4V, or sol-gel coated SS316), black dotted lines indicate external boundaries with zero flux; Note that gray domain represent solution, with the Laplace as the governing equation

The AA7075 panel was designed to be 0.25 inches thick and was 30 inches x 30 inches with respect to the width and length. The large size of the panel was to account for the large change in scribe length during testing; for all purposes, the panel can be thought of as "infinite" with a surface defect of a scribe surrounding a fastener and washer. The back and sides of the panel contained no scribes and were considered electrically insulating.

The length of the bolt was designed to be 0.25 inches long so that it terminated at the bottom of the panel. In practice, a nut usually secures the bolt to the panel; this was neglected in our model because we assumed that solution could only enter through the top of the panel. The fastener had a hexagonal head, with a diameter of 0.3 inches and a height of 0.18 inches. The fastener shaft geometry was built cylindrical, neglecting the presence of the threads, but the gap selected was close to the minimum gap observed in cross-sectional studies. This simplification was done to reduce the meshing of the geometry required. The washer was built with an outer diameter of 0.75 inches and a thickness of 0.03 inches.

The gaps between the fastener, washer, and panel were determined through cross-sectional analysis of a non-corroded assembly, as described previously (Figure *3.2*(a))[23]. To determine the effects of these gaps on the distribution of the galvanic current, a parameter sweep was done for each gap, ranging from the smallest gap measured to the largest gap measured experimentally in previously reported work[23]. As each gap size was changed, the remaining gaps were held at the values indicated with black dashed lines in Figure *3.2*(b) to (d).

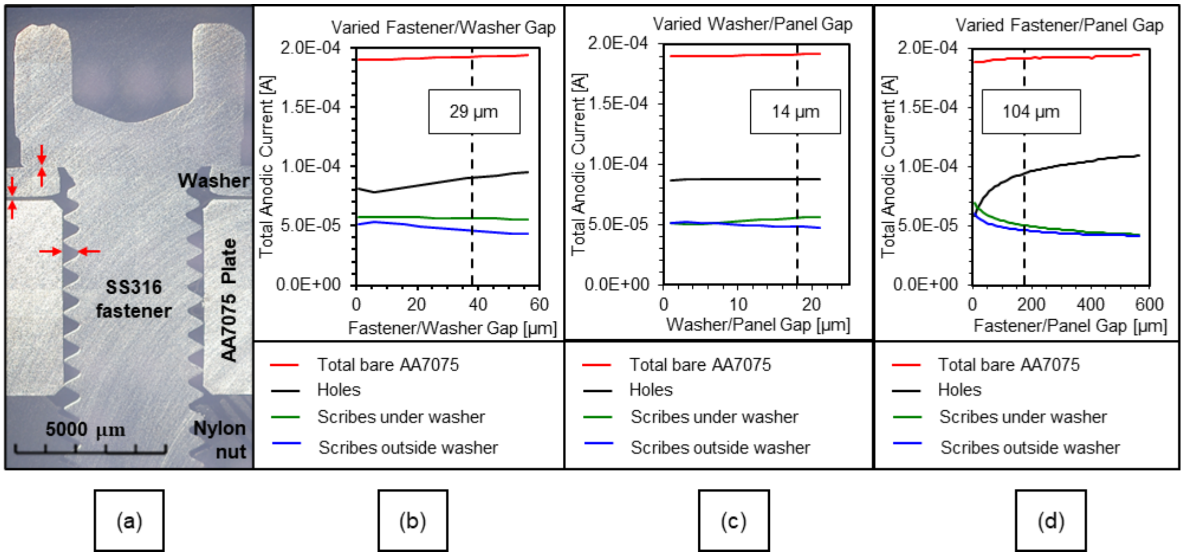

Figure 3.2: Current distributions on AA7075-T651 plate as function of gaps between fastener, washer, and substrate; (a) gaps measured on cross-sectioned fastener/panel assembly; (b) fastener/washer gap changed from 1 to 56 µm; (c) washer/substrate gap changed from 1 to 21 µm; (d) fastener/substrate gap changed from 5 to 565 µm; Note that the dashed lines in (b) to (d) represent the values held constant as other gap parameters were varied

In all computational studies, the water layer was set constant at 4,000 µm thick, as conducted in a previous study[23]. Kramer *et al*. previously utilized a water layer thickness of 1,000 µm in a FEM, stating that it represented bulk immersion[13]. Both of these water layer thicknesses are larger than the natural convection layer of 800 µm[27], which can correlate to bulk immersion of the samples. The model used water layer thicknesses ranging from 800 µm to 6,000 µm, and negligible differences were seen. Previous work, however, has also utilized a 4,000 µm water layer thickness model in comparison to experimental panels exposed to B117, with good agreement[23]; therefore 4,000 µm was chosen as the water layer thickness in this model as well.

The scribe lengths were varied from one inch to 30 inches. Note that "scribe length" in this work represents the entire distance from the tip of the scribe diagonally through the fastener to the opposite tip. With this convention, the "true" scribe length would be less slightly less than the value documented, because of the lack-of-scribe in the fastener hole. At each scribe length, the current density at the tip of the scribe was extracted as a measure of the intensity of the galvanic couple. The throwing power of a bare SS316 fastener, sol-gel coated SS316 fastener, and a Ti-6Al-4V fastener, as a function of distance, was found through this method. Comparing the throwing power of the bare vs. sol-gel coated fastener was one way to determine the effectiveness of the sol-gel coating.

The geometry of the cathodic hardware was then modified. In all of the following tests, SS316 boundary conditions were used for all cathodic surfaces. First, the washer diameter was decreased to the same surface area as the fastener head. Next, the entire fastener geometry was changed to represent a countersunk fastener in the panel, and the washer was eliminated. The surface area of the countersunk fastener was nearly identical to that of the raised fastener assembly (i.e., including the washer). Table 1 indicates the surface area breakdown on the cathodes in the assembly, both before and after changes to the geometry were made. The throwing power of the fastener was calculated again for both new geometries. Both the cathode:anode surface area ratio and position of the cathode were considered in order to determine their effect on the throwing power of the fastener.

Table 3.1. Breakdown of surface areas on different locations of the cathode in the fastener/panel assembly

Location in Assembly	Surface Area [in^2]
Total Raised Fastener + Washer	1.36
Raised Fastener Head	0.300
Raised Fastener Shaft	0.161
Washer	0.897
Total Raised Fastener + Modified Washer	0.761
Raised Fastener Head	0.300
Raised Fastener Shaft	0.161
Modified Washer	0.300
Countersunk Fastener	1.36

Potentiodynamic Scans

Rather than imposing purely theoretical (or “idealized”) boundary conditions, such as those based on the Butler-Volmer equation, experimental potentiodynamic scans were used. This approach provides a means to account for complex reactions that may be taking place on the surface of the metal, that are not considered or describable in the classical kinetic equations. Most polarization curves relevant to corrosion processes are not well described by standard kinetics expressions. Rather than a “one size fits all” model, each boundary condition is an experimental measurement on a specific material, in a specific solution capturing the observed current-potential relation most accurately.

Cathodic potentiodynamic scans of bare SS316 (UNS S31600) and Ti-6Al-4V (UNS R56400) were generated in 5 wt% NaCl (0.9 M NaCl) at 35°C and were utilized as boundary conditions in the model. A platinum mesh was used as the counter electrode, while Silver/Silver Chloride was used as the reference electrode. In addition, cathodic polarization data were generated on a sol-gel coated SS316 sample, applied in a similar manner as traditional organic coatings. The sol-gel coated metal was placed in the electrochemical cell with the electrolyte of choice in direct contact with sol-gel. The current response is typically on the order of microamperes per cm^2 or lower for the sol-gel coated system and orders of magnitude higher for uncoated metal systems. The sol-gel coating was developed by Luna Labs USA, LLC. and has been seen to mitigate corrosion damage both on the surface and down fastener holes, when applied directly on the fasteners[23].

A full scan, anodic and cathodic, was conducted on bare, activated AA7075 (UNS A97075) to represent an actively corroding surface. The activation was accomplished by first potentiostatically holding the AA7075 at -0.3V(SCE) for one hour before scanning in the negative direction. This activation was used to create conditions at the AA7075 surface representative of an active localized corrosion site. The cathodic scan on AA7075 was utilized to account for the self-dissolution of AA7075. All scans were generated in quiescent solution at a scan speed of 0.1 mV/sec.

These curves were input as boundary conditions on the surfaces representing each specific material (Figure *3.1*(a) and (b)), with current density as a function of potential. External surfaces represented the water/air or water/coated AA7075 panel interfaces, and were set to have zero current density flux. The domain in the model represented the water layer, with the Laplace as the governing equation, as stated above (Figure *3.1*(a)).

3.4 Results

Gaps in Raised Fastener Assembly

After the gaps between the fastener, washer, and panel were measured experimentally, they were input into the model. Three different gaps were of particular interest; the bolt/washer gap, the washer/panel gap, and the fastener/panel gap (Figure *3.2*). A parameter sweep was run to determine the effect of the size of the various gaps on the distribution of the current on the panel. Note that the range of the fastener/panel gap was large, due to the threads of the fastener (Figure *3.2*(d)). For all variations of the gaps studied here, the majority of the current was distributed down the fastener hole (Figure *3.2*(b) – (d)). The one exception to this constant trend was at small fastener/panel gaps, where the majority of the current transitioned from the hole to the scribes underneath the washer (Figure *3.2*(d)). The black dashed lines in Figure *3.2*(b) – (d) represent the values which were held constant as the other gap parameters were changed. These results helped determine the geometry of the standard model going forward. Because there was nominal change to the current throughout all of the gap values tested, the values indicated by the black dashed lines in Figure *3.2*(b) – (d) were taken to be “standards” in the model.

The potentiodynamic polarization scans were generated and plotted together (Figure *3.3*). The sol-gel coating was seen to lower the current density of the bare SS316 material. From the polarization curves, the Ti-6Al-4V surface has a lower current density than the bare SS316 surface, which is consistent with what has been seen previously[14,17]

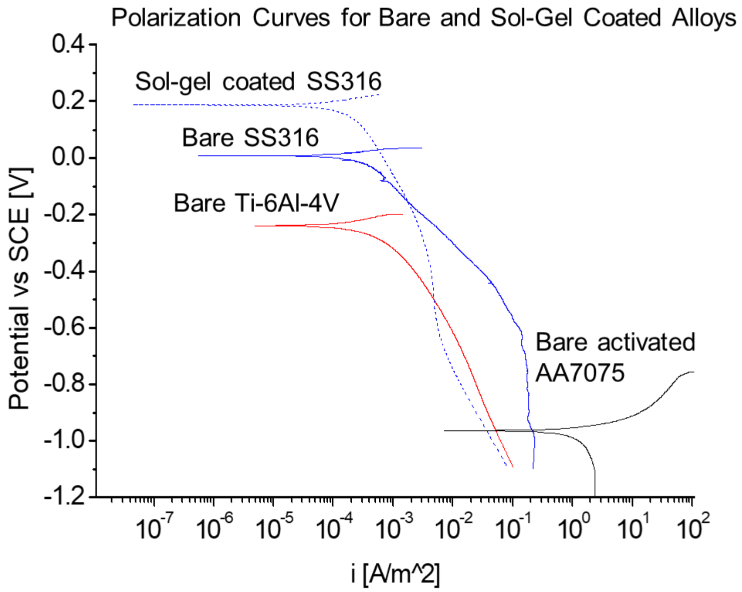

Figure 3.3: Potentiodynamic scans of bare SS316, sol-gel coated SS316, bare Ti-6Al-4V, and bare activated AA7075, input as boundary conditions into the finite element model[23]

Throwing Power in Raised Fastener Assembly

Once the geometry was built and the boundary conditions were input, the model was used to investigate the throwing power of the SS316 fastener and the washer. To accomplish this, the scribe length was changed from one inch to 30 inches, in one-inch increments (Figure 3.4(a) and (b)). At each new scribe length, the current density at the tip of the scribe was extracted from the simulation and plotted vs. scribe length in Figure 3.4(c). With increasing scribe length, the current density was seen to decay to the self-dissolution rate of the AA7075 panel. This decay indicates that at large scribe lengths, the SS316 fastener is no longer significantly galvanically coupling with the farthest part of the AA7075 panel. Rather, at the tip of long scribes, the panel is corroding at a rate nearly equal to that of a panel containing zero fasteners. As the distance increases, the IR resistance in solution increases, until the driving force to corrode AA7075 is no longer from the fastener, but from the reduction reaction on the AA7075 itself.

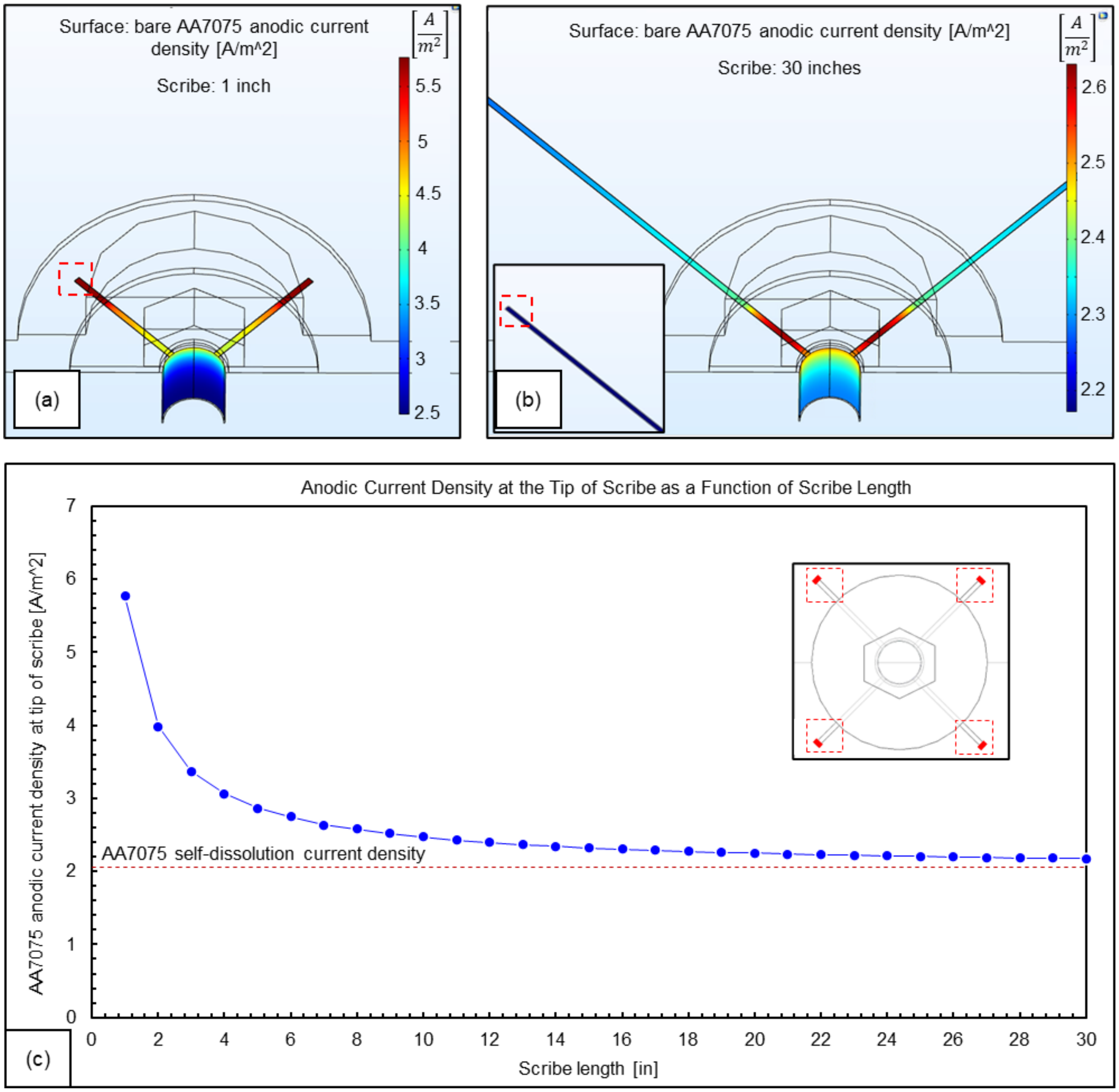

Figure 3.4: Raised fastener assembly; (a) false-color current density plot of bare AA7075 at scribe length of 1 inch; (b) at scribe length of 30 inches; (c) AA7075 anodic current density at scribe tip vs scribe length, decaying to the self-corrosion current of AA7075; inset image serves as a reminder that this is only the current density at the tip of the scribe, and not the total current density over AA7075

Previous work compared the total corrosion damage of a sol-gel coated fastener with that of a bare fastener, to evaluate the effectiveness of the sol-gel coating[23]. An alternative method of comparison is proposed in this work, through the calculation of the cathodic throwing power in the fastener assembly. Therefore, in the model two more simulations were performed; one using bare Ti-6Al-4V boundary conditions for the fastener and washer, and another using sol-gel coated SS316 boundary conditions for the fastener and washer. It was seen that the throwing power of the sol-gel coated SS316 fastener and washer was reduced *below* that of the throwing power of the Ti-6Al-4V fastener and washer (Figure 3.5).

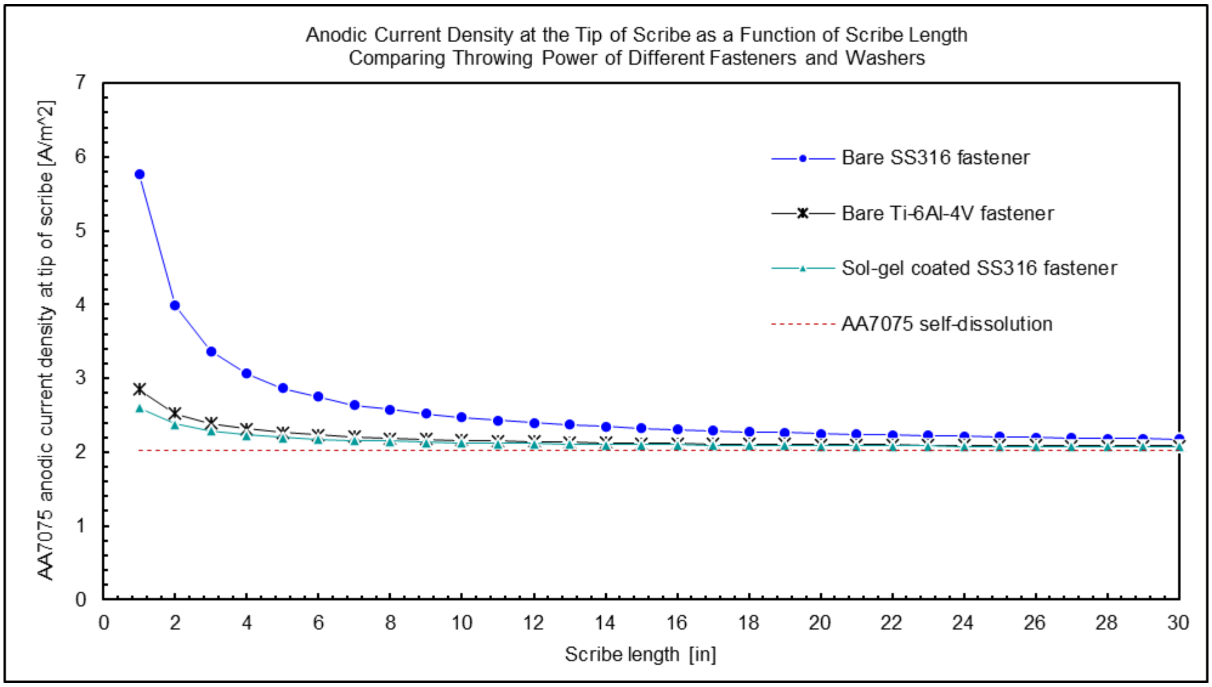

Figure 3.5: Comparison between the throwing power of SS316, Ti-6Al-4V, and sol-gel coated SS316 fasteners in an AA7075 panel

Throwing Power in Raised Fastener Assembly with Modified Washer Diameter

In the following raised fastener models, all fasteners and washers were set to have SS316 boundary conditions. To determine what region of the fastener and/or washer was contributing the majority of the galvanic current, the current was deconvoluted into contributions from the washer, the fastener head, and the fastener shaft. It was determined that throughout all scribe lengths, the *washer* was contributing the majority of the current, not the fastener (Figure 3.6).

The surface area of the three locations above was determined, and it was seen that the washer indeed had the largest surface area (**Table *3.1***). To confirm that the largest surface area would contribute the largest amount of current, the diameter of the washer was decreased until its surface area was equal to that of the fastener head (Figure 3.7). The contributions of the current on the cathode were seen to change, with both the washer and the fastener head contributing equal amounts of current (Figure 3.6). A throwing power plot was constructed from the modified washer assembly and was compared with that of the original washer assembly throwing power (Figure 3.7).

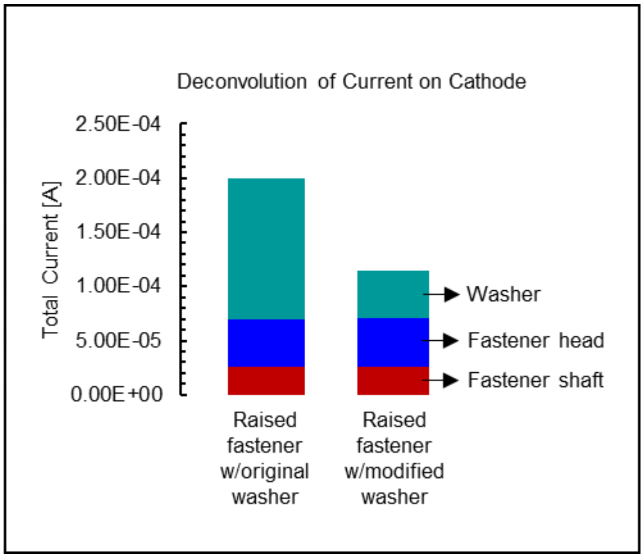

Figure 3.6: Deconvolution of the cathodic current to the locations of the washer, the fastener head, and the fastener shaft for the raised fastener assembly with the original and modified washer

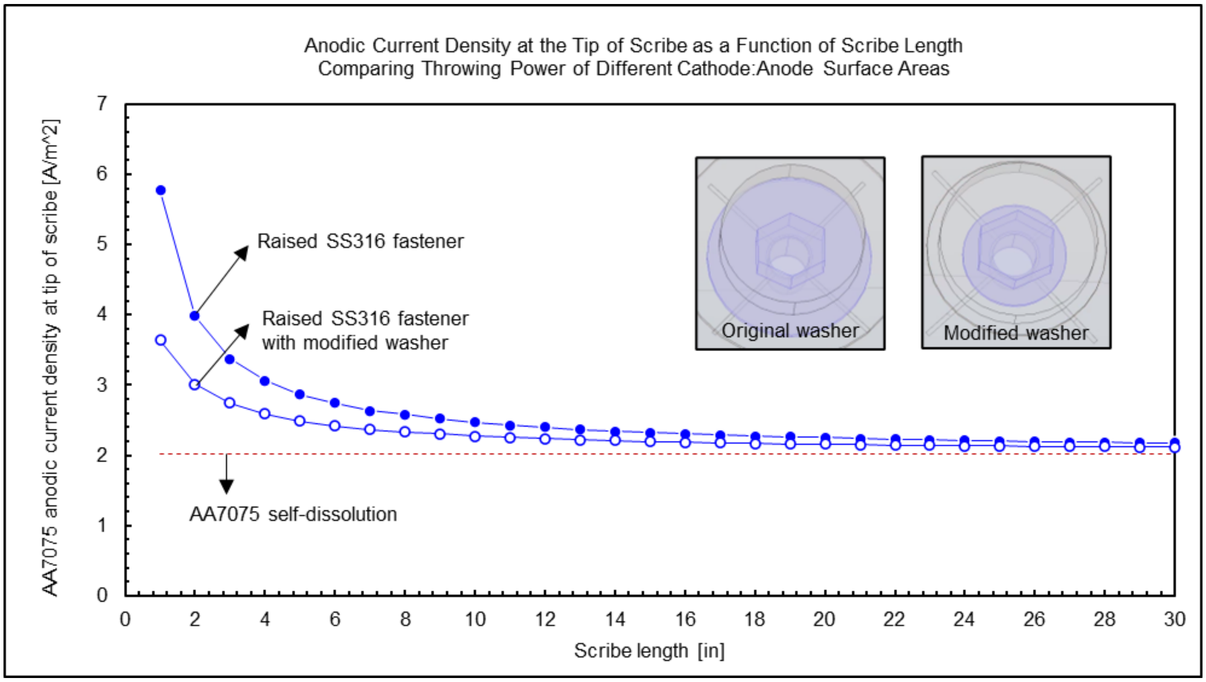

Figure 3.7: Throwing power of the raised fastener/panel assembly with washers of different diameters to determine the effect of cathode:anode surface area ratio; inset image show geometry of original and modified washer, where surfaces in blue represent SS316 boundaries

Throwing Power in Countersunk Fastener in Panel Assembly

To determine if the *position* of the cathode had an impact on the throwing power, a countersunk fastener geometry was run, with the same surface area as the raised fastener and washer assembly (**Table *3.1***). A false color plot of current density on the AA7075 surface in the new geometry can be seen at two different scribe lengths (Figure 3.8(a) and (b)). The throwing power of the new fastener assembly was plotted, and it was seen to be much less than that of the raised fastener (Figure 3.8(c)).

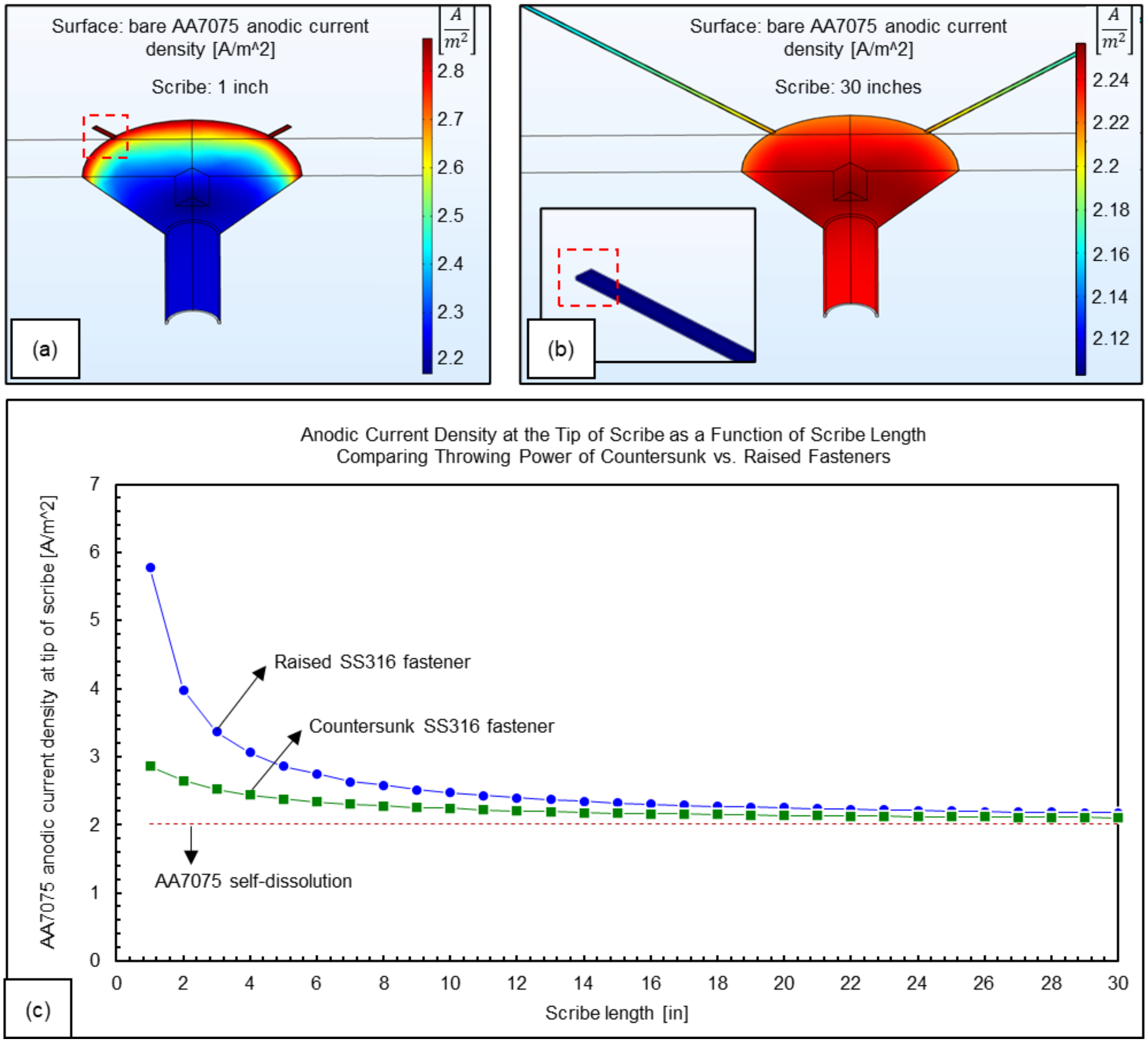

Figure 3.8: Countersunk fastener assembly; (a) false-color current density plot of bare AA7075 at scribe length of 1 inch; (b) at scribe length of 30 inches; (c) comparison of throwing power between raised and countersunk fastener assembly

3.5 Discussion

Application of the Sol-Gel Coating to the Fastener and Washer Lowers the Throwing Power

The throwing power plot of the SS316 fastener and washer (Figure 3.4(c)) has two main implications. It shows that SS316 hardware can still galvanically couple with AA7075 even up to

30 inches away, although the contribution is extremely small at that distance. It also shows that at a scribe length of approximately two inches long, the SS316 fastener and washer are contributing double the amount of cathodic current, as compared with the self-dissolution rate of the activated AA7075. This assessment helps explain the phenomenon seen experimentally, where the SS316 fastener was seen to couple with the bare AA7075 fastener hole one inch away[23].

When the boundary conditions were changed, a comparison could be made between the SS316 hardware, the Ti-6Al-4V hardware, and sol-gel coated SS316 hardware (Figure 3.5). Ti-6Al-4V is known to have minimal galvanic coupling with AA7075, because of the slow cathodic kinetics on their surface. Therefore, it is a significant result that the sol-gel coating reduces the throwing power of the SS316 hardware below that of the Ti-6Al-4V hardware.

The Cathode with the Largest Surface Area Contributes the Most Galvanic Current

The SS316 washer was seen to be the major contributor to the cathodic current in the galvanic couple (Figure 3.6). In a full panel, this results in the SS316 washers throwing current down the hole filled with the Ti-6Al-4V fastener. Without these calculations, experimental analyses could be misconstrued into thinking that the Ti-6Al-4V fasteners are just as deleterious in a galvanic couple of this configuration. Further investigations of the effect of changing the washer diameter demonstrated this observation as well. It is well known that the surface area ratio between the cathode and anode can have a large impact on the corrosion rate; however, to determine if the surface area was the reason behind the washer dominating in cathodic current, the washer diameter was changed. The modified washer had the same surface area as that of the fastener head (**Table *3.1***).

After decreasing the washer diameter, the peak current density at the tip of the scribes was seen to drop, but the throwing power followed the same function as it had with a larger washer diameter (Figure 3.7). The modified washer was seen to contribute an equal amount of cathodic current as the head of the fastener, in this new model (Figure 3.6). This result indicates that the location with the largest surface area will contribute the majority of cathodic current.

A Lower Throwing Power on the Surface Results in Increased Damage in the Hole

To determine if the position of the cathode had a large effect on the throwing power, a SS316 countersunk fastener panel was conducted in the model. It is important to remember that the total cathodic area in both the raised fastener model and countersunk fastener model were nearly identical (**Table *3.1***). A throwing power plot was constructed for the countersunk fastener panel by documenting the current density at the tip of the scribe at each scribe length, as has been previously described. The results of this plot showed that the peak current density was lower than that of the raised fastener (Figure 3.8(c)). However, the countersunk fastener's throwing power did not decay at the same rate as the raised fasteners, but at a slower rate.

At the longest scribe length of 30 inches, the highest current densities appear to be in the fastener hole, as shown by the increased intensity of red (Figure 3.8(b)). This result is in contrast to the raised fastener assembly, where the peak current was underneath the washer at a scribe length of 30 inches (Figure 3.4b). Although in both assemblies, there was a cathodic material inside of the fastener hole (that is, the fastener shaft), the peak current density only went inside of the fastener hole in the countersunk assembly scenario. This result is presumably because at long scribe distances, the ohmic drop is large, so the cathode will interact with the anode in closest proximity. For the raised fastener assembly, that location was underneath the washer, while for the countersunk assembly that location was inside of the fastener hole.

Although this analysis determined the distance at which the cathode fastener/washer system would be able to galvanically couple with bare AA7075, there are subtleties to appreciate. A “low” throwing power does not necessarily correlate to a lack of damage, as can be seen from the countersunk fastener assembly. The overall total current in the system *was the same* for both the raised fastener and the countersunk fastener assemblies, because the cathodic surface areas were the same. The countersunk fastener assembly could not galvanically couple with the bare AA7075 scribe at large distances, meaning that the bulk of the cathodic current was thrown down the fastener hole. Damage down the fastener hole can lead to cracking and failure, and is therefore by no means better than damage underneath the washer.

3.6 Conclusion

- Over the ranges observed in the panels, the size of the gaps between the fastener, washer, and panel has minimal effect on the current distribution in the raised fastener/panel assembly utilized in this study.
- SS316 hardware can have a strong galvanic affect up to two inches away under bulk immersion conditions. In the geometry considered, the SS316 fastener and washer throw enough current to double the AA7075 dissolution rate up to two inches away. At the tip of the scribe length 30 inches away, the galvanic couple between SS316 and AA7075 is minimal, but non-zero.
- Application of the sol-gel coating over the raised fastener and washer lowered the throwing power of the SS316 below that of the Ti-6Al-4V hardware.

- Through evaluation of the surface areas, it was determined that the SS316 *washer* was the cathodic surface which was contributing the majority of the galvanic current, not the fastener itself.

- Mitigation strategies to lower the throwing power of the cathode in a fastener/panel assembly include coating over the fastener or decreasing the overall surface area of the cathode, both of which decrease the total cathodic current available.

- Countersunk fasteners do not galvanically couple with scribes at long scribe lengths, rather the majority of the current is isolated to the fastener hole.

3.7 Acknowledgements

Any opinions, findings and conclusions or recommendations expressed in this material are those of the author(s) and do not necessarily reflect the views of Office of Naval Research. This work is supported by the Office of Naval Research under Contract No. N68335-16-C-0121 (Mr. William Nickerson) through a subcontract with Luna Labs USA, LLC.

3.8 References

1. Davis, J.R., *Corrosion of Aluminum and Aluminum Alloys* (1999).

2. Feng, Z., and G.S. Frankel, *Corrosion* 70 (2014): pp. 95–106.

3. Rafla, V.N., and J.R. Scully, *Corrosion Journal* 75 (2019): pp. 12–28.

4. Burns, J.T., J.M. Larsen, and R.P. Gangloff, *Fatigue & Fracture of Engineering Materials and Structures* 34 (2011): pp. 745–773.

5. Harrison, T.J., B.R. Crawford, G. Clark, and M. Brandt, *Advanced Materials Research* 891–892 (2014): pp. 242–247.

6. Harrison, T.J., B.R. Crawford, M. Brandt, and G. Clark, *Computational Materials Science* 84 (2014): pp. 74–82, http://dx.doi.org/10.1016/j.commatsci.2013.11.033.

7. Cole, G.K., G. Clark, and P.K. Sharp, "The Implications of Corrosion with Respect to Aircraft Structural Integrity" (DSTO Aeronautical and Maritime Research Laboratory, 1997).

8. Feng, Z., G.S. Frankel, and C.A. Matzdorf, *J Electrochem Soc* 161 (2014): pp. 42–49, http://jes.ecsdl.org/cgi/doi/10.1149/2.059401jes.

9. Matzdorf, C.A., W.C. Nickerson, B.C. Rincon Tronconis, G.S. Frankel, L. Li, and R.G. Buchheit, *Corrosion* 69 (2013): pp. 1240–1246.

10. Feng, Z., G.S. Frankel, W.H. Abbott, and C.A. Matzdorf, *Corrosion* 72 (2016): pp. 342–355.

11. King, A.D., J.S. Lee, and J.R. Scully, *Journal of The Electrochemical Society* 163 (2016): pp. 342–356.

12. Saeedikhani, M., S. Wijesinghe, and D.J. Blackwood, *Corrosion Science* 163 (2019): p. 108296, https://doi.org/10.1016/j.corsci.2019.108296.

13. Kramer, P., T. Curtin, M. Merrill, M. Kim, F. Friedersdorf, and R. Adey, "Atmospheric Corrosion Measurements to Improve Understanding of Galvanic Corrosion of Aircraft," in NACE International: CORROSION (2018), pp. 1–11.

14. Snihirova, D., D. Höche, S. Lamaka, Z. Mir, T. Hack, and M.L. Zheludkevich, *Corrosion Science* (2019).

15. Wang, H., F. Presuel, and R.G. Kelly, *Electrochimica Acta* 49 (2004): pp. 239–255.

16. Liu, C., and R.G. Kelly, *CORROSION* (2019).

17. Tattersall, C., “Modeling and Analysis of Geometrically Complex Corrosion,” University of Virginia, 2018.

18. Murer, N., R. Oltra, B. Vuillemin, and O. Néel, *Corrosion Science* 52 (2010): pp. 130–139, http://dx.doi.org/10.1016/j.corsci.2009.08.051.

19. Amorim, T.M., C. Allély, and J.P. Caire, “Modelling Coating Lifetime: First Practical Application for Coating Design,” in COMSOL Conference (Hannover, 2008).

20. Mizuno, D., and R.G. Kelly, *Corrosion* 69 (2013): pp. 681–692.

21. Murer, N., N.A. Missert, and R.G. Buchheit, *Journal of The Electrochemical Society* 159 (2012): p. C265.

22. Dolgikh, O., H. Simillion, S. V Lamaka, A.C. Bastos, H.B. Xue, M.G. Taryba, A.R. Oliveira, C. Allely, B. Van Den Bossche, K. Van Den Bergh, J. De Strycker, and J. Deconinck, *Materials and Corrosion* 70 (2018): pp. 780–792.

23. Marshall, R.S., R. Kelly, A. Goff, and C. Sprinkle, *Corrosion* 75 (2019): pp. 1461–1473.

24. Liu, C., and R.G. Kelly, *The Electrochemical Society Interface* 23 (2014): pp. 47–51.

25. Deshpande, K.B., *Corrosion Science* 52 (2010): pp. 3514–3522.

26. Benavides, S., ed., *Corrosion Control in the Aerospace Industry* (Woodhead Publishing, 2009).

27. Liu, C., J. Srinivasan, and R.G. Kelly, *J Electrochem Soc* 164 (2017): pp. C845–C855, http://jes.ecsdl.org/lookup/doi/10.1149/2.1641713jes.

Chapter 4: Galvanic Corrosion Between Coated Al Alloy Plate and Stainless Steel Fasteners, Part 2: Application of FEM and Machine Learning to Study Galvanic Current Distributions

Rebecca Skelton Marshall*, Katie A. Define*, Rachel S. Rosner*, Adam Goff**, Charles Sprinkle**, Prasanna V. Balachandran, Rob G. Kelly*

*University of Virginia, 395 McCormick Rd, Charlottesville VA 22903

**Luna Innovations, Inc., 706 Forest St. Suite A, Charlottesville VA 22903

Authorship contributions: R. Skelton Marshall (formal analysis, computational work, machine learning coding, and writing – original draft), K A. Define (select computational simulations), R. S. Rosner (select computational simulations), A. Goff (experimental polarization behavior, and writing – review & editing), C. Sprinkle (experimental polarization behavior), P. V. Balachandran (machine learning optimization code, feedback, and writing – review & editing)

4.1 Abstract

Aluminum alloy panels joined with stainless steel fasteners have been known to occur in aerospace structures, due to their respective optimized mechanical properties. When connected via a conductive solution, a high-driving force for galvanic corrosion is present. The combination of the dissimilar materials, indicating galvanic corrosion, and complex geometry of the occluded fastener hole, indicating crevice corrosion, leads to the detrimental combined effect of galvanic-induced crevice corrosion, as investigated previously in Part I. The present work extends the validated finite element method (FEM) model to predict the current distribution and magnitude

in a variety of geometric and environmental conditions, with the goal of preventing corrosion damage within the highly-susceptible fastener hole. Specifically, water layer thicknesses ranging from bulk full-immersion (800 μm) to atmospheric (89 μm) conditions was investigated, as well as the impact of external scribe dimensions. Two avenues for mitigation were determined, 1) to force the majority of current away from the fastener hole and onto the bulk surface of the panel, and 2) to lower the overall galvanic coupling current. A random forest machine learning algorithm was developed to generalize the FEM predictions and create an open-source applicable prediction tool.

4.2 Introduction

In aerospace structures, fasteners are commonly utilized to join together structural panels, which are often composed of a dissimilar and less electrochemically noble material[1]. Generally, aluminum alloys are utilized as the structural components due to their favorable density while more noble materials, such as Ti-alloys and stainless steels with Cd-plating to name a few, are used as the fasteners due to their high strength and durability[1]. The joining process, although mechanically favorable, presents the possibility of galvanic corrosion, a costly and structurally damaging mechanism. In addition, of the wide variety of noble fastener materials utilized, a bare SS316 surface presents the largest driving force for galvanic corrosion when coupled with the aluminum alloy panel, indicating a worst-case scenario.

Corrosion can initiate crack nucleation, through both acting as a stress concentrator and through increasing hydrogen in solution, leading to embrittlement of the material[2]. In addition, not all surfaces of the structural component have equal susceptibility for corrosion or cracking to occur. Occluded creviced regions build up aggressive ions which can increase the corrosion rate[3], while non-planar geometries can act as stress-concentrators, increasing crack susceptibility[2]. A fastener hole combines both aggravates to the corrosion and cracking, with the addition of the dissimilar materials leading to galvanic-induced crevice corrosion[4,5] and the cylindrical fastener hole magnifying the external stress by three times[6]. Utilizing cross-sectional post-metallographic analysis of the fastener holes, deep intergranular corrosion (IGC) ranging from 0.85 mm to 2 mm have been visualized, indicating the severity of galvanic-induced crevice corrosion[5,7,8]. In addition, fatigue testing of a pre-corroded SS316/AA7075 galvanic couple in a fastener/panel design resulted in cracks always initiating at the fastener hole, regardless of external defects, and corresponding surface corrosion, present[9].

Therefore, it is vital to know both the magnitude and distribution of current under various conditions, to limit when the majority of current would occur in the most-susceptible high-stress regions.

Quantifying the corrosion damage in a galvanically-coupled system can be conducted through mass loss over the entire sample or optical profilometry on surface damage, with non-planar geometries making “hidden” crevice damage quantification difficult and often destructive[7–17]. X-ray computed tomography (XCT) conducted by Rafla *et al.*, demonstrated a non-destructive method of quantifying the galvanic-induced crevice corrosion, although samples sizes of this technique are limited to the mm-scale or smaller[18–21].

Using Faraday’s law of electrolysis, corrosion damage can instead be directly correlated to the measured current in the system, allowing for non-destructive evaluation and large sample sizes. Thereby, ZRA and coupled micro-electrode arrays (CMEA) have been used as an alternative in quantifying corrosion damage within complex-geometric stainless steel/aluminum alloy galvanic couples[10–15,22]. Specifically, Rafla *et al.,* constructed a scaled-down SS316/AA7050 fastener assembly cross-section through CMEA, finding that the total current in the fastener geometry was 3.5 times greater than that of a planar geometry, with the highest currents occurring at the mouth and the base of the occluded fastener hole[22].

Although very useful in many applications, the spatial resolution of the current within the ZRA and CMEA techniques has a physical limit, as the resolution is a direct result of the number of electrode leads within a sample. Concerning the work by Rafla *et al.*, described above, each electrode was spaced 0.15 mm apart, with a total of 42 electrodes, resulting in a great distribution for the scale of the sample[22]. However, transitioning to a sample size which would be found in service, the number of electrodes and corresponding experimental difficulty would exponentially increase and would never achieves a continuous distribution.

This experimental resolution limit highlights one of the advantages of computational work. The basis of finite element method (FEM) modeling involves solving a complex differential equation at each node in the "meshed" geometric domain, before interpolating between each node to output a continuous distribution[23]. For finer resolution, the mesh size is decreased, correspondingly shortening the interpolation length.

Therefore, continuous FEM current distributions along geometrically complex galvanic couples have been utilized in literature[24,25]. Along such distributions, deconvoluting the current to any specific regions of interest is an inconsequential task to the computational solver[4,5]. Geometric and environmental parameters are also often investigated within FEM galvanic couples, as the corrosion rate and potential can be highly dependent on many given variables[26–30]. To account for such a large parameter space, even FEM can fall short, as the computational time is non-trivial and the mass-amounts of data can become unmanageable. In such cases of accumulated parameter space, data science and machine learning techniques are often needed, for interpolation, correlations and predictions. Literature has already shown the application of these techniques to the field of corrosion, from designing corrosion resistant alloys to predicting correlations between crack initiation and pit dimensions[31,32].

In previous work, FEM has been experimentally validated in the context of predicting the corrosion rate of a SS316/AA7075 fastener/panel galvanic couple, in a singular environment (Part I)[5]. In this continuation of the work, the validated model will be extended to various geometric, kinetic, and environmental factors to predict under which conditions the majority of current will fall into a creviced region of a fastener/panel geometry, which would indicate the highest susceptibility for cracking and failure to occur. In addition, large datasets from the validated FEM will be used as input into a classification predictive random forest (RF) model, to increase accessibility via the open-source code and more generally predict when the creviced region is most susceptible to corrosion damage.

4.3 Methods

4.3.1. Finite Element Methodology

The computational methodology in this work was based off of a validated baseline model previously described in literature[5].

The baseline Laplacian model assumed that concentration gradients in the electrolyte domain were negligible, as Na^+ and Cl^- species were dominant and acted as a supporting electrolyte. Therefore, the conductivity was constant, and the majority of ion transport was assumed to occur through migration, via the potential gradient in the electrolyte domain. Baseline boundary conditions from the previous model were bulk quiescent AA7075 and SS316 potentiodynamic scans (PDS) in 0.9 M NaCl. All models were assumed to be in steady-state corrosion, with no time-dependencies[5].

Variations to the baseline model were made only to the boundary conditions, scribe dimensions, and water layer thickness (WL), while the governing equation over the electrolyte domain and assumptions remained the same as previous work[5,7]. The overall solution of interest also remained the same, with 0.9 M NaCl at room temperature, representing the equilibrium chloride concentration at room temperature and 97% RH[33–35], resulting in a conductivity of 6 S/m.

The geometry was built to simulate a single, raised-head SS316 fastener and SS316 washer installed in an AA7075 plate. An exaggerated schematic was built using Inkscape, an open-source software, to more easily visualize the various defined geometric parameters (Figure 4.1)[36]. The fastener was dry-installed, with no sealant within the fastener hole, allowing for solution ingress and electrochemical reactions to take place in the creviced region. Although a wet-installation method is more common in aerospace structures, such fastener assemblies would have no electrolyte (and correspondingly, no corrosion) within the fastener hole. However, *if* dry-installation were to occur, as is a possible oversight during the repair of an aircraft, then corrosion within the fastener hole would be of utmost importance due to their stress-concentration nature. The present work therefore is focused on the latter worst-case scenario of the dry-installation process.

The AA7075 plate was designed to be 0.25 in (6.35 mm) thick ($\mathrm{x_{panel}}$), with an insulated back and inert nut securing the fastener in place. The washer radius ($\mathrm{r_w}$) was 0.375 in (9.5 mm), while gaps between the washer, fastener, and panel were determined through cross-sectional metallographic analysis, described previously[4,5].

External scribes on the AA7075 panel represented intentional surface defects in an otherwise perfect coating. All scribes were 2.0×10^{-3} in (0.5 mm) deep ($\mathrm{S_{depth}}$) into the panel, with a variable scribe width ($\mathrm{S_{width}}$) and scribe length ($\mathrm{S_{length}}$), ranging from 0.01 in to 0.13 in (0.25 mm to 3.3 mm) and 0.25 in to 8 in (6.4 mm to 203 mm), respectively. As the scribes were in an "X" formation, the $\mathrm{S_{width}}$ was limited to 0.13 in before coalescing with the adjacent scribe. Default values were set to 0.02 in and 1 in, for $\mathrm{S_{width}}$ and $\mathrm{S_{length}}$, respectively, as other parameters were varied unless otherwise noted.

Note that $\mathrm{S_{length}}$ referred to the total length of one scribe traversing from tip to tip, as a convenient computational parameter (Figure 4.1). However, a "true" scribe length ($\mathrm{S_{length}^{true}}$), describing the distance from the edge of the fastener hole to the tip of the scribe, was more useful in terms of surface area calculations, and could be defined by,

$$\mathrm{S_{length}^{true}} = \left(\mathrm{S_{length}} - 2(\mathrm{r_{FH}})\right) * 0.5 \qquad 4.1$$

where $\mathrm{r_{FH}}$ represents the radius of the fastener hole (9.55×10^{-2} in, 2.4 mm).

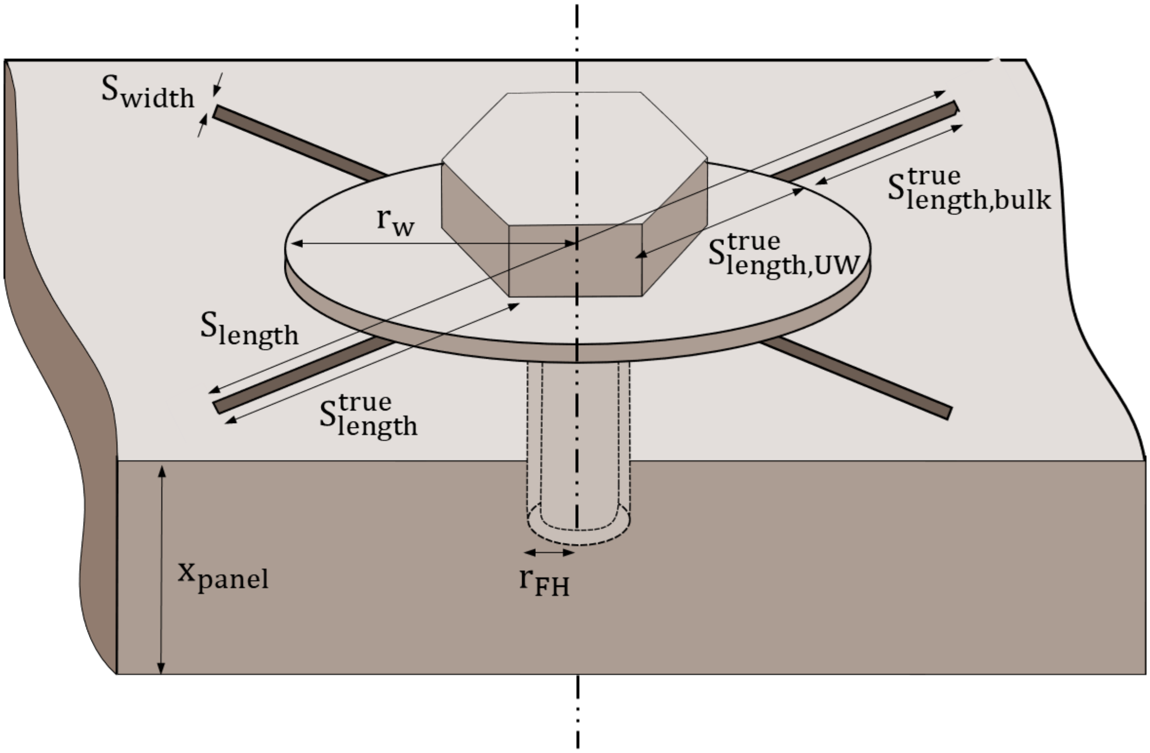

Figure 4.1: Schematic of fastener-in-panel system with geometric parameters labeled, built using Inkscape, an open-source software[36]; dot-dashed line represents the center of the fastener z-axis.

Previous experimentally-generated electrochemical kinetics on an activated AA7075, bare SS316, and a sol-gel coated SS316 were used as boundary conditions for the present computational model[4,5]. All potentiodynamic scans were conducted in bulk, quiescent 0.9 M NaCl solution, at a scan rate of 0.1 mV/s. The AA7075 surface was "activated" by a 1 hr potentiostatic hold above the pitting potential at -0.3 V_{SCE} prior to the electronegative anodic scan, inducing severe pitting on the surface. Utilizing this scan as a boundary condition implied that all designated surfaces of AA7075 (*i.e.*, the scribes and fastener hole) were actively corroding, which complemented the previous assumption that the system was in an actively corroding steady-state. Anodic and cathodic Tafel slopes were extracted from the activated AA7075 PDS, to account for both dissolution and local cathodic reactions occurring on the

AA7075 surface. In certain scenarios, the activated anodic AA7075 kinetics were scaled to larger and smaller current densities than the baseline, assuming that the Tafel slopes were constant. That is, the pseudo-exchange current density (i_0) was varied while the open circuit potential (OCP) remained constant.

The sol-gel coating applied on the SS316 surface could more accurately be considered a surface treatment, as the thickness ranged from 5 – 10 μm. The formulation of the sol-gel was identical to that used in previous work[4,5], although further modifications have been recently introduced, with the latest sol-gel coating identified as Blockade GC™, as used in recent work[9].

The WL was assumed to be conformal to the fastener surface and continuous across the entire panel and fastener assembly. Three bulk WL were simulated, 800 μm, 1,000 μm, and 4,000 μm, which utilized bulk cathodic kinetics while the geometric WL was varied. Extending the baseline model from bulk conditions to atmospheric conditions, new cathodic behavior had to be quantified to account for the increased diffusion path of $\mathrm{O_2}$ at WL less than the natural convection boundary layer thickness (δ_{nc})[37].

The cathodic behavior of SS316 in WL $< \delta_{nc}$ was determined by Liu *et al.*, through the rotating disk electrode (RDE) technique in 0.6 M NaCl[30]. Although the solution concentration used by Liu *et al.*, was 0.3 M NaCl lower than the focus of this work, recent results from Katona *et al.*, has found that there is only 80 μm difference between δ_{nc} on stainless steel at those two specific chloride concentrations, if all other parameters are the same[29]. Therefore, results from Liu *et al.*, with WL $= 44.5\ \mu\mathrm{m}, 89\ \mu\mathrm{m}, 200\ \mu\mathrm{m}$, and $400\ \mu\mathrm{m}$ were utilized as boundary conditions in this work, with each WL corresponding to a different rotation rate (ω). Note that the WL $= 400\ \mu\mathrm{m}$

was extrapolated, rather than measured, as the RDE was limited to $\omega \geq 10$ rpm. Back-calculations predict that $\omega = 2$ rpm would be required to produce a $\mathrm{WL} = 400$ µm.

Deaerated cathodic kinetics were not implemented as boundary conditions in the cathodic creviced surface areas, as their contribution of slow oxygen reduction reactions (ORR), via the competing consumption and diffusion of $\mathrm{O_2}$ into occluded regions, was seen to be negligible in the present system for two reasons. First, the surface area of the creviced fastener shaft in this work was only 12% of the total cathodic surface area, indicating that even if the fastener shaft was insulating (*i.e.*, non-existent chemical reactions on the surface), there would still be a significant driving force coming from the external cathodic surfaces (*i.e.*, the fastener head and washer)[4]. Second, the thin WL cathodic kinetics were orders of magnitude larger than the deaerated kinetics, indicating that the deaeration would have little influence over the total current. Deaeration on the sol-gel treated surface was found to be inconclusive, as the thin barrier coating already slows the diffusion of $\mathrm{O_2}$ to the surface and has more impact. If external cathodic surfaces were not present, and atmospheric conditions were not a focus of this study, then deaerated kinetics would be taken into further consideration.

Results of the FEM model focused on the current magnitude and distribution, which were calculated through integrating the current density over a given area. In all models, the conservation of charge was preserved, that is, the total anodic current (I_a) equaled the total cathodic current (I_c), within reasonable error.

FEM Database Construction and Random Forest Methodology

A database of the FEM results was accumulated, with varying $\mathrm{S_{width}}$ from 0.01 in to 0.13 in, $\mathrm{S_{length}}$ from 0.25 in to 8 in, and WL from 44.5 µm to 4,000 µm. In total, the database was 1534 rows. The columns included the independent parameters of interest, varying based on the model, and the dependent (resulting) parameter. Although I_{total}, I_{FH}, I_{UW}, $I_{crevice}$, and I_{bulk} were all dependent variables, the main variable of interest for the classification model was a binary classification variable, essentially determining "yes" or "no" as to whether the majority of current would occur in a creviced region or not. Elsewise, the majority of current must occur in a bulk region, as the total current is conserved. Note that the machine learning model did not predict the *magnitude* of the current distributions, but only predicted a binary classification of the current distributions.

At all parameters with $\mathrm{S_{length}} < 2\mathrm{r_w}$, there existed no current over the bulk anodic surfaces, that is, $I_{bulk} = 0$, as no anodic surface areas existed outside of the washer (in bulk regions) with these parameters. In certain scenarios comparing the creviced-to-bulk surface areas and currents, it was desirable to not include these values. Therefore, the database was revised and decreased to 1261 rows to preserve only non-zero I_{bulk} scenarios, with 760 rows in which the current in the crevice ($I_{crevice}$) was dominant ($I_{crevice} > I_{bulk}$) and 501 rows in which $I_{crevice} < I_{bulk}$. The numeric variables were scaled (normalized) and centered, to mitigate any large parameter values skewing the impact of smaller parameter values. The binary classification variable, determining whether the majority of current would occur in a creviced or bulk region, was exempt from these pre-processing methods. The total data, including the independent and dependent variables, were then separated by 50% into "testing" and "training" datasets, with both datasets confirmed to have an equal distribution of all variables.

R-studio (manufacturer) was used to develop a supervised classification machine learning algorithm with the goal of predicting where the majority of current would occur, whether within a creviced or bulk-exposed region[38,39]. An initial comparison between five linear and non-linear algorithms was conducted with a 10-fold cross-validation method, and it was determined that the random forest (RF) algorithm was able to best capture the trends in the dataset. RF models have been found to be useful in classification problems, with straightforward tuning parameters and efficient computations[40,41]. Therefore, further steps were taken to optimize the RF model.

The basis of a classification RF model is that various decorrelated “decision trees” are built, with each singular tree predicting the classification label based on the input variables. All trees in the “forest” are then compared, with the classification label most represented acting as the final prediction. A single tree is constructed by a random subset of the original training data, where the variable “nodes” are split into two branches based upon some inequality until a prediction “leaf” is determined, defining the “bootstrap” method[42]. The remaining data which were not included in each subset are then used to create an out-of-bag (OOB) error metric[43,44].

The number of trees (ntree) and the number of random variables at each tree split (mtry) were optimized for the entire scaled dataset, using a loop function of ntree and mtry varying from 50 to 1000 and two to five, respectively. The OOB error was minimized to 0.56% with ntree = 59 and mtry = 4. Once trained, the effectiveness of the RF model could then be immediately evaluated through the “testing” dataset. Input parameters from the testing dataset were fed into the RF model, producing an output of the predicted location of the peak current. This prediction was then compared with the known FEM prediction from the same set of testing parameters. Confusion matrices were made to evaluate the validity of the RF predictions with the FEM predictions between both the training and testing datasets.

The randomForest CRAN package was utilized to build the RF model in R-studio[45]. Additional numerous open-source CRAN packages were utilized in the preprocessing and visualization of the data. The RF code and FEM database are therefore both available upon request, if further specifications are desired.

4.4 Results

4.4.1. Electrochemical Boundary Conditions

PDS used as FEM boundary conditions in this work are shown in Figure 4.2**.** Solid lines represent bare polished surfaces in 5 wt% (0.9 M) NaCl quiescent bulk aerated conditions. The anodic AA7075 OCP was nearly 1 V lower than the cathodic SS316 OCP, leading to a large driving force for galvanic corrosion. Using mixed potential theory, the galvanic coupling current (i_{gal}) of SS316 and AA7075 (assuming a 1:1 area ratio) would occur at the clearly visible oxygen diffusion-limited region (i_{lim}) on the SS316 surface, indicating that the cathodic reactions would be mass-transport limited.

The electrochemical behavior of a sol-gel coated SS316 surface in bulk 0.9 M NaCl solution, utilizing the same surface treatment and formulation as shown previously[4], is indicated by the dotted line. The electrochemical kinetics were reduced via a barrier to ion flow, with i_{lim} on the sol-gel coated surface over an order of magnitude smaller than i_{lim} from the bare SS316 surface in bulk solution. In addition, the sol-gel coated surface increased the bare SS316 OCP by 0.2 V (Figure 4.2).

Dashed lines represent bare SS316 RDE scans at various ω, correlating to an effective WL ranging from 44.5 µm to 400 µm. The inverse relationship of ω with WL, described by the Levich equation, can be visualized in Figure 4.2 with increasing rotation rate leading to thinner WL and increased i_{lim}. At the smallest WL tested, 44.5 µm, i_{lim} was increased by an order of magnitude from bulk conditions, and the OCP was decreased by approximately 0.2 V. Recent work has found δ_{nc} to be dependent on the temperature, bulk solution chemistry, and solution concentration, with $\delta_{nc} = 740$ μm for a SS316 surface in 0.9 M NaCl at room temperature[29]. Details on the conversion from ω to WL using the Levich equation, and the measurement of δ_{nc}, can be found elsewhere[29,30,46,47].

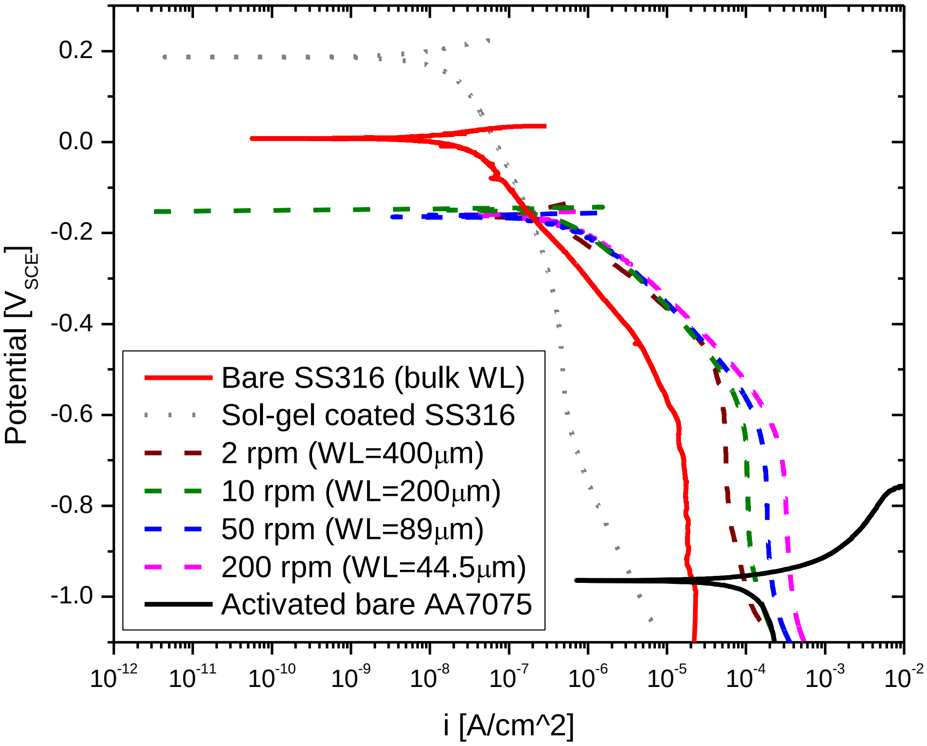

Figure 4.2: Potentiodynamic polarization curves. Solid lines represent SS316 and activated bare AA7075 in 0.9 M NaCl, bulk quiescent aerated conditions. Dotted line represents sol-gel coated SS316 in 0.9 M NaCl, bulk quiescent conditions. Dashed lines represent bare SS316 RDE in 0.6 M NaCl, with varying WL $< \delta_{nc}$.

4.4.2. FEM Current Distribution in Bulk WL on Bare Material Surfaces

Utilizing FEM, a model was built to simulate a single SS316 fastener dry-installed in an AA7075 panel exposed to different environments, with boundary conditions determined through the electrochemical PDS described above.

In bulk WL conditions and $\mathrm{S_{length}} = 1.75$ in, the total anodic current (I_{total}) was calculated as a function of $\mathrm{S_{width}}$. Deconvolution of I_{total} was then conducted, through integration of the current density over three specific anodic surface areas: the fastener hole, the scribed areas under the washer, and the scribed areas outside of the washer (Figure 4.3). Two noticeable trends were observed, with the current in the fastener hole (I_{FH}) decreasing with $\mathrm{S_{width}}$ while the currents in the scribes, both under the washer (I_{UW}) and in bulk conditions outside of the washer (I_{bulk}), increased with $\mathrm{S_{width}}$. In all scenarios, the sum of the deconvoluted current over the three anodic areas of interest equaled that of I_{total}.

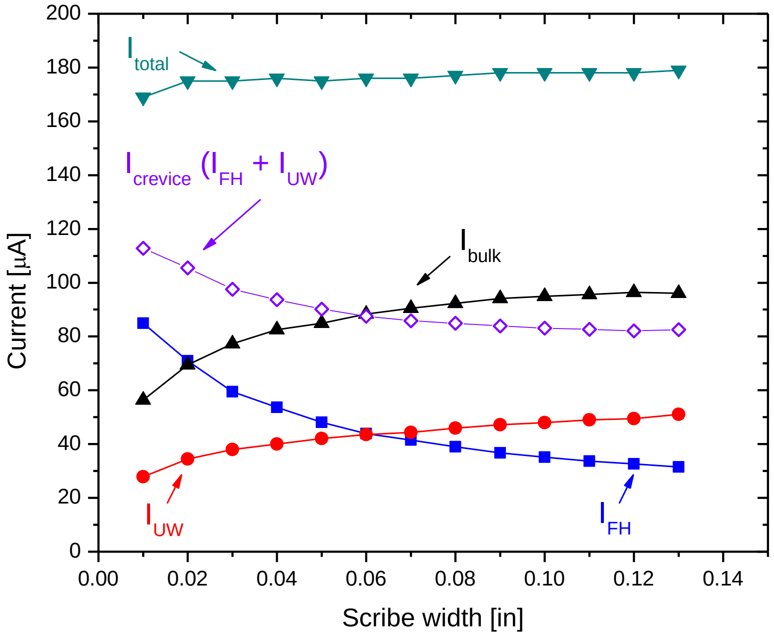

Figure 4.3: Current distributions on anodic surfaces, with $\mathrm{S_{length}} = 1.75$ in, bare SS316 fastener, and WL = 4,000 µm.

Through visualizing the deconvoluted currents, it was possible to identify where the maximum current would occur, and under which conditions. Within the present geometric and environmental conditions, a threshold of $\mathrm{S_{width}}$ of 0.02 in was seen to denote a change in the maximum amount of current; at smaller $\mathrm{S_{width}}$ values, the majority of current was predicted to occur within the fastener hole while at larger $\mathrm{S_{width}}$ values, the majority of current was predicted to occur in the bulk-exposed regions, that is, the scribes outside of the washer. As current can directly be correlated to mass loss via Faraday's law of electrolysis, assuming uniform dissolution, the location of peak current can then be thought of as the location of peak corrosion damage.

Similarly, a threshold could be determined when the majority of current would occur in a creviced or bulk region, with the current in the creviced regions ($I_{crevice}$) simply the sum of I_{FH} and I_{UW} (Figure 4.3). The binary threshold of $\mathrm{S_{width}}$ between the creviced and bulk surface was 0.06 in.

Expanding the methodology above to multiple values of $\mathrm{S_{length}}$, "damage maps" of the scribe dimensions could be created to denote if the highest current, and correspondingly the highest predicted corrosion damage, would be located in a creviced or bulk region (Figure 4.4). For example, at a constant scribe length of 1.75 in, the majority of damage transferred from occurring in a creviced region to occurring in a bulk-exposed region at $\mathrm{S_{width}} = 0.06$ in, also as seen in Figure 4.3. At small $\mathrm{S_{width}}$ and $\mathrm{S_{length}}$ values, the majority of current was pushed into the creviced regions (Figure 4.4). Conversely, at $\mathrm{S_{length}} = 1.75$ in (that is, one inch larger than the washer diameter), the peak current began to transition into the bulk anodic surfaces. Values of $\mathrm{S_{length}}$ were tested out to 8 in, although after 3.5 in the majority of current was always in the bulk-exposed regions, regardless of $\mathrm{S_{width}}$. The maximum and minimum range of $I_{crevice}$ and I_{bulk} values was 175 μA to 89 μA and 132 μA to 88 μA, respectively.

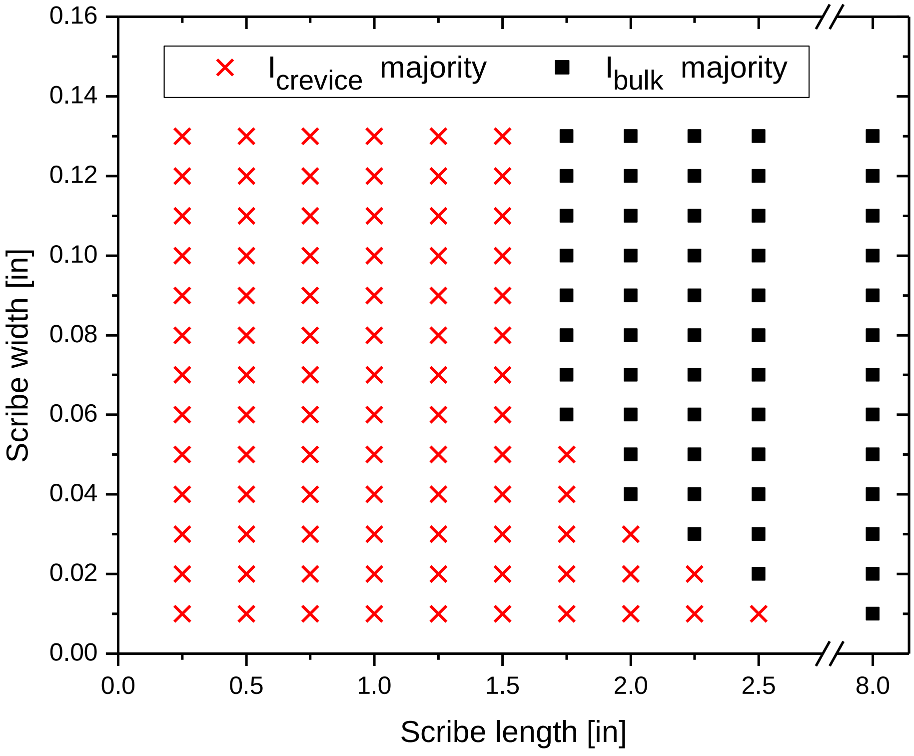

Figure 4.4: Current distributions in creviced and bulk regions as a function of scribe dimensions, for a bare SS316 fastener in WL = 4,000 µm

4.4.3. Cathodic and Anodic Kinetic Effects on the Current Distribution and Magnitude

To isolate any effects that the cathodic kinetics may have on the current distributions, the anodic boundary conditions were kept constant while the SS316 cathodic boundary conditions were varied with two new scenarios. The scribe dimension parameter space was again tested, with the two new cathodic boundary conditions.

Three-dimensional plots were generated, with I_{total} calculated at a range of scribe dimensions and separated into binary bins indicating the location of peak damage, either from $I_{crevice}$ or I_{bulk} (Figure 4.5). The current on the z-axis illustrated the transition of maximum current from the creviced regions to bulk regions, while the x-y plane represented the scribe dimensions seen in Figure 4.4.

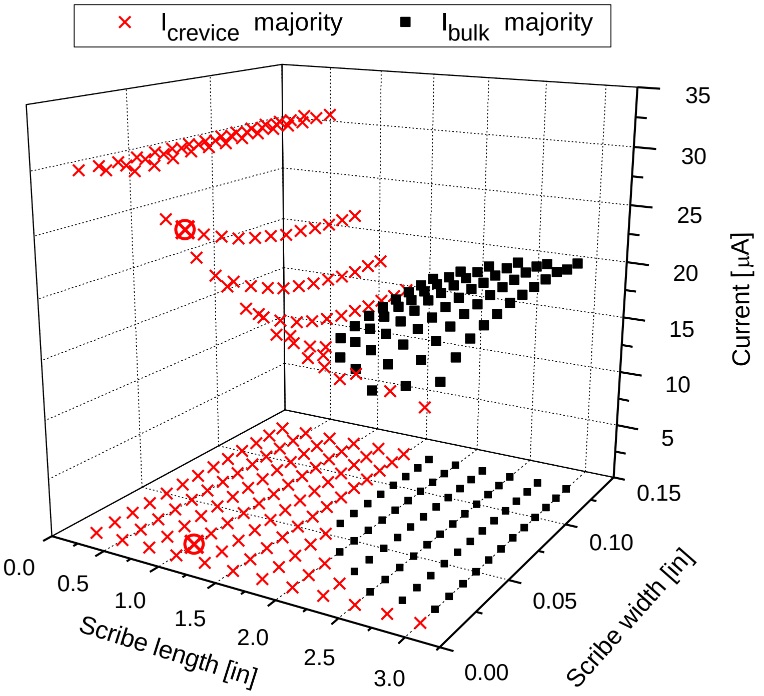

(a)

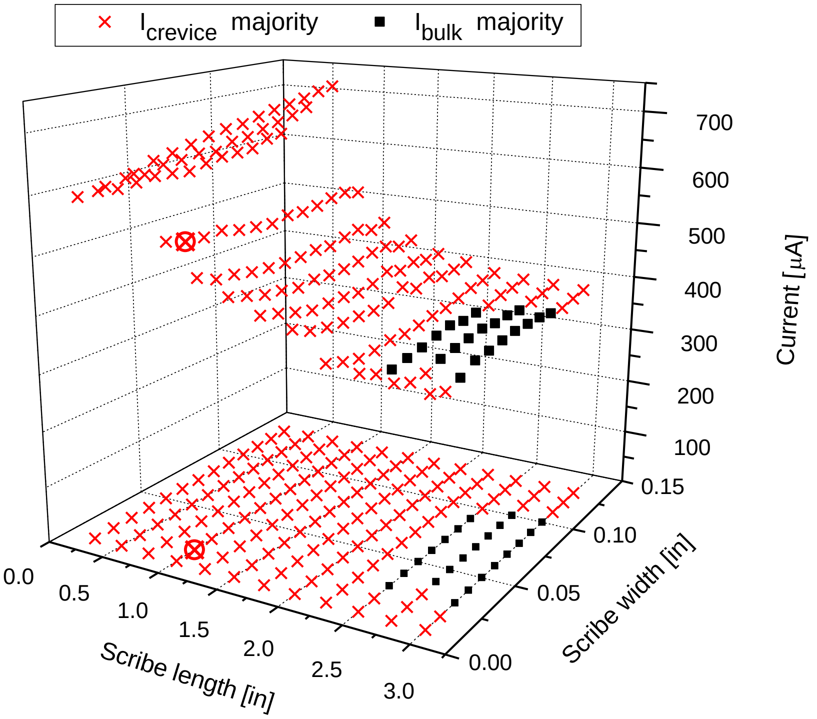

(b)

Figure 4.5: Current distribution in creviced and bulk regions, as a function of scribe dimensions; (a) sol-gel coated SS316 fastener, WL = 4,000 µm; (b) bare SS316 fastener, WL = 400 µm. Circled datapoints refer to the scribe dimensions held constant in Figure 4.6

To represent mitigation of the bare SS316 kinetics, boundary conditions for a sol-gel coated SS316 fastener in bulk, 4,000 µm WL conditions were utilized (Figure 4.5(a)). Although the location of predicted maximum damage was largely similar to that of a bare SS316 fastener, the magnitude of current at all scribe dimensions was significantly lower than the bare SS316 fastener couple.

In contrast, the WL was decreased by an order of magnitude from 4,000 µm to 400 µm which would lead to an acceleration of the bare SS316 kinetics (Figure 4.5(b)). In nearly all scribe dimensions tested, the susceptibility for corrosion to occur in a creviced region was increased in comparison to the corrosion distribution in bulk WL conditions (Figure 4.4). In addition, the magnitude of current was approximately four times higher than that of the bulk WL conditions.

To further explore the impacts of the electrochemical kinetics on the current, the scribe dimensions were held constant at a $\mathrm{S}_{\mathrm{width}}$ and $\mathrm{S}_{\mathrm{length}}$ of 0.02 in and 1 in, respectively, while both anodic and cathodic kinetics were systematically varied. In all calculations, the baseline boundary conditions represented a bare SS316 surface and activated AA7075 surface in bulk 0.9 M NaCl conditions, as shown by the solid lines in Figure 4.2. The experimentally determined cathodic kinetics on the thin WL of 400 µm and sol-gel coated surface continued to simulate how the current magnitude and distribution may change as the cathodic kinetics were varied. The anodic kinetics, however, were manually scaled by an order of magnitude larger and smaller than the baseline, to create an analogous comparison.

I_{total} was first evaluated, for each of the scaled kinetics scenarios (Figure 4.6(a)). Despite scaling the anodic kinetics to higher and lower current densities, I_{total} remained largely similar to that of the baseline. However, the cathodic kinetics had a much larger impact on I_{total}, with values decreasing and increasing nearly an order of magnitude from the baseline.

Looking instead at the current distributions of $I_{crevice}$ and I_{bulk}, normalized to account for the differences in current magnitude, the cathodic kinetic variations have very slight effects, with the majority of current ($> 75\%$ of I_{total}) always occurring in a creviced region (Figure 4.6(b)). Decreasing the anodic kinetics by an order of magnitude also showed a near-negligible increase in susceptibility to the majority of current occurring in a crevice. However, an *increase* to the anodic kinetics resulted in a sharp transition of the current distribution, with nearly 50% of current occurring in the bulk-exposed surfaces.

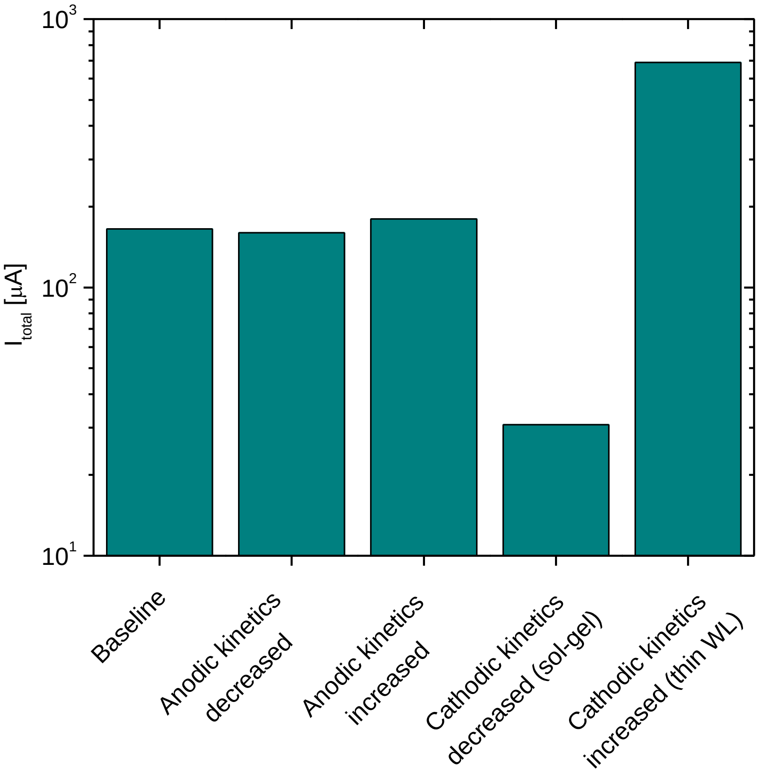

(a)

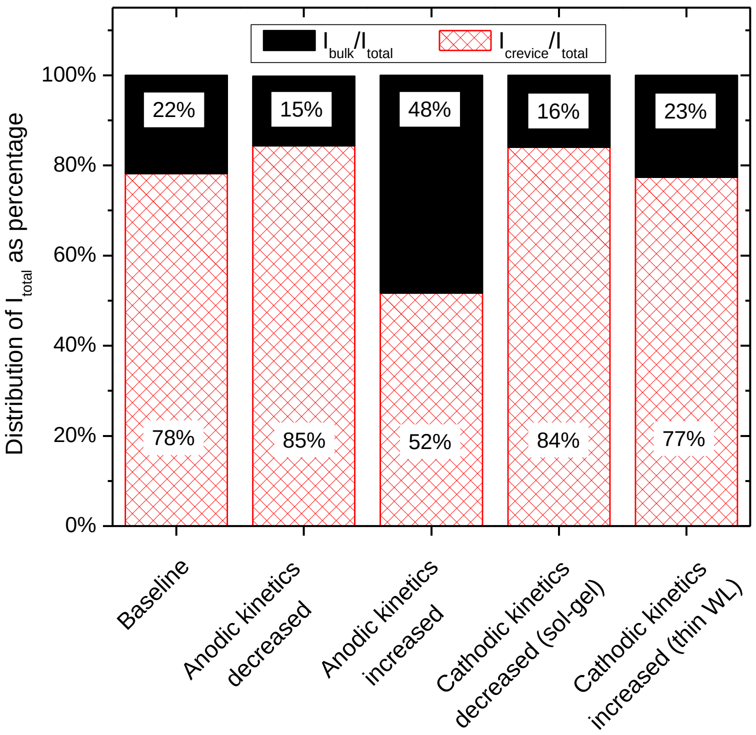

(b)

Figure 4.6: Anodic and cathodic kinetic variations, with $\mathrm{S_{length}} = 1$ in and $\mathrm{S_{width}} = 0.02$ in; (a) magnitude of I_{total}; (b) distribution of I_{total}, whether within the creviced or bulk regions

4.4.4. Atmospheric Conditions with Varying Scribe Dimensions

Due to the significant impact of the cathodic kinetics on the magnitude of current, in contrast to the anodic kinetics as described above, further work was conducted to evaluate a variety of WL below δ_{nc}, corresponding to new i_{lim} values. Boundary conditions on the anodic AA7075 surfaces remained constant to the baseline, while the bare SS316 cathodic boundary conditions ranged in WL from 44.5 μm to 4,000 μm. Values of $\mathrm{S_{width}}$ and $\mathrm{S_{length}}$ were again modified in the same range as tested above, at each distinct WL, creating three independent parameters.

The calculated values of I_{total}, $I_{crevice}$ and I_{bulk} were plotted against the varied WL, with the range of datapoints at each WL corresponding to the scribe dimension parameter space (Figure 4.7(a)). The magnitude of current was consistent for WL = 800 μm, 1,000 μm, and 4,000 μm, as they were all greater than δ_{nc} (740 µm) and therefore representative of bulk conditions. Notably, $I_{crevice}$ and I_{bulk} were nearly overlaid at these WL, with no clear delineation to predict the location of current. At WL = 400 µm, the current magnitude began to increase, as seen in Figure 4.5(b), as well as a portion of $I_{crevice}$ having visibly larger values than I_{bulk}. A divergence in the currents occurred at WL = 200 µm, where $I_{crevice} > I_{bulk}$ in all conditions, regardless of the scribe dimensions. This trend continued at WL = 89 µm and 44.5 µm, with the magnitude of $I_{crevice}$ continuing to increase at a steeper rate than I_{bulk}.

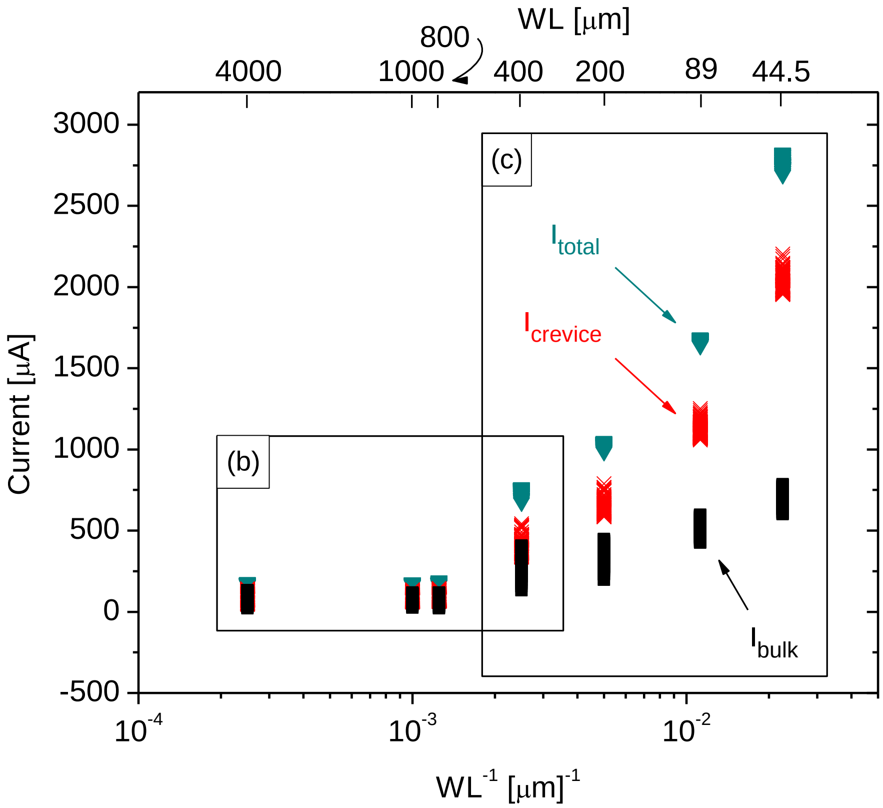
WL [μm]
800
4000
1000
400
200
89
44.5
(c)
(b)
I_{total}
$I_{crevice}$
I_{bulk}
Current [μA]
3000
2500
2000
1500
1000
500
0
-500
10^{-4}
10^{-3}
10^{-2}
WL^{-1} [μm]$^{-1}$

(a)

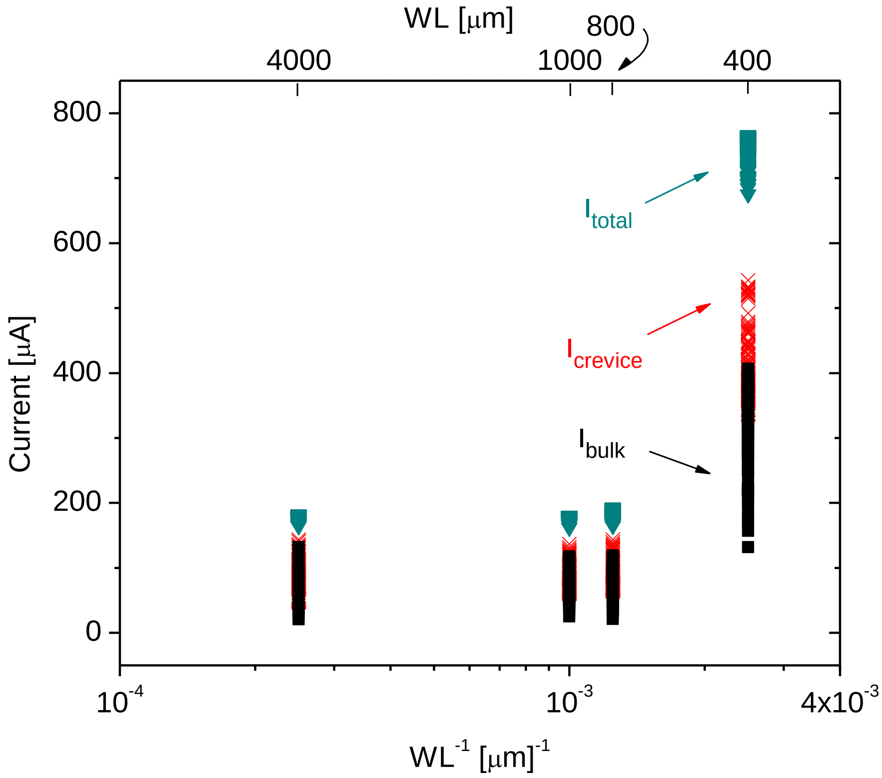
WL [μm]
800
4000
1000
400
I_{total}
$I_{crevice}$
I_{bulk}
Current [μA]
800
600
400
200
0
10^{-4}
10^{-3}
$4x10^{-3}$
WL^{-1} [μm]$^{-1}$

(b)

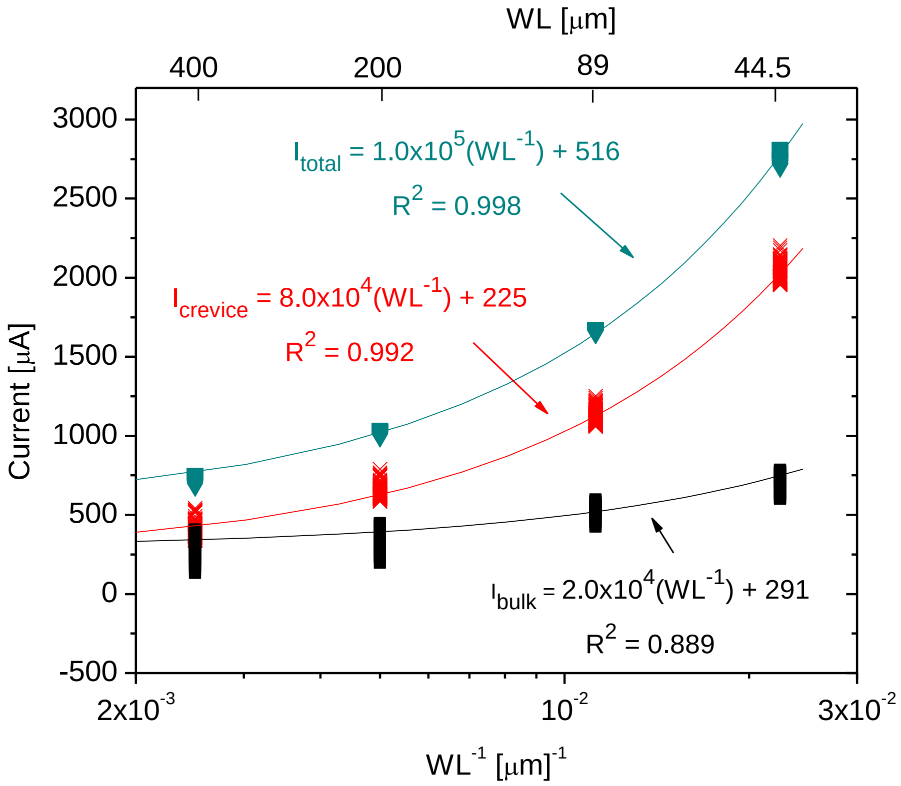

(c)

Figure 4.7: (a) Currents within a bare SS316 fastener system, with bulk and atmospheric (< δ_{nc}) WL and various scribe dimensions. (b) Closer inspection of the bulk WL and WL = 400 μm; (c) Closer inspection of the atmospheric (< δ_{nc}) WL, with fitted functions over the FEM results calculated with only atmospheric WL datapoints. At each WL, S_{width} and S_{length} ranged from 0.01 in to 0.13 in and 0.25 in and 0.8 in, respectively.

4.4.5. Random Forest Classification Prediction

Utilizing the FEM results with varied S_{width}, S_{length}, and WL parameters, a database was created to construct a RF model. The goal of the RF model was to interpolate between the FEM datapoints to predict whether the majority of current would occur in a crevice or bulk-exposed region, through using only the three input parameters. In addition, the overlapping datapoints seen in bulk WL motivated the use of the RF model, which is able to determine each variable importance (Figure 4.7 (a)). A model was trained with 50% of the full dataset, and then tested with the remaining 50% of the dataset, which were both selected randomly from the original

FEM dataset and were both confirmed to have a random distribution of the independent variables.

To quantify the predictive accuracy of the RF model, a confusion matrix was constructed, which included the number of correct and false predictions for both the creviced and bulk regions (Figure 4.8). Commonly shown in a tabular form, the confusion matrix represents the total FEM prediction of peak current occurring in a crevice (the sum of the top row, equaling 380), and the total FEM prediction of peak current occurring in the bulk (the sum of the bottom row, equaling 250) (Figure 4.8(a)). The columns represent instead the RF predicted location at which the peak current will occur, with the lower cell of the first column representing the number of "false bulk" predictions and the upper cell of the second column representing the number of "false crevice" predictions.

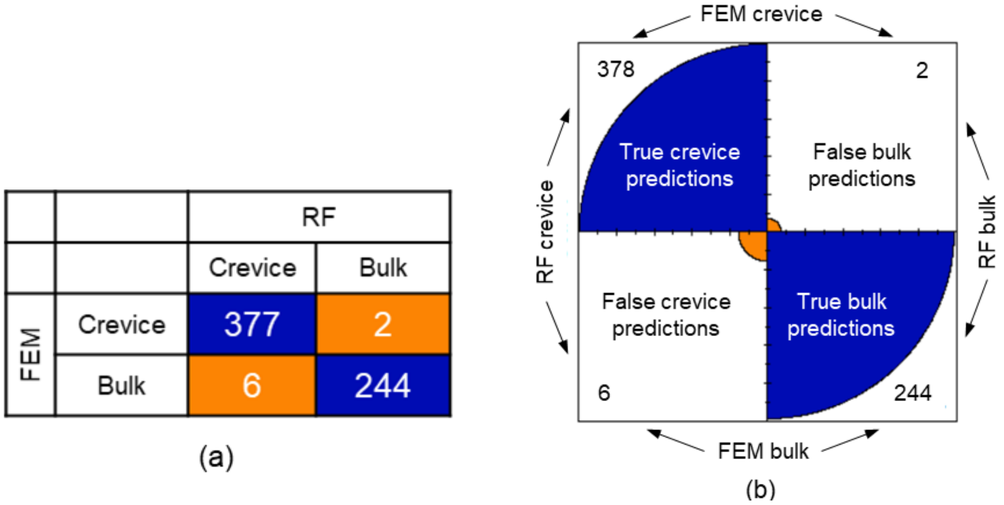

		RF	
		Crevice	Bulk
FEM	Crevice	377	2
	Bulk	6	244

(a)

(b)

Figure 4.8: Confusion matrix in (a) tabular and (b) graphical formats, with the false crevice and false bulk predictions highlighted in orange and the true crevice and true bulk predictions highlighted in blue, for a RF using S_{width}, S_{length}, and WL as input parameters. The total FEM predictions for the location of peak damage in the creviced and bulk regions (sum of the rows) are 380 and 250, respectively. Conversely, the RF model predicted that 384 scenarios would have a majority of current in the crevice and 246 would have a majority of current in the bulk-exposed regions (sum of the columns).

Analyzing the confusion matrix is often easier to quickly assess the error metrics and to compare multiple RF models against each other (Figure 4.8(b)). From this matrix, various other statistical error metrics could be calculated, such as the accuracy of the respective model,

$$Accuracy = \frac{TC + TB}{TC + FC + TB + FB} \times 100 \tag{4.2}$$

where the TC is the true crevice prediction, TB is the true bulk prediction, FC is the false crevice prediction, and FB is the false bulk prediction. Note that the denominator in Eq. 4.2 is equal to the sum of the FEM predicted peak current in the crevice and bulk locations, that is, the total of all predictions. Similarly, the precision of the RF model could be defined as,

$$Precision = \frac{TC}{TC + FC} \times 100 \tag{4.3}$$

The confusion matrix could be calculated with the training and testing datasets, for a given model, as seen in Figure 4.9(a) and (d). The accuracy and precision of the first RF model, when compared with the testing dataset, was 98.7% and 98.4%, respectively, while all error metrics against the training dataset were 100%.

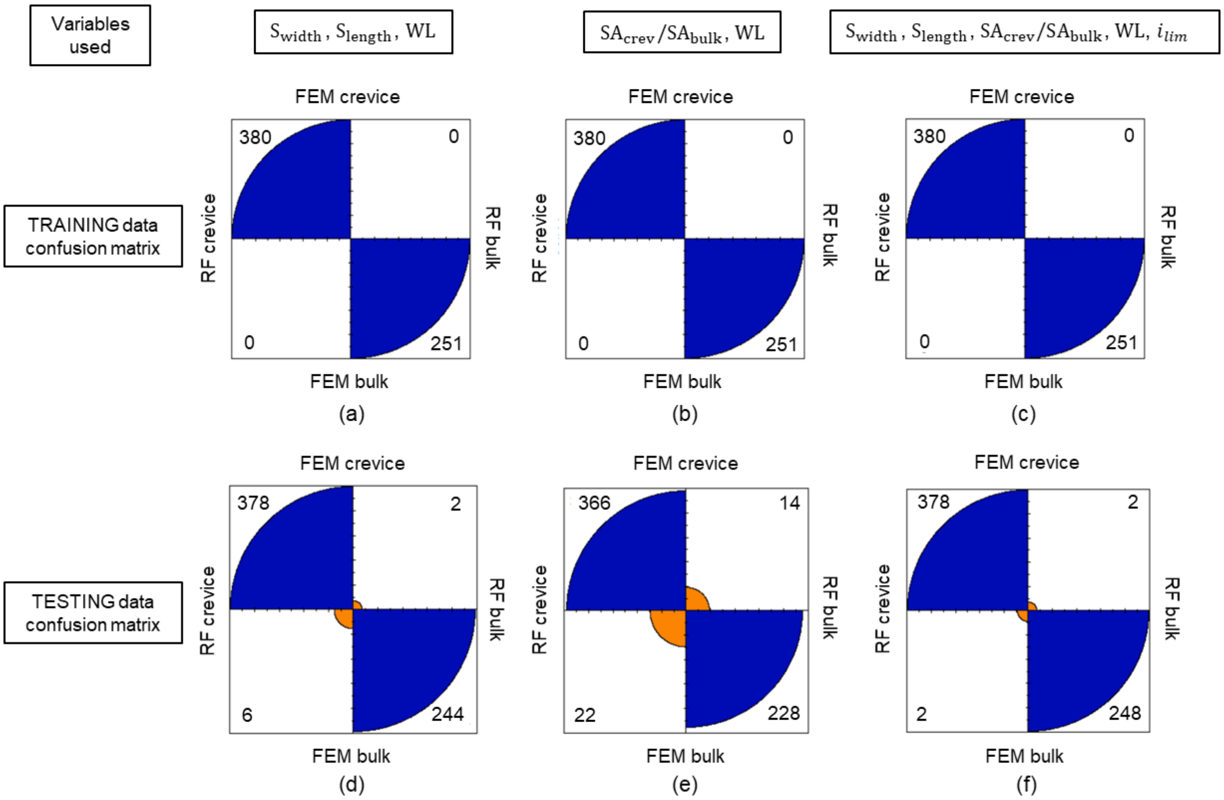

Figure 4.9: Graphical confusion matrix of (a) – (c) training data and (d) – (f) testing data, for three RF models, utilizing variable inputs of (a) and (d) S_{width}, S_{length}, and WL, (b) and (e) SA_{crev}/SA_{bulk}, and WL, (c) and (f) S_{width}, S_{length}, SA_{crev}/SA_{bulk}, WL, and i_{lim}

Although the RF model with the three input parameters (S_{width}, S_{length}, and WL) had very good accuracy and precision error metrics, the algorithm was specific to the geometry built in the FEM, limiting the applicability of the prediction tool to a narrow audience. In practice, geometric parameters of r_w, r_{FH}, S_{depth}, and x_{panel} may all vary depending on the overall structure and application (Figure 4.1). Therefore, in an effort to increase the applicability and accessibility of this work, the specific geometric features were generalized by creating a new parameter, the ratio of the creviced surface area to the bulk-exposed surface area (SA_{crev}/SA_{bulk}), which condensed all geometric variability into a single parameter. To calculate SA_{crev}/SA_{bulk}, the true scribe length (described in Eq. 4.1) first needed to be separated into regions under the washer and regions outside the washer,

$$\mathrm{S_{length,UW}^{true}} = (\mathrm{r_w} - \mathrm{r_{FH}}) \qquad 4.4$$

$$\mathrm{S_{length,bulk}^{true}} = \mathrm{S_{length}^{true}} - \mathrm{S_{length,UW}^{true}} \qquad 4.5$$

The total creviced surface areas ($\mathrm{SA_{crev}}$) and total bulk surface areas ($\mathrm{SA_{bulk}}$) could then be calculated.

$$\mathrm{SA_{crev}} = 2\pi(\mathrm{r_{FH}})\mathrm{x_{panel}} + 4(\mathrm{S_{width}}\mathrm{S_{length,UW}^{true}}) + 8(\mathrm{S_{depth}}\mathrm{S_{length,UW}^{true}}) \qquad 4.6$$

$$\mathrm{SA_{bulk}} = 4(\mathrm{S_{depth}}\mathrm{S_{width}}) + 4(\mathrm{S_{width}}\mathrm{S_{length,bulk}^{true}}) + 8(\mathrm{S_{depth}}\mathrm{S_{length,bulk}^{true}}) \qquad 4.7$$

Utilizing the same dataset as Figure 4.7(a), the new parameter $\mathrm{SA_{crev}/SA_{bulk}}$ was plotted on a log-scale y-axis in lieu of the current (Figure 4.10(a)). Values of $\mathrm{SA_{crev}/SA_{bulk}}$ spanned two orders of magnitude, based on the varying $\mathrm{S_{width}}$ and $\mathrm{S_{length}}$ values.

A WL threshold was again seen, as in Figure 4.7(a), with the majority of current occurring in a creviced region independent of $\mathrm{SA_{crev}/SA_{bulk}}$ at WL ≤ 200 μm. (Figure 4.10(a)). In addition, a threshold $\mathrm{SA_{crev}/SA_{bulk}}$ ratio of 2.2 was revealed, where all ratio values greater than 2.2 resulted in the majority of current being located in a creviced region (Figure 4.10(b)). However, all ratios less than 2.2 did not result in the majority of current being located in a bulk-exposed region, but instead an ambiguous region was also seen, where similar $\mathrm{SA_{crev}/SA_{bulk}}$ and WL combinations resulted in opposing predictions of the location of peak current (Figure 4.10(b)). Therefore, all ratios less than 0.4 resulted in the majority of current occurring in bulk regions, with the ambiguous region bounded by 2.2 and 0.4 values. This region will be discussed further in a later section.

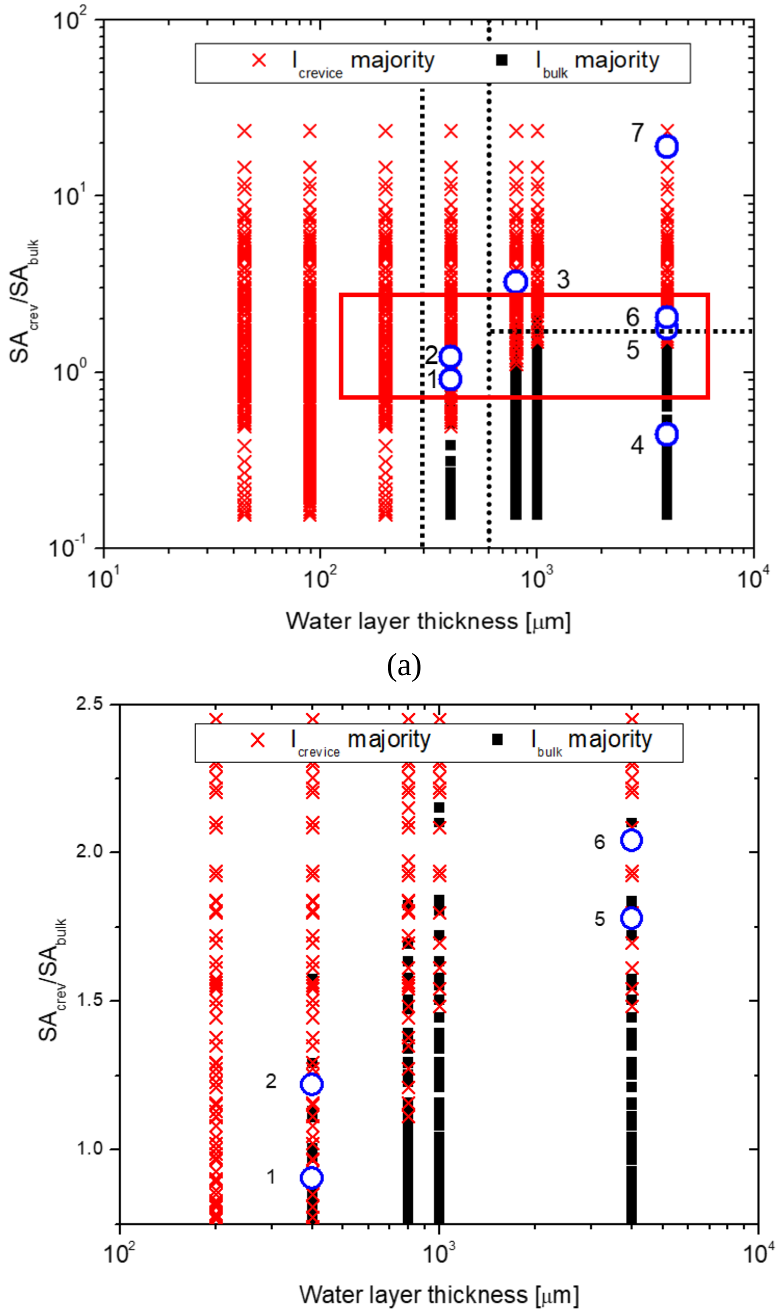

(a)

(b)

Figure 4.10: (a) Current distributions in creviced and bulk regions, as a function of SA_{crev}/SA_{bulk} and varying WL. (b) Inset of (a) as indicated by the red rectangle. Hollow circle datapoints represent the new tested scenarios, which included SA_{crev}/SA_{bulk} values not present in the testing nor training dataset, and are labeled according to Table 4.1. Dotted lines in (a) represent the first three decision nodes in Figure 4.12.

To generalize the RF algorithm, an additional model was created using only the two parameters of $\mathrm{SA_{crev}/SA_{bulk}}$ and WL. Confusion matrices were calculated for both the training and testing datasets (Figure 4.9(b) and (e)). The accuracy and precision of the generalized RF model in comparison to the training data were calculated to be 94.3% for both error metrics. The testing data error metrics were again both 100%.

A correlation matrix was built to evaluate the relationships between the independent parameters ($\mathrm{S_{width}}$, $\mathrm{S_{length}}$, $\mathrm{SA_{crev}/SA_{bulk}}$, WL, and i_{lim}), and the resulting measured values (I_{FH}, I_{UW}, I_{bulk}), with the entire dataset normalized between 1 and -1 (Figure 4.11). The currents were again deconvoluted into the three regions of interest, to tease out any differences between I_{FH} and I_{UW}, although $I_{crevice}$ is simply a summation of those two currents. Specifically, I_{FH} was seen to have a weak direct dependence on $\mathrm{SA_{crev}/SA_{bulk}}$, while I_{UW} did not have any correlation with $\mathrm{SA_{crev}/SA_{bulk}}$.

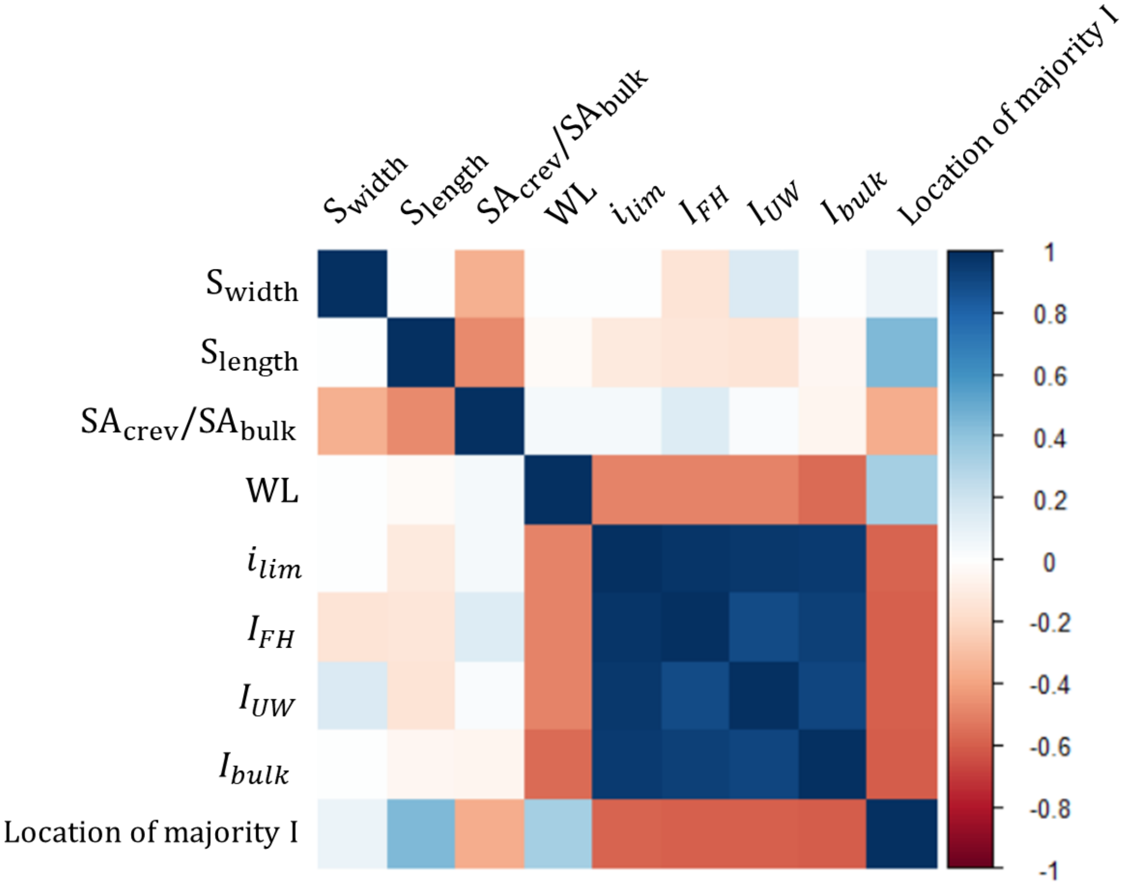

Figure 4.11: Correlation map of variables used in RF models (S_{width}, S_{length}, SA_{crev}/SA_{bulk}, WL, and i_{lim}), with FEM-calculated currents (I_{FH}, I_{UW}, and I_{bulk}) and the binary-location at which the majority of current occurs ($I_{crevice}$ or I_{bulk})

The location of predicted maximum current was also included, to determine what the relative influence that each parameter may have on the resulting location of damage. The binary regions of “crevice” or “bulk” were denoted as -1 and 1, respectively.

As expected, the parameter SA_{crev}/SA_{bulk} had a strong inverse correlation with both S_{width} and S_{length}, as both parameters were used to calculate SA_{crev}/SA_{bulk}. In addition, the correlation between SA_{crev}/SA_{bulk} and S_{length} was stronger, due to S_{width} impacting both SA_{crev} and SA_{bulk} while S_{length} only affected SA_{bulk}, as seen in Eq. 4.6 and Eq. 4.7 (Figure 4.11).

Both WL and i_{lim} had strong correlations with the measured currents, with WL having the largest magnitude of correlation with I_{bulk}. All currents were directly dependent on each other, and all inversely dependent with the location of damage, indicating that as the magnitude of currents increased, the location of maximum current was more likely to occur in a creviced region (corresponding to "-1"). In addition, on the location of the peak current prediction, $\mathrm{SA_{crev}/SA_{bulk}}$ and i_{lim} had strong inverse correlations, while $\mathrm{S_{length}}$ and WL had strong direct correlations, indicating that these parameters may be the most important in predicting whether $I_{crevice}$ or I_{bulk} will be dominant (Figure 4.11).

Therefore, a final RF model was created, which included all varied parameters of $\mathrm{S_{width}}$, $\mathrm{S_{length}}$, $\mathrm{SA_{crev}/SA_{bulk}}$, WL, and i_{lim}. Of the total 59 trees within the forest, the 6th tree was plotted in Figure 4.12 as an example of the RF process, with unscaled data used for clarity. The first three parameter nodes, with their respective split inequalities, can be visualized in Figure 4.10 as dotted lines. The respective confusion matrices indicated a very high-performing model, with an accuracy and precision of 99.4% and 99.5%, respectively, for the testing dataset and 100% for the training dataset (Figure 4.9(c) and (f)).

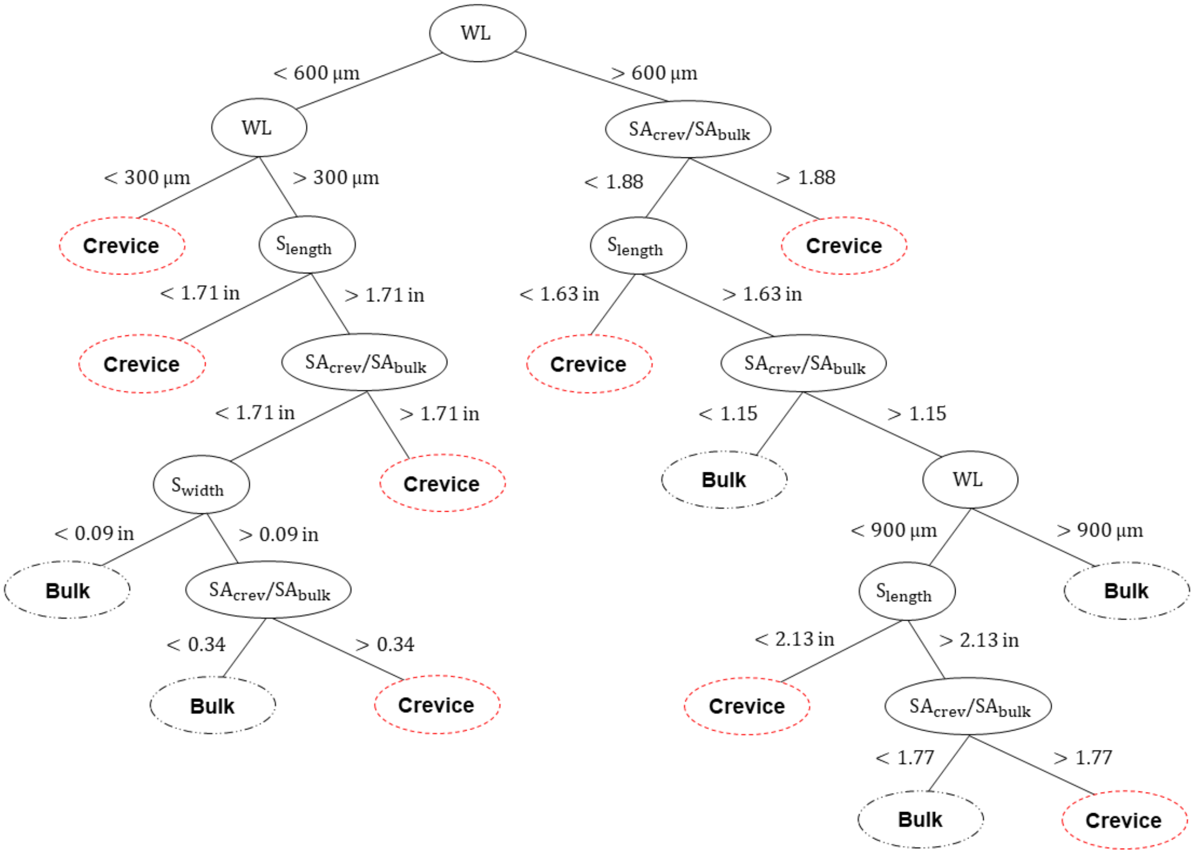

Figure 4.12: A representative tree (specifically, number 6 of the total 59 trees) within the RF model with all 5 input parameters (S_{width}, S_{length}, SA_{crev}/SA_{bulk}, WL, and i_{lim}), where the first three variable nodes can be visualized in Figure 4.10, to determine where the majority of current will occur (whether within a creviced or bulk region).

To further test the latest RF model and the generalized SA_{crev}/SA_{bulk} parameter, seven new unique computations were run in FEM with varying geometric parameters so that the SA_{crev}/SA_{bulk} values were not found in any of the training nor testing datasets. These seven new "tests" were denoted on the SA_{crev}/SA_{bulk} vs. WL plot as blue hollow circles, labeled numerically, and were designed to test the extent of generalizability within the RF model (Figure 4.10). In addition, four of the seven new tests fell within the ambiguous region of parameter space, described earlier, to see if the RF model could find a better partition between these datapoints which may not have been visible in Figure 4.10.

The RF model correctly predicted the location of majority damage for six of the seven new tests, with the confidence probability on each prediction recorded in Table 4.1.

Table 4.1 Summary of new unique datapoints to test the generalized RF model.

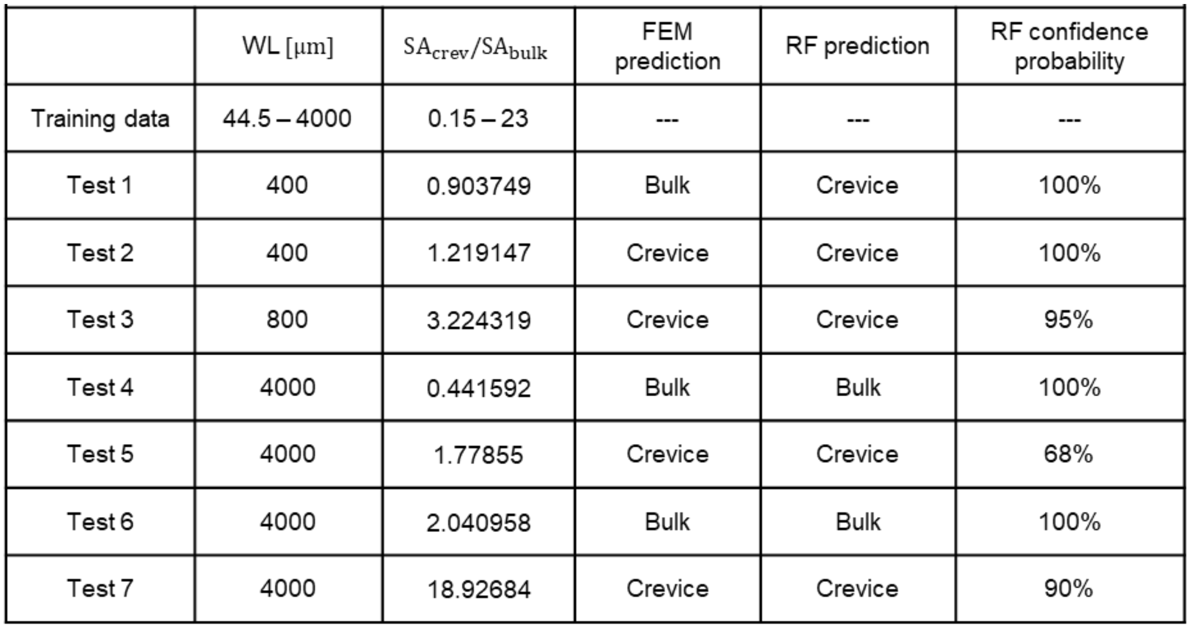

	WL [μm]	$\mathrm{SA_{crev}/SA_{bulk}}$	FEM prediction	RF prediction	RF confidence probability
Training data	44.5 – 4000	0.15 – 23	---	---	---
Test 1	400	0.903749	Bulk	Crevice	100%
Test 2	400	1.219147	Crevice	Crevice	100%
Test 3	800	3.224319	Crevice	Crevice	95%
Test 4	4000	0.441592	Bulk	Bulk	100%
Test 5	4000	1.77855	Crevice	Crevice	68%
Test 6	4000	2.040958	Bulk	Bulk	100%
Test 7	4000	18.92684	Crevice	Crevice	90%

4.5 Discussion

4.5.1. Predicted Location of Peak Current in Bulk WL and Baseline Kinetics

It is known that corrosion damage can act as a crack initiation site through local stress concentrators or through local hydrogen embrittlement via the cathodic electrochemical reaction[2]. Furthermore, the stress field on the surface of a given system is non-uniform, with certain geometric features acting as additional stress concentrators[2]. Creviced geometric regions can also accelerate the corrosion and can be difficult to detect. The combination of high corrosion rate in a susceptible geometric feature, such as an occluded fastener hole, could therefore have a combined detrimental effect, shortening the lifetime of a structure.

Therefore, knowing *a priori* where the majority of corrosion damage will occur would be helpful from three perspectives, 1) lifecycle enhancement (early failure assessment), 2) possible prevention and mitigation techniques, and 3) educated inspection and maintenance of the existing structure. These situations practically correlate to 1) knowing under which conditions the peak current would occur in a high-stress region, 2) knowing which conditions could act to move the peak current out of the high-stress region and defer it to a lower-stress region, and 3) knowing which locations to inspect for possibly hidden corrosion damage.

Furthermore, external defects, in the form of controlled scribes, are commonly used to approximate the lifetime of a coating on aluminum alloys through simulating a worst-case scenario in which the topcoat on the panel has been damaged[48]. Although scribes are often used in a laboratory setting with set dimensions, ranging from $\mathrm{S_{width}}$ and $\mathrm{S_{length}}$ of 9.8×10^{-3} in to 0.39 in (0.25 mm to 10 mm) and 0.79 in to 3.1 in (20 mm to 80 mm), respectively[9,11–14,16,26,27,49], in real applications the scribe dimensions are not “prescribed”. Instead, surface defects are measured *post factum* during maintenance inspection. Cui *et al.,* experimentally and computationally varied $\mathrm{S_{width}}$, finding a threshold $\mathrm{S_{width}}$ which denoted whether the throwing power of an Al-clad coating would protect the substrate or not, highlighting the importance of scribe dimensions[26]. Therefore, a wide range of scribe parameter space was tested in this work, to approximate a variety of realistic scenarios.

Utilizing FEM, “damage maps” were created through determining the distribution of the peak, that is, majority, current over a variety of different scribe dimensions in bulk WL (Figure 4.3, Figure 4.4, Figure 4.5(a)). It was seen that under all conditions, small scribe dimensions pushed the current into the creviced regions, whereas larger $\mathrm{S_{length}}$ values allow for the current to be distributed along the more-visible bulk surface (Figure 4.3, Figure 4.4, Figure 4.5(a)). Specifically, trends in Figure 4.3 indicated that with increasing $\mathrm{S_{width}}$, the current in the scribes (I_{UW} and I_{bulk}) increased while I_{FH} decreased. Note that as current was reported in this work, rather than current density, the surface areas of the various regions were directly proportional to the magnitude of current.

Therefore, the latter trend is rationalized by the fact that the fastener hole surface area was constant and non-dependent on the scribe dimensions. As $\mathrm{S_{width}}$ and $\mathrm{S_{length}}$ were increased, there was a larger surface area outside of the fastener hole for the current occur, pulling the current out of the fastener hole surfaces (Figure 4.4).

Similarly, the surface area under the washer was only impacted by $\mathrm{S_{width}}$ values after $\mathrm{S_{length}} \geq 0.75$ in, that is, $\mathrm{S_{length}} \geq 2\mathrm{r_w}$, indicating that as $\mathrm{S_{width}}$ increased I_{UW} also increased (Figure 4.3). However, as $\mathrm{S_{length}}$ increased ≥ 0.75 in, I_{UW} would start to decrease as the surface area in the scribes outside of the washer became larger than the surface area in the scribes under the washer. Therefore, $\mathrm{S_{width}}$ had a positive correlation with the magnitude of I_{UW} while $\mathrm{S_{length}}$ had a negative correlation with I_{UW} (Figure 4.11).

Note that with increasing $\mathrm{S_{length}}$, $I_{crevice}$ first increases at $\mathrm{S_{length}}$ values < 0.75 in, before decreasing with $\mathrm{S_{length}}$ values > 0.75 in, for the same reasoning described above. At increasing $\mathrm{S_{length}} < 0.75$ in, I_{FH} decreases while I_{UW} increases, while at increasing $\mathrm{S_{length}} > 0.75$ in, both I_{FH} and I_{UW} decrease as I_{bulk} increases (Figure 4.5(a)).

Figure 4.11 confirms the correlations between $I_{FH},\ I_{UW}$ and both scribe dimensions, with the caveat that both bulk and atmospheric WL conditions are included in the correlation matrix.

Repercussions of this caveat are clearly seen with I_{bulk} dependencies on the scribe dimensions, which appear nearly non-existent in Figure 4.11, although results in bulk WL from Figure 4.4 and Figure 4.5(a) show that I_{bulk} increases with both $\mathrm{S_{width}}$ and $\mathrm{S_{length}}$. The lack of correlation with I_{bulk} and the scribe dimensions in Figure 4.11 is due to the thin atmospheric WL dominating any influences over I_{bulk}.

Overall, however, the results above lead to the counterintuitive twofold conclusion that long external surface defects should be present on the surface to, 1) pull current away from the creviced regions and 2) create a known area to be inspected for maintenance (limiting insidious corrosion and inspections over large areas).

4.5.2. Isolated Kinetic Effects

Cathodic and anodic kinetics can be impacted by a variety of factors, from the geometry of the system surface chemistry to characteristics of the environment such as temperature, pH, and solution composition. Often intentional surface treatments and coatings are applied to decrease the kinetics[4,5,9,27,50,51], while less-predictable factors such as thin WL from a dynamic environment can act as accelerants to the reaction rates[52–55]. Galvanically coupled systems can add complexity, as both the local cathodic reaction rates on the anode and the global cathode reactions must be taken into consideration. Specifically, in the context of an aluminum alloy and SS316 galvanic couple, dissolution of the aluminum matrix produces an increase of Al^{3+} ions in solution which can diffuse away from the surface, hydrolyze, and form complexing species such as $Al(OH)_3$ and $AlCl^{+2}$ [27,56,57]. However, in a creviced region where diffusion is constricted, these ions can build up and increase both the cathodic kinetics occurring on the SS316 surface and the corrosion current density of the aluminum alloy[58,59].

Additional impacts to both the cathodic and anodic kinetics can occur through the presence of chromate or other inhibitors in solution, which may occur due to the leaching of pigmented protective coatings. Specifically, within a SS316/AA7050 galvanic couple and variations of 0.1 to 10 mM of chromate, the anodic and local cathodic reactions on AA7050 were decreased as well as the SS316 global cathodic reactions[18,46,60].

In such variable conditions, it is often useful to plan for the best- and worst-case scenarios.

In this work, the experimentally determined cathodic kinetics on the sol-gel coated surface and under thin WL conditions were representative of all mitigants and accelerants of the cathodic kinetics as best- and worst-case scenarios, respectively (Figure 4.2). Similarly, the theoretical variations of the anodic kinetics were representative of best- and worst-case real-life scenarios, such as passive film forming or Al^{3+} ions in solution, respectively[58,59].

Baseline kinetics included only bare surfaces (no coatings) and bulk WL conditions, with results reported in Figure 4.3 and Figure 4.4. Varying the anodic kinetics both to larger and smaller current densities did not have an impact on I_{total}, due to i_{gal} occurring in the diffusion limited regime (Figure 4.6(a)). In addition, increases to the anodic kinetics *reduced* susceptibility for corrosion to occur in any creviced regions, and instead pushed the current into the bulk regions (Figure 4.6(b)). This would indicate that for any galvanic couples with $i_{gal} \cong i_{lim}$, such as SS316/AA7075[4,30,61], SS316/Zn[62], and graphite/AA6061[63], any increase to the anodic kinetics would be counterintuitively favorable.

Conversely, the magnitude of I_{total} scaled directly with the cathodic kinetics, increasing and decreasing nearly an order of magnitude from the baseline (Figure 4.6(a)). Although the distribution of current in Figure 4.6(b) seemed as though the cathodic kinetics had negligible impact in comparison to the baseline, only a singular set of scribe dimensions was being captured. Looking instead at the scribe parameter space of Figure 4.5(b), it can clearly be seen that atmospheric conditions with thin WL both accelerate I_{total} and have a higher susceptibility of pushing the majority of corrosion into the creviced regions. This result confirms that atmospheric conditions accelerate corrosion, due in part to concentrated aggressive species and increased diffusion of $\mathrm{O_2}$ to the surface, and therefore will be investigated more fully in the following section[28].

The large influence of the cathodic reactions over I_{total} could be used as an advantage, as shown by the sol-gel coated surfaces, which lowered I_{total} by a factor of six (Figure 4.6(a)). Literature confirms that coating a stainless steel bolt acts as an effective means to mitigate the galvanic corrosion on an aluminum alloy[5,50]. Furthermore, the sol-gel coating did not increase the susceptibility of corrosion to occur in the creviced region, but maintained that values of $\mathrm{S_{length}} > 1.75$ in began to pull the majority of current into the bulk surfaces (Figure 4.5(a)).

Cocke *et al.*, also found that the sol-gel formulation of Blockade GC™ improved the resistance to corrosion-induced cracking of an AA7075 panel/SS316 fastener galvanic couple, increasing the total fatigue life (in cycles) by over five times when the scribes were oriented at 45° and by 17 times when the scribes were oriented at 90°, in comparison to their bare SS316 fastener counterparts[9].

Interestingly, despite lowering the fatigue life, the mean corrosion depth within all bare *and* sol-gel coated samples was always larger within the creviced fastener hole region, as opposed to occurring within the scribes on the surface[9]. The scribe dimensions and environment used by Cocke *et al.*, were $\mathrm{S_{width}} = 0.018$ in and $\mathrm{S_{length}} = 1$ in, exposed to B117 (continuous 0.9 M

NaCl salt spray) which can act as bulk WL conditions[5,64]. Utilizing Figure 4.4 and Figure 4.5(a) as damage maps under those conditions, the majority of current would be expected to occur within the creviced regions for both the bare and sol-gel coated SS316 fasteners, indicating agreement between the experimental findings and the computational predictions in this work.

Conclusions above suggest that further optimization of the component lifetime may be possible through combining multiple kinetic inhibition techniques and focusing on both the magnitude and distribution of current. That is, the sol-gel surface treatment was effective at decreasing I_{total}, but the majority of corrosion damage could still occur within the creviced region at a certain set of scribe dimensions. Additional kinetic inhibition techniques, such as controlling the external scribe dimensions to pull the current to the bulk surface or altering the global anodic kinetics, in combination with the sol-gel surface treatment, may decrease the severity of both the magnitude and distribution of I_{total}.

Chromate-containing coatings capture both of these features, decreasing both the anodic and cathodic kinetics on AA7075 and SS316[18,46,60], which may offer an explanation as to why these coatings have such strong corrosion-inhibiting properties.

4.5.3. Current Distributions and Relationships in Atmospheric Conditions

True atmospheric conditions involve a dynamic set of RH, WL, loading density (LD), and conductivity (κ) parameters. The LD, defining how much salt per area is present, mostly depends on the geographic location and exposure time while the RH varies throughout both the time of day and season of the year inducing a cyclic evaporation and deliquescence. During evaporation the WL is decreased from loss of liquid H_2O while the salt content remains constant, increasing the total concentration of the solution and correspondingly increasing κ. Similarly, during deliquescence, gaseous H_2O from the air condenses on the solid salt crystals, coalescing and diluting the solution, thereby lowering κ[34].

Chen *et al.*, derived an expression to relate these four parameters, with κ dependent on the RH and WL dependent on both the RH and LD, assuming room temperature and only NaCl present[33]. However, various other salts can be present in the atmosphere, such as magnesium and potassium, with recent work from Bryan *et al.*, showing that the ion concentration of these various salts do not change uniformly with RH[34]. Specifically, for sea salt aerosols, high RH correlate to NaCl-rich solutions while low RH correlate to $MgCl_2$-rich solutions, due to the difference in precipitation temperatures and O_2 solubility[34]. These results indicate that both the solution concentration, defining the amount of salt per liter, and solution chemistry, defining the elemental ions present, are important and can further complicate κ and WL calculations.

The interdependencies and dynamic conditions described above create a complex, albeit realistic, system. To therefore investigate such a complex system, it is useful to isolate singular parameters to determine their respective mechanisms, before approaching the multi-parameter system. Common approaches to investigate atmospheric conditions in literature involve the RDE, which can control the effective WL variations at a singular κ and RH, via a constant solution concentration and chemistry[29,30,35,46,65]. Note that if κ and RH are constant, LD must be increasing while WL is decreasing.

A similar investigation took place in this work to determine the isolated effect of WL on the distribution and magnitude of I_{total} through RDE boundary conditions. The thin WL were determined to induce a worst-case scenario, with the magnitude of I_{total} increasing and the distribution of I_{total} skewed towards creviced regions (Figure 4.5(b) and Figure 4.6). In addition, the correlation with WL and the resulting currents was much stronger than the correlation of the scribe dimensions with the currents, leading to high parameter significance for WL and i_{lim} (Figure 4.11). Therefore, further investigations were conducted at a range of WL both above and below δ_{nc}.

The results in Figure 4.5(b), indicating the increased susceptibility for corrosion to occur in a creviced region with decreasing WL, seemed to be a precursor for the trends in Figure 4.7. To clarify these trends, Figure 4.7(a) was subdivided into two plots, where Figure 4.7(b) included $WL \geq 400$ µm and Figure 4.7(c) included WL ≤ 400 µm.

In bulk WL (> 740 µm), there was no clear divide in determining whether the majority of current would occur within the creviced or bulk region, as the data ranges (representing the varied scribe parameters) overlapped (Figure 4.7(b)). However, the scribe dimensions at these WL were able to dictate the location of current, as seen through Figure 4.10(a), as large $\mathrm{SA_{crev}/SA_{bulk}}$ ratios result in the majority of current occurring in the crevice and small $\mathrm{SA_{crev}/SA_{bulk}}$ ratios result in the majority of current occurring in the bulk surface. This clear distinction was only visible once creating the geometric ration for the RF model.

In atmospheric WL conditions (≤ 200 µm), a clear separation occurred, where the majority of current occurred in the creviced regions, as seen in Figure 4.7(c), independent of the scribe geometry, as seen in Figure 4.10(a). Note that I_{bulk} was non-zero but was much less in magnitude under these conditions (Figure 4.7(c)). This separation occurred, as $I_{crevice}$ increased with decreasing WL at a steeper rate than I_{bulk}, until $I_{crevice} > I_{bulk}$ for all scribe dimensions. Correlations in Figure 4.11 support this conclusion, with all currents inversely proportional to the location of peak current (which, at a value of 1, represented the bulk surface) indicating that as the magnitude of all currents increase so does the susceptibility for the majority of current to occur in the creviced regions.

The results above indicate that the scribe dimensions dominate the resulting current distributions at WL ≥ 800 µm whereas the WL dominates the distributions at WL ≤ 200 µm. A transition region was clear at WL $= 400$ µm, where the currents were partially affected by the WL (as shown by the divergence of $I_{crevice}$) yet also influenced by the scribe dimensions (Figure 4.7(b), (c), Figure 4.5(b) and Figure 4.10(a)).

To quantify the relationship between the current at different locations and the WL, functions were fitted to all datapoints with WL $< \delta_{nc}$ (Figure 4.7(c)). The relationship of the limiting current density with WL is well described in literature[29,30,46]. That is, at WL $< \delta_{nc}$ the current should scale with WL^{-1}, through the relationship,

$$i_{lim} = nFD\left(\frac{C_{O_{2,bulk}} - C_{O_{2,surface}}}{WL}\right) \tag{4.8}$$

Where n is the number of electrons transferred, F is Faraday's constant, D is the diffusivity of oxygen, $C_{O_{2,bulk}}$ is the concentration of oxygen in the bulk and $C_{O_{2,surface}}$ is the concentration of oxygen on the electrode surface.

This relationship held true in the present results, mandated by the fact that i_{lim} at each new WL boundary condition was calculated using the Levich equation itself (Figure 4.7). Interestingly, however, was the divergence between the $I_{crevice}$ and I_{bulk} functions, which led to $I_{crevice}$ being dominate in the smaller WL.

At WL $< \delta_{nc}$, and a constant κ and RH, two factors can influence the current[28,30,66]. The kinetic factor is due to the shortened diffusion path of O_2 to the surface at thinning WL, which increases the cathodic oxygen reduction reaction (ORR) rate, and correspondingly i_{lim}, as described above. The second factor is a physical geometric constraint, where the solution acts as a resistor to the electrochemical circuit, with decreased WL increasing the resistance[28,30]. Note that the i_{lim} Eq. 4.8 increases the *total cathodic current* in the system; as the current is conserved, the total anodic current must also increase. However, R_{sol} impacts the *distribution* of current, and not the magnitude (the total current remains the same). These two competing factors can be visible when viewing the impact of $I_{crevice}$ and I_{bulk} with WL, but to understand the difference, the solution resistance (R_{sol}) must first be defined (Figure 4.7(c)).

Regarding a cross-section of the fastener/panel geometry, a characteristic length (l) describing the galvanic coupling distance from the cathode to the anode can be represented by $\mathrm{S_{length}}$[4], while a cross-sectional area of the anodic surface within the electrolyte (A) can be represented by $\mathrm{WL} \cdot \mathrm{S_{width}}$ (Figure 4.1). Therefore, R_{sol} can be defined by,

$$R_{sol} = \rho \left[\frac{l}{A}\right] \tag{4.9}$$

And furthermore,

$$R_{sol} = \rho \left[\frac{S_{length}}{(WL)(S_{width})}\right] \tag{4.10}$$

Therefore, it can be seen that R_{sol} is dependent on spatial (x, y, z) coordinates, while the kinetic contribution of i_{lim} is spatially *independent*, at a constant $\mathrm{WL} < \delta_{\mathrm{nc}}$. That is, if no ohmic drop existed (as could occur in a highly-conductive solution), the cathodic kinetics would be increased by $\mathrm{O_2}$ diffusion equally across all surfaces. The low increase of I_{bulk} with WL, as opposed to $I_{crevice}$, could then be attributed to a high R_{sol} via the large $\mathrm{S_{length}}$ values on the surface (Figure

4.7(c)). As R_{sol} restricts current spatially distant from the cathode, the current nearest to the cathode (including $I_{crevice}$) must increase.

Previous work conducted on the throwing power of the cathode, that is, the coupling distance between the anode and cathode, has also shown a decay in current density on the surface with increased $\mathrm{S_{length}}$ due to the increased R_{sol}, as shown in Eq. 4.10[4]. Note that the range of $\mathrm{S_{width}}$ values was physically limited to 0.01 in and 0.13 in, leading to any influences being outweighed by the magnitude changes in $\mathrm{S_{length}}$ and WL.

4.5.4. Initial and Generalized RF Model

FEM modeling, once verified, is advantageous to test a wide range of parameter space which can help inform experimental work along with the maintenance and design of new and existing structures. In lieu of solving every single parameter iteration, which can easily escalate to an infinite number of simulations, an educated step-size is chosen or best- and worst-case scenarios are used to bound the system, as has been utilized in this work (Figure 4.4, Figure 4.5, Figure 4.6, Figure 4.7). Conducting each simulation is not without computational cost, as the basis of FEM involves solving a governing equation at each node in the mesh[23]. For context, the number of nodes in the present geometry ranged from 3×10^4 to 2×10^5 for a singular scribe dimension and WL combination.

Instead of solving a governing equation, supervised classification machine learning maps a function and interpolates between the multi-variable input database. Although often the training and testing databases are amassed from experimental work in literature, difficulties can arise between the different experimental techniques or lack of experimental parameter description. Because FEM can provide a large database of consistent parameters and procedures, it can be extremely useful to train and test machine learning models, as demonstrated previously in literature[67,68].

In addition, the open-source software used in this work to create the RF model from the FEM database allowed for an optimized approach to conserve the computational cost, preserve the accuracy of the FEM, and increase the accessibility to real-time calculations. Creating the generalized $\mathrm{SA_{crev}/SA_{bulk}}$ parameter further increased the accessibility of the predictive tool to fastener-in-panel geometries which may have different geometric specifications than those chosen in this work.

The increased generalizability of the model was offset by a slight drop in accuracy, with 94.3% compared with the 98.7% of the initial RF model, although good performance was still indicated (Figure 4.9(a-b) and (d-e)). The drop in accuracy may be explained through the ambiguous region seen in Figure 4.10(b), where similar $\mathrm{SA_{crev}/SA_{bulk}}$ and WL combinations resulted in opposing predictions of the location of peak current. That is, the ambiguous region indicates that $\mathrm{SA_{crev}/SA_{bulk}}$ cannot explain the full story and other parameters may be more influential in those regions. Principle component analysis (PCA) was conducted on the entire testing and training dataset, and confirmed that all 5 variables were needed to capture all of the trends in the data. That is, four variables could only capture 93% of the data trends, while five variables captured 99% of the data trends.

Therefore, the best performing model with the training and testing datasets included all five parameters of interest, $\mathrm{S_{width}}$, $\mathrm{S_{length}}$, $\mathrm{SA_{crev}/SA_{bulk}}$, WL, and i_{lim}, indicating that additional value was added when including both the individual scribe dimensions and the generalized parameter (Figure 4.9(c) and (f)).

Using the five-parameter RF model, six of the seven new $\mathrm{SA_{crev}}/\mathrm{SA_{bulk}}$ ratio "tests" were identified correctly (Table 4.1). Specifically, scenarios 1, 2, 5, and 6, fell in the ambiguous region, with scenario 1 being the singular scenario incorrectly identified (Figure 4.10(b)). Further information can be gathered from the confidence probability of the RF predictions (Table 4.1). Scenario 5 was identified correctly, but the model was very unsure of the prediction, indicating that 68% of the trees classified the input parameters correctly and 32% did not. Also of concern is scenario 1, not only because it was classified incorrectly, but because the RF model was 100% certain in its incorrect classification. Therefore, the model has room for improvement in the ambiguous region, which may need a new variable combination to best tease out the correlations. Yet despite the ambiguous region shortcomings, over the majority of parameter space tested the RF model performed well at interpolating and correctly predicting the majority of data.

4.6 Limitations

Many of the assumptions within the present FEM framework have been validated and proven to capture the experimental behavior of fastener/panel geometries, both over the entire system and within the fastener hole specifically[5]. However, the present assumptions fall short at capturing time-dependencies in the system, such as the evolving electrolyte, and at predicting any local "hot spots" of anodic or cathodic activity which are inevitably present on an inhomogeneous alloy's surface[22,59]. In addition, the relative effects of corrosion products or build-up of aggressive species and corresponding pH distributions could not be considered in this work due to the present assumptions.

Limiting assumptions must also be appreciated in regards to the machine learning algorithm. The RF model, although generalized to a degree, was still built to capture an AA7075/SS316 galvanic couple in a fastener/panel configuration. Extrapolating beyond this alloy or geometry would require a new initial dataset to train and test the RF model, as well as optimization of the RF tuning parameters.

Furthermore, all computational work is only as good as the information used to build the model; the boundary conditions, in the case of FEM, and the training dataset, in the case of RF. When utilizing FEM results to inform and train the RF model, the possibility of error propagation is highlighted. Erroneous boundary conditions in the FEM would then carry through to impact the final prediction of the RF models. However, this combined-computational approach has been used previously in literature, once first experimentally validating the FEM results[68]. Benefits of using FEM to build the RF model include consistency of methodology and training datasets with large ranges of parameter space (as experimental work is often limiting).

4.7 Conclusion

In this work, finite element method (FEM) modeling was conducted to determine both the distribution and magnitude of current within a complex SS316/AA7075 fastener/panel galvanic couple. The impact of the water layer thickness (WL), external defect (*i.e.,* scribe) dimensions, and kinetic factors were evaluated, with the resulting galvanic currents compared. A machine learning algorithm was developed via FEM input parameters to create a generalizable predictive tool, which determined under which environmental and geometric conditions the majority of corrosion would occur in a creviced region.

- Conditions under which the majority of corrosion would occur in a creviced region were determined, for a variety of water layer thicknesses (WL), scribe dimensions, and kinetic factors, resulting in “damage maps” which cover a range of parameter space.

- In bulk water layers (> 800 µm), small scribe widths and lengths pushed current into the creviced regions (in the scribes under the washer and within the fastener hole). Conversely, longer scribe lengths (>1.75 in) were beneficial in pulling the current into more-visible bulk regions, which would aid the inspection and in limiting the amount of corrosion damage in the highest-stress regions (*i.e.*, the fastener hole).

- Anodic kinetic accelerants were found to focus the distribution of current into the bulk, rather than creviced, regions without impacting the total current. This benefit could be generalized to any non-polarizable active galvanic couple with the galvanic coupling current approximately equal to the O_2 diffusion limiting current density ($i_{gal} \cong i_{lim}$). Conversely, the cathodic kinetics largely influenced both the total current and distribution of current, leading to atmospheric conditions (thin WL) as a worst-case scenario.

- A WL $\cong 400$ µm threshold was determined, where at WL ≤ 200 µm the distribution of current was independent of the scribe dimensions (with all current pushed into the creviced regions) but dependent on the WL. In contrast, at WL ≥ 800 µm, scribe dimensions dictated the location and distribution of current, with no impact of the WL.

- FEM results were used to create a generalized RF model, capable of accuracies against the testing data up to 99% when including five input parameters of the scribe width, scribe length, a generalized geometric parameter of the crevice to bulk surface area ratio, WL, and i_{lim}. Additionally, six out of seven uniquely distinct data points were correctly identified with the RF model.

4.8 Acknowledgements

Any opinions, findings, and conclusions or recommendations expressed in this material are those of the author(s) and do not necessarily reflect the views of Office of Naval Research. This work is supported by the Office of Naval Research under Contract No. N68335-16-C-0121 (Mr. William Nickerson) through a subcontract with Luna Labs USA, LLC. In addition, financial support provided by the NASA Virginia Space Grant Consortium through a Graduate Research Fellowship is gratefully acknowledged.

4.9 References

1. Prasad, N.E., and R.J.H. Wanhill, eds., *Aerospace Materials and Material Technologies; Volume 1: Aerospace Materials* (Springer, 2017).
2. Burns, J.T., J.M. Larsen, and R.P. Gangloff, *Fatigue & Fracture of Engineering Materials & Structures* 34 (2011): pp. 745–773, https://doi.org/10.1111/j.1460-2695.2011.01568.x.
3. Kelly, R.G., *ASM Handbook - Corrosion: Fundamentals, Testing, and Protection* 13A (2003): pp. 242–247.
4. Marshall, R.S., A. Goff, C. Sprinkle, A. Britos, and R. Kelly, *Corrosion* 76 (2020): pp. 476–484.
5. Marshall, R.S., R. Kelly, A. Goff, and C. Sprinkle, *Corrosion* 75 (2019): pp. 1461–1473.
6. Mcmurtrey, M.D., D. Bae, and J.T. Burns, (2016).
7. Young, P.S., and J.H. Payer, *Corrosion* 71 (2015): pp. 1278–1293.
8. Moran, A., J. Jennings, H. Nee, S. Pearson, B. Clark, and R.S. Lillard, *Corrosion Journal* 75 (2019): pp. 484–498.

9. Cocke, C., R.S. Marshall, C. Sprinkle, A. Goff, R.G. Kelly, and J.T. Burns, *Corrosion* 78 (2022): pp. 152–162.

10. Feng, Z., G.S. Frankel, and C.A. Matzdorf, *J Electrochem Soc* 161 (2014): pp. 42–49, http://jes.ecsdl.org/cgi/doi/10.1149/2.059401jes.

11. Feng, Z., and G.S. Frankel, *Corrosion* 70 (2014): pp. 95–106.

12. Feng, Z., J. Boerstler, G.S. Frankel, and C.A. Matzdorf, *Corrosion* 71 (2015): pp. 771–783.

13. Feng, Z., G.S. Frankel, W.H. Abbott, and C.A. Matzdorf, *Corrosion* 72 (2016): pp. 342–355.

14. Wang, S., J. Boerstler, and G.S. Frankel, *Corrosion* 74 (2018): pp. 499–508.

15. Boerstler, J.T., M. Jokar, and G.S. Frankel, *Corrosion Engineering, Science and Technology* (2020): pp. 1–13, https://doi.org/10.1080/1478422X.2020.1732113.

16. Jokar, M., and G.S. Frankel, *Materials and Corrosion* (2022).

17. Jia, J.X., A. Atrens, G. Song, and T.H. Muster, *Materials and Corrosion* 56 (2005): pp. 468–474.

18. Rafla, V.N., and J.R. Scully, *Corrosion* 75 (2019): pp. 587–603.

19. Rafla, V., A. Davenport, and J.R. Scully, *Corrosion Communications* 71 (2015): pp. 1171–1176.

20. Rafla, V., A. Davenport, and J.R. Scully, *Corrosion, Poster Award Research Letters* 71 (2015): pp. 1300–1303.

21. Rafla, V.N., A.D. King, S. Glanvill, A. Davenport, and J.R. Scully, *Corrosion* 74 (2018): pp. 5–23.

22. Rafla, V.N., and J.R. Scully, *Corrosion Journal* 75 (2019): pp. 12–28.

23. Munn, R.S., and O.F. Devereux, *Corrosion* 47 (1991): pp. 618–634.

24. Liu, C., V.N. Rafla, J.R. Scully, and R.G. Kelly, "Mathematical Modeling of Potential and Current Distributions for Atmospheric Corrosion of Galvanic Coupling in Airframe Components," in NACE International: CORROSION (2015), pp. 1–11.

25. Snihirova, D., D. Höche, S. Lamaka, Z. Mir, T. Hack, and M.L. Zheludkevich, *Corrosion Science* 157 (2019): pp. 70–78, https://doi.org/10.1016/j.corsci.2019.04.036.

26. Cui, F., F.J. Presuel-Moreno, and R.G. Kelly, *Corrosion* 62 (2006): pp. 251–263.

27. Moraes, C. V., R.J. Santucci, J.R. Scully, and R.G. Kelly, *Journal of The Electrochemical Society* 168 (2021): p. 051505.

28. Simillion, H., O. Dolgikh, H. Terryn, and J. Deconinck, *Corrosion Reviews* (2014).

29. Katona, R., J. Carpenter, A. Knight, R.S. Marshall, B. Nation, E. Schindelholz, R.F. Schaller, and R. Kelly, *J Electrochem Soc* 168 (2021), https://iopscience.iop.org/article/10.1149/1945-7111/abeb29.

30. Liu, C., J. Srinivasan, and R.G. Kelly, *J Electrochem Soc* 164 (2017): pp. C845–C855, http://jes.ecsdl.org/lookup/doi/10.1149/2.1641713jes.

31. Nyby, C., X. Guo, J.E. Saal, S.-C. Chien, A.Y. Gerard, H. Ke, T. Li, P. Lu, C. Oberdorfer, S. Sahu, S. Li, C.D. Taylor, W. Windl, J.R. Scully, and G.S. Frankel, *Sci Data* 8 (2021): pp. 1–11.

32. Co, N.E.C., D.E. Brown, and J.T. Burns, *Jom* 70 (2018): pp. 1168–1174, https://doi.org/10.1007/s11837-018-2864-6.

33. Chen, Z.Y., F. Cui, and R.G. Kelly, *J Electrochem Soc* 155 (2008): pp. 360–368.

34. Bryan, C.R., A.W. Knight, R.M. Katona, A.C. Sanchez, E.J. Schindelholz, and R.F. Schaller, *Science of The Total Environment* 824 (2022): p. 154462.

35. Katona, R.M., J.C. Carpenter, A.W. Knight, C.R. Bryan, R.F. Schaller, R.G. Kelly, and E.J. Schindelholz, *Corrosion Science* 177 (2020): p. 108935, https://doi.org/10.1016/j.corsci.2020.108935.

36. Inkscape Project, "Inkscape" (2022), https://inkscape.org (May 2, 2022).

37. Tomashov, N.D., *CORROSION* 20 (1964).

38. RStudio Team, "RStudio: Integrated Development for R," PBC, Boston, MA (2022), http://www.rstudio.com/ (May 2, 2022).

39. R Core Team, "R: A Language and Environment for Statistical Computing. R Foundation for Statistical Computing," Vienna, Austria (2022), https://www.R-project.org/ (May 2, 2022).

40. Louppe, G., (2014), http://arxiv.org/abs/1407.7502.

41. Cutler, A., D.R. Cutler, and J.R. Stevens, "Random Forests," in Ensemble Machine Learning (Boston, MA: Springer US, 2012), pp. 157–175, http://link.springer.com/10.1007/978-1-4419-9326-7_5.

42. Efron, B., *The Jacknife, the Bootstrap and Other Resampling Plans* (Society for Industrial and Applied Mathematics, 1982), https://epubs.siam.org/terms-privacy.

43. Costine, A., P. Delsa, T. Li, P. Reinke, and P. v. Balachandran, *Journal of Applied Physics* 128 (2020): p. 235303.

44. Hartnett, T.Q., M. v. Ayyasamy, and P. v. Balachandran, *MRS Communications* 9 (2019): pp. 882–890.

45. Liaw, A., and M. Wiener, *R News* 2 (2002): pp. 18–22.

46. Charles-Granville, U.-E., C. Liu, J.R. Scully, and R.G. Kelly, *Journal of The Electrochemical Society* 167 (2020): p. 111507.

47. Levich, B., *Discuss Faraday Soc* 1 (1947): pp. 37–49.

48. Compton, K.G., A. Mendizza, and W.W. Bradley, *Corrosion* 11 (1955): pp. 35–44, http://corrosionjournal.org/doi/abs/10.5006/0010-9312-11.9.35.

49. Matzdorf, C.A., W.C. Nickerson, B.C. Rincon Tronconis, G.S. Frankel, L. Li, and R.G. Buchheit, *Corrosion* 69 (2013): pp. 1240–1246.

50. Mrema, E., Y. Itoh, A. Kaneko, and M. Hirohata, 62 (2016): pp. 525–536.

51. Mansfeld, F., and E.P. Parry, *Corrosion Science* 13 (1973): pp. 605–621.

52. Cai, Y., Y. Xu, Y. Zhao, and X. Ma, "Atmospheric Corrosion Prediction: A Review," Corrosion Reviews (De Gruyter Open Ltd, 2020).

53. Stratmann, M., and H. Streckel, *Corrosion Science* 30 (1990): pp. 681–696.

54. Stratmann, M., and H. Streckel, *Corrosion Science* 30 (1990): p. 697.

55. Stratmann, M., H. Streckel, K.T. Kim, and S. Crockett, *Corrosion Science* 30 (1990): pp. 715–734.

56. Xiao, J., and S. Chaudhuri, *Electrochimica Acta* 56 (2011): pp. 5630–5641, http://dx.doi.org/10.1016/j.electacta.2011.04.019.

57. Abodi, L.C., J.A. Derose, S. van Damme, A. Demeter, T. Suter, and J. Deconinck, *Electrochimica Acta* 63 (2012): pp. 169–178, http://dx.doi.org/10.1016/j.electacta.2011.12.074.

58. Liu, C., P. Khullar, and R.G. Kelly, *Journal of The Electrochemical Society* 166 (2019): pp. 153–161.

59. Charles-Granville, U.-E., R.S. Marshall, C. V. Moraes, C.F. Glover, J.R. Scully, and R.G. Kelly, *Journal of The Electrochemical Society* 169 (2022): p. 031502.

60. Charles-Granville, U.-E., C. Glover, J.R. Scully, and R. Kelly, *Journal of The Electrochemical Society* (2021).

61. Kramer, P., T. Curtin, M. Merrill, M. Kim, F. Friedersdorf, and R. Adey, "Atmospheric Corrosion Measurements to Improve Understanding of Galvanic Corrosion of Aircraft," in NACE International: CORROSION (2018), pp. 1–11.

62. Liu, C., G.W. Kubacki, and R.G. Kelly, *Corrosion Journal* 75 (2019): pp. 465–473.

63. Hihara, L.H., and R.M. Latanision, *Corrosion Science* 34 (1993): pp. 655–665.

64. Katona, R.M., S. Tokuda, J. Perry, and R.G. Kelly, *Corrosion Science* 175 (2020): p. 108849, https://doi.org/10.1016/j.corsci.2020.108849.

65. Palani, S., T. Hack, J. Deconinck, and H. Lohner, *Corrosion Science* 78 (2014): pp. 89–100, http://dx.doi.org/10.1016/j.corsci.2013.09.003.

66. Steiner, P.J., Z.D. Harris, C.V. Moraes, R.G. Kelly, and J.T. Burns, *Corrosion* 77 (2021): pp. 838–852.

67. Martínez-Martínez, F., M.J. Rupérez-Moreno, M. Martínez-Sober, J.A. Solves-Llorens, D. Lorente, A.J. Serrano-López, S. Martínez-Sanchis, C. Monserrat, and J.D. Martín-Guerrero, *Computers in Biology and Medicine* 90 (2017): pp. 116–124.

68. Ye, Z., S.-C. Hsu, and H.-H. Wei, *Automation in Construction* 136 (2022).

Pitting Corrosion

Summary:

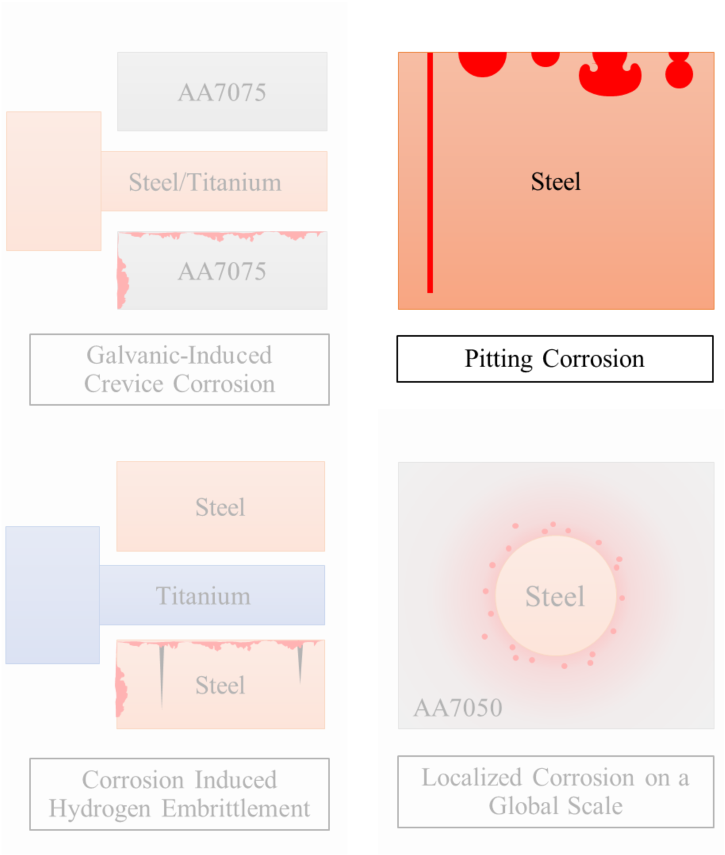

In this second section of the work, micro-galvanic coupling in the form of pitting corrosion was the focus of a FEM Laplacian model. In Chapter 5, isolated single pits, assumed to be after the initiation period and before the stable growth period, were investigated. Stability thresholds, such as the repassivation potential $\left(\boldsymbol{E_{rp}}\right)$ and the pit stability product $(\boldsymbol{i} \cdot \boldsymbol{x})$, offer a practical application of corrosion **mitigation** through keeping the system below these values thereby preventing any stable pit growth. Therefore, a critical pit radius, water layer thickness, and cathode diameter which satisfied the stability threshold of either $\boldsymbol{E_{rp}}$ or $(\boldsymbol{i} \cdot \boldsymbol{x})$ were **predicted** and compared. Multiple pit geometries were tested, to see any impact through 3-D or 1-D pitting assumptions. It was determined that the surface area of the pit is more important for stability than the pit shape, when using the 3-D $\left(\frac{I}{r}\right)_{crit}$ stability criterion. Thin WL, decreased chloride concentration, and smaller cathode diameters all contributed towards lowering the stability of a single pit, thereby increasing the susceptibility for the metastable pit to repassivate. Using more-realistic boundary conditions and assumptions than the maximum pit model, preliminary estimates suggest that the maximum pit model may be conservative by a factor of two and that conventional measurements of $\boldsymbol{E_{rp}}$ may be too conservative as well.

Therefore, Chapter 6 follows up on the work by discussing the present field of pit stability thresholds. In addition, an alternative calculation of $\boldsymbol{E_{rp}}$ was proposed, in which the resulting values were less conservative than those measured conventionally through cyclic potentiodynamic polarization, and values were unified with the same critical radius as predicted from $(\boldsymbol{i} \cdot \boldsymbol{x})$. Consistent values of the newly proposed $\boldsymbol{E_{rp}}$ were seen through in-house 1-D scans and computational work, offering **validation**.

Publications resulting from this section of the work:

- **R. Skelton Marshall,** R. M. Katona, M. A. Melia, & R. G. Kelly. (2022). Pit Stability Predictions of Additively Manufactured SS316 Surfaces Using Finite Element Analysis. *Journal of The Electrochemical Society, 169*(2), 021506
- **R. Skelton Marshall,** A. Shehi, R. M. Katona, M. A. Melia, R. G. Kelly. (2022). Perspective – An Alternative Calculation of the Repassivation Potential, to Represent Less Conservative and More Realistic Values. *Journal of The Electrochemical Society, (To be submitted to the Journal of the Electrochemical Society, Perspective)*

Chapter 5: Pit Stability Predictions of Additively Manufactured SS316 Surfaces Using Finite Element Analysis

Rebecca Skelton Marshall*, Ryan M. Katona**, Mike A. Melia**, Rob G. Kelly*

*University of Virginia, 395 McCormick Rd, Charlottesville VA 22903

**Sandia National Laboratories, Albuquerque, NM 87123 USA

Authorship contributions: R. Skelton Marshall (formal analysis, computational work, and writing – original draft), R. M. Katona (experimental polarization behavior, and writing – review & editing), M. A. Melia (funding acquisition, and writing – review & editing)

5.1 Abstract

Stainless steels are susceptible to localized forms of corrosion attack, such as pitting. The size and lifetime of a nucleated pit can vary, depending on a critical potential or current density criterion, which determines if the pit repassivates or continues growing. This work uses finite element method (FEM) modeling to compare the critical pit radii predicted by thermodynamic and kinetic repassivation criteria. Experimental electrochemical boundary conditions are used to capture the active pit kinetics. Geometric and environmental parameters, such as the pit shape and size (analogous to additively manufactured lack-of-fusion pores), solution concentration, and water layer thickness were considered to assess their impact on the pit repassivation criterion. The critical pit radius (the transition point from stable growth to repassivation) predicted for a hemispherical pit was larger when using the repassivation potential (E_{rp}) criteria, as opposed to the current density

criteria (pit stability product). Including both the pit stability product and E_{rp} into its calculations, the analytical maximum pit model predicted a critical radius two times more conservative than the FEA approach, under the conditions studied herein. The complex pits representing lack-of-fusion pores were shown to have minimal impact on the critical radius in atmospheric conditions.

5.2 Introduction

Metals with a passive film, such as stainless steel (SS) and aluminum, are susceptible to the localized corrosion phenomenon of pitting.[1] It is commonly agreed in literature that there are three main stages in pitting; 1) nucleation, which includes the local breakdown of a passive film; 2) metastable pitting, in which a nucleated pit repassivates; and 3) stable growth, in which pits spontaneously continue growing.[1–4] Recognizing under which conditions the transition from 2) metastable to 3) stable pitting will occur is extremely important, as pits can be difficult to detect or mitigate once initiated.[5] Left unmitigated, pits can grow to hundreds of microns in size[6,7], leading to the potential for component failure by perforation or environmentally assisted cracking with the pit acting as the stress concentrator.[8–10]

For additively manufactured (AM) passive metals, processing defects including lack-of-fusion (LoF) porosity have been shown to act as preferential initiation sites for pitting. The studies to date investigating porosity's influence on pit initiation have been carried out with experimental methods utilizing polarization measurements under full immersion environments. These experiments provide information on a pore's propensity to initiate a pit, but lack the dexterity to assess how a pit, once initiated in the pore, can maintain the required chemistry to propagate pit growth at open circuit conditions (a more likely real-world scenario). If a pit initiates inside a pore, then aspects of the pore's geometry such as aspect ratio, tortuosity, etc., may control diffusion of ions in and out of the pore, determining if that pit remains active or repassivates. Furthermore, a recent perspective has shown that in materials prone to pitting (such as the porous AM surface described above), the rate limiting step is not the initiation of pits but rather the transition from metastable to stable growth.[2] The current study develops a steady-state finite element method (FEM) model, which assumes a metastable pit has initiated inside a computer generated surface pore and focuses on using electrochemical criteria to predict a critical radius defining a threshold of when the pit will transition to stable growth or repassivate (growth stops). The model is then broadly applied to metastable pits under different pore geometries and environmental parameters. Determining a criterion to predict whether or not an initiated pit will continue growing or will repassivate has been heavily researched. Pitting criteria based on exceeding a critical potential, such as the pitting potential (E_{pit}) and the repassivation potential (E_{rp}), are thresholds that can be identified empirically using potentiodynamic scans (PDS). Traditionally, E_{pit} has been thought to represent a threshold at which pits are able to stably grow and is commonly determined by a sharp increase in current density to a stable value defined by the mass transport limitations of the corroding system during an anodic PDS.[11,12] Below E_{rp}, which has also been referred to as the protection potential, lies a threshold at which all pits stop nucleating and growing.[3,11,13,14] E_{rp} is generally considered the lower bound for pitting, making it a popular parameter when discussing a conservative approach to pit prediction.[13,15]

Rather than using a voltage criterion, the mass transport characteristics of maintaining a stable pit can be used to determine a kinetic-based criteria. Galvele proposed that a certain pit stability product ($i{\cdot}x$) was needed to maintain the pit chemistry at the base of a 1-D pit in order to allow continued growth, in which the rate of dissolution (i) at the base of the pit with depth (x) is in competition with diffusion out of the pit. It was demonstrated that the product ($i{\cdot}x$) could be used to determine the chemical composition at the bottom of the pit. Vetter & Strehblow, among other researchers, extended the 1-D ($i{\cdot}x$) to a 3-D criterion $\left(\frac{I}{r}\right)$, which is more applicable to the higher spatial dimensionality of pits in bulk samples.[4,16–19] In the 3-D criterion I is the current and r is the hemispherical pit radius. Straightforward measurements of 1-D pit electrodes (*i.e.*, using artificial pits or lead-in-pencil electrodes), in which the limiting current density i_{lim} is extracted at a variety of pit depths, allows determination of ($i{\cdot}x$) for salt film (sf) conditions (i.e., 100% saturation of the solution with respect to metal chlorides at the bottom of the pit), $(i{\cdot}x)_{\mathrm{sf}}$ and, thus, $\left(\frac{I}{r}\right)_{sf}$.[5,20–23] However, the presence of a salt film at the bottom of the pit is not necessary for pit growth, as shown by observation of crystallographic facets within pits[24], making the above criteria too conservative. Using artificial SS304 pits, Gaudet was the first to conclude that pitting occurred when the concentration at the pit surface was between 60% and 80% saturation.[25] More recent work has suggested that the critical saturation concentration may actually be as low as 50% of the fully saturated concentration.[22,26]

Chen & Kelly developed a mathematical model incorporating multiple pit threshold criteria to determine the maximum radius (r_{max}) that a hemispherical pit can attain under thin electrolytes for atmospheric environments.[27] The concept is based on combining E_{rp}, $(i{\cdot}x)_{\mathrm{crit}}$, ohmic drop in thin electrolytes, and the finite kinetics of cathodic reactions. The potential threshold, E_{rp}, creates a bound above which the pit mouth must remain for stability, as observed experimentally. The ohmic drop, combined with the finite cathodic kinetics, defines the maximum cathodic current ($I_{\mathrm{c}}^{\mathrm{ext}}$) available to support pit growth. The calculation of $I_{\mathrm{c}}^{\mathrm{ext}}$ takes advantage of the fact that only the total cathodic current supplied to the pit is needed; the actual spatial distribution of the current is not important in determining pit stability. Thus, a mathematically equivalent cathode was constructed for which $I_{\mathrm{c}}^{\mathrm{ext}}$ is constant with position and is quantitatively equal to that of the maximum possible current that the actual cathode could provide given its electrochemical kinetics and the solution conductivity and thickness of the water layer. The finite ideal cathode size to maintain stable pit propagation can be back-calculated based on the given conditions.[27] If conditions are such that more anodic current (I_{LC}) is required than I_c^{ext}, the pit will stifle due to dilution of the aggressive pit environment. Stable pitting only occurs when I_{LC} is equal to or less than I_c^{ext}.[27] Both currents, I_{LC} and I_c^{ext} depend on r, so $I_{\mathrm{LC}} = I_c^{\mathrm{ext}}$ defines the magnitude of r_{max}. The effects of environmental variables on the mathematical model's prediction of r_{max} have been studied, from water layer thickness (WL) and relative humidity (RH) effects to solution chemistry considerations.[19,23,28] Although the maximum pit model predicts the maximum radius that a 3-D hemispherical pit may grow under a given set of conditions, the question remains as to the level of conservatism it represents when compared to a non-ideal system. Furthermore, the maximum pit model predicts stability through a combination of E_{rp} and $(i{\cdot}x)_{\mathrm{crit}}$; separately, the predicted results from these pit stability criteria have never been compared.

Most modeling of stainless steel pits has focused on either 1-D[3,22,29–31] or hemispherical[29,32,33] geometries, due to their mathematical simplicity, with a few recent works using a deformable mesh to investigate the evolution of more complex geometries.[34–36] The work performed here focuses on predicting the stability of four computer-generated pit geometries that represent two common observations from corrosion experiments (1-D and hemispherical pits) as well as two complex-shaped pits, similar to LoF pores found in AM metals. A steady-state FEM model was built to explore how potential and current distributions vary across four stainless steel (SS316) pit geometries, as a function of r, x, WL, and cathode diameter (D). Then, two pit stability criteria were employed; E_{rp} and $(i{\cdot}x)$ for 1-D pits and E_{rp} and $\left(\frac{I}{r}\right)$ for 3-D pits, to determine if the pits will remain growing or repassivate. Results calculated using more realistic cathodic boundary conditions in comparison to assuming an ideal cathode were also discussed.

5.3 Methods

Computational Governing Equation

The FEM model was conducted using the Corrosion Module in COMSOL Multiphysics© (version 5.5). In all calculations, the migration of Cl^- ions was assumed to transport all of the current, due to the high concentration of supporting NaCl electrolyte in both 3 M and 0.6 M NaCl scenarios considered. The main mass transport mechanism within a pit is conventionally assumed to be diffusion, thus following Fick's laws. However, recent work has shown that migration within the pit is not negligible[31], and may even contribute up to two thirds of the limiting current density.[37] Therefore, this work will assume that migration is dominant over diffusion or convection, thereby allowing for the full Nernst-Planck equation to be simplified into,

$$i = - \kappa \nabla \Phi \qquad 5.1$$

where i is the current density, κ is the conductivity, and Φ is the potential in the electrolyte. Accounting for the conservation of charge ($\nabla i = 0$), the Laplace (Eq. ***5.2***) can be derived and used to solve for the potential.

$$\nabla^2 \Phi = 0 \qquad 5.2$$

The potential on the electrode surface (E) was calculated by taking the inverse sign of the electrolyte potential, at the electrode/electrolyte interface (Eq. 5.3).

$$E = 0 - \Phi \qquad 5.3$$

A thorough discussion of utilizing the Laplace equation, in lieu of the full Nernst-Plank equation, is described in a recent review paper by Liu & Kelly.[38] In line with the Laplace equation, the water layer domain was assumed to have a constant bulk conductivity (κ_{bulk}), that is, assuming that the solution is homogeneous and well-mixed. Values of conductivity were calculated via OLI Studio Analyzer© 9.5 (OLI Systems, Inc., Cedar Knolls, NJ) software to be 19.7 S/m for 3 M NaCl and 5.5 S/m for 0.6 M NaCl.

Simulated Pit Geometries

Four pit shapes were studied, two geometrically simple pits and two more geometrically complex pits. To reduce the computational cost, all of the geometries were built in a 2-D domain which was axisymmetric about the z-axis (Figure 5.1). Note that the parameter D is on the order of cm, and therefore the entire electrolyte domain is not shown in Figure 5.1 due to the extremely small aspect ratio. The two simple pits consisted of a hemispherical and rectangular pit, representing a 3-D and 1-D pit, respectively. These geometries are commonly used to represent pitting corrosion in modeling, because of their mathematical simplicity.[3,22,29,30,32,33] However, in realistic structures, pitting morphologies are not constrained to geometric simplicity. Therefore, complex pit geometries, based as an extension of the hemispherical pit, were created to represent common surface defects to both wrought and AM structures. These geometries consisted of a “double pit” and an “undercutting pit” (Figure 5.1(c) and (d)).

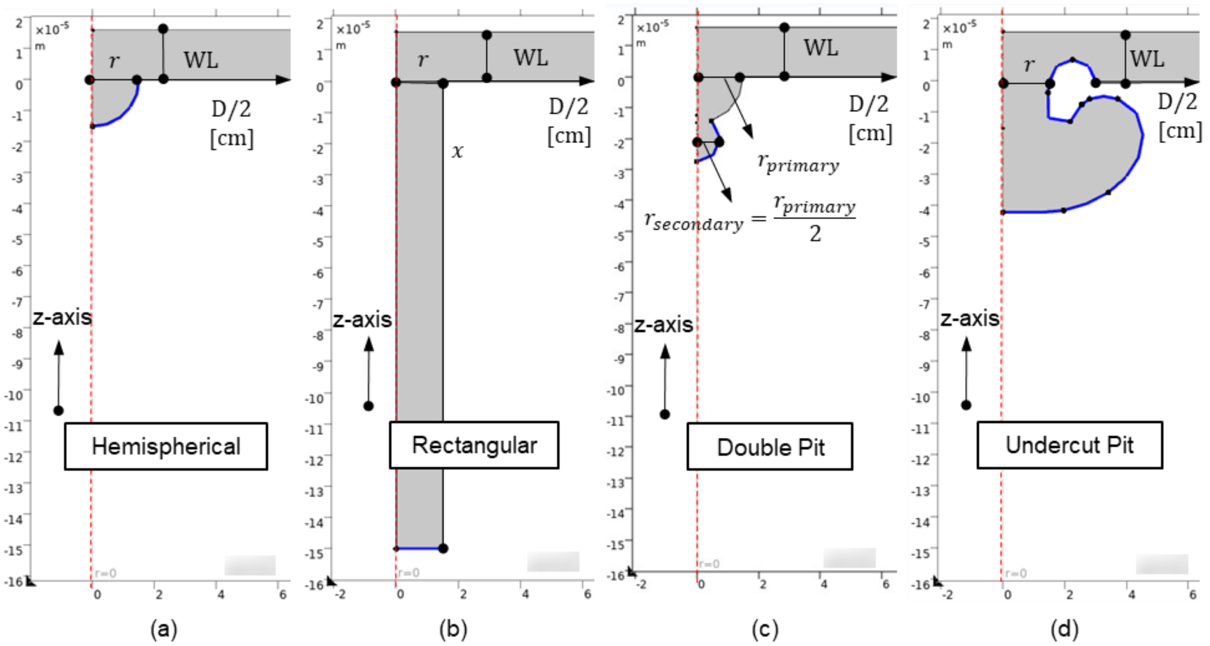

Figure 5.1: Various pit geometries built in the model, with geometric parameters labeled as the water layer thickness (WL), pit mouth radius (r), cathode diameter (D), and depth of a rectangular pseudo-1-D pit (x); (a) and (b) simple pits; (c) and (d) complex pits. The blue surfaces represent active anodic dissolution.

For consistency, the opening pit radius r in all of the geometries was equal, although the total anodic surface area was not. This distinction can be seen in Figure 5.1, denoted by r in comparison to the blue anodic surfaces. In order of increasing active anodic surface area, the geometries are the double pit, rectangular pit, hemispherical pit, and undercutting pit (with all regions active). A variable mesh was built on all geometries, to allow for finer resolution along the actively dissolving surfaces and the z-axis of symmetry (Figure 5.2). The mesh was coarser along D to limit computational cost. Parameter sweeps of r, x, WL, and D were conducted to determine the magnitude of effect each parameter had on the pit stability.

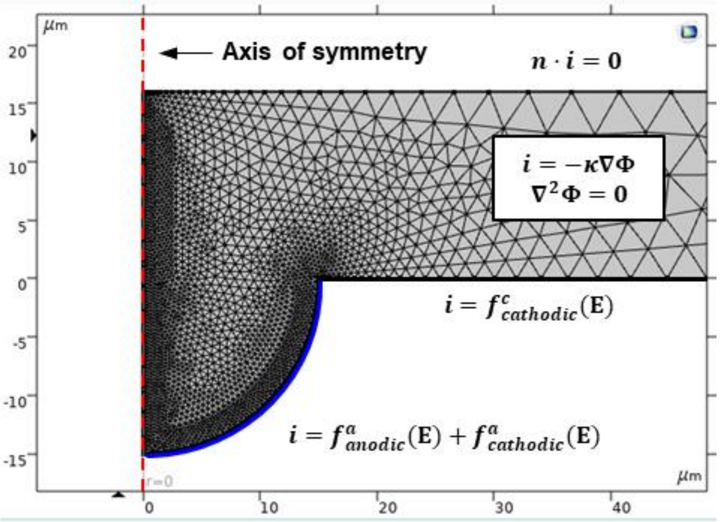

Figure 5.2: The FEM model mesh construction of 2-D axisymmetric hemispherical (r = 15 µm, D = 30 cm, and WL = 16 µm) pit, with the boundary conditions labeled on each surface; the red dashed line represents the rotational axis.

After each simulation, the distribution of potential in the system and the current density along the surface of the pit were calculated. The current density was integrated over the anodic surfaces in order to determine the total anodic current of the system. In all models, the total anodic current equaled the total cathodic current, with less than 0.25% difference.

In all pit geometries except the rectangular pit, a constant κ_{bulk} was assumed throughout the entire domain. Although simplifications within the Laplace equation limit the model from solving κ as a function of evolving species, a linear gradient inside the rectangular pit was invoked manually to account for a singular concentration gradient. Quasi-linear concentration gradients have been observed within a 1-D pit, so long as the pit is stable and a passive film is not present.[30] The concentration gradients were assumed to be more relevant for the 1-D, rather than 3-D, geometries due to the more constrained diffusion path. Steady-state conductivity of 3 M NaCl solution within the pit (κ_{pit}) was calculated via OLI Studio Analyzer© to be 21.8 S/m, assuming a saturated metal salt film (~5 M) to represent the worst-case scenario. The linear gradient was constrained to have κ_{pit} at the base of the pit and κ_{bulk} at the mouth of the pit, varying along the z-axis as a function of x. Although $\Delta\kappa$ was not very large (2.1 S/m), at a constant pit depth of 10 times the pit radius, the absence of a linear gradient was seen to lower the current by 0.18 µA which was a 3% difference of the total currents.

Boundary Conditions

Cathodic and anodic PDS were input into the model as boundary conditions to represent the behavior of SS316 at room temperature in two different NaCl concentrations. The PDS were input as a function of the electrode potential (Figure 5.2). Although not visible, the far field boundary conditions used the same insulating conditions as imposed on the top surface of the electrolyte. The activated pit scans were conducted via lead-in-pencil experiments, to capture the behavior of an actively corroding pit, with a scan rate of 50 mV/sec starting with the pit under salt film conditions and scanning in the negative direction. Anodic and cathodic Tafel slopes were extracted from the active pit polarization curves and were input separately into the model.

The procedure for determining the cathodic kinetics was the same as Katona *et al.*.[23] Briefly, cathodic kinetics were determined in solutions less corrosive than NaCl in order to prevent convolution of the cathodic kinetics with anodic dissolution due to open circuit localized corrosion.[27] Sodium bromide (NaBr) was chosen as it was shown to be less corrosive than NaCl as characterized by transient free OCP values and a post-scan visual inspection of the surface revealing no pitting. Concentrations of surrogate catholyte solutions of NaBr (0.73 M and 7.34 M to represent 0.6 M and 3 M NaCl, respectively) were determined based on the Levich equation concerning the mass transfer diffusion limited current density for oxygen reduction.[39] Thus, based on the Levich equation, the concentration of NaBr which matched the quantity of $i_{\text{lim}} \propto D_{O_2}^{2/3} \nu^{-1/6} C_{O_2}^{sat}$ for NaCl solutions at a given temperature was chosen. In order to determine this quantity, the solution thermodynamics database of the OLI Studio Analyzer© software was utilized. The quantity of $D_{O_2}^{2/3} \nu^{-1/6} C_{O_2}^{sat}$ was first calculated for NaCl at the desired concentration given by experimental parameters. The solution of NaBr that matched the given quantity was then chosen as the surrogate solution. The efficacy of this has been shown by Liu *et al.*.[40] Cathodic polarizations were scanned from OCP (after 1 hour stabilization) in the negative direction at a scan rate of 0.167 mV/sec until a final potential of -0.7 V_{SCE}.

Stability Thresholds Considered

Three different stability criteria were assessed on the simulated pit geometries, to determine whether the pit will repassivate or grow with the given set of parametric conditions:

1) $E_{\text{mouth}} > E_{\text{rp}}$

2) $(i \cdot x)_{\text{FEM}} > (i \cdot x)_{\text{crit}}$

3) $\left(\frac{\mathrm{I}}{\mathrm{r}}\right)_{\text{FEM}} > \left(\frac{\mathrm{I}}{\mathrm{r}}\right)_{crit}$

Where E_{mouth} is the potential at the mouth of the pit, E_{rp} is the repassivation potential, i is the current density, x is the pit depth (in a rectangular-pit context), I is the current from the pit, and r is the pit radius (in a hemispherical-pit context). In each of the criteria, if the inequality is true, then the pit is predicted to grow. Conversely, if the inequality is false, then spontaneous repassivation is predicted to occur.

5.4 Results

5.4.1. Measured Pit Stability Criteria

Both E_{rp} and $(i{\cdot}x)_{sf}$ were determined through successive lead-in-pencil measurements based on the procedure of Srinivasan *et al.*, while $\left(\frac{I}{r}\right)$ was calculated from $(i{\cdot}x)$ data[5,12,25,41] (**Table *5.1***). The first criterion, E_{rp}, is well known as a critical threshold for both pitting and crevice corrosion[22] and is applicable to predict the stability of all pit geometries. Conversely, the $(i{\cdot}x)$ stability criterion assumes a 1-D pit, and has been shown to be an accurate representation of the mass transport in a 1-D pit for pit depths x eight to ten times greater than r.[11] The last criterion, $\left(\frac{I}{r}\right)$, is an extension of $(i{\cdot}x)$ making it applicable to 3-D hemispherical pit geometries.[4,16–19]

As pitting can occur when a salt film is not present on the surface of the pit, $(i{\cdot}x)_{crit}$ can be calculated through the degree of pit solution saturation required to maintain stable propagation, *f*, through $(i{\cdot}x)_{crit} = f\,(i{\cdot}x)_{sf}$. The I_{LC} required for a pit of radius r to grow stably as a hemisphere, rather than a 1-D pit, can be calculated by,

$$I_{LC} = \left(\frac{I}{r}\right)_{crit} r = [3(i{\cdot}x)_{crit}]r \qquad 5.4$$

The calculation of I_{LC} is directly related to the pit stability product for a hemisphere, as described in Chen & Kelly.[27] That is, for a 3-D hemispherical pit, the pit stability product is defined as $\left(\frac{I}{r}\right)$, which can be related to $(i{\cdot}x)$ by a geometric factor of three.[4,16,17,19] Both the second and third criteria above represent the minimum current required to maintain a sufficiently low pH against dilution by diffusion.

Recent findings in literature have suggested that f is between 43% to 50%[22,26]; in this work, we will assume $f = $ 50% saturation unless otherwise noted. The measured $(i{\cdot}x)$ and calculated $\left(\frac{I}{r}\right)$ values for all pit stability criteria under full salt film conditions are shown in **Table *5.1*** and are consistent with values seen in literature.[21–23]

Table 5.1: Pit stability criteria for SS316 in 0.6 M NaCl and 3 M NaCl

Solution Concentration of NaCl [M]	E_{rp} [V_{SCE}]	$\left(\frac{I}{r}\right)_{sf}$ [A/m]	$(i{\cdot}x)_{sf}$ [A/m]
0.6	-0.218	2.7	0.9
3	-0.227	1.5	0.5

5.4.2. Potentiodynamic Scans

Anodic polarization scans were conducted on SS316 in 3 M and 0.6 M NaCl solution, while cathodic polarization data were generated in a NaBr solution equivalent to 3 M and 0.6 M NaCl solution in terms of diffusion-limited ORR kinetics, all at room temperature (Figure 5.3). Note that all potentials in this work are in reference to a saturated calomel electrode (SCE). Both cathodic and anodic curves had little distinction between the two environments, albeit with i_{lim} in 3 M NaCl being slightly lower (1×10^{-5} A/cm^2) in comparison to i_{lim} for ORR in 0.6 M NaCl (2×10^{-5} A/cm^2), as indicated in Figure 5.3. In this work, 3 M NaCl was the main solution of interest.

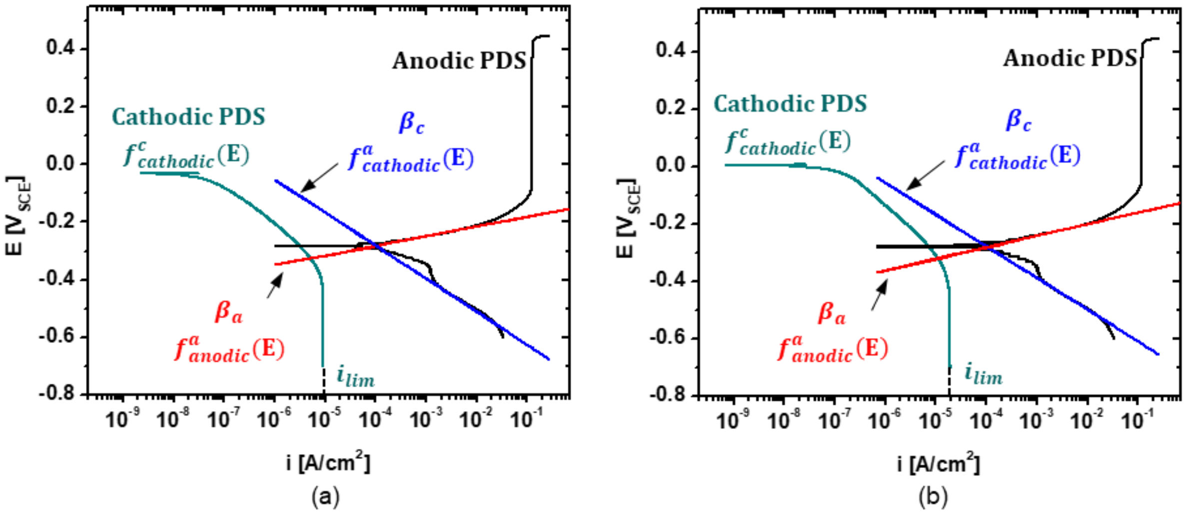

(a) (b)

Figure 5.3: Cathodic and anodic potentiodynamic scans of SS316 in (a) 3 M NaCl and (b) 0.6 M NaCl.

The anodic and cathodic Tafel slopes of the lead-in-pencil anodic polarization scans were determined to be 33 mV/decade and 115 mV/decade, respectively, in 3 M NaCl. Similarly, in the 0.6 M NaCl environment, anodic and cathodic Tafel slopes were determined to be 40 mV/decade and 110 mV/decade, respectively (Figure 5.3). Both anodic and cathodic Tafel slopes were imported into the model as boundary conditions on the active pit surfaces, for each respective environment, to account for localized cathodic reactions among the active pit dissolution (Figure 5.2). Reversible potentials were chosen at a constant exchange current density along the Tafel slopes, representing a computational limit rather than the true electrochemical parameters (Table 5.2). The cathodic polarization scans were used as boundary conditions on the large exterior surface in the system, which represented the main source of cathodic reactions (Figure 5.2).

Table 5.2: Computational input parameters

Solution [M]	Parameter	Description	Value
0.6	β_a	Anodic Tafel slope	40 mV/decade
	E_0^a	Anodic reversible potential	-0.368 V_{SCE}
	i_0^a	Anodic exchange current density	1.02×10^{-5} A/cm^2
	β_c	Cathodic Tafel slope	110 mV/decade
	E_0^c	Cathodic reversible potential	-0.036 V_{SCE}
	i_0^c	Cathodic exchange current density	1.02×10^{-5} A/cm^2
	κ_{bulk}	Bulk solution conductivity	5.5 S/m
3	β_a	Anodic Tafel slope	33 mV/decade
	E_0^a	Anodic reversible potential	-0.3157 V_{SCE}
	i_0^a	Anodic exchange current density	6.6×10^{-7} A/cm^2
	β_c	Cathodic Tafel slope	115 mV/decade
	E_0^c	Cathodic reversible potential	-0.1672 V_{SCE}
	i_0^c	Cathodic exchange current density	6.6×10^{-7} A/cm^2
	κ_{bulk}	Bulk solution conductivity	19.7 S/m
	κ_{pit}	Solution conductivity within a pit, assuming saturated metal salt film	21.8S/m

5.4.3. *Maximum Pit Model Construction*

To support dissolution of an active pit, I_{LC} and I_c^{ext} were calculated as a function of r, following the same procedure as Katona *et al.*.[23] Conditions representing 50% and 100% salt film were considered and compared in the I_{LC} calculations, although stability at 50% saturation was the main focus of this work. The intersection between the anodic and cathodic curves predicts the maximum size at which a pit can grow before repassivating as shown in Figure 5.4. In 3 M NaCl, r_{max} of a 3-D hemispherical pit is indicated by arrows for both 50% and 100% salt film conditions. Any combination of I_{LC} and I_c^{ext} that falls in the region bounded by the two currents, and below r_{max}, predicts stable pit growth. The hatched region represents stability if 50% saturation is required, while the cross-hatched region represents stability if 100% saturation is required, showing that less saturation results in both a greater r_{max} and greater stable region for pit growth (Figure 5.4(a)).

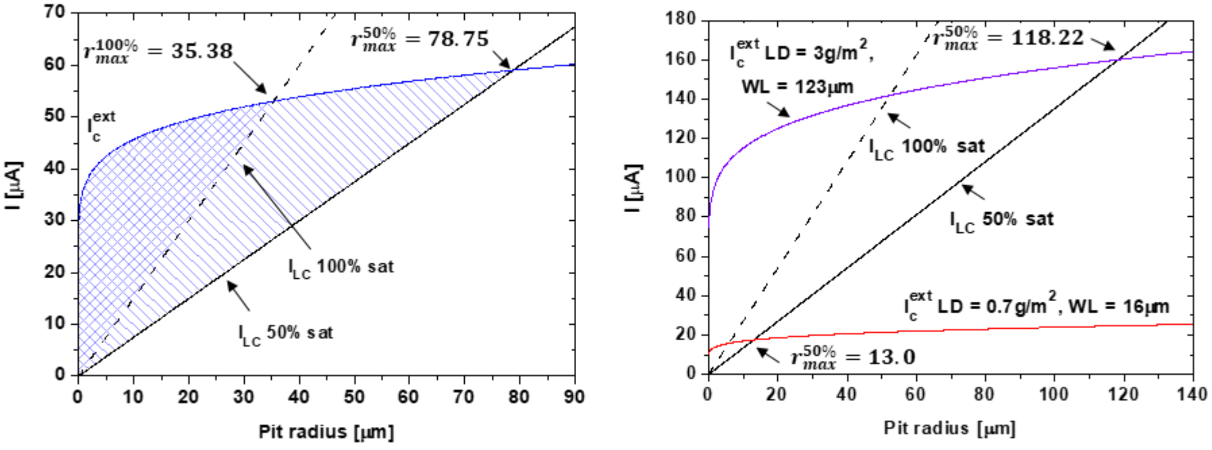

(a) (b)

Figure 5.4: Maximum pit model calculations for an environment of (a) 3 M NaCl, with WL = 16 μm, RH = 88.3%, and LD = 3 g/m^2 and (b) 0.6 M NaCl, with both the conditions of WL = 16 μm consistent with (a) and LD = 3 g/m^2 consistent with (a). Note the differences in the ordinate between (a) and (b).

Two NaCl concentrations, 3 M and 0.6 M, were considered to represent the equilibrium solution concentration at a RH of 88.3% and 98%, respectively (Figure 5.4). Changes to WL represented changes in LD while RH, κ, and by extension salt concentration were held constant, as described in Chen *et al.*.[42] Therefore, when comparing the 3 M NaCl and 0.6 M NaCl scenarios, one can consider that either the WL or the LD between them were the same, while the remaining parameter was independent. This difference can be seen in the 0.6 M NaCl cathodic current capacity (Figure 5.4(b)), in which the red curve represents a WL that is consistent with 3 M NaCl and the violet curve represents a LD that is consistent with 3 M NaCl. Choosing the consistent parameter can have large impacts on the maximum pit predictions, as denoted by $r_{max}^{50\%}$ salt film in Figure 5.4(b) (13 µm for LD = 0.7 g/m^2 and 118 µm for LD = 3.0 g/m^2). It is important to note that although $I_{\mathrm{c}}^{\mathrm{ext}}$ depends on environmental factors and cathodic kinetics, I_{LC} only depends on geometric factors of the pit and $(i{\cdot}x)$, as seen in Eq. 5.4.[27] Therefore, I_{LC} at both 100% and 50% salt film saturation does not change with WL or LD (Figure 5.4(b)).

5.4.4. Simple Hemispherical Pit Stability

The hemispherical pit was the first geometry of interest, as it represented a widely considered case in which the pit surface undergoes uniform dissolution and is a pore shape commonly seen in polished AM metals (Figure 5.1(a)).[43,44] The parameter r was varied from 15 – 500 µm in a 3 M NaCl environment, while WL was held constant at 16 µm and D was held constant at 15 cm. These combinations resulted in the cathode to anode surface area ratio ranging from 1.25×10^7 to 1.12×10^4.

The electrolyte potential distribution from a single 15 µm radius pit can be seen near the vicinity of the pit (Figure 5.5(a)) and spatially along the cathode radius to the pit mouth (Figure 5.5(b)). To easily visualize the potential distributions over the entire parameter space tested, the potentials at three different points in the geometry were extracted as a function of r (Figure 5.5(c)). These points were at the base of the pit (E_{base}), the mouth of the pit (E_{mouth}), and the farthest edge of the cathode from the anode (E_{edge}), as indicated in Figure 5.5(a). Note that due to the extreme aspect ratio of the geometry, the true edge of the cathode is not visible in Figure 5.5(a); however, the black point of E_{edge} is included for symbolic reasons. Physically, the potential at the edge of the cathode cannot exceed the open circuit potential of the cathode ($E_{\mathrm{OCP}}^{\mathrm{cath}}$). That is, the inequality $E_{\mathrm{edge}} < E_{\mathrm{OCP}}^{\mathrm{cath}}$ must be valid at all points in the system to be physically attainable. To maintain pit stability, the potential at the mouth of the pit must be greater than the E_{rp}, as described in the first stability criterion. Therefore, E_{OCP}^{cath} and E_{rp} were included in Figure 5.5(c) as an upper and lower bound to maintaining stable pit growth. All potentials decreased with increased r values. From the intersection of E_{mouth} and E_{rp}, as indicated by a circle in Figure 5.5(c), radii less than 420 μm were predicted to be stable under the given set of conditions.

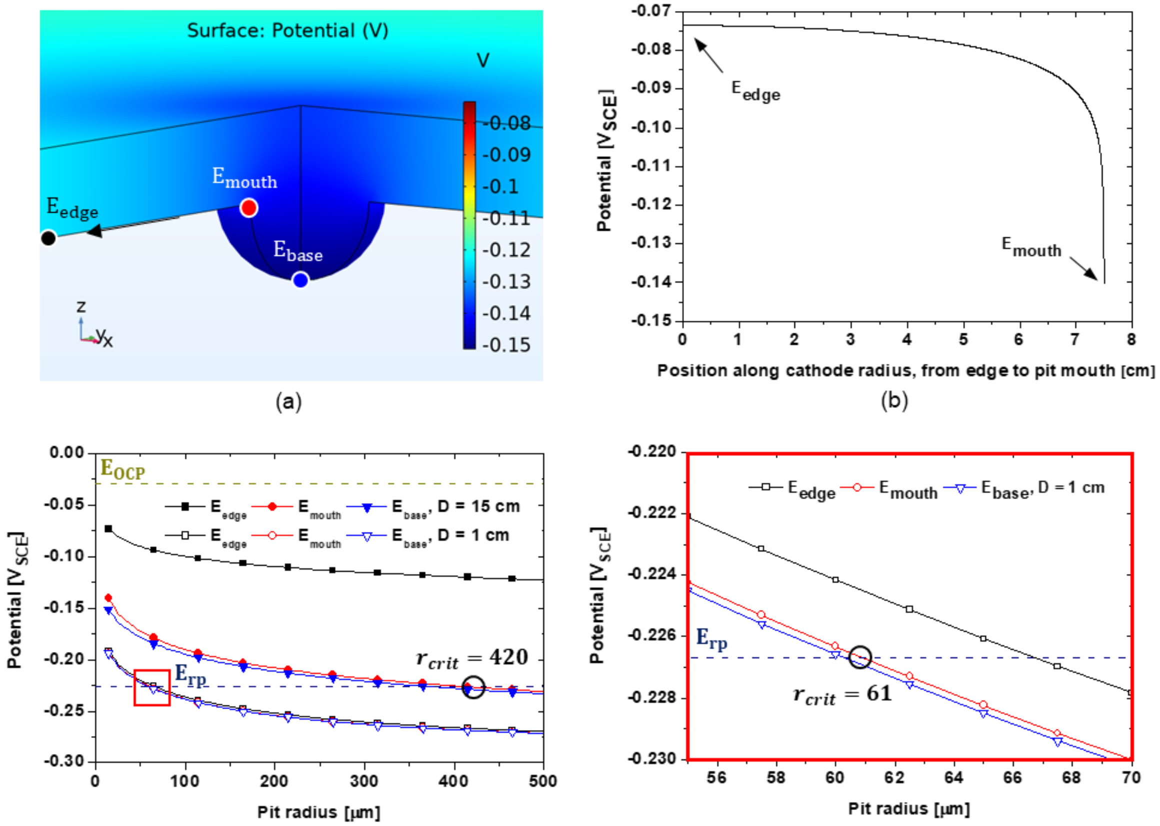

(a) (b)

(c) (d)

Figure 5.5: 3 M NaCl hemispherical pit, WL = 16 μm, D = 15 cm; (a) 270° volumetric potential distribution at r = 15 μm; potential distribution as a function (b) spatially along the cathode to the pit mouth, and (c) of r; (d) inset of (c) showing a close-up of the potential distribution with D = 1 cm. Note the blue, red, and black spheres in (a) represent the points at which the potential was calculated in (c) and (d).

The cathode was decreased in size to D = 1 cm (open symbols), and two main differences in the potential distribution were observed (Figure 5.5(c)). First, the ohmic drop became nearly negligible, with a maximum of 5 mV difference between E_{edge} and E_{base} along all r values tested. Second, all potentials within the system were more negative in value, indicating that the smaller cathode size was not able to polarize the pit to the degree of the larger cathode size. This lack of polarization lowered the critical radius for stable growth (r_{crit}) from 420 μm to 61 μm as indicated in Figure 5.5(d).

The current density distribution along the same hemispherical pit surface with r = 15 μm can be seen in Figure 5.6(a). The total anodic current was determined by integrating the current density over the active anodic surface area. Results were then overlaid on the maximum pit model for 3 M NaCl as a function of r, to compare the FEM results with the predicted stability of the third criterion, $\left(\frac{\mathrm{I}}{\mathrm{r}}\right)_{\mathrm{FEM}} > \left(\frac{\mathrm{I}}{\mathrm{r}}\right)_{crit}$. These results are the curves labeled with the different diameters. The calculated current from the FEM model (I_{FEM}) predicted active pit growth for r < 25 μm, when under 50% saturation for a constant WL = 16 μm and D = 15 cm (Figure 5.6(b)). The impact of deviations of D both above and below the 15 cm baseline were calculated, and these led to proportional changes to both I_{FEM} and r_{crit}, indicating that a larger cathode size produces the highest current and the most stable pits via the largest r_{crit} (Figure 5.6(b)).

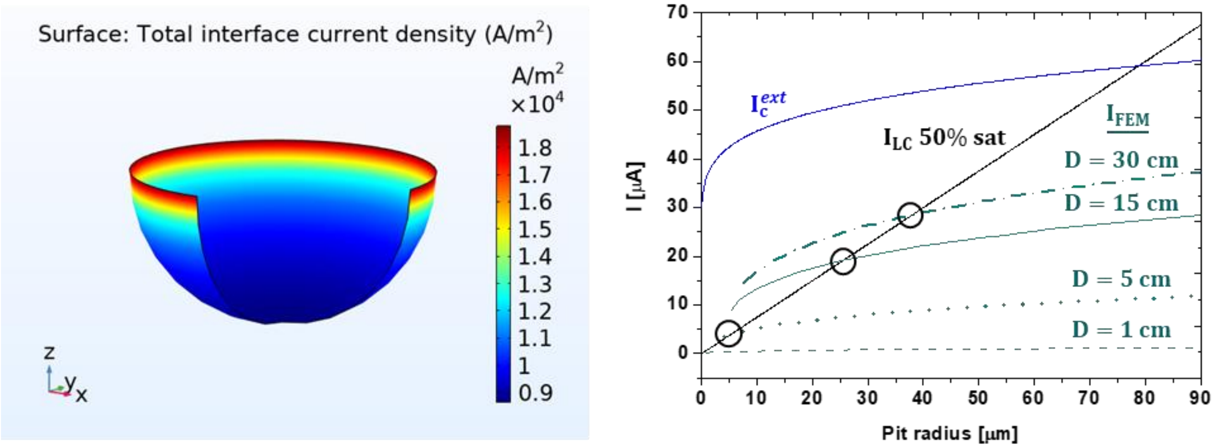

(a) (b)

Figure 5.6: 3 M NaCl hemispherical pit, WL = 16 μm, D = 15 cm; (a) 270° current density surface at r = 15 μm; (b) I_{FEM} as a function of r with the maximum pit model

Note the difference between I_{FEM} and I_c^{ext}. The higher values of I_c^{ext} are due the ideal cathode assumption, whereas the FEM assumes a more-realistic cathode which accounts for the spatial distribution of the current. Consequences of this assumption will be discussed in detail in a later section.

Raising the WL to 150 μm, while holding the remaining parameters above constant, resulted in an increased r_{crit} based on FEM from 25 to 91 μm (Figure 5.7(a)). This analysis was extended to a variety of WL ranging from 10 – 500 μm. At a constant D = 15 cm, I_{FEM} from a 3 M NaCl hemispherical pit was plotted as the 3-D surface corresponding to combinations of r and WL (Figure 5.7(b)).

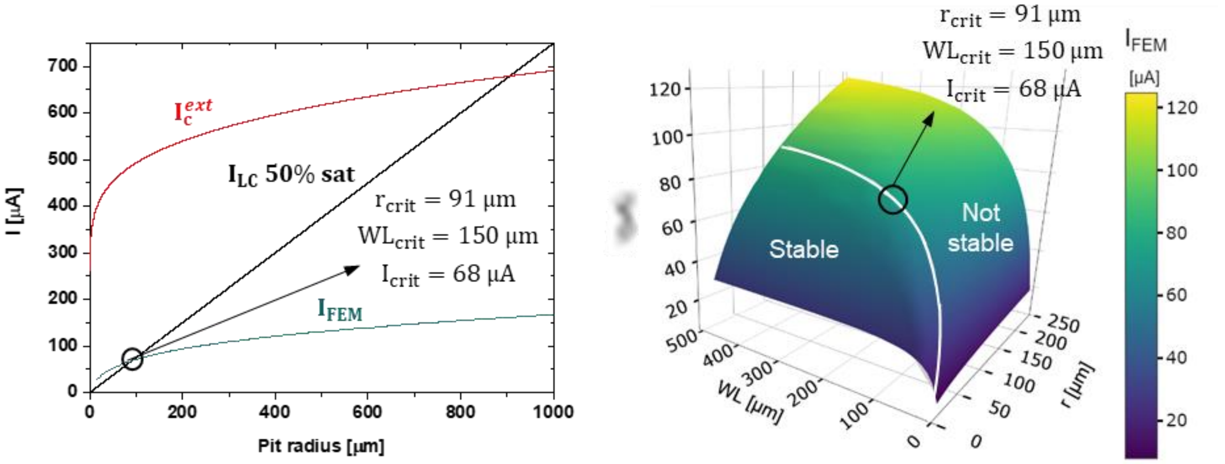

(a) (b)

Figure 5.7: 3 M NaCl hemispherical pit, D = 15 cm; (a) I_{FEM} at WL = 150 µm as a function of r with the maximum pit model; (b) I_{FEM} as a function of WL and r. Note the circle in (a) and (b) represents the same critical triple points in both plots.

The peak current appears in the top corner of the plot, indicating that the current is proportional to both WL and r. The critical values at 50% salt film saturation which predict the transition from stability to repassivation are plotted as a white line over the contour plot. Each point along this line represents a combination of r_{crit}, $\mathrm{WL}_{\mathrm{crit}}$, and I_{crit} at which stability of a pit will occur within a 3 M NaCl environment. At a WL of 150 µm, I_{crit} and r_{crit} were seen to be 68 µA and 91 µm, respectively (Figure 5.7(a)). This triple point along the white line is denoted as a circle in Figure 5.7(b).

To more thoroughly study the effects of D, the parameters r and WL were held constant at 15 µm and 16 µm, respectively, while the diameter range probed was from 1 to 50 cm, affecting the cathode-to-anode surface area ratio by four orders of magnitude. The potential distributions (E_{edge}, E_{mouth}, and E_{base}) diverged at large D values, as shown in Figure 5.8(a), indicating that the ohmic drop was impacted to a greater extent by variations in the cathode geometry in contrast to the pit geometry. The increase in all potentials at larger D implies that pits will be less stable (more likely to repassivate) at small D values, although in the range of parameters tested, E_{rp} did not predict the repassivation of any pits (Figure 5.8(a)).

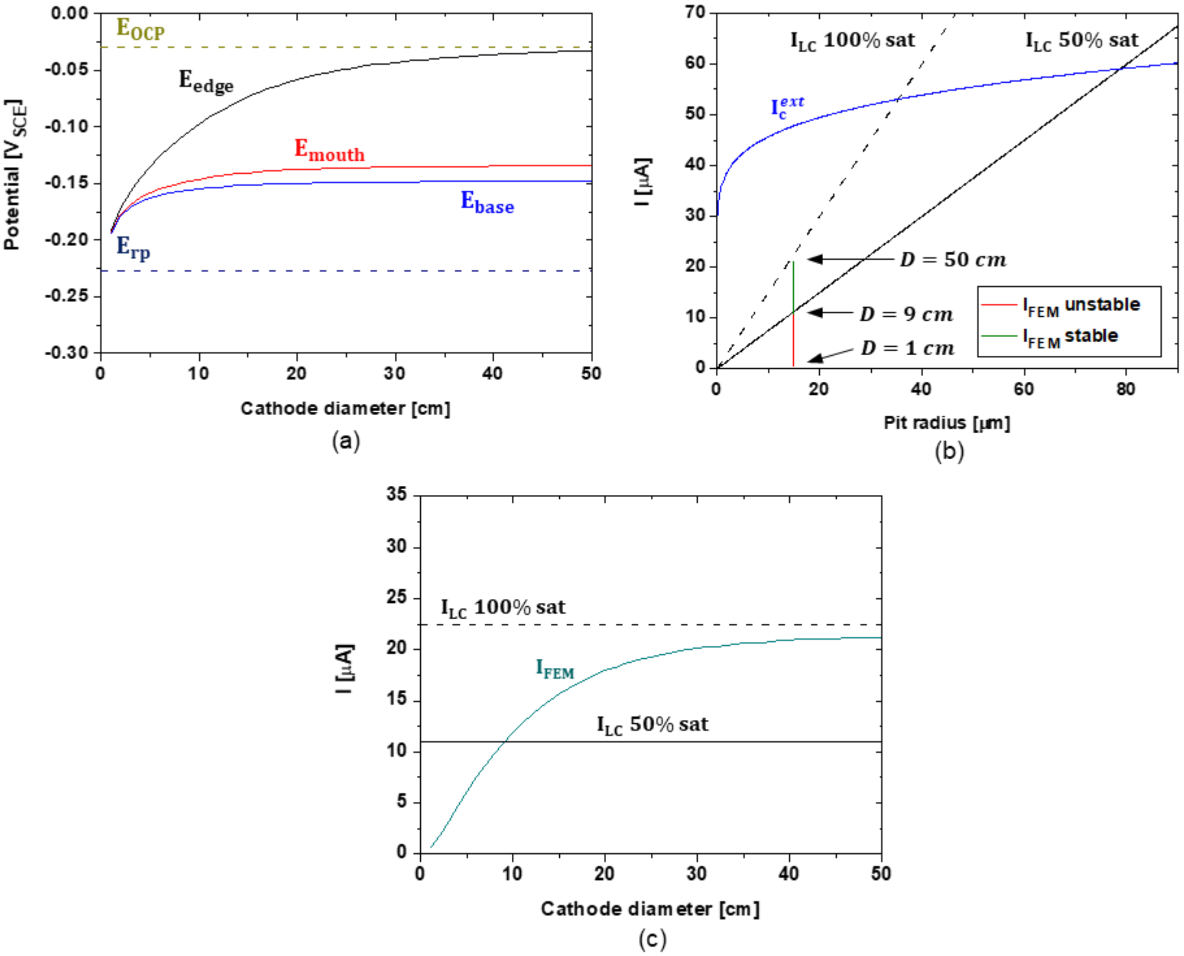

(a)

(b)

(c)

Figure 5.8: 3 M NaCl hemispherical pit, r = 15 μm and WL = 16 μm; (a) potential distribution as a function of D; (b) I_{FEM} as a function of r with the maximum pit model; (c) I_{FEM} as a function of D.

The maximum pit model and I_{FEM}, derived for the same environmental conditions, were plotted for a constant r and WL (Figure 5.8(b)). At D < 9 cm, all pits were predicted to repassivate. As D increased, I_{FEM} also increased, passing through I_{LC} 50% saturation at D = 9 cm, but falling just short of I_{LC} 100% saturation. Although it may seem that D > 50 cm would continue this rising current trend, instead I_{FEM} is seen to be asymptotically approaching I_{LC} 100% saturation (Figure 5.8(c)). At large D values, $\mathrm{E}_{\mathrm{edge}}$ quickly approaches $\mathrm{E}_{\mathrm{OCP}}^{\mathrm{cath}}$, signifying that the cathode is exhausting nearly all of its available current (Figure 5.8(a)). Therefore, in this scenario, if 100% saturation was needed for stability, even an extremely large cathode with finite kinetics used in this work would not be able to consume enough current to achieve stability.

The impact of varying WL and D with a constant r of 15 µm was also investigated. A contour plot was used to visualize the 3-D data, with the I_{FEM} color bar describing the pseudo z-axis contours. As before, the white line represented the set of critical triple points at which stability at 50% saturation was achieved (Figure 5.9(a)).

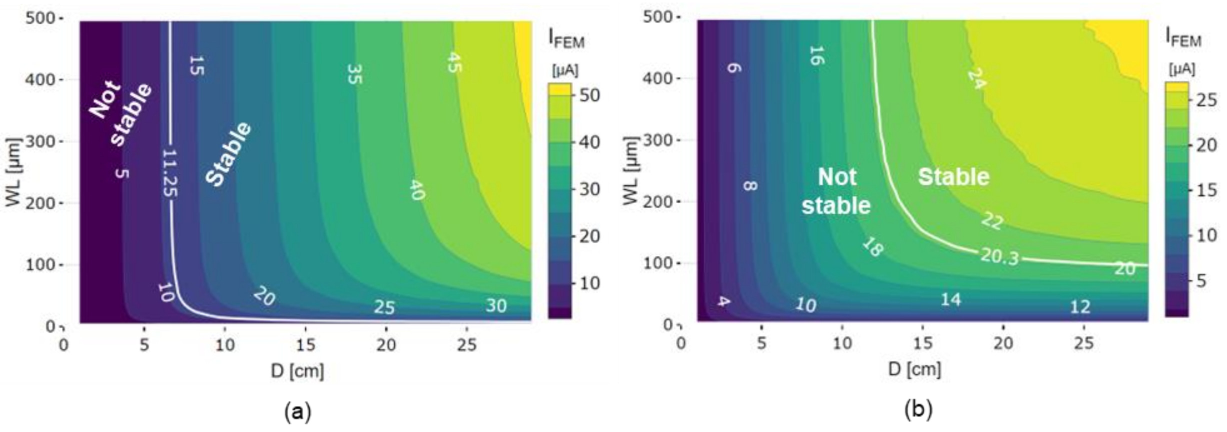

(a)

(b)

Figure 5.9: I_{FEM} as a function of WL and D for a hemispherical pit, r = 15 µm in (a) 3 M NaCl and (b) 0.6 M NaCl.

The pit solution was changed to 0.6 M NaCl, and identical simulations regarding the WL and r parameter space were conducted. There were two important distinctions between the trends seen in 3 M NaCl and 0.6 M NaCl. First, the stable region, as indicated to the right of the critical white line, is smaller in the less concentrated solution. Second, at all parameters tested, I_{FEM} was also lower in this solution for all D and WL (Figure 5.9(b)).

5.4.5. Simple Rectangular Pit Stability

In a 3 M NaCl solution, the stability of a rectangular pit (Figure 5.1(b)) was investigated as a function of both WL and x. For consistency, r and D were held constant at 15 µm and 15 cm, respectively. To have true 1-D diffusion, it is known that x must be about ten times larger than r.[45] In the given scenario, this constraint bounds x to values larger than 150 µm. Despite this apparent limitation, a benefit of the FEM model is the ability to go beyond what may be physical constraints. Therefore, the range of pit depths tested was from 1 to over 43 times the radius of the pit.

Galvele's $(i \cdot x)$ was utilized as the stability criterion to account for the new pit dimensionality. Therefore, contours of the calculated current density multiplied with the varied pit depth, rather than the total current, were plotted as a function of WL and x (Figure 5.10). In this way, $(i \cdot x)_{\mathrm{crit}}$ follows a singular contour line of 0.25 A/m. To better visualize the white stability line representing the triple points of $\mathrm{WL}_{\mathrm{crit}}$, x_{crit}, and $(i \cdot x)_{\mathrm{crit}}$, a magnified portion of the contour plot was inlaid. The majority of the selected parameter space predicted a stable growing pit. Repassivation was only achieved at extremely low WL and x; far below what is accepted as 1-D behavior (Figure 5.10).

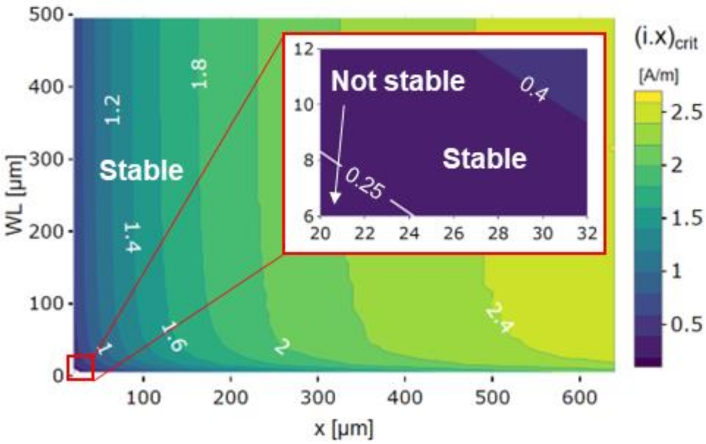

Figure 5.10: $(i{\cdot}x)_{\text{crit}}$ stability as a function of WL and x for a rectangular pit, r = 15 μm and D = 15 cm in 3 M NaCl.

5.4.6. Geometrically Complex Pit Stability

The geometries within the model were modified to represent irregular, but realistic, pits. In all scenarios going forward, only a 3 M NaCl environment was considered, as it was determined in the previous section to produce the most stable pits. As each parameter was varied, the other parameters were always held constant at r = 15 μm, WL = 16 μm, and D = 15 cm, unless otherwise noted.

A pit-within-a-pit was built, as one step towards increasing the complexity relative to the simple hemispherical geometry (Figure 5.1(c)). This simulation represents a new pit growing in a region where a previously active pit has repassivated, creating a deeper overall pit depth. Only the secondary pit had active anodic surfaces, with $r_{secondary} = 0.5(r_{primary})$; both pit radii were changed with respect to this relationship. When the "pit radius (r)" is referenced in this geometry, it is referring to the opening of the primary pit unless otherwise noted.

At a constant r = 15 µm, the potential distribution within the double pit is shown in Figure 5.11(a). Colored dots represent the points at which the potential was extracted as r was increased from 15 to 150 µm. The potential distributions from the simple hemispherical pit as a function of r were included as dotted lines to easily compare the different geometries. Results indicated that the double pit geometry had negligible effects on E_{edge} and E_{base} in comparison to the hemispherical geometry (Figure 5.11(b)). However, E_{mouth} was much more positive in the double pit than the simple hemispherical geometry. This result is likely due to the primary pit not being active, and therefore the smaller secondary pit being polarized by the cathode to a higher potential. The maximum pit model and I_{FEM} were plotted with the radius of the complex geometry being with respect to the secondary pit (Figure 5.11(c)). When plotted in terms of the radius of the secondary pit, the pit stability, as determined by $\left(\frac{I}{r}\right)_{crit}$, was identical to that of a hemispherical pit of the same radius.

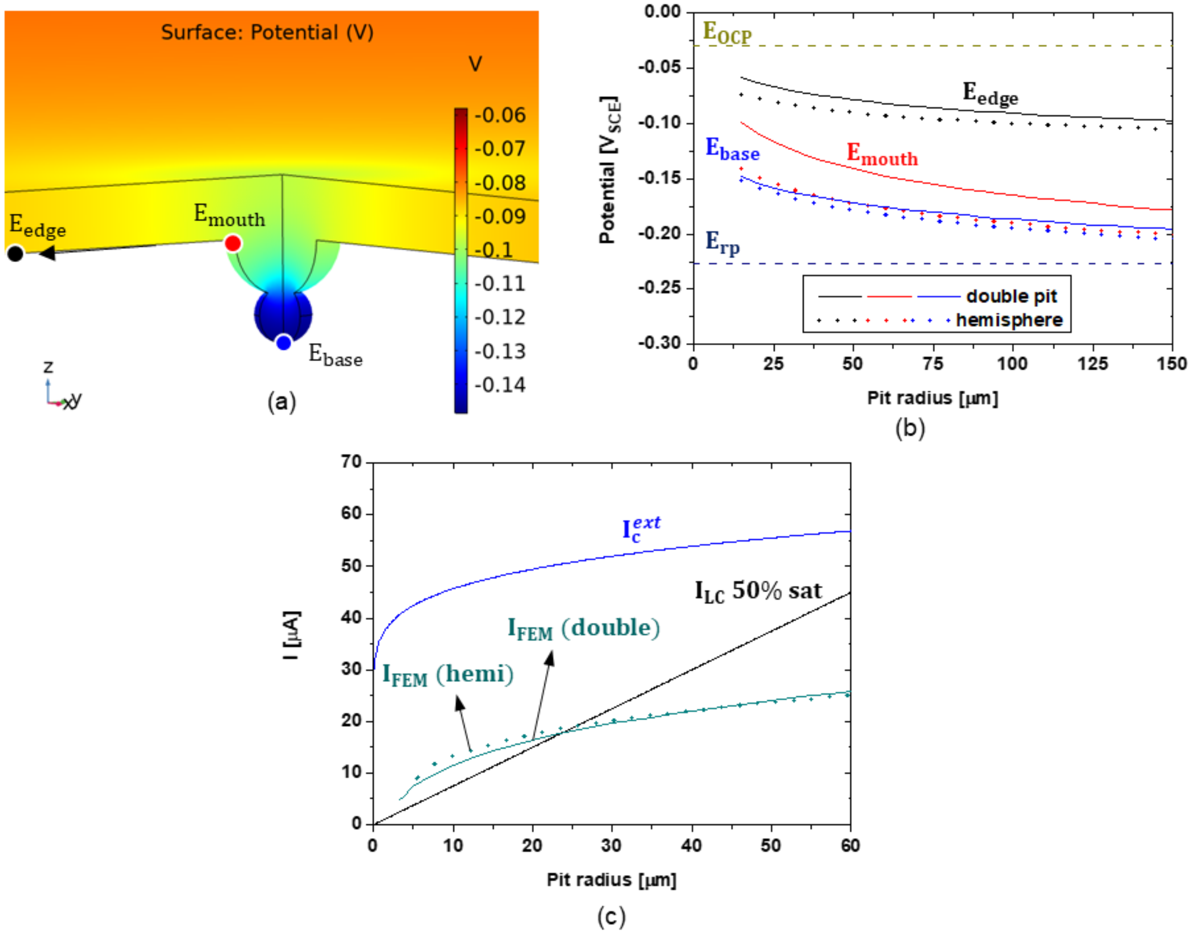

Figure 5.11: (a) Potential distribution in a double pit, WL = 16 μm, r = 15 μm , and D = 15 cm; (b) comparison of potential distribution between simple hemispherical pit and complex double pit; (c) I_{FEM} as a function of r for hemisphere and double pit geometries, with the maximum pit model. Note the blue, red, and black spheres in (a) represent the points at which the potential was calculated in (b).

Lastly, the undercutting pit geometry was considered to represent a pit that initiated in a hemispheric geometry but subsequently propagated underneath the surface (Figure 5.1(d)). Particular portions of the pit surface were defined to be anodically active while other regions within the pit were defined as inert. The regions were defined by red bisectors and were labeled numerically in Figure 5.12(a). Note that the different numerical regions of the pit had different surface areas. Again, the correlative hemispherical pit results were included as hollow points, for comparative purposes (Figure 5.12(b), (c), and (d)).

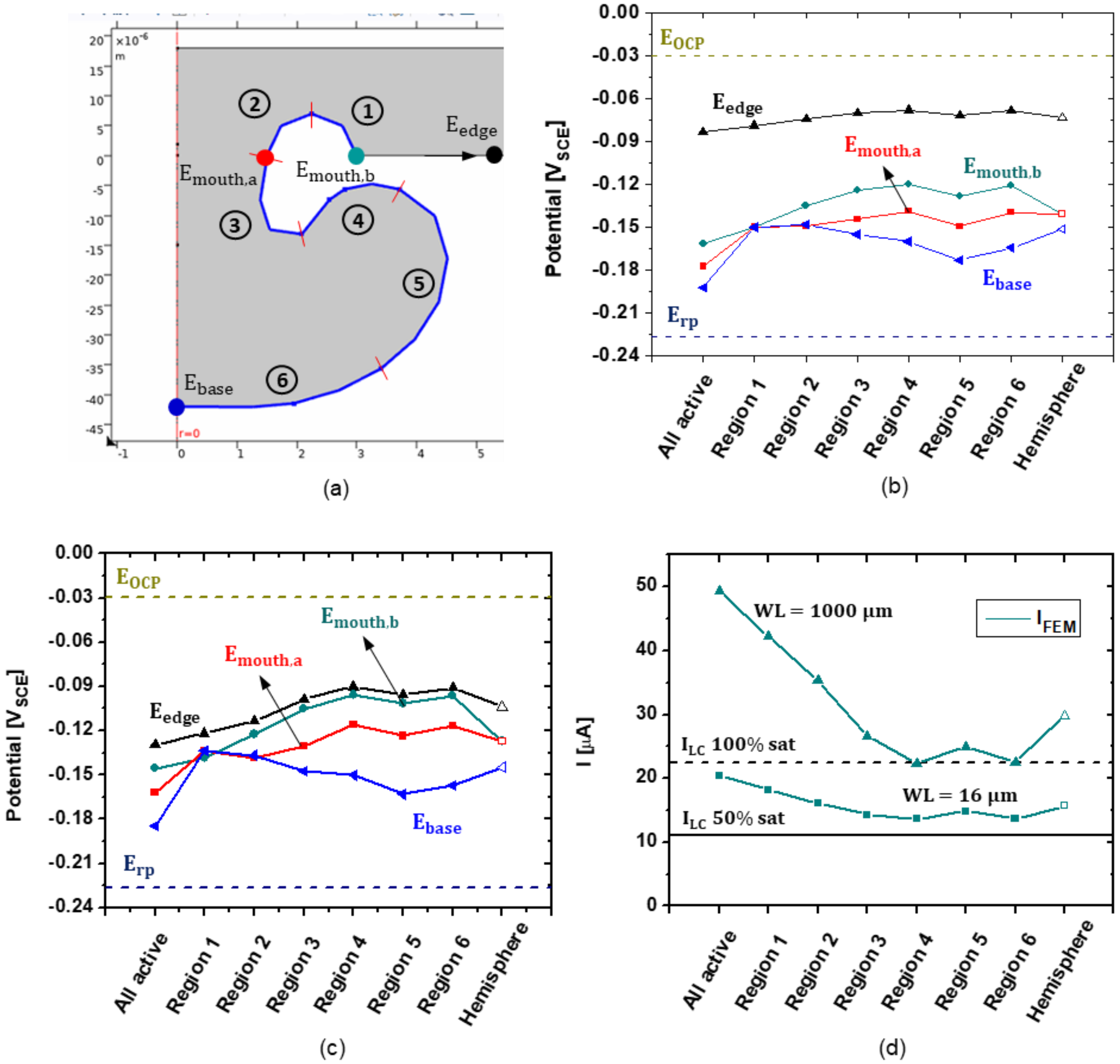

Figure 5.12: (a) Graphical illustration of different regions in undercut pit, along with points at which the potential was calculated; (b) potential distribution in undercut pit, WL = 16 µm, r = 15 µm , and D = 15 cm; (c) potential distribution in undercut pit, WL = 1,000 µm, r = 15 µm ,

and D = 15 cm; (d) I_{FEM} from different regions active within the undercut pit compared with maximum pit stability predictions for 50% and 100% saturation. Note the blue, red, teal, and black spheres in (a) represent the points at which the potential was calculated in (b).

The potential distributions between these different regions were evaluated at a r, and D, with WL = 16 µm in Figure 5.12(b) and WL = 1,000 µm in Figure 5.12(c). All potentials fell within the bounds of $\mathrm{E}_{\mathrm{OCP}}^{\mathrm{cath}}$ and E_{rp}, indicating that the first criterion would predict all stable pit propagation for the given parameters. In the thin WL system, there were not any large fluctuations in $\mathrm{E}_{\mathrm{edge}}$ between any of the scenarios tested, despite the nearly 50 mV available in the system before reaching $\mathrm{E}_{\mathrm{OCP}}^{\mathrm{cath}}$ which would indicate that the cathode was not at its full capacity to polarize the pit. In comparison, $\mathrm{E}_{\mathrm{edge}}$ was very dependent on the location of the active regions when in a bulk WL = 1,000 µm.

At two constant WL of 16 and 1,000 µm, I_{FEM} was compared with $\left(\frac{I}{r}\right)_{crit}$ and $\left(\frac{I}{r}\right)_{sf}$ (Figure 5.12(d)). As seen previously, a larger WL (1,000 µm) increased I_{FEM}, which in turn increased the stability, even to the point of satisfying I_{LC} 100% saturation in this scenario. However, the jump in pit stability was much more dramatic when external regions (such as regions 1 and 2) were active. Conversely, there was a minimal increase in stability when more occluded regions were active, such as regions 4, 5, and 6. When active, region 3 appeared to have the best resemblance to the hemispherical pit, in both the potential distribution and current. As the depth of the active region was very similar to that of the hemisphere, the resulting ohmic drop was nearly identical as well.

5.5 Discussion

5.5.1. Importance of Choosing Pit Stability Criteria

Three stability criteria were investigated in this work: E_{rp}, $(i{\cdot}x)$, and $\left(\frac{I}{r}\right)$. All criteria describe a threshold for reaching and maintaining a critical solution chemistry required for stable pit growth albeit from two perspectives. Considered to be the lowest potential at which a critical chemistry at the pit mouth can be maintained, E_{rp} indicates that any polarization above this point would result in nucleation and growth of pits.[5] Experimental measurements have found that E_{rp} decreases with increasing pit depth, until reaching a plateau at sufficiently deep pits which is considered the "true" E_{rp}.[22] The $(i{\cdot}x)$ approach instead focuses on the accumulation of complexed salts and acid as corrosion by-products, which form at the base of the pit. Only once a critical fraction of species has been reached, can pits maintain their chemistry against the natural diffusional outflow of the pit. Recent experimental and computational data have found that the critical saturation required (f) is about 50% that of a fully saturated and formed salt film.[22,26] A mathematical maximum pit model takes into account both of these stability criteria to determine the size of an ideal, maximum pit, where $I_{\mathrm{c}}^{\mathrm{ext}} = I_{\mathrm{LC}}$. The value of $I_{\mathrm{c}}^{\mathrm{ext}}$ takes into account E_{rp}, while $(i{\cdot}x)$ is used to calculate I_{LC}.

In this work, E_{rp} and $(i{\cdot}x)$ are compared separately to data calculated through the FEM model. A comparison of E_{mouth} with E_{rp} was conducted to assess the first stability criterion. To isolate Galvele's $(i{\cdot}x)$ criterion in the maximum pit model, the simulated data were compared to I_{LC} only. Therefore, I_{LC} 50% saturation correlates directly to $\left(\frac{I}{r}\right)_{crit}$, the third stability criterion. It was determined that the stability from both criteria scaled directly with WL and D, and inversely with r and x (Figures 5 – 10). For example, large r values are more likely to repassivate due to the potential distributions approaching E_{rp} as r increases (Figure 5.5(c)). A similar result is seen when comparing the current with the second stability criterion, such as in Figure 5.7(b). Any combination of parameters to the left of the white line (such as small r values) would predict a stably propagating pit, whereas any combination of parameters to the right of the white line (such as large r values) would predict pit repassivation, for a given D (Figure 5.7(b)). However, when WL and D were concurrently changed (Figure 5.9(b)), parametric combinations to the left of the critical white line (such as small D and small WL) predicted repassivation while combinations to the right of the white line (such as large D and large WL) predicted stable growth. Experimental results from literature confirm that larger WL (200 – 400 μm) are more favorable for stable pit growth, whereas smaller WL (5 – 10 μm) require a higher chloride concentration before stability can occur.[46] The same methodology as above can be applied to Figure 5.10 to see the correlation with pit stability and x.

Note also a distinction in the critical white line between Figure 5.7(b) and Figure 5.9. Because I_{LC} 50% saturation is dependent on the pit geometry, *i.e.* I_{crit} changes at each new r, the white line is not parallel to the current contours in Figure 5.7(b). However, the critical white line follows the contours in Figure 5.9(a), rather than going across them. This trend derives from the fact that I_{LC} 50% saturation is *independent* of both WL and D. That is, the $\left(\frac{I}{r}\right)_{crit}$ criterion is constant for these parameters. As each of the contours represents a constant current value, it follows that I_{crit} would also abide by the contours.

Although the two stability criteria had similar correlations with the parameters of interest, that is where the commonalities ended. The $\mathrm{E_{rp}}$ criterion predicted much larger r_{crit} values when compared to the 3-D pit stability criterion. At a constant D and WL of 15 cm and 16 μm, respectively, $\mathrm{E_{rp}}$ predicted r_{crit} to be 420 μm (Figure 5.5(c)), whereas $\left(\frac{I}{r}\right)_{crit}$ predicted r_{crit} to be

25 µm (Figure 5.6(b)). Under the same set of conditions, the maximum pit model approximated $r_{max}^{50\%}$ = 78.75 µm through utilization of *both* stability criteria (Figure 5.4(a)). This result places $r_{max}^{50\%}$ between the critical radii calculated from each stability criterion alone, although not equidistant. However, the maximum pit model provides the theoretical limit for cathodic current capacity, implying that there can be no pits greater than $r_{max}^{50\%}$ at a given set of conditions. As the geometric parameters were all consistent through the calculations, there are only two parameters to consider which may be incorrect, 1) the critical percent saturation chosen, or 2) the repassivation potential. To reconcile the predicted r_{crit} value from the two stability criteria using the critical percent saturation, it was calculated that the solution would only need to be 7% saturated, rather than the 50% saturation used in this work. However, assuming instead that the percent saturation was correct, an E_{rp} = -0.154 V_{SCE} would be required to reconcile the predicted r_{crit}.

The considerably large discrepancy in pit stability as calculated through E_{rp} and $\left(\frac{I}{r}\right)_{crit}$ persisted throughout all parameter space tested, although the difference was not consistent. In Figure 5.6(b), D was lowered from 15 cm to 5 cm, resulting in a 79% decrease in r_{crit} as predicted by $\left(\frac{I}{r}\right)_{crit}$. The potential distribution was also calculated with the parameters above and r_{crit} as defined by $E_{mouth} > E_{rp}$ was seen to decrease by 41%. These results signify that the $\left(\frac{I}{r}\right)_{crit}$ criterion is more sensitive to parametric changes than the E_{rp} criterion. Note that in the pseudo 1-D pit, both E_{rp} and $(i \cdot x)_{crit}$ predicted stable growth in nearly all scenarios, preventing a comparison of the two criteria.

5.5.2. Consequences of an Ideal Cathode Assumption

A common method of studying pitting in materials is through the use of potentiostatic holds, in which increased currents directly correlate to metastable (if transient spikes) or stable pit initiation/growth whereas a sharp decrease to the current indicates repassivation.[4,6,47,48] Although useful in extracting pit kinetics over a wide range of potentials, potentiostatic conditions imply an infinite cathode in which pits are only limited anodically; this condition is often not seen in service. To attain the most realistic measurements, the material of interest should be at open circuit conditions where the conservation of charge applies, usually expressed as $\sum I_\mathrm{a} = \sum I_\mathrm{c}$. Under these conditions, the total anodic current (I_a) comes from the pit(s) with a small contribution from the surrounding passive surface while the cathodic current (I_c) is a combination of the external cathodic reaction occurring on the surfaces surrounding the pit and local cathodic reactions within the pit itself.[30] As both the anode and the cathode are finite, either can act as the limiting factor in stifling pit growth.

The maximum pit model takes one step towards modeling a more realistic cathode by including both anodic and cathodic limitations in pit development.[27] One of the main assumptions of the maximum pit model is that all positions along the cathode provide a constant current density, determined by integrating the cathodic polarization from $\mathrm{E}_\mathrm{OCP}^\mathrm{cath}$ to E_rp. As stated previously, this idealized, equivalent cathode assumption provides a theoretical limit of cathodic current and allows for the calculation of r_max for a given set of environmental conditions. To gain information on pits that are not at their theoretical limit, a spatial distribution of current density is needed, with the peak current density expected to be nearest to the pit mouth.

Rather than assuming either an infinite or an ideal cathode, this work aims to describe a realistic cathode in a pitting scenario in which the current density is not constant with position. The potential along the cathode was also not assumed to be constant, but rather the gradient between the less-negative cathode edge and more-negative pit mouth was calculated (Figure 5.5(b)). Experimentally determined PDS were used as boundary conditions for both the cathode and the anode, to capture the active kinetics which take place during the pitting process. To estimate the level of conservatism that comes with an ideal cathode assumption, r_{crit} (as calculated through the FEM model in this work) and r_{max} (as calculated from the maximum pit model) were compared.

At a variety of different D values, r_{crit} was calculated via FEM in 3 M NaCl for a constant WL of 16 µm (Figure 5.13). That is, r_{crit} was determined through the same procedure as described for Figure 5.6(b). The predicted $\mathrm{r}_{\mathbf{max}}^{\mathbf{50\%}}$ under the same conditions as above was included in the plot as a horizontal line, though the maximum ideal cathode (D_{max}) for these conditions is predicted to be 12.8 cm. Although the FEM model simulated D values out to 65 cm, nearly 5 times of that needed by an ideal cathode, r_{crit} never reached the predicted r_{max} but instead plateaued at $D \approx 45$ cm (Figure 5.13). This result suggests that the theoretical estimate of r_{max} is conservative by about a factor of 2 under these conditions. Interestingly, a similar comparison between the maximum pit model and outdoor exposure testing on SS316 is seen in literature.[27] Although the experimental exposures of pit depth varied with location and exposure time, a comparison of the averaged exposure values with r_{max} calculation also demonstrates the maximum pit model overestimating the experimental results by a factor of two.[27]

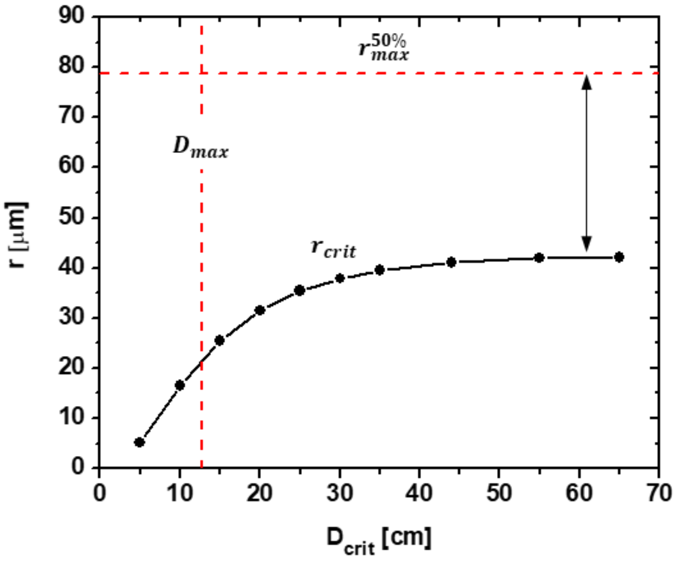

Figure 5.13: Critical hemispherical pit radius as a function of critical cathode radius, with WL = 16 µm, as calculated via the FEM model using $\left(\frac{I}{r}\right)_{crit}$ as the pit stability criterion, in 3 M NaCl; the horizontal red dashed line represents r_{max} at 50% saturation in the same conditions, while the vertical red dashed line represents D_{max}, as predicted by the maximum pit model.

Another interesting point is the extreme size required for a realistic cathode to achieve its full current capacity. The maximum pit model predicts that if a cathode was perfectly consuming all of the available current from one single r = 15 µm pit, the cathode diameter D would only need to be 12.8 cm for a WL = 16 µm. However, a 12.8 cm realistic cathode does not behave ideally, as evident by the lack of polarization of E_{edge} at D = 12.8 cm (Figure 5.8(a)). Not until D values of nearly 45 cm is the entire current capacity being used, and even at these large dimensions the total current is nearly 50% less than the predicted current from a 12.8 cm idealized cathode as stated above (Figure 5.8(b)). That is to say, the FEM model predicts D = 45 cm is needed to provide the full current capacity to one pit. This prediction assumes that no other pits are present within this diameter, as then the cathode current would be shared among all active pits. Experimentally, however, Budiansky et al. have shown that pits interact and form clusters on a SS316 surface at much smaller size scales.[49] Furthermore, experimental samples used to study pitting behaviors usually range from 10's of µm-sized wires to planar samples on the mm-scale.[4,6,11,12,49,50] The results from this work indicate that those sample sizes will not be able to provide the maximum amount of available current under open circuit conditions, which may underpredict the worst-case pitting scenario. An additional challenge to achieving these values of D in service is the low probability that a WL of 16 µm would be maintained over such a large distance.

5.5.3. Environmental Influences on Pit Stability

Pit stability in different environments has been widely studied, varying from different aggressive solutions[6,7,13,21–23,27,28,33] and temperature impacts[13,23,51], to a variety of WL[28,46,50]. This work conducts an initial analysis of environmental impact by extending the current framework to a lower chloride concentration and a 500 µm range of WL.

A decrease in stability occurred when the chloride concentration was decreased from 3 M NaCl to 0.6 M NaCl, representing an increase in equilibrium RH of 88.3% to 98%, respectively (Figure 5.9). Multiple factors contributed to this reduction of stability. When maintaining a constant WL and transitioning from a solution of 3 M NaCl to 0.6 M NaCl, an increase in $\left(\frac{I}{r}\right)_{crit}$ occurs, from 0.75 A/m to 1.35 A/m, respectively, as inferred from **Table *5.1***. Correspondingly, r_{max} is lowered under these conditions, as both $I_{\mathrm{c}}^{\mathrm{ext}}$ and I_{LC} are dependent on the chloride concentration (Figure 5.4). This direct correlation between r_{max} and chloride concentration at a constant temperature is consistent with what has been seen in literature.[23]

A decrease in I_{FEM} was seen in 0.6 M NaCl, making it more difficult to achieve the higher $\left(\frac{I}{r}\right)_{crit}$ threshold, thereby lowering the stability (Figure 5.9). Although a difference in kinetics is usually the main culprit when impacting the current within a constant geometry, in this scenario that was not the case. The PDS revealed very similar kinetics behavior between the two environments, with only a 7 µA/cm^2 difference between the galvanic coupling currents for a 1:1 cathode-to-anode area ratio (Figure 5.3). However, κ_{bulk} between the 3 M NaCl and 0.6 M NaCl solutions differed by 14 S/m, (a factor of 3.6), indicating that the decreased I_{FEM} was due to increased ohmic drop rather than slow kinetics. This result highlights the impact that κ_{bulk} can have on the stability of a pit, and is consistent with Katona *et al.*'s finding that lower conductivity solutions ($MgCl_2$ in contrast to NaCl) decrease the severity of pitting.[52]

Variations in WL were also investigated in a 3 M NaCl solution, as a function of both r, x and D. For a given geometry, I_{FEM} becomes independent of WL beyond a certain threshold value as shown by near-vertical contour lines in Figure 5.7(b), Figure 5.9(a), and Figure 5.10. For example, at an arbitrary x = 100 µm, WL > 50 µm have a negligible effect on I_{FEM} (Figure 5.10). As x (or r) increases, the threshold for WL impact increases as well. Although an interesting observation, this parameter independence did not impact the pit stability.

However, when the critical white line was directly correlated to the contour lines (such as in Figure 5.9(a)), the pit stability was impacted by the near-vertical contour line, which indicated WL independence. That is, only extremely small WL (on the order of a few microns in a 3 M NaCl solution) at D > 6.5 cm could prevent the stability of a pit; all other WL will have no contribution in determining pit growth or repassivation. In a 0.6 M NaCl solution, much larger WL ≈ 100 µm could have an impact on stability, implying that in lower chloride concentrations (and correspondingly higher RH) WL may play a more significant role in pit stability as opposed to 3 M NaCl solutions (Figure 5.9(b)).

5.5.4. Dimensionality Impact of the Anode and Cathode on Pit Stability

The impact of r on stability has been well documented in literature.[11,20,21,48] Using the FEM model, this work has confirmed that smaller pits are more stable via their lower current demand, and are less likely to grow into larger pits where the higher current demand cannot be maintained (Figures 5 – 7). Additionally, the decrease in potential as a function of r demonstrates a much larger polarization than predicted from an ideal pit (Figure 5.5(c)). Although thorough studies on r are common, less work has been conducted on the impact of the cathode geometry.

An important parameter in maintaining stability, D was able to both polarize the system above E_{rp} (Figure 5.5c), and consume current (Figure 5.6(b)). Indeed, when WL and D were changed concurrently in 3 M NaCl, the importance of D was magnified (Figure 5.9(a)). At D = 6.5 cm, this parameter became nearly the sole criteria for stability, indicating that any small deviations could determine the final outcome of a metastable pit. An interesting point to note is that in 0.6 M NaCl, a stability region existed around WL = 100 μm which was independent of D (Figure 5.9(b)). That is, at this WL, variations in D would have little effect on the pit stability.

5.5.5. Implications of the Pit Geometry

Although this work focused on a simple hemispherical pit, the nature of the model allowed for the pit geometry to be transformed while keeping all other boundary conditions and assumptions constant. A pseudo-1-D pit, represented in 2-D as a rectangle and in 3-D as a cylinder, was the first geometry to be compared (Figure 5.1(b)). This geometry displayed impressive stability in terms of both E_{rp} and $(i \cdot x)_{crit}$ (Figure 5.10). While the potential distributions in this geometry are not shown, $E_{mouth} > E_{rp}$ for the range of pit depths tested, up to x = 1,000 μm.

At first glance, the rectangular pit seems much more likely to stably grow as opposed to a hemispherical pit, however, caution must be taken. Geometrically, r (of the hemisphere) and x (of the 1-D pit) represent the same pit depth, as $r \equiv x$ along the z-axis. The pit depths were tested with the same range of $r = x =$ (15 µm to 500 µm). The caveat being the that the total anodic surface areas were not equal; the hemispherical anodic surface scaled with r^2 while the active surface area in the 1-D pit remained constant.

The total anodic surface area can impact the anodic demand for current, making a comparison between pit stability rather difficult. One similarity that can be made, however, involves WL. In both geometries, WL has little effect on I_{FEM}, or $(i \cdot x)$ in the case of the 1-D pit, as represented by the vertical contours (Figure 5.9 and Figure 5.10).

The remaining two pit geometries considered were complex deviations of a basic hemispherical design (Figure 5.1(c) and (d)). These pits were chosen to represent porosity and roughness features typically observed in/on AM surfaces.[53,54] The roughness of stainless steel surfaces has been shown to play an important role in pitting. Literature has demonstrated an inverse correlation between the critical pitting temperature and the surface roughness, indicating that pitting occurs more easily on a rougher surface, possibly via an increase in the effective diffusion path making it easier to maintain the aggressive chemistry in an occluded site.[51,55] In a 3 M NaCl environment, as-printed powder bed fusion (PBF) and selective laser melting (SLM) SS316 samples were seen to have a higher affinity for pitting, as opposed to wrought SS316, further highlighting the importance of surface roughness.[6,53] Moreover, the shape of the individual pits has been postulated to have a large impact on stability, via differences in the degree of occlusion controlling the retention of the aggressive species. Duan *et al.* found experimentally that a covered gas pore, akin to the undercut pit geometry, transitions to stable growth more easily than an open gas pore, *i.e.*, a simple hemispherical pit.[6]

Therefore, in this work, a double pit and undercut pit geometry were investigated (Figure 5.1(c) and (d)). The double pit geometry expanded on a simple hemispherical design by representing an active pit growing inside of a previously repassivated pit. Experimentally, it has been shown that repassivated pits are still a valid location for active pits to nucleate and grow.[7,56,57] In the context of AM, this scenario also corresponds to a gas pore with an affinity for pitting initiation.[6] The active surface, labeled the "secondary pit", was half of the radius of the repassivated surface, labeled the "primary pit". The opening of the secondary pit was 60% of the radius, $r_{secondary}$, in all studies (Figure 5.1(c)).

The last complex geometry considered was made to represent the phenomenon of undercutting pits which have been seen to occur in stainless steels.[7,53,58] An obtrusion was included at the pit mouth to account for an additional surface defect, such as a partially melted powder particle from the AM process (Figure 5.1(d)).[53] Within the undercut pit, additional simulations were conducted by varying the active regions (Figure 5.12). Defining particular locations in the pit to be anodically active while other features within the pit are inert could be useful in future work to determine which facets, on a real as-printed surface, may be the most likely to maintain pit stability. To easily compare the effects of these features, the current calculated in all hemispherical-based pit simulations were plotted together, as a function of WL. Both saturation conditions, $\left(\frac{I}{r}\right)_{crit}$ and $\left(\frac{I}{r}\right)_{sf}$, were included as red and black dashed lines, respectively (Figure 5.14).

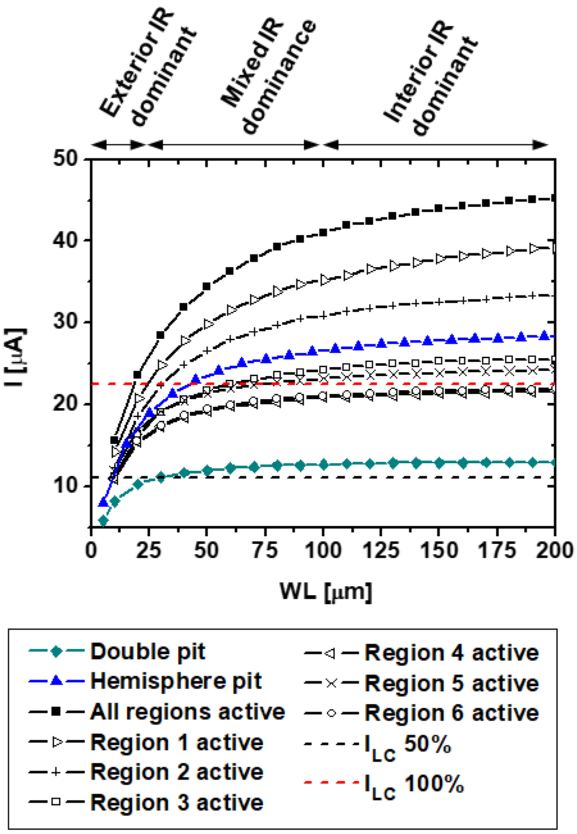

Figure 5.14: I_{FEM} for all hemispherical-based pits as a function of WL, with r = 15 µm , and D = 15 cm; black and red horizontal dashed lines represent the pit stability criterion at 50% and 100%, respectively. Arrows denote dominant regions of ohmic drop either within the pit (interior) or outside of the pit (exterior).

The second criterion $\left(\frac{I}{r}\right)_{crit}$, through using I_{LC} 50% saturation, was satisfied WL ≈ 10 µm for all geometries except for the double pit. However, as WL increased, I_{FEM} of each unique pit scenario diverged, spanning a range of 32 µA. The repercussions of the divergence are clearly seen if I_{LC} 100% saturation was needed to obtain stability. For example, the undercut pit with all regions active could obtain stable growth at WL = 20 µm, as seen by the intersection of I_{FEM} and I_{LC} 100%

saturation. However, for a hemispherical pit in that same scenario, WL = 42 µm is required. If an undercut pit had only the side walls active, as represented by region 5, then an even larger WL = 70 µm is required to maintain stable growth at I_{LC} 100%.

The double pit exhibited a much lower I_{FEM} than the remaining geometries. Recall that the active secondary pit had a radius half the size of all other pit radii, so it follows that the active anodic surface area would be the smallest in comparison to the remaining geometries. Rerunning the simulation as a function of WL with $r_{secondary}$ = 15 µm and $r_{primary}$ = 30 µm, that is, with $r_{secondary}$ equal to the opening of the other pit geometries, I_{FEM} was increased within the range of the other geometries seen in Figure 5.14. However, for the consistency of all initial pit openings being equal, the lower surface area result remained included.

One main conclusion deduced from Figure 5.14 is that at thin WL (5 to 20 µm), the ohmic drop *outside* of the pit is the limiting factor dominating I_{FEM}. This conclusion is evident by the negligible effects of the pit geometries at these thin WL. However, as the WL increases, ohmic drop *inside* of the pit becomes more important. At larger WL (> 100 µm), I_{FEM} is nearly constant but distinct between each individual pit geometry, indicating that the ohmic drop *inside* the pit is dominant and limiting the current. Distinctions within the constant I_{FEM} values are attributed to a difference in anodic surface area in each simulation, as discussed with the double pit geometry above.

Looking specifically at the undercut pit simulations, the contributions of the ohmic drop could be seen from a different perspective. The potential distribution in a thin WL = 16 µm revealed the largest amount of ohmic drop was always *outside* of the pit (difference between E_{edge} and $E_{\mathrm{mouth,b}}$), regardless of which region was active (Figure 5.12(b). However, at bulk WL (1,000 µm), the largest ohmic drop was always *inside* of the pit (difference between E_{base} and $E_{mouth,a}$), except when regions 1 or 2 were active (Figure 5.12(c)).

By testing a variety of scenarios, the impact of the ohmic drop on the individual regions could further be evaluated. Regions 1 and 2 were active exterior surfaces, and therefore did not have any ohmic drop within the pit. More secluded regions (such as regions 4, 5 and 6) always had a larger interior ohmic drop in all WL than region 3 or the hemispherical pit, due to the longer diffusion path. The diffusion path was comparable between region 3 and the hemispherical pit, and therefore both scenarios had similar potential distributions and total currents.

Larger WL corresponded to an increase in I_{FEM} for all scenarios (Figure 5.12(d)). However, at small WL = 16 µm I_{FEM} across all scenarios was very similar, with 6.8 µA of variance, in comparison to WL = 1,000 µm which enlarged the disparity in I_{FEM} to 27 µA, an increase by a factor of four. The disparity in I_{FEM} across the different scenarios was increased in the larger WL because the active regions dominated by an *exterior* ohmic drop (regions 1 and 2) accrued much more current than those dominated by an *interior* ohmic drop (regions 4, 5, and 6). Therefore, it can be inferred that the ohmic drop outside of the pit is more dependent on WL, then the ohmic drop inside of the pit. In practical terms, the pit geometry has a greater impact on stability when thicker WL are present (> 100 µm in our scenario), as opposed to thinner WL in which all geometries behave hemispherically.

5.6 Limitations

Although the current framework is useful, it includes simplifying assumptions which should be appreciated. The governing equation assumes a steady-state system and does not take into account any chemical reactions, pH, or κ variations. Additionally, the WL is assumed to be uniform, which neglects the possibility of imperfect wetting or a discontinuous droplet layer. A recent review by Herman Terryn and coworkers highlights the impact that WL geometry can have on modeling results.[59]

The PDS boundary conditions within the model also include an important caveat, that they were conducted on wrought SS316 surfaces. Although the application of this complex pit stability work can be generalized to AM or irregular wrought SS316 surfaces, the boundary conditions which were used did not technically portray the kinetics of an AM SS316 surface. The level to which these boundary conditions impact the results is currently being investigated. Further work will involve the generation of electrochemical boundary conditions on AM SS316 surfaces to capture the correct kinetics for this application.

Limitations of the pit stability criteria should also be considered. When predicting the stability of a simple 1-D or 3-D hemispherical pit, determining which threshold criteria to use is straightforward, with a geometric factor of 3 acting as the conversion of the pit stability product.[4,16,17,19] However, as more details within a 3-D pit geometry are included, using $\left(\frac{I}{r}\right)$ as a threshold for stability may no longer be an accurate assumption due to both a change in surface area and a possible non-uniform rate of propagation. No derivation exists, that the authors are aware of, which converts $(i{\cdot}x)$ or $\left(\frac{I}{r}\right)$ to complex non-hemispherical pit geometries. However, in one instance to account for an undercut pit, Ghahari *et al.* used a modified $(i{\cdot}x)$ stability criterion which multiplied the current by the *local pit depth*, rather than the overall pit radius.[7] In this work, the conventional $\left(\frac{I}{r}\right)$ is assumed to be applicable as a stability criterion for all hemispherical-based pit geometries. On the other hand, E_{rp} is applicable to all pit geometries; measurements of E_{edge} in bulk samples and artificial 1-D pits revealed similar values.[5] Relying on E_{rp} to predict stability, however, may result in much larger r_{crit} estimations than predicted by $\left(\frac{I}{r}\right)_{crit}$ as discussed in a previous section of this work. If both criteria are accurate, then E_{rp} is providing a more conservative, and $\left(\frac{I}{r}\right)_{crit}$ a more stringent, prediction of stability. Current work is underway to determine a less conservative value of the E_{rp}.

Note that an additional pit stability criterion $(i\sqrt{\tau})$ exists, which takes into account the critical time to pit initiation (τ).[48,60,61] Limitations of the steady-state model prevented the use of $i\sqrt{\tau}$ in this work, although Li *et al.* describes how $(i{\cdot}x)$, $\left(\frac{I}{r}\right)$ (described as (ir) in their work), and $i\sqrt{\tau}$ are really all equivalent.[62]

Lastly, it is of utmost importance to remember that WL variations in this study were all conducted at a constant chloride concentration, in either 3 M NaCl or 0.6 M NaCl. The LD was therefore changed with each new WL under investigation, while RH remained constant. This methodology is in contrast to wet-dry cyclic studies, in which a given WL is evaporated, increasing the chloride concentration, but with a (relatively) constant LD. Experimental wet-dry exposures on stainless steels have found that thinner WL are most aggressive for pitting nucleation and growth, due to restricted diffusion of aggressive species away from the anodic region and a lack of convection.[50] This result may seem to be in direct contrast to the conclusions presented in this work, which state that small WL should result in less stable pits, when in fact they are complimentary. The thinner WL described by Vera Cruz *et al.* are at a higher chloride concentration than their initial bulk sample.[50] Results from this work have also shown that higher chloride concentrations (3 M NaCl) achieve more stability than their lower counterparts (0.6 M NaCl). Combining these conclusions leads to the theory that chloride concentration is more important to pit stability than WL, although further investigations need to be conducted.

5.7 Conclusion

In this work, a finite element method model framework was developed to describe the conditions under which a pit would cross the threshold from metastable to stable pit growth. Different geometries were investigated, to determine the impact of pit shape on pit stability. Each new pit geometry was compared with a baseline hemispherical pit. The environmental impact on pit stability was also investigated through two different chloride concentrations and a range of water layer thicknesses. To determine pit stability, results from the model were compared with the repassivation potential and both the 1-D and 3-D pit stability products. The main conclusions of this work are below:

- A framework was created using experimentally determined potentiodynamic boundary conditions to describe the transition of an actively corroding pit to either stable growth or repassivation, via the comparison of different stability criteria (E_{rp}, $(i \cdot x)$ or $\left(\frac{I}{r}\right)$). The E_{rp} was found to be more conservative in predicting pit stability, when compared to the pit stability product for a 3-D geometry.
- Between two common simplified pit geometries, it was seen that the pseudo-1-D pit was much more likely to transition to stable growth in all environments than the 3-D hemispherical pit, neglecting any differences in anodic surface area. This may suggest the aspect ratio of processing defects found in AM metals will be the most critical factor when it comes to corrosion susceptibility.
- A thorough study of parameter space determined that the following parameters all *lower* the stability of a pit, increasing the possibility of repassivation, independent of pit shape: lower chloride concentration, smaller cathode diameter, and smaller water layer thickness.

Furthermore, it was confirmed that small hemispherical pits and small 1-D pits are likely to repassivate after a certain pit radius, due to the inability to maintain the higher current demand of the increased pit size.

- Initial results conclude that the maximum current from a realistic cathode is achieved around a diameter of 45 cm, where the open circuit potential is nearly reached, as opposed to an idealized cathode in the same scenario which is predicted to be 12.8 cm. However, this current is still 50% less than the predicted current from an ideal cathode, implying an overestimation of the maximum pit model by a factor of 2 with the parameters tested. This finding was confirmed through a comparison of outdoor exposure with the maximum pit model by Chen & Kelly in 2009.[27]
- According to the present model, under atmospheric conditions, the pit geometry does not have a significant impact on the pit stability. That is, the complex-shaped pits generated in this study behave similarly to a simple hemispherical pit in thin water layers (≤ 20 μm) due to the ohmic drop outside of the pit being the limiting factor.

5.8 Acknowledgements

This paper describes objective technical results and analysis. Any subjective views or opinions that might be expressed in the paper do not necessarily represent the views of the U.S. Department of Energy or the United States Government. Sandia National Laboratories is a multimission laboratory managed and operated by National Technology & Engineering Solutions of Sandia, LLC, a wholly owned subsidiary of Honeywell International Inc., for the U.S. Department of Energy's National Nuclear Security Administration under contract DE-NA0003525. This work was supported through a DOE funded ACT program. This document is SAND2022-0335 J. In addition, support was also provided by the NASA Virginia Space Grant Consortium through a Graduate Research Fellowship.

5.9 References

1. G. S. Frankel, *J. Electrochem. Soc.*, **145**, 2186–2198 (1998).

2. G. S. Frankel, T. Li, and J. R. Scully, *J. Electrochem. Soc.*, **164**, C180–C181 (2017).

3. K. L. Kreider, J. M. Mckinnon, C. B. Clemons, R. S. Lillard, and G. W. Young, *Corros. Sci.*, **179**, 109086 (2021).

4. P. C. Pistorius and G. T. Burstein, *Phil. Trans. R. Soc. L.*, **341**, 531–559 (1992).

5. J. Srinivasan, M. J. McGrath, and R. G. Kelly, *J. Electrochem. Soc.*, **162**, C725–C731 (2015).

6. Z. Duan, C. Man, C. Dong, Z. Cui, D. Kong, L. Wang, and X. Wang, *Corros. Sci.*, **167**, 108520 (2020).

7. M. Ghahari, D. Krouse, N. Laycock, T. Rayment, C. Padovani, M. Stampenoni, F. Marone, R. Mokso, and A. Davenport, *Corros. Sci.*, **100**, 23–35 (2015).

8. N. E. C. Co and J. T. Burns, *Int. J. Fatigue*, **103**, 234–247 (2017).

9. M. D. Mcmurtrey, D. Bae, and J. T. Burns, (2016).

10. J. T. Burns, J. M. Larsen, and R. P. Gangloff, *Fatigue Fract. Eng. Mater. Struct.*, **34**, 745–773 (2011).

11. J. Srinivasan and R. G. Kelly, *Corrosion*, **73**, 613–633 (2017).

12. N. J. Laycock and R. C. Newman, *Corros. Sci.*, **39**, 1771–1790 (1997).

13. A. Anderko, N. Sridhar, and D. S. Dunn, *Corros. Sci.*, **46**, 1583–1612 (2004).

14. J. R. Galvele, *Corros. Sci.*, **47**, 3053–3067 (2005).

15. D. S. Dunn, G. A. Cragnolino, and N. Sridhar, *Corrosion*, **56**, 90–104 (2000).

16. S. T. Pride, J. R. Scully, and J. L. Hudson, *J. Electrochem. Soc.*, **141**, 3028–3040 (1994).

17. K. J. Vetter and H. H. Strehblow, in *NACE-3*, R. W. Staehle, B. F. Brown, J. Kruger, and A. Agrawal, Editors, p. 240 (1974).

18. D. E. Williams, J. Stewart, and P. H. Balkwill, *Corros. Sci.*, **36**, 1213–1235 (1994).

19. M. T. Woldemedhin, M. E. Shedd, and R. G. Kelly, *J. Electrochem. Soc.*, **161**, 3216–3224 (2014).

20. M. H. Moayed and R. C. Newman, *J. Electrochem. Soc.*, **153**, B330 (2006).

21. M. T. Woldemedhin, J. Srinivasan, and R. G. Kelly, *J. Solid State Electrochem.*, **19**, 3449–3461 (2015).

22. J. Srinivasan and R. G. Kelly, *J. Electrochem. Soc.*, **163**, C759–C767 (2016).

23. R. M. Katona, J. Carpenter, E. J. Schindelholz, and R. G. Kelly, *J. Electrochem. Soc.*, **166**, C3364–C3375 (2019).

24. R. P. Frankenthal and H. W. Pickering, *J. Electrochem. Soc.*, **119** (1972).

25. G. T. Gaudet, W. T. Mo, T. A. Hatton, J. W. Tester, J. Tilly, H. S. Isaacs, and R. C. Newman, *AIChE J.*, **32**, 949–958 (1986).

26. T. Li, J. R. Scully, and G. S. Frankel, *J. Electrochem. Soc.*, **166**, C3341–C3354 (2019).

27. Z. Y. Chen and R. G. Kelly, *J. Electrochem. Soc.*, **157**, 69–78 (2009).

28. R. M. Katona, A. W. Knight, E. J. Schindelholz, C. R. Bryan, R. F. Schaller, and R. G. Kelly, *Electrochim. Acta*, **370**, 137696 (2021).

29. W. Mai, S. Soghrati, and R. G. Buchheit, *Corros. Sci.*, **110**, 157–166 (2016).

30. X. Sun, J. Srinivasan, R. G. Kelly, and R. Duddu, *Corros. Sci.*, **179**, 109130 (2021).

31. V. A. Nguyen and R. C. Newman, *Corros. Sci.*, **186**, 109461 (2021).

32. N. J. Laycock and S. P. White, *J. Electrochem. Soc.*, **148**, B264 (2001).

33. N. J. Laycock, J. S. Noh, S. P. White, and D. P. Krouse, *Corros. Sci.*, **47**, 3140–3177 (2005).

34. T. Q. Ansari, J.-L. Luo, and S.-Q. Shi, *npj Mater. Degrad.*, **3**, 1–12 (2019).

35. S. Salleh, 413 (2012).

36. S. Jafarzadeh, Z. Chen, J. Zhao, and F. Bobaru, *Corros. Sci.*, **150**, 17–31 (2019).

37. K. Wang, M. Salasi, S. Bakhtiari, and M. Iannuzzi, *J. Electrochem. Soc.*, **168**, 061506 (2021).

38. C. Liu and R. G. Kelly, *CORROSION*, **75** (2019).

39. V. G. Levich, *Acta Physicochim. Urss*, **17**, 257 (1942).

40. C. Liu and R. G. Kelly, *Corrosion*, **75**, 1087–1099 (2019).

41. T. R. Beck, *J. Electrochem. Soc.*, **126**, 1662 (1979).

42. Z. Y. Chen, F. Cui, and R. G. Kelly, *J. Electrochem. Soc.*, **155**, 360–368 (2008).

43. B. AlMangour and J.-M. Yang, *Mater. Des.*, **110**, 914–924 (2016).

44. E. J. Schindelholz, M. A. Melia, and J. M. Rodelas, *Corros. J.*, **77**, 484–503 (2021).

45. J. Srinivasan, C. Liu, and R. G. Kelly, *J. Electrochem. Soc.*, **163**, C694–C703 (2016).

46. Y. Tsutsumi, A. Nishikata, and T. Tsuru, *J. Electrochem. Soc.*, **152**, B358–B363 (2005).

47. G. S. Frankel, R. C. Newman, C. V. Jahnes, and M. A. Russak, *J. Electrochem. Soc.*, **140**, 2192–2197 (1993).

48. G. S. Frankel, L. Stockert, F. Hunkeler, and H. Boehni, *Corrosion*, **43**, 429–436 (1987).

49. N. D. Budiansky, L. Organ, J. L. Hudson, and J. R. Scully, *J. Electrochem. Soc.*, **152**, B152–B160 (2005).

50. R. P. Vera Cruz, A. Nishikata, and T. Tsuru, *Corros. Sci.*, **40**, 125–139 (1997).

51. M. H. Moayed, N. J. Laycock, and R. C. Newman, *Corros. Sci.*, **45**, 1203–1216 (2002).

52. R. M. Katona, J. C. Carpenter, A. W. Knight, C. R. Bryan, R. F. Schaller, R. G. Kelly, and E. J. Schindelholz, *Corros. Sci.*, **177**, 108935 (2020).

53. M. A. Melia, J. G. Duran, J. R. Koepke, D. J. Saiz, B. H. Jared, and E. J. Schindelholz, *npj Mater. Degrad.*, **4**, 1–11 (2020).

54. B. Whip, L. Sheridan, and J. Gockel, *Int. J. Adv. Manuf. Technol.*, **103**, 4411–4422 (2019).

55. T. Zhang, D. Wang, Y. Shao, G. Meng, and F. Wang, *Corros. Sci.*, **58**, 202–210 (2012).

56. G. Sander, V. Cruz, N. Bhat, and N. Birbilis, *Corros. Sci.*, **177**, 109004 (2020).

57. C. Punckt, M. Bölscher, H. H. Rotermund, A. S. Mikhailov, L. Organ, N. Budiansky, J. R. Scully, and J. L. Hudson, *Science (80-.).*, **305**, 1133–1136 (2004).

58. A. B. Kale, B. Kim, D. Kim, E. G. Castle, M. Reece, and S. Choi, *Mater. Charact.*, **163**, 110204 (2020).

59. B. G. Koushik, N. Van den Steen, M. H. Mamme, Y. Van Ingelgem, and H. Terryn, *J. Mater. Sci. Technol.*, **62**, 254–267 (2021).

60. H. H. Strehblow and J. Wenners, *Electrochim. Acta*, **22**, 421–427 (1977).

61. H. C. Kuo and D. Landolt, *Corros. Sci.*, **16**, 915–922 (1976).

62. T. Li, J. R. Scully, and G. S. Frankel, *J. Electrochem. Soc.*, **166**, C115–C124 (2019).

Chapter 6: Perspective – An Alternative Calculation of the Repassivation Potential, to Represent Less Conservative and More Realistic Values

Rebecca Skelton Marshall*, Armando Shehi*, Ryan M. Katona**, Mike A. Melia**, Rob G. Kelly*

*University of Virginia, 395 McCormick Rd, Charlottesville VA 22903

**Sandia National Laboratories, Albuquerque, NM 87123 USA

Authorship contributions: R. Skelton Marshall (conceptualization, formal analysis, computational work, and writing – original draft), A. Shehi (experimental polarization behavior, and writing – review & editing), R. M. Katona (experimental polarization behavior), M. A. Melia (funding acquisition)

6.1 Abstract

The repassivation potential (E_{rp}) represents the lower threshold for stable pit growth to occur, and therefore, has many practical applications towards the maintenance of pit-susceptible alloyed structures. However, measurements of E_{rp} throughout literature are not straightforward and conventional techniques result in a dependence of E_{rp} on experimental parameters. This perspective has two main goals, 1) to unify the new pitting parameters described in literature with more conventional parameters, while highlighting shortcomings and accomplishments from both fronts, and 2) to propose a more conservative value of E_{rp}, built upon the foundational work

in literature, yet calculated through easily-measured parameters such as the anodic Tafel slope (b_a) and the transition potential (E_T).

6.2 Introduction

Corrosion can occur on metallic surfaces in nearly any humid environment, leading to either early failure or costly repairs. Specifically, localized corrosion, such as pitting, can be difficult to identify at an early stage and can act as crack nucleation sites [1,2]. Predicting long-term corrosion susceptibility and designing corrosion resistant alloys (CRA) are both popular topics of interest to help mitigate failure and excessive repair costs. Recent advances in computational work have provided a useful tool in both areas. Software on the area numerical modeling have led to the prediction of a maximum pit size while machine learning algorithms have improved alloy design that minimize corrosion susceptibility [3–5]. However, both computations base their work on the large reservoir of corrosion parameters and characterization developed throughout the field [3–5]. Imperative to all forms of computational work are the accuracy and reliability of the input parameters. Specifically, in the context of preventing pitting or designing materials resistant to it, a reliable method of measuring pitting susceptibility must be in place.

From the empirically measured pitting and repassivation potentials (E_{pit} and E_{rp}, respectively) to the calculated pitting resistant equivalence number (PREN), multiple parameters that seek to characterize pitting exist. The PREN value is purely based on the material composition, with a focus on known inhibiting alloying elements such as molybdenum and chromium [3]. Conversely, E_{pit} and E_{rp} values are measured electrochemically on the surface of the material, therefore offering the ability to take into account not only compositional variations but also heat treatments, environments, and other factors which may vary sample to sample [6].

Specifically, E_{rp} empirically describes the lower threshold of potential at which active pits repassivate and cease growing [7–10]. Theoretically, this threshold is thought to occur when an oxide forms on the active surface and becomes a passive film [8]. Due to this definition, E_{rp} was originally described as the "protection potential", as all potentials more negative ($E < E_{rp}$) should be protected from pitting [8,11]. Conversely, E_{pit} determines when stable pits will initiate and has been known as the breakdown potential in literature [8,12] (point 2 in Figure 6.1(a)). Although both thresholds are useful for maintenance and design, the lower limit E_{rp} is popular for long-term predictions due to its conservativeness. Yet since conception, there has been debate in how best to measure E_{rp} in a reliable and repeatable way [12].

The conventional means of measuring E_{rp} is through a cyclic potentiodynamic polarization (CPP) scan, in which the intersection of the passive current density during the forward scan (more noble) and the reverse scan (more active) defines E_{rp} [9] (point 1 in Figure 6.1(a)). However, observations of a strong dependence on experimental details, such as the scan rate [11,13] and chosen turn-around current density [14], led to seemingly inconsistent and unreliable values of E_{rp}, as well as questioning whether E_{rp} is a useful parameter [14] .

Various novel methods of measuring E_{rp} have been proposed, from discrete potential holds on bulk samples and pseudo-1-D pit electrodes, to alternative threshold criteria during the CPP [13,15,16]. However, one significant advancement towards determining a reliable lower-limit localized corrosion threshold was the calculation of anodic charge passed at each measurement of E_{rp}, which lead to the finding that E_{rp} decreased with increasing charge density (or correspondingly, pit depth) before reaching a plateau [13,17].

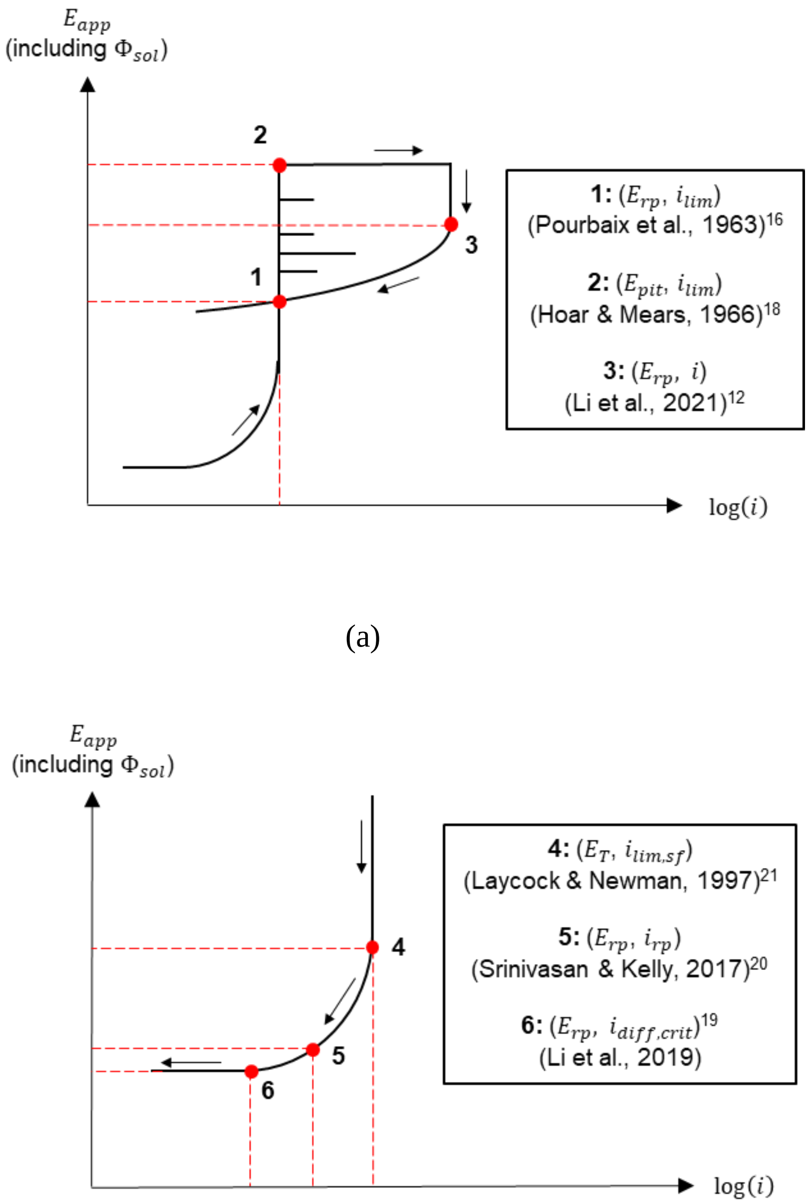

(a)

(b)

Figure 6.1: Schematics of (a) 3-D bulk and (b) 1-D pit electrode E-log(i) relationships, to highlight the various methods of measuring and defining $\boldsymbol{E_{rp}}$ throughout literature [9,16,18–21].

Dunn *et al*., further verified the existence of an E_{rp} plateau at sufficient charge densities, by exposing samples up to three and even 25 years, without any visible corrosion present [22,23]. At potentials below the designated E_{rp}, there was no pitting or crevice corrosion present, with the time of pit/crevice initiation decreasing rapidly (*i.e.*, faster pitting) as the potentials became more noble than E_{rp} [23]. During the plateaued potential, E_{rp} was found to be time-independent (*i.e.*, independent of scan rate [24]), leading to a supposed "true" E_{rp} value, although still dependent on the material and environment (bulk chloride concentration and temperature) [23].

It is of value to note that Thompson & Syrett observed that E_{rp} and E_{pit} collapse into a singular parameter, denoted a "unique pitting potential" (E_u), with the most noble values of E_{rp} at short exposure times (analogous to small pit depths) strikingly similar to the most active values of E_{pit} at long exposure times [12]. These results were confirmed using different experimental methods by Dunn, Sridhar, and Cragnolino [25].

In additional to potential thresholds defining pitting, Galvele's pit stability product $(i \cdot x)_{sf}$ can also be used to determine when a pit will continue growing or repassivate, through accounting for the competing factors of dissolution and dilution in 1-D at 100% salt film saturation [26]. Critical values of the pit stability product $(i \cdot x)_{crit}$ are often utilized, as pitting is known to occur at a saturation less than 100%, based on observations of crystallographic dissolution within pits [27]. If a salt film was present during growth, the pit surface would be electropolished [27]. As E_{rp} also represents the lower limit threshold for pitting, it follows that E_{rp} must occur at the same critical saturation as $(i \cdot x)_{crit}$. Although supposedly representing the same lower pitting threshold through two different points of view, recent work found a discrepancy between the predicted critical radius of E_{rp} and $(i \cdot x)_{crit}$, with E_{rp} consistently the more conservative prediction [28].

Despite the recent advancements in pitting research described above, there remains a pivotal issue in determining a consistent and reliable E_{rp}, with its dependence on pit depth leading to ambiguity in literature. Values measured at deep pit depths (*i.e.*, the plateau) may be too conservative while values measured at small pit depths (*i.e.*, E_u) may not be conservative enough [10]. In this work, an alternative method is proposed to calculate a less-conservative E_{rp}, unifying it with $(i \cdot x)_{crit}$, with validation consistent across literature and computational predictions. Stainless steels are used as the platform to explain and demonstrate the present framework.

6.3 Current Status

One consideration in measuring pitting thresholds is whether to use 1-D lead-in-pencil electrodes, which can simplify the number of variables, or bulk samples, which may be more realistic. For example, $(i \cdot x)_{sf}$ is measured with 1-D pit electrodes but dependent on the pit geometry, with a conversion factor needed to scale from 1-D to 3-D hemispherical pits [29–33]. The conversion factor falls short with more-realistic bulk samples, in which pits are neither purely 1-D nor hemispherical [34–37]. However, there exists no geometric dependence on E_{rp}, as measurements on bulk samples and on 1-D pit electrodes have yielded the same results, leading to flexibility in the measurement techniques [15].

Two new frameworks using both 1-D pit and 3-D bulk electrodes have recently been proposed to describe pitting, and correspondingly, to measure E_{rp}.

The Srinivasan & Kelly framework focuses on a critical pH within the pit ($\mathrm{pH_{crit}}$) below which a protective oxide cannot grow, thereby preventing repassivation [20,24,38,39]. This work follows the foundational theory set up by Okada [8,40], and then Anderko [10], which connected a critical surface chemistry (via oxide nucleation) required to initiate repassivation through E_{rp}. To maintain

pH_{crit}, a ratio of local cathodic current to total anodic current within the pit ($i_{c,local}/i_a$) cannot be exceeded, from which a critical repassivation current density (i_{rp}) is derived. The potential at i_{rp}, as determined through a 1-D pit polarization, was defined as E_{rp} (point 5 in Figure 6.1(b)). As seen in bulk samples, the measured E_{rp} decreased with increasing charge density until reaching a plateau.

Additionally, an equation was proposed, $E_{rp} = E_{corr,f_{crit}} + \eta_{pH_{crit}}$, where $E_{corr,f_{crit}}$ is the corrosion potential at the critical pit solution chemistry, and $\eta_{pH_{crit}}$ is the potential at the ($i_{c,local}/i_a$) [20]. A similar equation was proposed by Sridhar & Cragnolino, $E_{rp} = E_{corr} + \eta + \Phi_{pit}$, in which E_{corr} is the corrosion potential, Φ_{pit} is the potential drop within the pit, and η is the potential required to maintain $(i \cdot x)$ [13]. However, neither relationship above has been validated through calculations nor comparisons from literature, and both are dependent on the corrosion potential which is known to fluctuate with time in a given material.

One large achievement from this framework was the ability to measure both $(i \cdot x)_{sf}$ and E_{rp} from the same set of 1-D pit experiments, which had to reach a certain pit depth (8× – 10× the pit diameter) to achieve 1-D diffusion [38,41]. However, measurements of E_{rp} were very dependent on two factors, 1) the chosen value of i_{rp} and 2) the critical percent saturation (f), which dictated the foundational pH_{crit}.

Initial values of i_{rp} in the Srinivasan & Kelly framework were chosen arbitrarily to be 30 $\mu A/cm^2$, resulting in E_{rp} values nearly equal to the OCP of the 1-D pit experiment, which was known to be a conservative estimate [15]. However, using mixed potential theory with the fixed ratio of ($i_{c,local}/i_a$), i_{rp} could be calculated. A strong dependence on the theoretical anodic and local cathodic Tafel slopes, varying between 40 mV/dec to 70 mV/dec and 30 mV/dec to 118 mV/dec, respectively, resulted in i_{rp} values two to three orders of magnitude larger than the initial 30 $\mu A/cm^2$ argument, corresponding to ~100 mV variation in E_{rp}, which highlighted the sensitivity of this parameter [20]. Note that using a threshold current density to define the repassivation time or E_{rp} has been used previously in literature, with values from ~~[2]~~$i = 2$ $\mu A/cm^2$ [42] to $i = 10\ mA/cm^2$ [10] being utilized.

The critical percent saturation in the Srinivasan & Kelly framework was found to be around 50%, which was lower than initial estimates from literature of around 60% - 80% [43]. However, recent calculations have ranged from 43% to 75% saturation, indicating that the field is continually evolving in this area and that determining f is non-trivial [19,41,44].

Another limitation of this work was the neglection of any contributions of Φ_{pit}, as the low current densities for repassivation were used to calculate negligible Φ_{pit} values between 0.1 and 0.7 mV [20]. Although not an uncommon assumption [10], recent work has found Φ_{pit} to be a non-negligible factor, with near-constant values around 67 mV independent of pit depth [45,46], due to the opposing contributions of increased resistance and decreased currents [20]. In addition, calculated ohmic potential drop within the bulk solution and the pit (Φ_{sol}) ranged in literature from 52 mV to 136 mV, at a constant pit depth of 800 μm, even in mild 0.6 M NaCl solutions [16,19]. In addition, the plateau of E_{rp} with increasing charge density has been attributed to the system being controlled by Φ_{sol} at large pit depths [13,23].

Building upon the advances in literature, another recent framework was proposed, described by Li, Scully, and Frankel (herein referred to as the LSF framework) [16,19,47–50]. The basis of this framework proposed that a diffusion limited current density occurs at a critical saturation ($i_{diff,crit}$), in addition to the conventional diffusion limited current density occurring due to the salt film ($i_{lim,sf}$). Setting these two values equal with the charge-transfer limited current density and potential relationship resulted in two new potential criteria, E_{crit} (occurring at $i_{diff,crit}$) and E_{sat} (occurring at $i_{lim,sf}$), which were independent of Φ_{sol} considerations [16,19,47–49].

$$E_{crit} = E_{corr} + \beta_a \, ln \left[\frac{nFDC_{crit}}{i_{corr}x}\right] \tag{6.1}$$

$$E_{sat} = E_{corr} + \beta_a \, ln \left[\frac{nFDC_{sat}}{i_{corr}x}\right] \tag{6.2}$$

where E_{corr} is the corrosion potential, β_a is the anodic Tafel slope, n is the number of electrons transferred, F is Faraday's constant, D is the diffusivity of metal ions, C_{crit} is the critical concentration of metal ions, C_{sat} is the saturated concentration of metal ions, i_{corr} is the corrosion current density, and x is the 1-D pit depth.

Establishing pitting thresholds independent of Φ_{sol} could be very beneficial from two perspectives. First, the dependence of E_{rp} and E_{pit} on bulk chloride concentration has been well studied [13,17,21,23,51], with the dependence attributed to Φ_{sol} [51]. If E_{crit} and E_{sat} are independent of Φ_{sol}, then it follows that they may also be independent of bulk chloride concentration. Furthermore, the pit stability product is also independent of Φ_{sol}, possibly making a more straightforward comparison of the two thresholds [46].

Note that using a 1-D pit electrode to determine $i_{lim,sf}$ is very straightforward, as it represents the saturation limit of metal salts in the pit of a given depth and corresponds to the current density that is independent of potential as shown as point 4, in Figure 6.1**(**b). Correspondingly, the transition potential (E_T) and E_{sat}, both representing a threshold at 100% salt film between charge-transfer and diffusion-limited control, can also be straightforward to measure [21,48] (point 4 in Figure 6.1(b)). However, a limitation of this work is the ambiguity in measuring $i_{diff,crit}$ and respectively, E_{crit} and E_{rp}. Decreasing the scan rate was one approach to providing a clearer indication of $i_{diff,crit}$, through allowing more time for diffusion out of the large pit depths, whereas another alternative method involved calculating $i_{diff,crit}$ through f and the relationship of the pit stability product [19],

$$nFDC_{crit} = (i \cdot x)_{crit} = (i_{diff,crit} \cdot x) \tag{6.3}$$

Correspondingly, an equation can be written to relate $i_{lim,sf}$ with the pit stability product,

$$nFDC_{sat} = (i \cdot x)_{sat} = (i_{lim,sf} \cdot x) \tag{6.4}$$

The above equations can be related through,

$$(i \cdot x)_{crit} = f(i \cdot x)_{sat} \tag{6.5}$$

$$\left(i_{diff,crit} \cdot x\right) = f\left(i_{lim,sf} \cdot x\right) \tag{6.6}$$

Both $i_{diff,crit}$ and $i_{lim,sf}$ can be measured at a given pit depth, further simplifying the expression to,

$$i_{diff,crit} = f \cdot i_{lim,sf} \tag{6.7}$$

However, the decay of current densities less than $i_{lim,sf}$ was dependent on the scan rate and pit depth, which would impact the calculated $i_{diff,crit}$ [19].

In addition to the proposed E_{sat} and E_{crit}, measured on 1-D pit electrodes, Li *et al.*, suggested an alternative method of measuring E_{rp} during bulk CPP scans in which the potential at the base of the sharp potential drop occurring during the reverse (more active) scan defines E_{rp} and corresponds to a critical pit solution, C_{crit} [16] (point 3 in Figure 6.1(a)). However, similar dependencies on the scan rate and turn-around current density could impact the measured value of E_{rp}.

6.4 Future Needs and Prospects

Although the current state of pitting research is advancing in leaps and bounds, the future work still needed is a consistent and verifiable way to calculate E_{rp}. One suggested way in which to do this will be discussed below, with the goal of incorporating both advantages of the frameworks discussed above.

Because both E_{crit} and E_{sat} of the LSF framework's pivotal equations, (Eq. 6.1 and Eq. 6.2), refer to the same material in the same environment, then it follows that all material constants, including E_{corr}, must also be equal. Therefore, Eq. 6.1 and Eq. 6.2 can be set equal to E_{corr},

$$E_{crit} - \beta_a \ln\left[\frac{nFDC_{crit}}{i_{corr}x}\right] = E_{sat} - \beta_a \ln\left[\frac{nFDC_{sat}}{i_{corr}x}\right] \qquad 6.8$$

In the resulting equation, after invoking the rule of logarithms, i_{corr} and x fall out,

$$E_{crit} = E_{sat} + \beta_a \ln\left[\frac{nFDC_{crit}}{nFDC_{sat}}\right] \qquad 6.9$$

Note that often the overall diffusivity (D) of metal salts is assumed to be constant, due to the competing effects of electromigration and diffusion [38,52,53]. However, recent computational work has indicated that the diffusivity is strongly dependent on chloride concentration, making the above assumption questionable [46,54,55]. In the present derivation, any assumptions about diffusivity dependencies are inconsequential as the ratio of critical-to-saturation conditions in Eq.

6.9 would result in the dependencies cancelling out, due to the constant environment between both parameters.

Therefore, further simplifications can be conducted by combining Eq. 6.3. Eq. 6.4 and Eq. 6.9,

$$E_{crit} = E_{sat} + \beta_a \, ln\left[\frac{(ix)_{crit}}{(ix)_{sat}}\right] \qquad 6.10$$

A simple conversion can relate the LSF framework parameters to more conventional pitting parameters (points 4 and 6 in Figure 6.1(b)),

$$E_{crit} = E_{rp} - \Phi_{sol} \text{ [16]} \qquad 6.11$$

$$E_{sat} = E_T - \Phi_{sol} \text{ [19]} \qquad 6.12$$

Note that through Eq. 6.11 and Eq. 6.12, it can be seen that E_{crit} and E_{sat} truly represent the critical pit thresholds on the *electrode surface*. However, combining Eq. 6.5, Eq. 6.10, Eq. 6.11 and Eq. 6.12, two final relationships can be derived and converted from the natural logarithm to log base-10, through incorporating the conversion factor to the anodic Tafel slope (b_a).

$$\mathrm{E_{crit}} = \mathrm{E_{sat}} + \mathrm{b_a} \log[f] \qquad 6.13$$

$$E_{rp} = E_T + b_a \, log[f] \qquad 6.14$$

Where at $f = 1$, *i.e.*, 100% metal salt saturation, $E_{crit} = E_{sat}$ and $E_{rp} = E_T$. The above two equations are unique in that they relate potentials at a critical saturation (E_{crit} and E_{rp}) to easily measured potentials at full saturation (E_{sat} and E_T).

To validate the usefulness of Eq. 6.13 and Eq. 6.14, E_{sat} and b_a data were extracted from the literature and E_{crit} was calculated. Due to the lack of consensus for values of f, two calculations were made to bound the problem at 50% and 80% saturation, which encompasses the majority of literature [41,43,44]. In all data extracted from literature, a SS316 wire approximately 50 μm ($\pm$ 0.8 μm) in diameter was exposed to approximately 0.6 M NaCl ($\pm$0.03 M NaCl), unless otherwise specified.

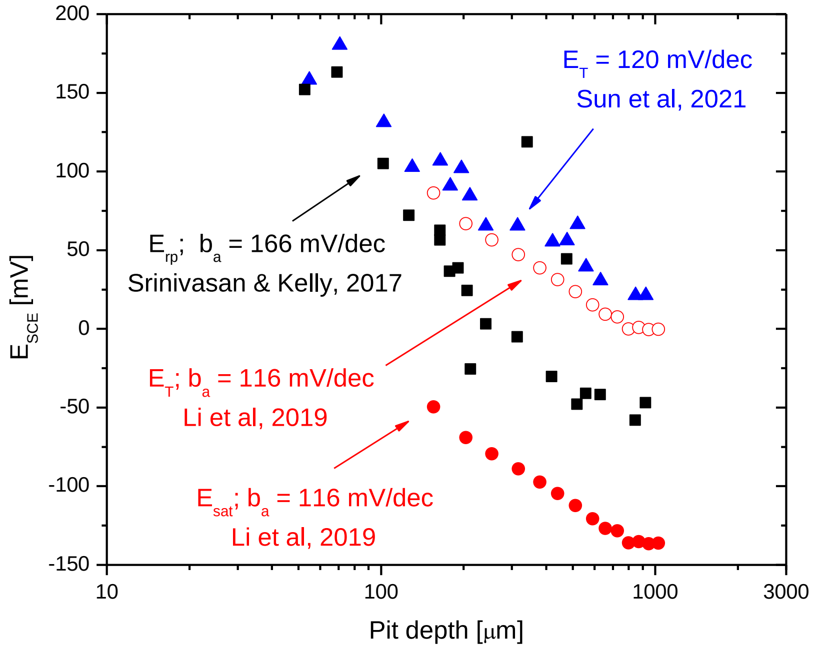

(a)

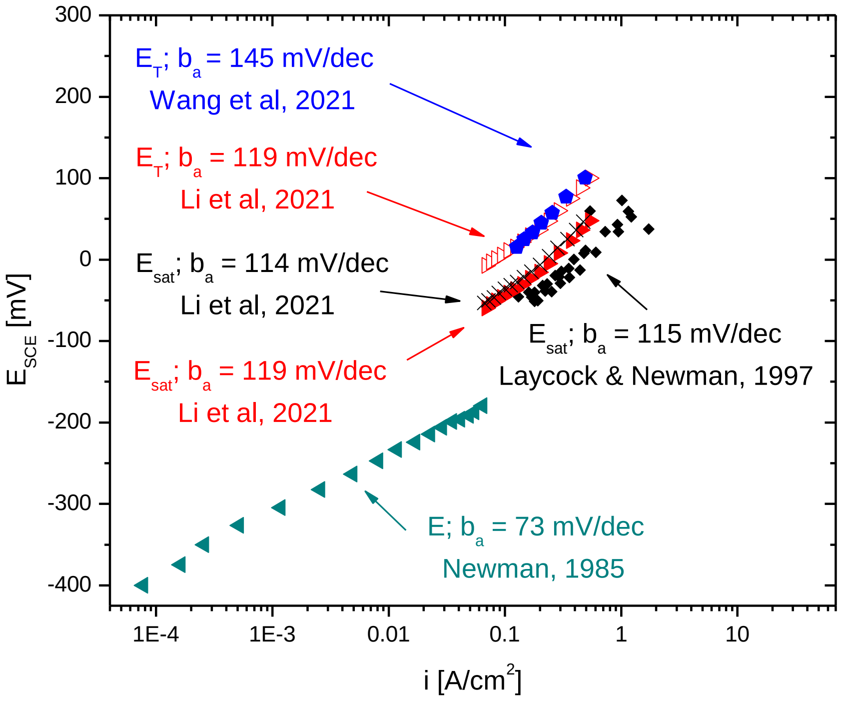

E_T; b_a = 145 mV/dec
Wang et al, 2021
E_T; b_a = 119 mV/dec
Li et al, 2021
E_{sat}; b_a = 114 mV/dec
Li et al, 2021
E_{sat}; b_a = 119 mV/dec
Li et al, 2021
E_{sat}; b_a = 115 mV/dec
Laycock & Newman, 1997
E; b_a = 73 mV/dec
Newman, 1985
300
200
100
0
-100
-200
-300
-400
E_{SCE} [mV]
1E-4
1E-3
0.01
0.1
1
10
i [A/cm^2]

(b)

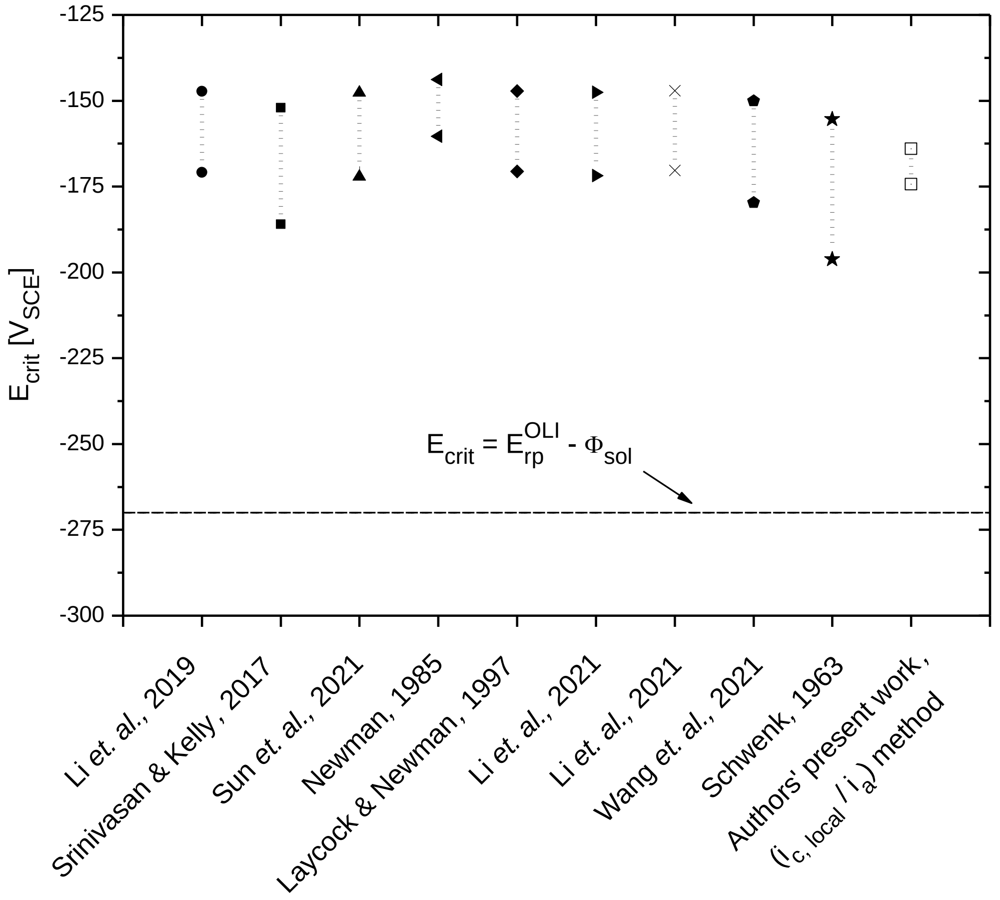

-125
-150
-175
-200
-225
-250
-275
-300
E_{crit} [V_{SCE}]
$E_{crit} = E_{rp}^{OLI} - \Phi_{sol}$
Li et. al., 2019
Srinivasan & Kelly, 2017
Sun et. al., 2021
Newman, 1985
Laycock & Newman, 1997
Li et. al., 2021
Li et. al., 2021
Wang et. al., 2021
Schwenk, 1963
Authors' present work, ($i_{c,\ local}$ / i_a) method

(c)

Figure 6.2: (a) Plotted data from literature of critical potential thresholds vs. log($\boldsymbol{x}$), with Tafel slope indicated, (b) plotted data from literature of critical potential thresholds vs. log($\boldsymbol{i}$), with Tafel slope indicated, (c) calculated values of $\boldsymbol{E_{crit}}$ at $\boldsymbol{f = 50\%}$ and $\boldsymbol{80\%}$ saturation (electronegative and electropositive datapoints, respectively), using equation (13), with symbols corresponding to (a) and (b) datasets. Hollow points in (a) and (b) represent values scaled with $\boldsymbol{\Phi_{sol}}$ found in the respective literature. [16,19–21,41,55–58]

Using the extracted data, the semi-log anodic Tafel relationships were first determined **(**Figure 6.2(a) and (b)). When calculating the slopes of the E vs. x curves, only potentials at pit depths less than the E-value plateau, as seen in Li *et al.*, were considered [19]. Note the striking similarities between the E vs. log(x) (Figure 6.2(a)) and the conventional E vs. log(i) (Figure 6.2(b)) Tafel slope relationships. The correlation above may not be too surprising, as at a critical concentration the pit depth would be expected to scale linearly (yet inversely proportional) with the current density, per Galvele's postulate of a constant $(i \cdot x)$ [26]. Furthermore, the relationship of E_T vs. log($i_{lim,sf}$) is expected to equal the anodic Tafel slope in pit solution [21]; similarities in Figure 6.2(a) and (b) indicate that the relation of E_T vs. log(x) would therefore also represent the anodic Tafel slope in the pit solution.

The datasets from literature were plotted together, despite the different critical potentials plotted, as indicated next to each slope **(**Figure 6.2(a) and (b)). Subtleties existed when extracting out the data. For example, Wang *et al.*, labeled their plotted potentials as E_{sat}, although no correction for Φ_{sol} was described, leading to their data being labeled as E_T in this work [55]. In contrast, Laycock & Newman discuss their data on SS302 in 1 M NaCl as an Φ_{sol}-corrected E_T, which is labeled in this work as E_{sat} [21]. Values of E_{sat} from Li *et al.*, were scaled using the provided Φ_{sol} calculations in their work, 136 mV [19] and 52 mV [16] at a critical pit depth of $800\ \mu m$, to attain E_T using Eq. 6.12 [16,19]. Once scaled, E_{sat} and E_T potentials naturally clustered amongst themselves.

Note that there did exist some outliers to the consistent Tafel slopes, such as Gaudet *et al.*, and Newman & Isaacs finding anodic E vs. $\log(i)$ relationships of 44 mV/dec and 54 mV/dec, respectively, on SS304 in 1 M NaCl whereas Tavassolian *et al.*, determined an E_{sat} vs. $\log(i_{lim,sf})$ relationship of 542 mV/dec on 2205 duplex SS in 0.5 M NaCl [43,44,52]. These outliers may indicate a sensitivity to the material, solution, or experimental technique, although Newman measured a consistent Φ_{sol}-corrected anodic Tafel relationship on an Fe-19Cr-10Ni alloy in 1 M KCl (73 mV/dec), despite slight variations in alloy and solution composition [58] (Figure 6.2(b)).

To calculate E_{crit}, a singular value of E_{sat} was needed. Although a very distinguishable parameter to measure in 1-D pit electrode scans, E_{sat} decreased with pit depth, as seen in Figure 6.2(a) and (b). Li *et al.*, measured a distinct plateau of $E_{sat} = -136$ mV$_{\text{SCE}}$ for deep pits ($x = 800\ \mu m$), similar to the plateau of E_{rp}, arguing that it represented E_{corr} of the material in its critical pit solution [19]. As the calculated Φ_{sol} at $x = 800\ \mu m$ in the same experiment was positive 136 mV, it is inferred that at the plateau, Φ_{sol} is dominant [19]. Therefore, a constant value of -136 mV$_{\text{SCE}}$ was used in Eq. 6.13 to calculate E_{crit} for each distinct Tafel slope shown in Figure 6.2(a) and (b), as the material, solution, and environments were all similar in the literature used.

Figure 6.2(c) shows the ranges of the calculated E_{crit} from the literature between $f = 50\%$ and 80% saturation, representing the lower and upper bounds, respectively. In addition to the datasets shown in Figure 6.2(a) and (b), E_{crit} was determined from a calculated anodic Tafel slope at the base of a stainless steel pit (200 mV/dec), in 1 M NaCl bulk solution, based on Schwenk's derivation that $b_a = \frac{E}{\log(i)} = -\frac{3}{2}\left(\frac{E}{\log(t)}\right)$, with t representing the time to reach a particular current density [57].

All calculated E_{crit} values based on data from literature were within 50 mV of each other, ranging from -143 mV to -196 mV.

The Srinivasan & Kelly framework could also be used to determine the critical potential based on the $\mathrm{pH_{crit}}$ values required to form a passive film (specifically to SS316, CrO(OH)). This framework built on the work of Okada[8,40] and Anderko et al.[10]. For values of f between 50 and 80% critical pH values were calculated via OLI to be between 2.65 and 2.34, respectively. The proposed ratios from Tafel extrapolation were correspondingly determined, assuming stoichiometric dissolution of Fe, Cr, Ni, and Mo in SS316L, to be $(i_{c,local}/i_a) = 0.335\%$ and $(i_{c,local}/i_a) = 0.165\%$, for 50% and 80% saturation, respectively [20]. 1-D pitting scans on SS316L in 0.3 M $\mathrm{MgCl_2}$, having identical chloride concentration to 0.6 M NaCl, were conducted. Note that in regard to the calculation of $(i \cdot x)$, solutions of 0.6 M NaCl and 0.3 M $\mathrm{MgCl_2}$ have yielded identical values [59]. The anodic Tafel slope in the 1-D pits of interest was 43 mV/dec, while the cathodic Tafel slope, taken from the HER reaction rather than the more electropositive Cu-reduction, was 150 mV/dec. Note that utilizing the LSF notation, the critical potentials determined through the $(i_{c,local}/i_a)$ methodology would be E_{crit}, rather than E_{rp}, as the Tafel slope extrapolations are independent of Φ_{sol}. The resulting E_{crit} was 174.32 $\mathrm{mV_{SCE}}$ and 164.01 $\mathrm{mV_{SCE}}$, relating to 50% and 80% salt film saturation, respectively, and was plotted in-line with the theoretical previously described calculations **(**Figure 6.2(c)).

OLI predictions of E_{rp} for SS316 in 0.6 M NaCl were scaled to represent E_{crit}, using Eq. 6.12, with a chosen Φ_{sol} from literature for a SS316 wire in 0.6 M NaCl, 52 mV, respectively [16]. All E_{crit} calculations based off of the derivations in this work offered less-conservative values than those predicted by OLI (Figure 6.2(c)).

Further validation was conducted through a combined approach of finite element method (FEM) modeling and the maximum pit numerical model. The goal of FEM was to predict a more-realistic current distribution surrounding and within a pit, as the cathode size was finite and the potential was not constant with position, whereas the goal of the maximum pit model was to set an upper limit on pit size through looking at both the anodic current demand and cathodic current supply [4]. Detailed methods of both computational techniques can be found in reference [28].

The potential at the pit mouth (E^*_{mouth}) and the pit base (E^*_{base}) were calculated via FEM at a critical set of parameters which satisfied $(i \cdot x)_{crit}$ for a hemispherical pit $\left(\left(\frac{I}{r}\right)_{crit} = 0.75\,\frac{A}{m}\right)$, assuming $f = 50\%$ (Figure 6.3). Note that multiple combinations of the pit radius, cathode radius, and water layer thickness parameters all resulted in potentials satisfying $\left(\frac{I}{r}\right)_{crit}$, however, when plotted together as E vs. r_{crit}, all values collapsed onto a single line for each respective potential location.

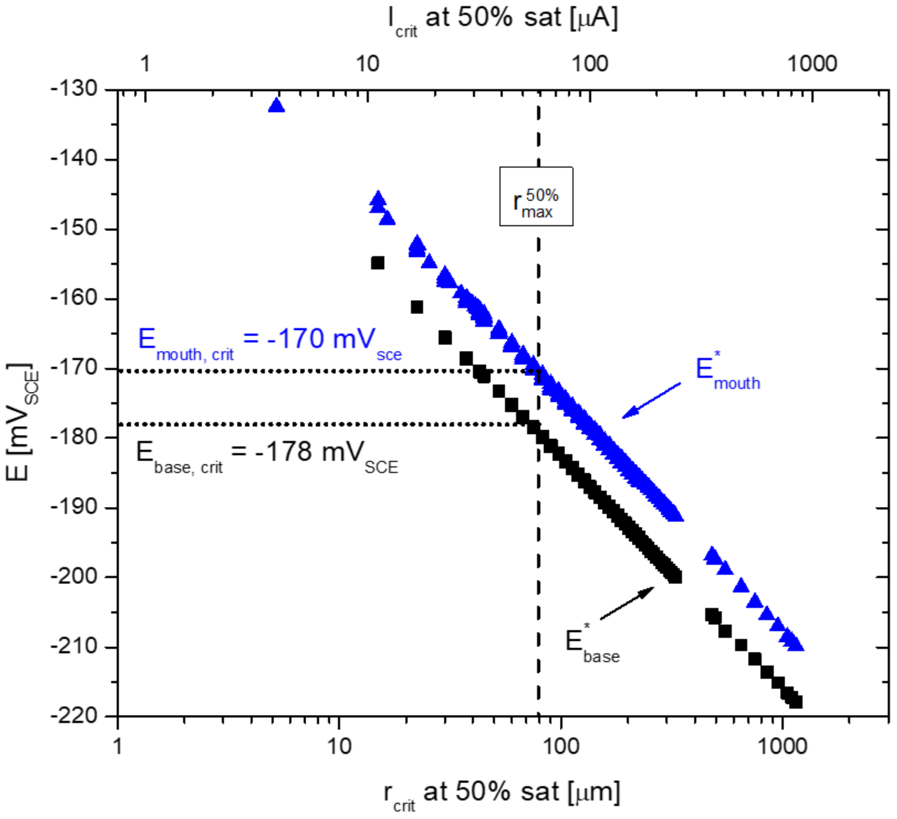

Figure 6.3: Computational potentials calculated at the radius (lower x-axis) and current (upper x-axis) which satisfy $(ix)_{crit}$, assuming 50% saturation. Dashed line represents the maximum pit defined by the max pit model for 50% saturation ($r^{50\%}_{max}$). Dotted lines indicate the potentials at the intersection between $r^{50\%}_{max}$, E^*_{base}, and E^*_{mouth}.

Both E^*_{mouth} and E^*_{base} were calculated, as there is no consensus in literature as to which location the repassivation potential is most important (*i.e.*, at which location within the pit repassivation initiates). It is known that passivation (oxide formation) usually starts at the edges of the pit [57], indicating that E_{mouth} may be a better threshold for stability. However, stability also depends on the maintenance of the critical metal salt saturation which occurs at the base of the pit, indicating that E_{base} is of more importance [7]. It is possible that the potential at both locations may be significant, even leading to non-hemispherical pit shapes if an oxide nucleates at a singular location with $E < E_{rp}$, while dissolution continues occurring at an adjacent location with $E > E_{rp}$. Therefore, both potentials were calculated to understand the range of critical potentials within a pit.

Recalling that $(i \cdot x)_{crit}$ should represent the same lower threshold condition as E_{rp} and E_{crit}, it follows that E^*_{mouth} and E^*_{base} may be considered E_{crit}, resulting in a similar semi-log relationship of E_{rp} and pit radius (r) as seen in literature (Figure 6.3) [20]. Although a plateau of the potential at deep pits is expected, numerical predictions by Anderko *et al.*, and this work extend the semi-log relationship indefinitely, unless accounting for complex thermodynamic and kinetic reactions, which highlights a computational limitation [10]. That is, larger and larger pits have lower and lower E_{rp}, *ad infinitum*. To account for this limitation, the predicted maximum pit radius at 50% saturation ($r_{max}^{50\%}$) for the material and solution of interest was calculated via the maximum pit model and overlaid on the FEM predicted potentials to represent an upper bound of the pit radii (Figure 6.3). Therefore, the intersection of $r_{max}^{50\%}$ with E_{mouth} and E_{base} should represent bounds of critical potentials, $E_{mouth,crit}$ and $E_{base,crit}$, within the pit (at $f = 50\%$, specifically).

As indicated on Figure 6.3**,** $E_{mouth,crit}$ and $E_{base,crit}$ were determined to be -170 mV_{SCE} and -178 mV_{SCE}, respectively. In comparing these computational critical potentials with the calculated critical potentials from Eq. 6.13, specifically the less-noble datapoints relating to $f = 50\%$, and the calculated potentials through the $(i_{c,local}/i_a)$ method, very good correlation can be seen (Figure 6.2(c) and Figure 6.3). Both methods confirm that a less-conservative E_{crit} (and correspondingly, E_{rp}) may be more realistic and may be achievable through calculations based on experimental data or computational predictions.

6.7 Conclusion

In this perspective, pitting notation and pit threshold parameters across literature were clarified, with a special emphasis on their respective limitations and advantages. Specifically, the repassivation potential ($\boldsymbol{E_{rp}}$) has been a controversial parameter in literature, with no consensus on how to take consistent and reliable measurements. In this work, an equation was derived to calculate a consistent and less-conservative $\boldsymbol{E_{rp}}$ through relating $\boldsymbol{E_{rp}}$ with parameters more easily measured, such as the transition potential ($\boldsymbol{E_T}$) and the anodic Tafel slope ($\boldsymbol{b_a}$). Calculations were conducted based on data found in literature. In addition, finite element method (FEM) modeling and the maximum pit model were combined to predict a range of critical potentials within a pit, unified with the critical pit stability product $(\boldsymbol{i \cdot x})_{\boldsymbol{crit}}$, and consistent with the calculated values above.

6.8 Acknowledgements

Any opinions, findings and conclusions or recommendations expressed in this material are those of the author(s) and do not necessarily reflect the views of Sandia National Laboratory. Sandia National Laboratories is a multimission laboratory managed and operated by National Technology & Engineering Solutions of Sandia, LLC, a wholly owned subsidiary of Honeywell International Inc., for the U.S. Department of Energy’s National Nuclear Security Administration under contract DE-NA0003525. This work was supported through a DOE funded ACT program. This document is SAND####.

6.9 References

1. Co, N.E.C., and J.T. Burns, *International Journal of Fatigue* 103 (2017): pp. 234–247, http://dx.doi.org/10.1016/j.ijfatigue.2017.05.028.

2. Burns, J.T., J.M. Larsen, and R.P. Gangloff, *Fatigue & Fracture of Engineering Materials & Structures* 34 (2011): pp. 745–773, https://doi.org/10.1111/j.1460-2695.2011.01568.x.

3. Nyby, C., X. Guo, J.E. Saal, S.-C. Chien, A.Y. Gerard, H. Ke, T. Li, P. Lu, C. Oberdorfer, S. Sahu, S. Li, C.D. Taylor, W. Windl, J.R. Scully, and G.S. Frankel, *Sci Data* 8 (2021): pp. 1–11.

4. Chen, Z.Y., and R.G. Kelly, *J Electrochem Soc* 157 (2009): pp. 69–78.

5. Katona, R.M., J. Carpenter, E.J. Schindelholz, and R.G. Kelly, *J Electrochem Soc* 166 (2019): pp. C3364–C3375.

6. Brennert, S., *The Journal of the Iron and Steel Institute* 135 (1937): pp. 101P-111P.

7. Frankel, G.S., *J Electrochem Soc* 145 (1998): pp. 2186–2198.

8. Okada, T., *J Electrochem Soc* 131 (1984): pp. 1026–1032.

9. Pourbaix, M., L. Klimzack-Mathieiu, C. Mertens, J. Meunier, C. Vanleugenhaghe, L. de Munck, J. Laureys, L. Neelemans, and M. Warzee, *Corrosion Science* 3 (1963): pp. 239–259.

10. Anderko, A., N. Sridhar, and D.S. Dunn, *Corrosion Science* 46 (2004): pp. 1583–1612.

11. Freiman, L.I., and L. le Min, *Z. Phys. Chemie* 252 (1973): pp. 65–75.

12. Thompson, N.G., and B.C. Syrett, *Corrosion* 48 (1992): pp. 649–659.

13. Sridhar, N., and G.A. Cragnolino, *Corrosion* 49 (1993): pp. 885–894.

14. Wilde, B.E., and E. Williams, *Journal of The Electrochemical Society* 118 (1971): p. 1057.

15. Srinivasan, J., M.J. McGrath, and R.G. Kelly, *Journal of The Electrochemical Society* 162 (2015): pp. C725–C731.

16. Li, T., J. Wu, and G.S. Frankel, *Corrosion Science* 182 (2021): p. 109277, https://doi.org/10.1016/j.corsci.2021.109277.

17. Yashiro, H., and K. Tanno, *Corrosion Science* 31 (1990): pp. 485–490.

18. Hoar, T.P., and D.C. Mears, *Proceedings of the Royal Society of London. Series A, Mathematical and Physical Sciences* 294 (1966): pp. 486–510.

19. Li, T., J.R. Scully, and G.S. Frankel, *Journal of The Electrochemical Society* 166 (2019): pp. C3341–C3354.

20. Srinivasan, J., and R.G. Kelly, *Corrosion* 73 (2017): pp. 613–633.

21. Laycock, N.J., and R.C. Newman, *Corrosion Science* 39 (1997): pp. 1771–1790.

22. Sridhar, N., and G. Cragnolino, “EVALUATION OF ANALOGS FOR THE PERFORMANCE ASSESSMENT OF HIGH-LEVEL WASTE CONTAINER MATERIALS” (San Antonio, Texas, 2002).

23. Dunn, D.S., G.A. Cragnolino, and N. Sridhar, *Corrosion* 56 (2000): pp. 90–104.

24. Srinivasan, J., and R.G. Kelly, *J Electrochem Soc* 163 (2016): pp. C759–C767.

25. Dunn, D.S., N. Sridhar, and G.A. Cragnolino, “Long-Term Prediction of Localized Corrosion of Alloy 825 in High-Level Nuclear Waste Repository Environments,” CORROSION SCIENCE 115 CORROSION (1996), http://meridian.allenpress.com/corrosion/article-pdf/52/2/115/1530281/1_3292102.pdf.

26. Galvele, J.R., *J Electrochem Soc* 123 (1976): pp. 464–474.

27. Frankenthal, R.P., and H.W. Pickering, *Journal of The Electrochemical Society* 119 (1972).

28. Marshall, R.S., R.M. Katona, M.A. Melia, and R.G. Kelly, *J Electrochem Soc* 169 (2022): p. 021506.

29. Pride, S.T., J.R. Scully, and J.L. Hudson, *J Electrochem Soc* 141 (1994): pp. 3028–3040.

30. Pistorius, P.C., and G.T. Burstein, *Phil. Trans. R. Soc. Lond* 341 (1992): pp. 531–559.

31. Vetter, K.J., and H.H. Strehblow, "Localized Corrosion," in NACE-3, eds. R.W. Staehle, B.F. Brown, J. Kruger, and A. Agrawal (1974), p. 240.

32. Williams, D.E., J. Stewart, and P.H. Balkwill, *Corrosion Science* 36 (1994): pp. 1213–1235.

33. Woldemedhin, M.T., M.E. Shedd, and R.G. Kelly, *J Electrochem Soc* 161 (2014): pp. 3216–3224.

34. Sander, G., V. Cruz, N. Bhat, and N. Birbilis, *Corrosion Science* 177 (2020): p. 109004.

35. Punckt, C., M. Bölscher, H.H. Rotermund, A.S. Mikhailov, L. Organ, N. Budiansky, J.R. Scully, and J.L. Hudson, *Science (1979)* 305 (2004): pp. 1133–1136.

36. Ghahari, M., D. Krouse, N. Laycock, T. Rayment, C. Padovani, M. Stampanoni, F. Marone, R. Mokso, and A.J. Davenport, *Corrosion Science* 100 (2015): pp. 23–35, http://dx.doi.org/10.1016/j.corsci.2015.06.023.

37. Alkire, R.C., and K.P. Wong, *Corrosion Science* 28 (1988).

38. Srinivasan, J., C. Liu, and R.G. Kelly, *J Electrochem Soc* 163 (2016): pp. C694–C703.

39. Srinivasan, J., and R.G. Kelly, *J Electrochem Soc* 163 (2016): pp. C768–C777.

40. Okada, T., *J Electrochem Soc* 131 (1984): pp. 241–247.

41. Sun, X., J. Srinivasan, R.G. Kelly, and R. Duddu, *Corrosion Science* 179 (2021): p. 109130, https://doi.org/10.1016/j.corsci.2020.109130.

42. Sridhar, N., C.S. Brossia, D.S. Dunn, and A. Anderko, *CORROSION SCIENCE SECTION CORROSION* 60 (2004): pp. 915–936, http://meridian.allenpress.com/corrosion/article-pdf/60/10/915/1533797/1_3287826.pdf.

43. Gaudet, G.T., W.T. Mo, T.A. Hatton, J.W. Tester, J. Tilly, H.S. Isaacs, and R.C. Newman, *AIChE Journal* 32 (1986): pp. 949–958.

44. Tavassolian, R., M.H. Moayed, and M. Mirjalili, *J Electrochem Soc* 168 (2021): p. 111505.

45. Wang, K., M. Salasi, and M. Iannuzzi, *J Electrochem Soc* 168 (2021).

46. Wang, K., M. Salasi, S. Bakhtiari, and M. Iannuzzi, *J Electrochem Soc* 168 (2021): p. 061506.

47. Li, T., J.R. Scully, and G.S. Frankel, *J Electrochem Soc* 165 (2018): pp. C484–C491.

48. Li, T., J.R. Scully, and G.S. Frankel, *J Electrochem Soc* 165 (2018): pp. C762–C770.

49. Li, T., J.R. Scully, and G.S. Frankel, *J Electrochem Soc* 166 (2019): pp. C115–C124.

50. Frankel, G.S., T. Li, and J.R. Scully, *J Electrochem Soc* 164 (2017): pp. C180–C181.

51. Laycock, N.J., D.P. Krouse, S.M. Ghahari, A.J. Davenport, T. Rayment, and C. Padovani, *ECS Transactions* 41 (2012): pp. 3–16.

52. Newman, R.C., and H.S. Isaacs, *Journal of The Electrochemical Society* 130 (1983): pp. 1621–1624.

53. Sridhar, N., *Corrosion* 73 (2017): pp. 18–30.

54. Nguyen, V.A., and R.C. Newman, *Corrosion Science* 186 (2021): p. 109461, https://doi.org/10.1016/j.corsci.2021.109461.

55. Wang, K., M. Salasi, and M. Iannuzzi, *J Electrochem Soc* 168 (2021): p. 121504.

56. Li, T., J. Wu, X. Guo, A.M. Panindre, and G.S. Frankel, *Corrosion Science* 193 (2021): p. 109901, https://doi.org/10.1016/j.corsci.2021.109901.

57. Schwenk, W., *Corrosion* 20 (1964): pp. 129t–139t.

58. Newman, R.C., *Corrosion Science* 25 (1985): pp. 341–350.

59. Katona, R.M., A.W. Knight, E.J. Schindelholz, C.R. Bryan, R.F. Schaller, and R.G. Kelly, *Electrochimica Acta* 370 (2021): p. 137696, https://doi.org/10.1016/j.electacta.2020.137696.

Computational Methodologies to Accommodate Complex Systems

Summary:

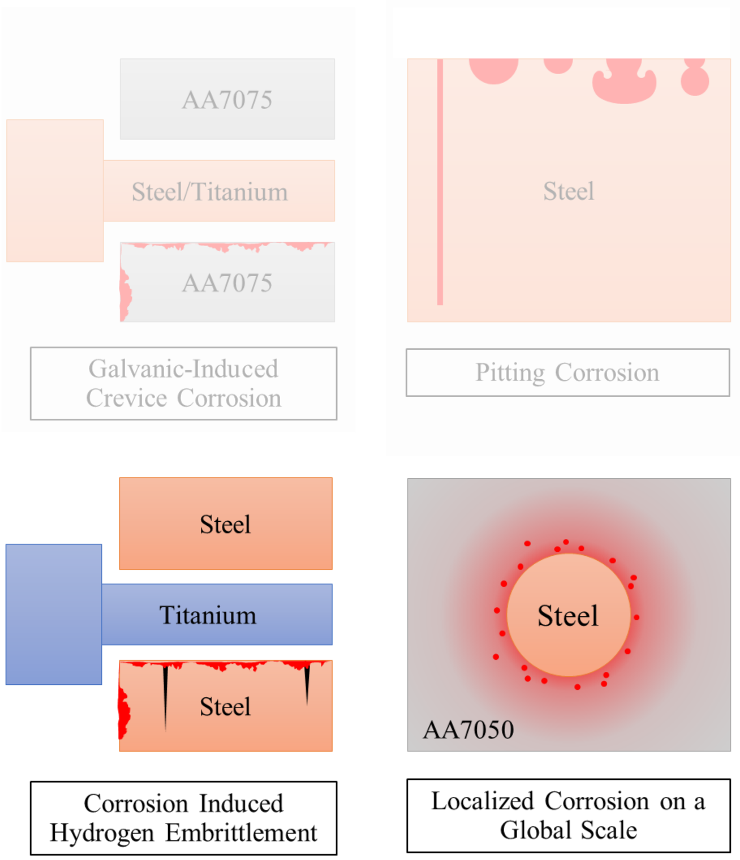

In this section of the work, two complex processes are added into the model, with the goal of simulating more-realistic systems. Chapters 7 and 8 begin with a galvanic-induced crevice corrosion simulation in a fastener-in-panel geometry. Rather than only accounting for corrosion processes in the complex geometry, such as Chapters 2 through 4, stress corrosion cracking through hydrogen embrittlement (HE) was also considered. A framework was developed, in which potentiodynamic electrochemical boundary conditions were generated and input into a model which calculated the distributions of potential over the spatial coordinates. Cracking kinetics at a given dK/dt resulted in outputs of the crack growth rate as a function of potential. Combining these results, the E-values resulting in low crack growth rates could be optimized to occur at regions which concentrate the external stress, thereby **mitigating** HE. The effect of local pit "hot spots" within the fastener hole on the distribution of potential was also considered. It was determined that two main tuning parameters can be used engineer the potential into the low-crack growth rate region, as well as minimize the galvanic corrosion rate of the system, 1) selective plating of Zn-Ni on the surface of the panel, and 2) surface treatments (or lack thereof) of the noble fastener.

Chapter 9 instead focused on **predicting** the overall behavior of a macro-scale surface undergoing localized corrosion. Rather than considering the isolated effects of a single pit, such as Chapters 5 and 6, a global planar surface undergoing pitting was considered. An iterative methodology of developing boundary conditions to represent the highly-inhomogeneous surface for a SS316/AA7050 galvanic couple was developed. **Validation** and comparisons were conducted with the scanning vibrating electrode technique (SVET). It was determined that modifying both the cathodic and anodic boundary conditions to account for the aggressive solution over the pitted surface was necessary to continue assuming the Laplace equation within the computational model.

Publications resulting from this section of the work:

- Z. D. Harris, **R. S. Marshall,** J. T. Burns, R. G. Kelly. (2022). Coupling Fracture Mechanics Experiments and Electrochemical Modeling to Mitigate Environment-Assisted Cracking in Engineering Components, *(to be submitted)*

- **R. Skelton Marshall,** Z. D. Harris, M. K. Small, K. L. Brunner, J. T. Burns, & R. G. Kelly. (2022). A Materials Selection Framework for Fastener-in-Panel Geometries Using FEM, to Mitigate Coating Degradation and Hydrogen Embrittlement, *(to be submitted)*
- U.-E., Charles-Granville[=], **R. Skelton Marshall[=],** C. V. Moraes[=], C. F. Glover, J. R. Scully, & R. G. Kelly. (2022). Application of Finite Element Modeling to Macro-Galvanic Coupling of AA7050 and SS316: Validation Using the Scanning Vibrating Electrode Technique. *Journal of The Electrochemical Society, 169*(031502), 1–14.

[=] denotes equal authorship

Chapter 7: An Initial Analysis of Coupling Fracture Mechanics Experiments and Electrochemical Modeling to Mitigate Environment-Assisted Cracking in Engineering Components

Rebecca Skelton Marshall[=], Zach D. Harris[=], Jimmy T. Burns, Rob G. Kelly

University of Virginia, 395 McCormick Rd, Charlottesville VA 22903

Authorship contributions: R. Skelton Marshall (formal analysis, computational work, experimental polarization behavior, and writing – original draft), Z. D. Harris (fracture mechanics investigation, and writing – original draft), J. T. Burns (funding acquisition, technical expertise, and advice)

[=] Equal contribution

7.1 Abstract

Stress corrosion cracking (SCC), defining the interdisciplinary and destructively synergistic mechanisms of fracture mechanics and electrochemical behavior, is known to occur on aluminum alloys and steels. SCC has many interconnecting parameters, resulting in a highly-complex system which can make mitigation methods difficult, as it may not be known which environments or material combinations are contributing to an increased SCC susceptibility. The present work proposes a new interdisciplinary framework to predict and prevent SCC susceptibility, through using both finite element method (FEM) modeling and linear elastic fracture mechanics (LEFM). Results from LEFM indicate a clear potential dependence on the

crack growth rate, with a low crack growth rate "well" in a moderate potential range and high crack growth rates at both potential extremities tested. The FEM modeling can then predict the given galvanic coupled potential in a given environment and system, and can harness the iterative capabilities of the computational methodology to determine which material or coating selection would result in a potential range indicative of the lowest crack growth rates. Initial analysis of this framework were conducted on bulk water layer conditions (4,000 μm) of 0.6 M NaCl, and two mitigation techniques were determined.

7.2 Introduction

Environment-assisted cracking (EAC) is a critical failure mode across a wide range of applications and industries[1,2]. Specifically, stress corrosion cracking (SCC) is of vital importance on pitting-susceptible materials, such as aluminum alloys and steels, where the crack nucleates at the pitted location[3–5]. Environmental and geometric effects can lead to increased SCC susceptibility[6–9]. Acidification of the solution and production of H_2 impact SCC[10,11], and can both be encompassed by a potential dependence on the crack growth rate kinetics. Specifically, on aluminum alloys and steels, the crack growth rate at a constant dK/dt has been found to have a "U"-shaped dependence on the potential[2,11,12]. In addition to the micro-scale effects of the pits, realistic geometries with macro-scale stress concentrators, such as a cylindrical fastener hole, can further escalate the system and increase the probability of failure[8]. Therefore, as such, it is critical that SCC susceptibility be considered when designing components to be employed in aggressive environments.

Continued advancements and refinement of fracture mechanics-based assessments of SCC susceptibiltiy has led to interest in utilizing damage tolerant design frameworks for SCC management. In order to effectively employ these damage tolerant design frameworks, it is critical that the environmental conditions pertinent to the service environment be well understood, as well as the geometric feature which may experience the highest level of stress. Moreover, it is critical that proposed mitigation strategies do not pull materials into potential SCC susceptibility regimes. As the environment is often more difficult to predict than the known geometry of the structure, the focus of SCC research in literature has been on stress-concentrating geometries, such as the fastener assemblies with cylindrical holes[13–17].

Experimental investigations within fastener hole occluded regions often involve post-exposure destructive analysis or scaled-down replications for the use of non-destructive electrochemical techniques[18–24]. However, finite element method (FEM) modeling has gained popularity through its usefulness to determine the potential and current density distributions in non-planar electrochemical systems, as the governing equation is solved at each spatial (x, y, z) position[18,25–31]. Therefore, the investigation of the potential or current density can be focused over a specific occluded region, which may have a higher susceptibility to mechanical failure, such as occurs through the stress-concentrating effects within the cylindrical fastener hole[8]. The efficacy of this computational method has been experimentally validated on fastener-in-panel galvanic couples[18]. Moreover, if informed by SCC measurements, then FEM can also be utilized to engineer mitigation strategies. However, despite the possible benefits of such an approach, the efficacy of this coupled method has yet to be demonstrated.

The objective of this study is to demonstrate the efficacy of coupled fracture mechanics-based SCC susceptibility measurements and FEM modeling of the electrochemical potential distribution for engineering SCC mitigation strategies in a real-world geometry. The SCC susceptibility of a corrosion-resistant martensitic steel (Pyrowear 675®) is measured at electrochemical potentials ranging from -1.2 to -0.1 V_{SCE} in 0.6 M NaCl solution under both rising and static stress intensity (K) loading. Experimentally-informed FEM is then performed on a representative plate and fastener geometry under bulk WL conditions, with the electrochemical potential distribution across the geometry calculated for a range of different fastener materials and coating scenarios. The results of these two approaches are then synthesized to demonstrate specific SCC mitigation strategies that could be employed for the modeled geometry.

7.3 Methods

7.3.1 Material

All experiments were conducted on specimens excised from a single ring forging segment of Pyrowear 675® (P675) provided by the Rolls-Royce Corporation. P675 is a corrosion-resistant martensitic steel specifically designed to have a highly carburized case for wear resistance, while maintaining the fracture toughness necessary for applications such as aerospace bearings and gears [32,33]. Typical mechanical properties for non-carburized P675 (*i.e.*, properties expected in the core region) are as follows: yield strength of ~1000 MPa, hardness of ~40 HRC, ultimate tensile strength of ~1275 MPa, reduction of area of ~70%, and a fracture toughness (K_Q) of ~145 MPa√m [34]. The nominal composition of P675 is reported in Table 7.1[32,34].

Table 7.1: Nominal elemental composition of P675 (in wt. %)

Fe	Cr	Co	Ni	Mo	Mn	V	Si	C
Bal.	13.00	5.40	2.60	1.80	0.65	0.6	0.4	0.07

Single edge notch tensile (SEN(T)) specimens were extracted from the ring forging such that the loading axis was parallel to the circumferential direction of the ring, and Mode I crack growth occurred in the radial direction (*i.e.*, C-R orientation). The gage section of the SEN(T) was machined with a thickness (B) of 2.60 ± 0.05 mm and width (W) of 9.40 ± 0.05 mm. A slot notch (height of 0.2 mm) with a depth of 0.750 ± 0.05 mm was cut at the gage section mid-height using electrical discharge machining (EDM) with a tungsten wire. Specimens for polarization scans were excised from the forgings through an 8-inch precision wet cut-off saw with continuous anti-corrosion coolant. Samples were then either rinsed with DI water and polished to 400 grit with SiC paper to achieve the “bare” surface of the material, or were rinsed with DI water without polishing, to preserve the original surface treatment or coating. All samples were dried with pressurized air.

An anodized Ti-6Al-4V bolt was also received by Rolls Royce Corporation, with a proprietary anodization layer for increased wear resistance. The tip of the bolt shaft was cut using the 8-inch precision wet cut-off saw with continuous anti-corrosion coolant to use for electrochemical testing. For bare Ti-6Al-4V surface testing, the anodization was polished off with 400 grit SiC paper and rinsed with DI water between tests.

7.3.2 Fracture Mechanics-Based SCC Testing

Fracture mechanics-based testing was conducted using a servohydraulic mechanical load frame equipped with a Fracture Technology Associates (FTA) direct current potential difference (dcPD) crack length monitoring system. The SEN(T) specimens were placed into the load frame using a pinned-ends configuration, where the threaded ends of the specimen were screwed into tangs that were pinned into clevises attached to the crosshead and actuator of the load frame *via* threaded adapters. The tangs, clevis, pins, and threaded adapters were all machined from 17-4PH stainless steel heat-treated to the H900 condition[35]. Each specimen was aligned with the clevises to allow for free rotation, in compliance with the K solution boundary conditions for a pinned end SEN(T) specimen[36].

Crack extension was actively monitored throughout each experiment using the dcPD technique[37,38]. A constant current of 4.000 ± 0.005 A was applied through 10-gage copper leads attached to the customized tangs that were located outside of the environmental cell. Voltage measurements were taken using 36-gage alumel wires spot welded above and below the EDM notch at a distance of 0.6 to 0.75 mm from the notch mid-plane, yielding a total dcPD gage length of 1.2 to 1.5 mm. The dcPD-measured potential was converted to a crack length value using Johnson's equation[39], with the initial voltage (V_0) defined by the voltage associated with the initial EDM notch length, which was measured pre-test using a calibrated Hirox RH8800 digitial microscope. All dcPD-measured potentials were corrected for thermally-induced voltages using current-polarity reversal, represent the average of at least 500 individual voltage readings, and were normalized by a simultaneous reference voltage measurement taken from leads located below the crack plane[38]. The crack growth rate (da/dt) was then calculated from the dcPD-measured crack length versus time trace using the polynomial (n = 3) method described in ASTM E647[40]. The effect of crack tip plasticity on the mechanical driving force was considered *via* the calculation of the total K (*e.g.,* K_J) using the EPRI method[41].

Prior to each experiment, the gage section of the SEN(T) specimen was placed inside a custom 240 mL cylindrical acrylic cell, which allowed the SCC experiment to be conducted with only the gage section in the environment of interest. All specimen surfaces within the environmental cell were covered with a butyl rubber-based lacquer (Tolber Miccro XP-2000 Stop-off Lacquer), except for a 1.25 mm-wide window on each side of the SEN(T) gage section, centered along the Mode I crack path. Specimens were then fatigue precracked in laboratory air using the following protocol: constant K_{max} of 12 MPa√m at a stress ratio (R) of 0.1 and frequency (*f*) of 5 Hz from the initial EDM notch length (a_0) to a cumulative notch plus crack length of 1.25 mm.

After the fatigue precracking segment was completed, the specimen was held at 1 kN (corresponding to K of ~3 MPa√m) and the environmental cell was filled with 0.6 M NaCl solution, which was circulated from a 2L reservoir at 20-40 mL/min. One experiment was also performed in dry N_2 (RH < 5%) to quantify the extent of 'false' dcPD-indicated crack growth due to strain-induced artifacts for the current material/geometry combination[42]. Once the cell was filled with electrolyte, the open circuit potential was monitored for 1 hour using a Biologic PG581 potentiostat operated in floating ground mode, followed by the specimen being polarized to the electrochemical potential of interest for 1 hour. A typical three cell electrode setup was used, with the specimen acting as the working electrode, a saturated calomel electrode serving as the reference electrode, and Pt-coated Nb mesh that completely encircled the specimen within the cell acting as the counter electrode. After the 1-hour hold at the test potential, the SCC portion of each experiment was initiated. SCC testing was completed using a fixed stress intensity rate (dK/dt) protocol that leverages the active crack length measurement *via* the dcPD system with software-controlled actuator displacement to maintain a specified K versus time profile[38]. For the current study, the actuator displacement was adjusted every 10 seconds to hold the programmed dK/dt = 4.0 MPa√m/hr test profile, starting at K = 3 MPa√m. This dK/dt was selected based on prior studies examining the influence of dK/dt on SCC across several alloy systems, which collectively demonstrate that dK/dt = 4.0 MPa√m/hr generally provides conservative SCC metrics[42–44].

Once the applied K reached 45 MPa√m, the software automatically transitioned to hold K = 45 MPa√m; the crack growth rate collected under this static K (*i.e.*, dK/dt = 0) test condition was then used to inform the influence of dK/dt on SCC for this material/environment combination. After ~40,000 seconds of static K loading, the specimen was unloaded to 0.25 kN and the environmental cell was drained. While this static K segment was limited to a single potential on the majority of experiments, a series of potentials were evaluated under static K loading on a single sample as follows. The sample underwent rising-K loading at dK/dt = 4 MPa√m/hr at -500 mV_{SCE}, followed by a hold at -500 mV_{SCE} at K = 45 MPa√m for 35,000 seconds, followed by the sample being polarized under the same static K condition at -800 through -100 mV_{SCE} in 100 mV increments (30,000 seconds each), -1200 mV_{SCE} (9,500 seconds), -1100 mV_{SCE} (15,000 seconds), -1000 mV_{SCE} (30,000 seconds), -900 mV_{SCE} (30,000 seconds). The crack growth rate for each static K segment was then determined via fitting a line to the measured crack length versus time trace.

Due to the limited number of samples that could be excised from the provided ring forging, a second SCC experiment was conducted on four SEN(T) specimens. A 'new' precrack was introduced *via* a K-shed cyclic loading protocol, with an initial K_{max} = 30 MPa√m that decreased to 12 MPa√m at R = 0.1 and f = 5 Hz from the final crack length of the first SCC segment to a crack length of 2.15 mm. The fatigue crack growth rates measured at the end of this second precrack were always within the scatter observed during the initial constant K_{max} precrack, indicating that the K-shed protocol is unlikely to affect the second SCC experiment. The second SCC segment was then performed using the same procedures as the first experiment. Note that environmental conditions expected to result in minimal SCC were purposefully selected for the first SCC segment on a given sample, with more aggressive conditions employed during the second SCC segment. This approach was used to minimize the extent of crack path tortuosity, which can introduce error in the dcPD-measured crack length during the second precrack.

However, this use of a more aggressive environment during the second SCC segment often resulted in significant corrosion damage to the fracture surface (*e.g.*, due to anodic polarization), obfuscating a detailed fractographic evaluation of the first SCC segment.

After completion of the last SCC experiment for a given specimen, the sample was then cyclically loaded using a rising K_{max} protocol, where K_{max} increased from 17.5 to 22 MPa√m at R = 0.5 and f = 5 Hz from the final SCC crack length to a/W ≈ 0.75. This post-test fatigue step was used to better delineate the SCC portion of the experiment on the specimen fracture surface. Once the post-test fatigue increment was completed, the specimen was final fractured under displacement control, removed from the acrylic cell, and then ultrasonically cleaned in acetone for 15 minutes, followed by methanol for 15 minutes, and finally dried with canned air. Each specimen was then evaluated using a Quanta 650 scanning electron microscope (SEM) to obtain direct measurements of the precrack length and general images of the fracture morphology. The dcPD-measured V_0 was then recalibrated to the as-measured precrack length and the crack length versus time trace reanalyzed using Johnson's equation[39].

7.3.3 Measurement of Electrochemical Kinetics

All potentiodynamic polarization curves (PDS) were conducted using a Bio-Logic Multichannel Potentiostat (Bio-Logic SAS,Claix, France) running EC-Lab (Version 11.27) software in quiescent, full immersion conditions within a conventional three-electrode flat cell. A saturated calomel electrode (SCE) was used as a reference electrode, while a Pt mesh was used as a counter electrode in all scans. The exposed area of the working electrode sample was 0.12566 cm^2 and the scan rate was 10 mV/sec throughout all scans. Before each scan, the working electrode surfaces considered "bare" were polished to 400 grit using SiC paper. Surface treatments and coatings were preserved on the remaining samples by the lack of polishing, with tests run on the as-received surfaces. Duplicate scans were conducted to maintain consistency between both bare and treated/coated surfaces.

Anodic scans were conducted in 0.6 M NaCl solution at room temperature, with an open circuit potential (OCP) period of approximately 30 minutes before scanning in the electropositive direction to 1.5 V vs. OCP. Sporadic pitting on the surface was visible after each test, which was removed via grinding before subsequent tests.

Cathodic scans were conducted in a sodium sulfate ($\mathrm{Na_2SO_4}$) solution at room temperature to prevent localized pitting but maintain the same cathodic kinetics as NaCl[45]. Both $\mathrm{Na_2SO_4}$ and sodium bromide (NaBr) have been shown to be efficient surrogate solutions to NaCl, so long as the O_2 diffusion limited current densities (i_{lim}) are constant[45–47]. To simulate 0.6 M NaCl, an approximate value of 0.6 M $\mathrm{Na_2SO_4}$ was used, as the solutions are similar at low concentrations, but diverge at higher molarities. Each sample was allowed to be at OCP for approximately 30 minutes, before scanning electronegatively to -1.5 V vs. OCP commenced. Visually, no pitting was seen to occur on the sample surface after the cathodic scan, although for consistency, the surface was still polished between scans.

The working electrode surfaces included bare P675, Zn-Ni coated P675, anodized Ti-6Al-4V, and bare Ti-6Al-4V. Cathodic scans were conducted on all surfaces except the Zn-Ni coated P675, due to the relevant potential range never dropping below the Zn-Ni coated P675 OCP. Similarly, anodic scans were conducted on bare P675 and Zn-Ni coated P675, as either anodized Ti-6Al-4V or bare Ti-6Al-4V acted as the global cathode and their corresponding OCP mandated the noble bound of the potential. The Zn-Ni coating used on the P675 was designed to have a composition within the range of 12% Ni to 15% Ni.

Additional polarization behavior from literature was used to define representative deaerated conditions on the cathodic surfaces as may occur in occluded regions with restricted diffusion access. Under deaerated conditions, the cathodic kinetics of i_{lim} on austenitic stainless steels (such as SS316 and SS304) and platinum have been seen to decrease approximately an order of magnitude in 0.3 M NaCl to 0.9 M NaCl solutions, due to the decreased oxygen reduction reaction (ORR) rate[18,26,48]. Therefore, the bare P675 polarization behavior was scaled by an order of magnitude to lower current densities, to represent pseudo-deaerated conditions when needed and were denoted as "scaled-deaerated" conditions throughout this work. In the potential range of interest, anodized Ti-6Al-4V and bare Ti-6Al-4V do not have an O_2 diffusion limiting region, which would indicate that any deaeration effects on their respective cathodic kinetics would be minor.

7.3.4 Finite Element Modeling

Finite element method (FEM) modeling was conducted via COMSOL Multiphysics©, version 5.6.0.341, with the accompaniment of the Corrosion Module. Secondary current distributions were assumed throughout all systems, which considered electrochemical kinetics through the E vs. i dependence of the PDS, while the evolution of the species in the electrolyte and corresponding concentration dependencies on the current was neglected. That is, the Laplace Equation was used as the governing equation (Eq. 7.1), which innately assumes the conservation of charge and electroneutrality, and that all concentration gradients are negligible in comparison to the migration of ions within the electric field.

$$\nabla\Phi^2 = 0 \qquad 7.1$$

The electrolyte potential (Φ), current density (i), and conductivity (σ) can all be related through a form of Ohm's law (Eq. 7.2), which results from the simplified Nernst-Planck equation with the described assumptions above.

$$i = -\sigma \nabla \Phi \tag{7.2}$$

Due to the assumptions of electroneutrality and negligible concentration gradients, the conductivity must also be assumed to be constant. These assumptions were justified by the high concentrations of NaCl in relation to the concentration of any metal ions in solution, leading to NaCl acting as a supporting electrolyte. Further derivations and discussions of the use of the Laplace equation in localized corrosion modeling can be found elsewhere[49,50].

Therefore, the system was assumed to be in steady-state, with no time-dependencies. In all simulations, the current density and potential distributions were calculated. The total current in the system could be determined by an integration of the current density over the region of interest, such as all anodic or all cathodic surface areas. The conservation of charge, defining that the total anodic currents equal the total cathodic currents ($\sum I_a = \sum I_c$), was confirmed during each simulation, with the percent difference between the anodic and cathodic currents less than 0.0027% in all scenarios.

The geometry was built to represent a single raised fastener in a structural panel, with no washer present (Figure 7.1). Fastener/panel gaps were relatively large (200 μm), to simulate a clearance-fit system. The fastener was centered in an approximately 2 x 2 inch panel, and was assumed to be dry-installed, with solution in the fastener hole. The structural panel materials were either bare P675 or Zn-Ni coated P675, while the fastener material was either anodized or bare Ti-6Al-4V. Deaerated conditions of bare P675 were used within the fastener hole (Figure 7.1).

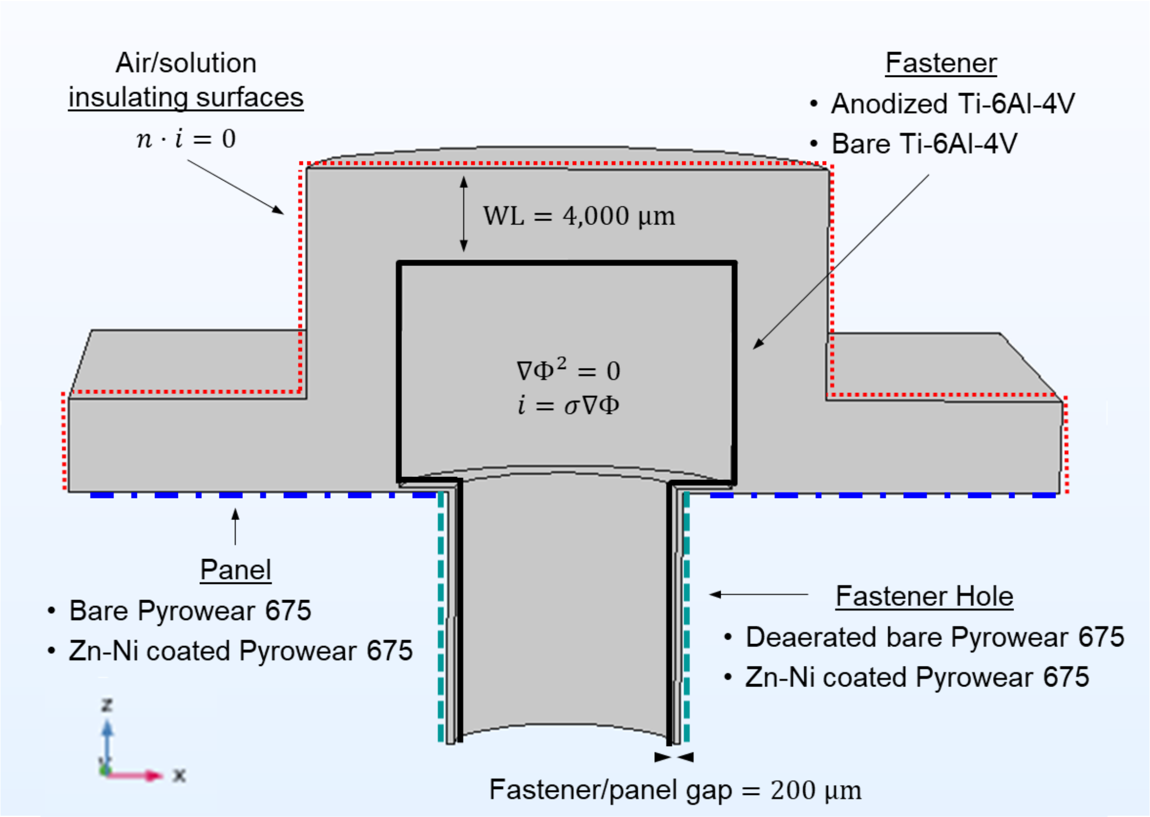

Figure 7.1: Schematic of the geometric variables and boundary conditions relation to the various scenarios tested, described in Table 7.2

The 3-D modeled domain represented the electrolyte, with boundary surfaces indicating either the material/solution interface or an insulating air/solution interface. A dynamic tetrahedral mesh was built with finer resolution near the fastener/panel gap, and the governing equation was solved spatially at each node in the mesh.

The experimentally determined PDS were fitted using a piece-wise cubic interpolation and input as boundary conditions on the respective material/solution interface surfaces as $i = f(E)$, where E is the electrode potential. In addition to the in-house tested PDS, polarization behavior from literature was used to inform a "scaling" factor to represent scaled-deaerated conditions, as described in the previous section above.

The water layer thickness (WL) was assumed to be continuous over the entire panel and conformal over the fastener head, representing full-immersion conditions. The natural convection boundary layer thickness (δ_{nc}), defining a threshold between bulk immersion kinetics and atmospheric conditions of accelerated cathodic kinetics, has been found to be approximately $800\ \mu\text{m}$ at room temperature in 0.6 M NaCl[51–54]. Therefore, any $\text{WL} > 800\ \mu\text{m}$ indicates full-immersion conditions. In this work, a $\text{WL} = 4{,}000\ \mu\text{m}$ was chosen with the solution of interest as 0.6 M NaCl, corresponding to a conductivity of 5.5 S/m, which is consistent with other full-immersion computational methods in literature[18,28,55].

7.4 Results

7.4.1. Effect of Applied Potential on SCC of P675

The measured stress intensity versus crack growth rate relationships for P675 immersed in 0.6 M NaCl at dK/dt = 4.0 MPa√m/hr are shown in Figure 7.2, at a variety of potentials ranging from -0.1 V_{SCE} to -0.9 V_{SCE}. A companion experiment performed in a known inert environment for high strength steels (dry N_2 gas at RH < 5%) at dK/dt = 4.0 MPa√m/hr is also included in Figure 7.2, to demonstrate the resolution limit of the experimental technique. At a constant K_J ~ 50 MPa√m, the crack growth rates at each applied potential were plotted, as shown in Figure 7.3. This process was replicated with new samples at a dK/dt = 0 MPa√m/hr.

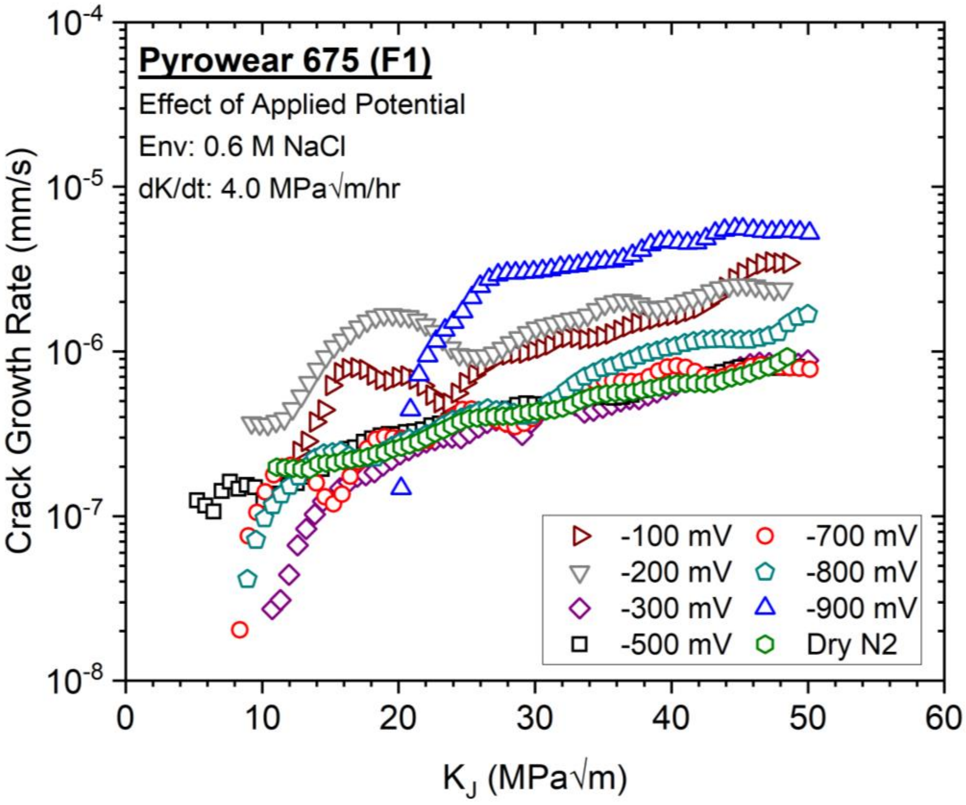

Figure 7.2: Measured crack growth rate versus K_J relationships as a function of applied potential for P675 immersed in 0.6 M NaCl under rising-K loading (dK/dt = 4.0 MPa√m/hr). The 'false' crack growth rate versus K_J relationship measured for P675 under a known inert environment of dry N_2 (RH < 5%) at dK/dt = 4 MPa√m/hr is provided for reference.

The dK/dt = 4 MPa√m/hr crack growth rate behavior indicated a clear U-shaped dependence, as seen in literature[2,11,12]. The high crack-growth rates occurring at electronegative potentials have been attributed to H_2 production and embrittlement, via the electrochemical cathodic reactions[12]. Conversely, the electropositive high crack-growth rates have been attributed to acidification via anodic dissolution[12].

The dK/dt = 4 MPa√m/hr indicates a more-aggressive environment than dK/dt = 0, via the narrowed gap in the low crack growth rate potential range and the higher crack-growth rates at a given potential (Figure 7.3). The range of low crack growth rate E-range for dK/dt = 4 was -0.7 V_{SCE} to -0.3 V_{SCE}, whereas the low crack growth rate E-range for dK/dt = 0 was -0.8 V_{SCE} to > -0.1 V_{SCE}. Therefore, going forward, the crack growth rates of dK/dt = 4 MPa√m/hr will be utilized in comparison with the FEM simulated data, to account for a worst-case scenario.

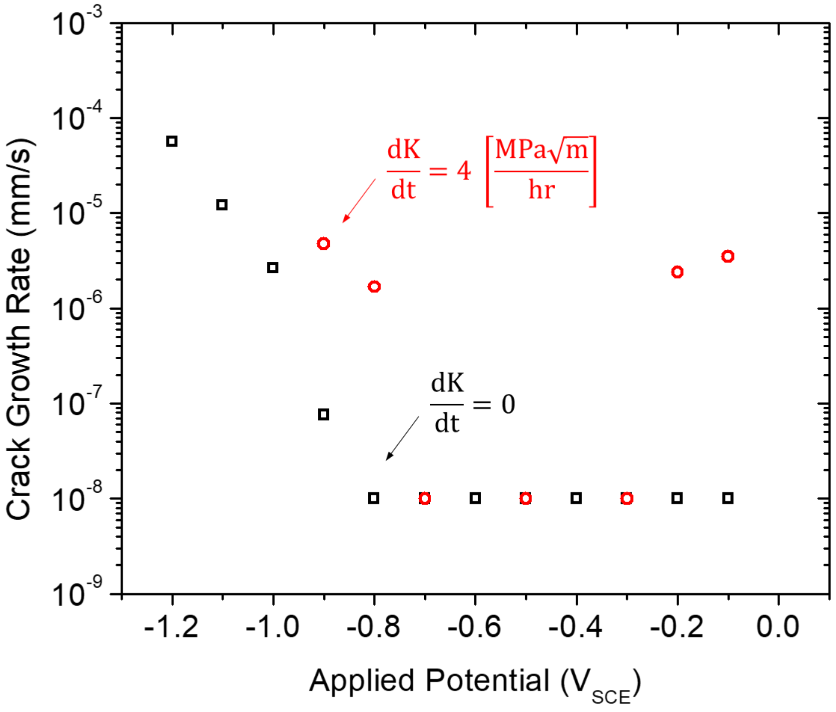

Figure 7.3: Effect of applied loading rate on the crack growth rate at $K_J \approx 50$ MPa√m as a function of applied potential for P675 immersed in 0.6 M NaCl.

7.4.2. Polarization Curves for Materials of Interest

On a bare P675 surface, separate anodic and cathodic PDS were conducted in 0.6 M NaCl and 0.6 M Na_2SO_4 solutions, respectively (Figure 7.4). The OCP was determined to be -0.38 V_{SCE}. On the anodic scan, metastable pitting events were visible prior to reaching the pitting potential

(E_{pit}), around 0.1 V_{SCE}. This value is consistent with literature, where E_{pit} on P675 in 0.01 M NaCl has been seen to be slightly lower (~0.075 V_{SCE}), as would be expected from the lower molarity solution[56].

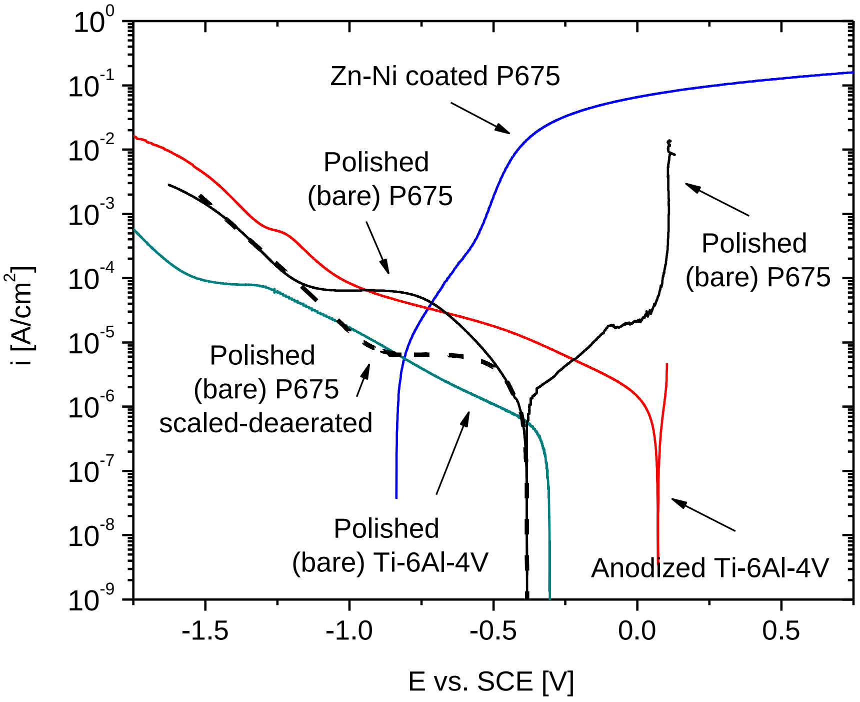

Figure 7.4: Potentiodynamic scans on 0.6 M NaCl (anodic) and 0.6 M Na_2SO_4 (cathodic)

The cathodic scan indicated a clear transition of cathodic reactions from the ORR to the hydrogen evolution reaction (HER) around -1.25 V_{SCE}, with $i_{lim} = 6.5 \times 10^{-5}$ A/cm^2. Scaled-deaerated conditions scaled back i_{lim} by an order of magnitude, simulating a decrease in the ORR rate, while the HER remained constant.

Zn-Ni coated P675 behaved as a strong sacrificial anode, with low potentials near that of pure Zn and an active surface indicated by the low polarizability (Figure 7.4). The OCP was determined to be -0.84 V_{SCE}. Note that a 48-hour OCP exposure on both the bare P675 and Zn-Ni coated P675 was conducted, as duplicate scans revealed a slight variation in the OCP of these samples. The Zn-Ni coated P675 OCP slowly varied between -0.84 V_{SCE} and -0.81 $V_{SCE,}$ while the bare P675 OCP steadily rose at a rate of approximately 0.9 mV/hr. Variations in P675 OCP have been seen previously in literature, with values differing up to -0.2 V, for a given heat treatment[56–58].

The polished bare Ti-6Al-4V surface had lower current densities than the bare P675 at all potentials, which has been seen previously in comparison to other stainless steels, due to the slow reaction rates on the Ti-6Al-4V surface (Figure 7.4)[18,28,59]. However, cathodic scans on anodized Ti-6Al-4V revealed both increased kinetics and an increased OCP, of -0.29 V_{SCE} to 0.07 V_{SCE}, in comparison to its bare-surfaced condition. Note that anodization surface treatment on the Ti-6Al-4V bolt was conducted to increase wear resistance and not corrosion resistance. In both Ti-6Al-4V surfaces, a limiting current density was observed around -1.3 V_{SCE}, which was outside of the potential range of interest in this work.

7.4.3. Modeling of Electrochemical Potential Distributions for Representative Geometry

Computational models were conducted with varying material selection combinations of boundary conditions on the fastener, panel surface, and panel within the fastener hole, described in Table 7.2. The first material combination represented one extreme scenario, in which the entire panel was bare P675, as could occur if the surface topcoat was delaminated or mechanically damaged and the fastener was dry-installed with no sealant applied within the hole. Anodic bare P675 curves were used as boundary conditions on the surface of the panel and within the fastener hole, whereas anodized Ti-6Al-4V was chosen to represent the fastener bolt. Based on mixed potential theory of the galvanic couple, the anodized Ti-6Al-4V material would act as the cathode while the bare P675 would act as the anode, with a driving force of 0.45 V_{SCE}, via the difference in the respective OCPs.

Table 7.2: Descriptions of the tested scenarios in a 0.6 M NaCl environment, with a continuous conformal WL = 4,000 µm over the entire panel and fastener

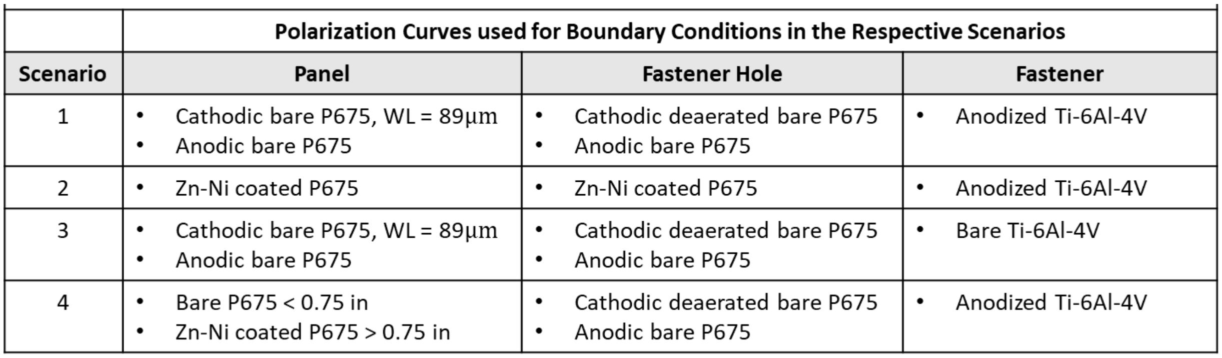

	Polarization Curves used for Boundary Conditions in the Respective Scenarios		
Scenario	**Panel**	**Fastener Hole**	**Fastener**
1	• Cathodic bare P675, WL = 89µm • Anodic bare P675	• Cathodic deaerated bare P675 • Anodic bare P675	• Anodized Ti-6Al-4V
2	• Zn-Ni coated P675	• Zn-Ni coated P675	• Anodized Ti-6Al-4V
3	• Cathodic bare P675, WL = 89µm • Anodic bare P675	• Cathodic deaerated bare P675 • Anodic bare P675	• Bare Ti-6Al-4V
4	• Bare P675 < 0.75 in • Zn-Ni coated P675 > 0.75 in	• Cathodic deaerated bare P675 • Anodic bare P675	• Anodized Ti-6Al-4V

False-color plots of the electrode potential on the anodic panel surfaces indicated a near uniform distribution on the surface, while a small gradient of potential occurred within the fastener hole (Figure 7.5(a)). As the fastener hole was a more occluded region than the surface of the panel, the solution resistance (ohmic potential drop) was larger, resulting in a gradient of potential. As the fastener hole represented the high-stress region of interest in the present geometry, focus was given to the potential distribution along that surface. Therefore, the distribution of potential only within the fastener hole could be plotted to determine both the most electronegative (-0.2850 V_{SCE}) and most electropositive (-0.2835 V_{SCE}) potentials which may occur (Figure 7.5 (b)).

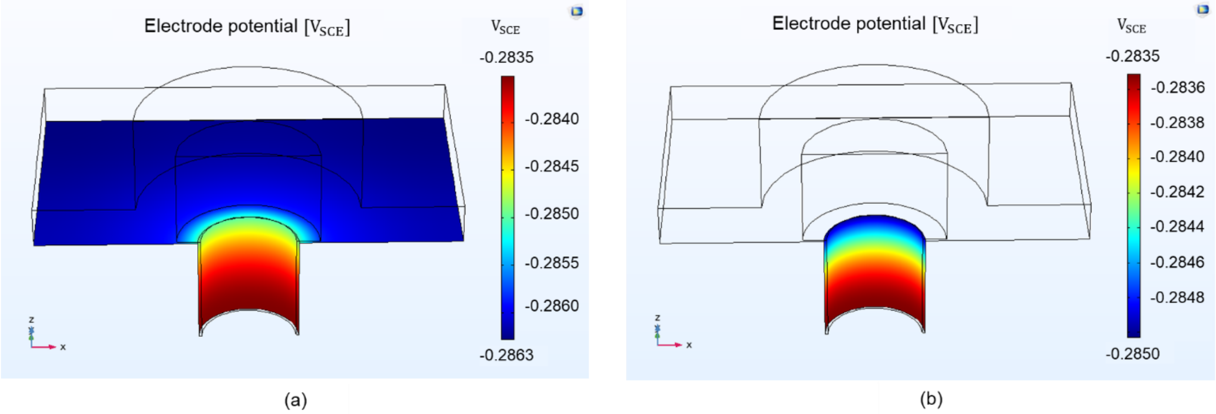

Figure 7.5: False-color plot of a bare P675 panel with an anodized Ti-6Al-4V bolt (scenario 1) with the potential distribution (a) over the entire panel and (b) only within the fastener hole, in a 0.6 M NaCl environment

The "maximum" and "minimum" potential range within the fastener hole were then plotted on a number line, where the width of the line represented the distribution, and correspondingly the ohmic drop, within the fastener hole (Figure 7.6). Dashed vertical lines represented the OCP of each material for clarity, as mixed potential theory dictates that the potential in the system must be bounded between the OCP of the given anode and the cathode.

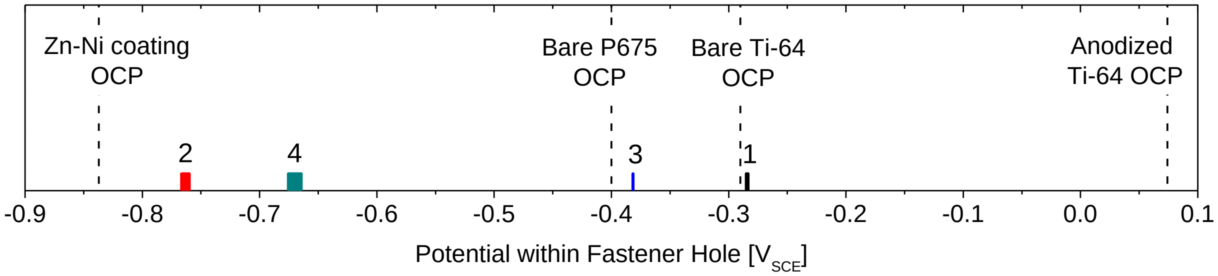

Figure 7.6: Potential distribution within the fastener hole in a 0.6 M NaCl environment, with numeric labels correlating to the defined scenarios in Table 7.2. Dashed lines represent the OCP of the respective tested materials.

Using the same methodology as above, the boundary conditions were modified to simulate the anodic panel material coated with Zn-Ni, which would correspond to a sacrificial anode (that is, cathodic protection) without any surface defects or delamination (Table 7.2). The fastener remained as an anodized Ti-6Al-4V bolt, resulting in nearly a 1 V driving force for galvanic corrosion. The resulting potential distribution within the fastener hole was pulled electronegatively nearly -0.5 V from the potential in the first scenario which corresponded to a bare P675 panel (Figure 7.6).

An additional simulation was performed in which the panel was bare P675 (anodic) and the fastener was bare Ti-6Al-4V (cathodic), as installed bolts may not always have a surface treatment or coating (Table 7.2). The bare Ti-6Al-4V OCP was very similar to the bare P675, resulting in a low driving force and a narrow window for the potential to occur between the two bounds of OCP. Therefore, the potential range within this third material selection scenario was very narrow, with 0.1 mV difference between the top and base of the fastener hole (Figure 7.6).

Lastly, a distant coating was simulated at a radius of 0.75 in from the fastener, as might be achieved through selective plating of the Zn-Ni (Table 7.2). The remaining panel, within the 0.75 in radius and within the fastener hole, was bare P675 while the fastener was an anodized Ti-6Al-4V bolt. In this three-material system, both the bare P675 and anodized Ti-6-Al-4V contributed cathodic current towards preferential dissolution of the anodic Zn-Ni coating. Scaled-deaerated bare P675 cathodic boundary conditions were used within the fastener hole, to represent the limited diffusion and corresponding low O_2 concentrations in the occluded region, while aerated quiescent boundary conditions of bare P675 were used on the non-coated surface portions of the panel (Figure 7.4).The resulting potential distribution within the fastener hole was slightly more electropositive than the second scenario, due to less total Zn-Ni surface area, which reduces the electronegative polarization of the sample (Figure 7.6).

7.5 Discussion

The preceding results demonstrate that P675 immersed in 0.6 M NaCl is highly resistant to SCC under both active and static loading conditions when polarized to electrochemical potentials between -0.7 and -0.3 V_{SCE}. The objectives of the following discussion are twofold: 1) comment on the utility of coupling SCC measurements and FEM of electrochemical potential distributions for informing engineering design, and 2) highlight the limitations and areas for improvement in the current approach.

Although the potential ranges within the fastener hole (ranging from 0.1 mV to 11 mV) seemed negligible with the present material selection scenarios, their importance would be highlighted if the edge of the crack growth rate well coincided with those potentials. As the edge of the cracking well rapidly increases (on a log-scale) to high crack growth rates, any small variations in potential, even to the 10's of mV range, could severely impact the cracking kinetics.

Conventional corrosion prevention techniques often include cathodic protection through a sacrificial anodic coating[60,61]. Although technically corrosion is still occurring, and not being "prevented" at all, the corrosion damage through this technique is controlled and deferred to occur on the coating rather than any structural components of the system. As the coating preferentially deteriorates, a fresh coat of the metallic film could revitalize the system and the cathodic protection process. Therefore, out of the material combinations tested in this work, the second scenario would seemingly correspond to a corrosion-friendly system. However, when the potential distribution within the fastener hole was plotted with the LEFM crack growth rate data, it was seen that this was not the case, as the Zn-Ni coating *overpolarized* the system into the electronegative side of the high crack growth rates (Figure 7.7).

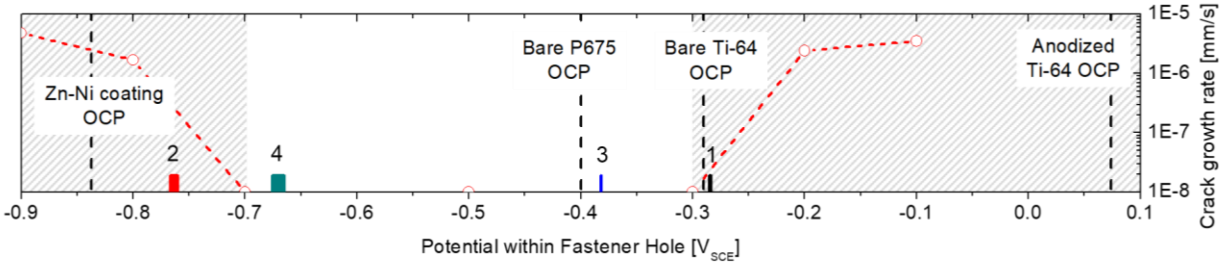

Figure 7.7: Simulated potential distributions within the fastener hole, with various material selection scenario, (Figure 7.6) overlaid with the crack growth rate as a function of applied potential (Figure 7.3) on the secondary x-axis. Grey dashed regions represent high crack growth rates

However, not coating the system with Zn-Ni at all and relying on the bare P675, corresponding to scenario one, was also problematic as the high OCP of the anodized Ti-6Al-4V bolt pulled the potential range into the electropositive side of the high crack growth rate well (Figure 7.7). Utilizing instead a bare Ti-6Al-4V bolt, the potential within the fastener hole was restricted to occur between the respective OCP of the two materials, which happened to lie in the low crack growth regime (Figure 7.7). However, the bare P675 still acted as the global anode in the system, which could result in mass loss of the structural component.

The distant coating scenario combined the benefits of cathodically polarizing the structural bare P675 (switching the surface reactions from anodic dissolution to cathodic reduction reactions), while also maintaining the potentials within the low crack growth regime (Figure 7.7). Although the delineation of the 0.75 in radius from the fastener was chosen arbitrarily, the decrease in surface area of the Zn-Ni coating prevented overpolarization of the system.

7.6 Limitations

Within the present work, the FEM model was assumed to be in full-immersion conditions. Although useful for a first-approximation, atmospheric conditions may be more realistic for applications involving fastener-in-panel designs. Furthermore, the WL may not be completely continuous over the entire surface, which could result in increased current densities and more electropositive polarization through unfavorable cathode:anode surface area ratios.

In addition, the electrolyte was assumed to be homogenous and in steady-state, which may be a simplification based on the localized corrosion pitting events which are common on steel surfaces[62–64]. However, recent work has shown that if the boundary conditions correctly capture the active corrosion behavior occurring on the surface, then the steady-state Laplace equation (and corresponding homogenous electrolyte assumption) is valid for a global approximation[65].

Assumptions on the distant coating mitigation strategy resulting from this work should also be appreciated. The computational model did not account for the dissolution of the coating, which, over time, would change the surface area and correspondingly the polarization of the fastener hole. In addition, no compositional variations within the Zn-Ni coating were considered.

Note that the effect of atmospheric conditions, a discontinuous WL, local hot spots, and varying Zn-Ni compositions on the potential distribution within the fastener hole will be investigated in Chapter 8.

7.7 Conclusion

An initial framework to mitigate stress corrosion cracking system via material and coating selection has been proposed, through a combined analysis of FEM and LEFM results. Of four total material selection scenarios tested, two were concluded to result in high crack-growth rate susceptibilities of the fastener hole through overpolarization electronegatively and electropositively by the Zn-Ni coating and anodization on the Ti-6Al-4V fastener, respectively. Two remaining scenarios resulted in optimum, low crack-growth rate susceptibilities, through selective plating and a bare Ti-6Al-4V surface. The present initial analysis will be extended in Chapter 8.

7.8 Acknowledgements

This research was financially supported by Rolls Royce Corporation, with specific thanks to Michelle Boehm, Megan Snellenberger, JD Smith, Skylar Conn, Brian Drier, Tim Cummings, Bradford Wiley, Randa Brice, Mike Whitten, and Ann Heeter.

7.9 References

1. Brown, B.F., *Stress Corrosion Cracking Control Measures* (1977).
2. Harris, Z.D., and J.T. Burns, *Corrosion and Materials Degradation* 2 (2021): pp. 360–375.
3. Newman, R.C., *CORROSION* 57 (2001): pp. 1030–1041, http://meridian.allenpress.com/corrosion/article-pdf/57/12/1030/1534678/1_3281676.pdf.
4. RAO, A.C.U., V. VASU, M. GOVINDARAJU, and K.V.S. SRINADH, *Transactions of Nonferrous Metals Society of China (English Edition)* 26 (2016): pp. 1447–1471, http://dx.doi.org/10.1016/S1003-6326(16)64220-6.
5. Horner, D.A., B.J. Connolly, S. Zhou, L. Crocker, and A. Turnbull, *Corrosion Science* 53 (2011): pp. 3466–3485, https://www.sciencedirect.com/science/article/pii/S0010938X11002721 (Jun. 17, 2018).

6. Steiner, P.J., and J.T. Burns, *Corrosion* 74 (2018): pp. 1117–1131.

7. Steiner, P.J., Z.D. Harris, C.V. Moraes, R.G. Kelly, and J.T. Burns, *Corrosion* 77 (2021): pp. 838–852.

8. Mcmurtrey, M.D., D. Bae, and J.T. Burns, (2016).

9. Burns, J.T., J.M. Larsen, and R.P. Gangloff, *Fatigue & Fracture of Engineering Materials & Structures* 34 (2011): pp. 745–773, https://doi.org/10.1111/j.1460-2695.2011.01568.x.

10. BROWN BF, FUJII CT, and DAHLBERG EP, *Journal of The Electrochemical Society* 116 (1969): pp. 218–219.

11. Cooper, K.R., and R.G. Kelly, *Corrosion Science* 49 (2007): pp. 2636–2662.

12. Lee, Y., and R.P. Gangloff, *Metallurgical and Materials Transactions A: Physical Metallurgy and Materials Science* 38 A (2007): pp. 2174–2190.

13. Harrison, T.J., B.R. Crawford, G. Clark, and M. Brandt, *Advanced Materials Research* 891–892 (2014): pp. 242–247.

14. Harrison, T.J., B.R. Crawford, M. Brandt, and G. Clark, *Computational Materials Science* 84 (2014): pp. 74–82, http://dx.doi.org/10.1016/j.commatsci.2013.11.033.

15. Harrison, T.J., B.R. Crawford, C. Loader, G. Clark, and M. Brandt, *International Journal of Fatigue* 82 (2016): pp. 700–707, http://dx.doi.org/10.1016/j.ijfatigue.2015.09.028.

16. Lo, M., R. Jones, A. Bowler, M. Dorman, and D. Edwards, *Fatigue and Fracture of Engineering Materials and Structures* 40 (2017): pp. 1664–1675.

17. Cocke, C., R.S. Marshall, C. Sprinkle, A. Goff, R.G. Kelly, and J.T. Burns, *Corrosion* 78 (2022): pp. 152–162.

18. Marshall, R.S., R. Kelly, A. Goff, and C. Sprinkle, *Corrosion* 75 (2019): pp. 1461–1473.

19. Young, P.S., and J.H. Payer, *Corrosion* 71 (2015): pp. 1278–1293.

20. Moran, A., J. Jennings, H. Nee, S. Pearson, B. Clark, and R.S. Lillard, *Corrosion Journal* 75 (2019): pp. 484–498.

21. Rafla, V.N., and J.R. Scully, *Corrosion Journal* 75 (2019): pp. 12–28.

22. Rafla, V., A. Davenport, and J.R. Scully, *Corrosion Communications* 71 (2015): pp. 1171–1176.

23. Rafla, V.N., A.D. King, S. Glanvill, A. Davenport, and J.R. Scully, *Corrosion* 74 (2018): pp. 5–23.

24. Rafla, V.N., and J.R. Scully, *Corrosion* 75 (2019): pp. 587–603.

25. Snihirova, D., D. Höche, S. Lamaka, Z. Mir, T. Hack, and M.L. Zheludkevich, *Corrosion Science* 157 (2019): pp. 70–78, https://doi.org/10.1016/j.corsci.2019.04.036.

26. Liu, C., V.N. Rafla, J.R. Scully, and R.G. Kelly, "Mathematical Modeling of Potential and Current Distributions for Atmospheric Corrosion of Galvanic Coupling in Airframe Components," in NACE International: CORROSION (2015), pp. 1–11.

27. Moraes, C. v., R.J. Santucci, J.R. Scully, and R.G. Kelly, *Journal of The Electrochemical Society* 168 (2021): p. 051505.

28. Marshall, R.S., A. Goff, C. Sprinkle, A. Britos, and R. Kelly, *Corrosion* 76 (2020): pp. 476–484.

29. Marshall, R.S., R.M. Katona, M.A. Melia, and R.G. Kelly, *J Electrochem Soc* 169 (2022): p. 021506.

30. Li, W., D. Li, Z. Yu, Y. Xie, F. Liu, and Y. Jin, *Journal of Electroanalytical Chemistry* 882 (2021): p. 114977, https://doi.org/10.1016/j.jelechem.2021.114977.

31. Duddu, R., N. Kota, and S.M. Qidwai, *Journal of Applied Mechanics, Transactions ASME* 83 (2016): pp. 1–10.

32. McCaffrey, T.J., and D.E. Wert, "Development of a Stainless Corrosion Resistant Carburizing Bearing Steel," in ASTM Special Technical Publication 1195: Creative Use of Bearing Steels, ed. J.J.C. Hoo (Philadelphia: American Society for Testing and Materials, 1993), pp. 137–148.

33. Trivedi, H.K., L. Rosado, D.T. Gerardi, G.D. Givan, and B. McCoy, "Fatigue Life Performance of Hybrid Angular Contact Pyrowear 675 Bearings," in Bearing Steel Technologies: 11th Volume, Advances in Steel Technologies for Rolling Bearings, ASTM STP1600, ed. J.M. Beswick (West Conshohocken, PA: ASTM International, 2017), pp. 275–295.

34. *Alloy Digest* 43 (1994): pp. 10–11.

35. ASTM A693-16, *ASTM International* (2016).

36. Tada, H., P. Paris, and G. Irwin, *The Stress Analysis of Cracks Handbook* (St. Louis, MO: Paris Productions Incorporated, 1985).

37. Gangloff, R.P., D.C. Slavik, R.S. Piascik, and R.H. Van Stone, "Direct Current Electrical Potential Measurement of the Growth of Small Cracks," in Small-Crack Test Methods, ASTM STP 1149, eds. J.M. Larsen, and J.E. Allison (Philadelphia: American Society for Testing and Materials, 1992), pp. 116–168.

38. Donald, J.K., and J. Ruschau, "Direct Current Potential Difference Fatigue Crack Measurement Techniques," in Fatigue Crack Measurement: Techniques and Applications, eds. K.J. Marsh, R.A. Smith, and R.O. Ritchie (EMAS, 1991), pp. 11–37.

39. Johnson, H.H., *Materials Research and Standards* 5 (1965): pp. 442–445.

40. "ASTM Standard E647-13: Standard Test Method for Measurement of Fatigue Crack Growth Rates" (West Conshohocken, PA: ASTM International, 2013).

41. Kumar, V., M.D. German, and C.F. Shih, "An Engineering Approach for Elastic-Plastic Fracture Analysis" (Palo Alto, CA: Electric Power Research Institute, 1981).

42. Harris, Z.D., E.M. Dubas, A.S. Popernack, B.P. Somerday, and J.T. Burns, *Theoretical and Applied Fracture Mechanics* 111 (2021): p. 102846.

43. Harris, Z.D., and J.T. Burns, *Corrosion and Materials Degradation* 2 (2021): pp. 360–375.

44. Harris, Z.D., and J.T. Burns, *Corrosion Science* 201 (2022): p. 110267.

45. Liu, C., and R.G. Kelly, *Corrosion* 75 (2019): pp. 1087–1099.

46. Katona, R.M., J. Carpenter, E.J. Schindelholz, and R.G. Kelly, *J Electrochem Soc* 166 (2019): pp. C3364–C3375.

47. Katona, R.M., A.W. Knight, E.J. Schindelholz, C.R. Bryan, R.F. Schaller, and R.G. Kelly, *Electrochimica Acta* 370 (2021): p. 137696, https://doi.org/10.1016/j.electacta.2020.137696.

48. Liu, C., P. Khullar, and R.G. Kelly, *Journal of The Electrochemical Society* 166 (2019): pp. 153–161.

49. Liu, C., and R.G. Kelly, *Corrosion Journal* 75 (2019): pp. 1285–1299.

50. Newman, J., and K.E. Thomas-Alyea, *Electrochemical Systems*, Third Edit (Wiley-Interscience, 2004).

51. Liu, C., J. Srinivasan, and R.G. Kelly, *J Electrochem Soc* 164 (2017): pp. C845–C855, http://jes.ecsdl.org/lookup/doi/10.1149/2.1641713jes.

52. Katona, R., J. Carpenter, A. Knight, R.S. Marshall, B. Nation, E. Schindelholz, R.F. Schaller, and R. Kelly, *J Electrochem Soc* 168 (2021), https://iopscience.iop.org/article/10.1149/1945-7111/abeb29.

53. Charles-Granville, U.-E., C. Liu, J.R. Scully, and R.G. Kelly, *Journal of The Electrochemical Society* 167 (2020): p. 111507.

54. Tomashov, N.D., *CORROSION* 20 (1964).

55. Liu, C., G.W. Kubacki, and R.G. Kelly, *Corrosion Journal* 75 (2019): pp. 465–473.

56. Kvryan, A., C.M. Efaw, K.A. Higginbotham, O.O. Maryon, P.H. Davis, E. Graugnard, H.K. Trivedi, and M.F. Hurley, *Materials* 16 (2019).

57. Kvryan, A., “The Influence of Heat Treatment on Corrosion Behavior of Martensitic Stainless Steel Uns 42670,” Boise State University, 2019.

58. Kvryan, A., N.A. Carter, H.K. Trivedi, and M.F. Hurley, *Tribology Transactions* 63 (2020): pp. 265–279.

59. Matzdorf, C.A., W.C. Nickerson, B.C. Rincon Troconis, G.S. Frankel, L. Li, and R.G. Buchheit, *Corrosion* 69 (2013): pp. 1240–1246.

60. Wint, N., S.L. Wijesinghe, W. Yan, W.K. Ong, L.Y. Wu, G. Williams, and H.N. McMurray, *Journal of The Electrochemical Society* 166 (2019): pp. C434–C444.

61. Sadananda, K., J.H. Yang, N. Iyyer, N. Phan, and A. Rahman, *Corrosion Reviews* 39 (2021): pp. 487–517.

62. Schwenk, W., *Corrosion* 20 (1964): pp. 129t–139t.

63. Frankel, G.S., L. Stockert, F. Hunkeler, and H. Boehni, *Corrosion* 43 (1987): pp. 429–436.

64. Pistorius, P.C., and G.T. Burstein, *Phil. Trans. R. Soc. Lond A* (1992): pp. 531–559.

65. Charles-Granville, U.-E., R.S. Marshall, C. v. Moraes, C.F. Glover, J.R. Scully, and R.G. Kelly, *Journal of The Electrochemical Society* 169 (2022): p. 031502.

Chapter 8: A Materials Selection Framework for Fastener-in-Panel Geometries Using FEM and LEFM, to Mitigate Coating Degradation and Hydrogen Embrittlement

Rebecca Skelton Marshall, Zach D. Harris, Morgan K. Small, Keegan L. Brunner, Jimmy T. Burns, Rob G. Kelly

University of Virginia, 395 McCormick Rd, Charlottesville VA 22903

Authorship contributions: R. Skelton Marshall (formal analysis, computational work, experimental polarization behavior, and writing – original draft), Z. D. Harris (fracture mechanics investigation, and writing – review & editing), M. K. Small (experimental polarization behavior), K. L. Brunner (experimental polarization behavior), J. T. Burns (funding acquisition, technical expertise and advice)

8.1 Abstract

A finite element method (FEM) model was used to determine the resulting potential, current, and current density distribution of a multi-material fastener/hole-in-plate configuration in an atmospheric environment. The plate consisted of bare Pyrowear 675 (P675) with or without a ZnNi coating, and the fastener consisted of Ti-6Al-4V with or without an anodization surface treatment. The potential distribution within the fastener hole was the focus of this work, as this region would represent the location of highest stress within the fastener/panel geometry. Separately, fracture mechanics testing was used determined the crack growth rate as a function of potential on a bare P675 in both a 0.6 M NaCl and 3 M NaCl environment. Combining the

LEFM and FEM results allowed for a united framework which was able to narrow a material selection matrix of 13 total scenarios to three scenarios, in an atmospheric environment of 0.6 M NaCl, specifically. Accounting for a decrease in RH, and the corresponding evaporation of the WL, was also simulated with only one of the studied material selection combinations able to reduce the crack susceptibility. A single pit within the fastener hole was also considered, and it was determined that the size of the pit had a larger impact on the potential than the location of the pit, which will aid in future computational assumptions.

8.2 Introduction

Cracking and corrosion kinetics are arguably two of the most important properties when determining structural maintenance and design, as the cost due to these processes is significant[1–3]. For structures under mechanical loads in corrosive environments, stress-corrosion cracking (SCC) is a concern. The SCC process is extremely complex, as both corrosion and cracking mechanisms are dependent on the location and environment of a system[4–10].

Complex geometries can complicate design consideration with respect to corrosion and SCC. In particular, a fastener hole can serve as a location in which the corrosion rate increases via an accumulation of aggressive species from galvanic-induced crevice corrosion[11–14], and acts as a stress concentrator[15], increasing the probability of crack nucleation and growth. Cocke *et al.,* conducted fatigue cracking of a pre-corroded fastener panel geometry with external surface defects, and found that cracks initiated at corrosion damage within the fastener hole, independent of the surface corrosion damage[5].

In addition, stress corrosion cracking on high-strength steels is enhanced by hydrogen embrittlement[16,17]. Specifically, on a high-strength steel (AERMET 100) SCC kinetics has been found to have a U-shaped dependence on the applied potential, with the high-crack growth rates at electronegative potentials attributed to H_2 production and embrittlement, and the electropositive high-crack growth rates attributed to acidification via anodic dissolution[18]. A potential dependence on the crack growth rate has also been observed to occur within aluminum alloys (AA), AA7XXX[19,20]. When an electrolyte is present over a multi-material system, galvanic coupling can occur, shifting the coupled potential to more electropositive or more electronegative values[21–28].

Mixed potential theory can predict the coupled potential based off of the individual electrochemical kinetics of each material, but predictions are limited to systems with no ohmic drop and simple geometries[29]. Therefore, only small, planar bulk-immersion geometries can be used in these predictions, as no potential distributions or coupling of more than two materials can be considered. However, in recent years, FEM modeling has been used to determine the current and potential distributions along complex geometries or multi-material galvanic systems[21–25,30].

Furthermore, FEM models are able to calculate the ohmic potential drop present in thin-film atmospheric conditions, which are often useful for structural applications on land, as opposed to full-immersion marine applications[31–33] . Corrosion kinetics in atmospheric conditions have been found to increase with decreasing water layer thicknesses less than the natural convection boundary layer thickness, which results in a more-aggressive environment than bulk conditions[34–38]. In addition, a novel method by Steiner *et al.*, was recently developed using aluminum oxide films to investigate the linear elastic fracture mechanics (LEFM) behavior on AA 5XXX in thin-film conditions, finding a difference in crack growth rate kinetics as opposed to full immersion conditions[4,39].

To prevent structural degradation of structural steel components, in full-immersion or atmospheric conditions, cathodic protection is often employed[40]. Zn-Ni has become a popular alternative to the more-toxic Cr-coatings for the protection of ferrous alloys, as the low open circuit potential (OCP) of Zn leads to a strong driving force for sacrificial anodic dissolution, while the addition of Ni moderates the highly-active surface, enhancing the coating lifetime[40,41].

Computational simulations on fastener/panel complex geometries have either assumed that no coating was present on the surface of the panel, or that the coating (such as a topcoat) was perfectly insulating except for intentional surface defects[21,22,25,30]. Other computational works have focused on the leaching and degradation of a coating, with emphasis on the coating potential and current density, as the coating and solution evolve with time[42–44]. However, a simplified scribe geometry was used in these leaching models, thereby focusing on the galvanic coupling between the coating and the matrix and not accounting for any macro-cathodic surfaces, such as the presence of a fastener.

Therefore, the present work focuses on coating the structural anode in a fastener/panel geometry with a sacrificial coating (cathodic protection), with consideration given to both the coating composition and location. In addition, the surface treatment of a fastener will be evaluated as an additional mitigation technique, with the goal of engineering the potential into low-cracking regimes. The structural material under investigation is Pyrowear 675®, as it was found to have optimized mechanical properties in comparison to other conventional bearing steels [45,46], whereas the fastener material of focus was Ti-6Al-4V. Thorough research on the crack growth and corrosion properties on Pyrowear 675® are lacking in literature, not to mention the effects of its coupling to a Ti-6Al-4V fastener.

Previous work laid the foundation for combining LEFM and FEM techniques as a materials selection framework to prevent hydrogen embrittlement in full-immersion conditions with a single molarity solution of 0.6 M NaCl (Chapter 7). The present work expands on that foundation through considering atmospheric conditions, rather than full immersion, as well as more thorough combinations of the materials of interest. In addition, the presence of a pitting "hot spot" and a discontinuous water layer thickness (WL) were considered, to increase the robustness of the present framework to more-complex, albeit realistic, systems.

8.3 Methods

Fracture Mechanics

The fracture mechanic methodology conducted was identical to that in Chapter 7, with the exception of the solution concentration of 3 M NaCl, rather than 0.6 M NaCl. Additional experimental details can be found in a recent publication by Harris *et al.*,[47].

Electrochemical Polarization

Using a three-electrode flat cell, potentiodynamic polarization curves (PDS) were conducted using a Bio-Logic Multichannel Potentiostat (Bio-Logic SAS,Claix, France) running EC-Lab (Version 11.27) software, in quiescent, full immersion conditions. A saturated calomel electrode (SCE) and platinum mesh were used as a reference electrode and counter electrode, respectively, in all scans. The exposed area of the working electrode on each respective sample was 0.12566 cm^2, and was polished to 400-grit using SiC paper, if considered "bare" surfaces. Otherwise, surface treatments and coatings were preserved by the lack of polishing, rinsed with DI water a Kim wipe, and scans were run on the as-received surfaces. All potentials were scanned at a rate of 10 mV/sec, with duplicate tests conducted to assess reproducibility.

Anodic scans were conducted in 3 M NaCl solutions at room temperature, with an open circuit potential (OCP) exposure of approximately 30 minutes before scanning in the electropositive direction to 1.5 V vs. OCP. Cathodic scans were conducted in sodium sulfate ($\mathrm{Na_2SO_4}$) solutions at room temperature to prevent localized pitting but maintain the same cathodic kinetics as NaCl[48]. Both Na_2SO_4 and sodium bromide (NaBr) have been shown to be efficient surrogate solutions to NaCl, as long as the O_2 diffusion limited current densities (i_{lim}) are constant[48–50]. Equivalent values of i_{lim} were calculated through the Levich equation, which relates the O_2 diffusivity, saturated O_2 concentration, and kinematic viscosity of the respective solution, with the thermodynamic constants above calculated through OLI Studio Analyzer™.

A solution of 1.55 M Na_2SO_4 was found to have an equivalent i_{lim} to 3 M NaCl and was used as a surrogate solution for that environment. No pitting was observed on the sample surfaces after the cathodic scan, although for consistency, the surface was still polished to 400-grit between scans. Each scan was first exposed at OCP for approximately 30 minutes before scanning electronegatively to -1.5 V vs. OCP.

The materials of interest included bare Pyrowear 675® (P675), Zn-Ni coated P675, anodized Ti-6Al-4V, and bare Ti-6Al-4V. Cathodic scans were conducted on all surfaces except the Zn-Ni coated P675, and anodic scans were conducted on all surfaces except the anodized Ti-6Al-4V, due to the relevant potential range never exceeding either the Zn-Ni coated P675 OCP nor the anodized Ti-6Al-4V OCP.

The Zn-Ni-coated P675 was designed to be within the range of 12% Ni to 15% Ni. However, comparing the previously measured behavior in 0.6 M NaCl with composition-controlled Zn-Ni coatings in 0.6 M NaCl from literature, the in-house tested Zn-Ni coated P675 seemed to align best with a composition of 11% Ni[51] (Chapter 7). Therefore, in the work going forward, the coated P675 tested in-house will be defined as Zn-11%Ni. To evaluate the impact of the coating composition, results from Tafreshi *et al.,* in 0.6 M NaCl for Zn-14% and Zn-17%Ni were extracted and utilized in this work, as a comparison to the Zn-11%Ni in-house scan[51].

Additional polarization data from literature were used to define representative deaerated and thin-film conditions on bare P675. Pryor et al., demonstrated that the current density of a given galvanic couple would decrease in solutions with little-to-no $\mathrm{O_2}$ (such as when purged with helium), and would correspondingly increase to higher rates than natural aerated conditions, when $\mathrm{O_2}$ was bubbled in solution[52]. More specifically, under deaerated conditions, the cathodic kinetics on austenitic stainless steels (such as SS316 and SS304) and platinum have been seen to decrease approximately an order of magnitude in 0.3 M NaCl, 0.5 M NaCl and 0.9 M NaCl solutions, due to the decreased oxygen reduction reaction (ORR) rate[21,25,53]. Although the focus of this work is on a martensitic stainless steel of P675, austenitic stainless steel can be used to broadly estimate the electrochemical behavior under the given system. Therefore, the bare P675 polarization behavior was scaled by an order of magnitude to lower current densities, to represent deaerated conditions.

Conversely, under thin-film solutions with thickness less than the natural convection boundary layer thickness (δ_{nc}), the cathodic kinetics can be increased due to faster O_2 diffusion to the surface, which correspondingly increases the ORR rate. As atmospheric conditions were the focus of this work, both previously conducted 0.6 M NaCl and presently-conducted 3 M NaCl PDS were scaled to represent the thin-film accelerated kinetics (Chapter 7). In a 0.6 M NaCl and 3 M NaCl solution at room temperature, δ_{nc} has been found to be approximately 800 µm and 600 µm, respectively[35–37]. Therefore, in 0.6 M NaCl at a WL $= 89$ µm, $< \delta_{nc}$, Liu *et al.,* determined the increased cathodic kinetics on SS316 to be $i_{lim} \cong 1.9 \times 10^{-4}\ \mathrm{A/cm^2}$, through a rotating disk electrode (RDE) spinning at 50 rpm[35]. Correspondingly, the bare P675 behavior in full immersion 0.6 M NaCl solution was scaled by 2.85 to have an equal i_{lim} to the accelerated kinetics found on SS316.

Polarization curves by Katona *et al.,* on SS304 in 3 M NaCl also indicated an increase in cathodic kinetics, with $i_{lim} = 2 \times 10^{-4}\ \mathrm{A/cm^2}$ at a $\mathrm{WL} = 20\ \mu\mathrm{m}$ (approximately 1000 rpm)[36]. Correspondingly, the bare P675 in 3 M NaCl was scaled by 4.4 to have an equivalent i_{lim} representing the thin-film conditions of $\mathrm{WL} = 20\ \mu\mathrm{m}$. Note that Alexander *et al.,* also found similar values of i_{lim} on SS304 surfaces, for $\mathrm{WL} = 88\ \mu\mathrm{m}$ in 0.6 M NaCl and $\mathrm{WL} = 20\ \mu\mathrm{m}$ in 3 M NaCl[38].

In addition, anodic and cathodic scans in 0.6 M NaCl and 0.6 M $\mathrm{Na_2SO_4}$, respectively, were conducted in previous work on the identical materials of interest. The 0.6 M NaCl PDS were utilized in the present work as well, with a different WL and to compare the impact of RH on the system. Details on the methodology of the 0.6 M NaCl scans has been discussed previously (Chapter 7). Additionally, kinetics on activated P675 surfaces in 0.6 M NaCl were conducted, in which the surface was held by a high potential hold above the pitting potential (1 V vs. OCP) for 1 hr after the OCP hold, before scanning electronegatively towards the OCP. Visually, samples suffered from extreme pitting after these scans, in comparison to the conventional electropositive anodic scans. Scanning from positive potentials to more negative potentials has been used previously in literature, to capture the active anodic pitting kinetics of aluminum alloys[25,26]. Pitting scans were conducted only on the bare P675 surface.

Electrochemical Modeling

Finite element method (FEM) modeling was conducted via COMSOL Multiphysics©, version 5.6.0.341, utilizing the Corrosion Module. Secondary current distributions were assumed throughout the system, which invokes the Laplace Equation as the governing equation (Eq. 8.1).

$$\nabla\Phi^2 = 0 \qquad 8.1$$

where Φ is the electrolyte potential. To derive the Laplace Equation, two main assumptions must be made: 1) electroneutrality and the conservation of charge are maintained in the system, and 2) diffusion of ions is negligible in comparison to migration, via the potential difference in the system being dominant over the concentration gradients. From these assumptions, the conductivity (σ) is mandated to be constant throughout the electrolyte domain, and the system must be in steady-state conditions with no time-dependencies of the ion motion or evolving electrolyte.

The current density (i), Φ, and σ can all be related through a form of Ohm's law (Eq. 8.2), which results from the simplified Nernst-Planck equation after applying the assumptions above.

$$i = -\sigma\nabla\Phi \qquad 8.2$$

The constant σ assumption can be justified through the high concentrations of NaCl in relation to the concentration of any metal ions in solution, leading to NaCl act as a supporting electrolyte. Previous work with experimental validation found that the Laplace equation (secondary current distribution) can effectively solve galvanic couple complex geometries[11,26]. Further derivations of the Laplace Equation and the use of the full Nernst-Planck equation can be found elsewhere[54,55].

The current density, total current, and potential distributions were calculated throughout all simulations. The conservation of charge, defining that the total anodic currents equal the total cathodic currents ($\sum I_a = \sum I_c$) was confirmed during each simulation, with the percent difference between the anodic and cathodic currents less than 0.55% in all scenarios described in Table 8.1 **&** Table 8.3.

A 3D simulation was created with the domain representing the electrolyte and boundary surfaces indicating either the material/solution interface or an insulating air/solution interface. The geometry and mesh were built to be identical to that of previous work, representing a dry-installed fastener in a 2 x 2 in panel (Chapter 7). Although many fasteners are designed to be wet-installed with a sealant, dry installation represents a worst-case scenario.

The water layer thickness (WL) was assumed to be continuous over the entire panel and conformal over the fastener head in the majority of tested scenarios. In some cases, a discontinuous WL as might occur due to evaporation or surface roughness was simulated, in which the solution only existed within the fastener hole, with a thickness exactly equal to the fastener/panel gap (200 μm). The solution of interest was either 0.6 M NaCl or 3 M NaCl, with conductivities of 5.5 S/m and 19.7 S/m, respectively. The relative humidity (RH) of the systems correlated to 98% and 88% for 0.6 M and 3 M NaCl, respectively, whereas the salt loading density (LD) of the system was assumed to remain constant at 3.5 $\mathrm{g/m^2}$. Therefore, the equilibrated WL was 89 μm for 0.6 M NaCl and 20 μm for 3 M NaCl, based on the empirical relation derived by Chen *et al.*,[56].

The experimentally determined PDS were input as boundary conditions for the surfaces of the panel surface, fastener hole, or the fastener, with $i = f(E)$ for the respective functions, fitted using a piece-wise cubic interpolation. Boundary conditions in 0.6 M NaCl were conducted previously in literature, while 3 M NaCl conditions were conducted in this work (Chapter 7). In addition to the in-house tested PDS, polarization behavior from literature was used both as boundary conditions and to inform a “scaling” factor to represent pseudo-thin film and pseudo-deaerated conditions, denoted throughout this work as “scaled-WL” or “scaled-deaerated” conditions. The present model was set up with assumptions and geometries identical to that of previous work, where additional details on the electrochemical modeling methods can be found (Chapter 7).

8.4 Results

8.4.1. Potentiodynamic Behavior

Polarization behavior in 0.6 M NaCl on bare P675, Zn-11%Ni, anodized Ti-6Al-4V, and bare Ti-6Al-4V were conducted previously (Chapter 7). New additions to this work included the atmospheric scaling of the bare P675, to account for the thin-film WL in which the cathodic kinetics were numerically accelerated based on i_{lim} values in literature for $WL = 89\ \mu m$ [35–37] (Figure 8.1(a**)**). Furthermore, kinetics in 0.6 M NaCl with composition variations within the sacrificial coating, for Zn-14%Ni and Zn-17%Ni specifically, were extracted from work of Tafreshi *et al.*,[51] (Figure 8.1 **(b)**). Lastly, it was determined from previous work that the OCP was more noble when comparing the anodized surface treatment to the bare polished surface, in 0.6 M NaCl (Chapter 7). Therefore, if the anodized and bare Ti-6Al-4V surfaces were ever in electrochemical contact, the bare Ti-6Al-4V would be the anode and preferentially dissolve in the galvanic couple. To account for this interaction within the model, an anodic PDS with consistent scan parameters was conducted on the bare Ti-6Al-4V surface (Figure 8.1**(c)**).

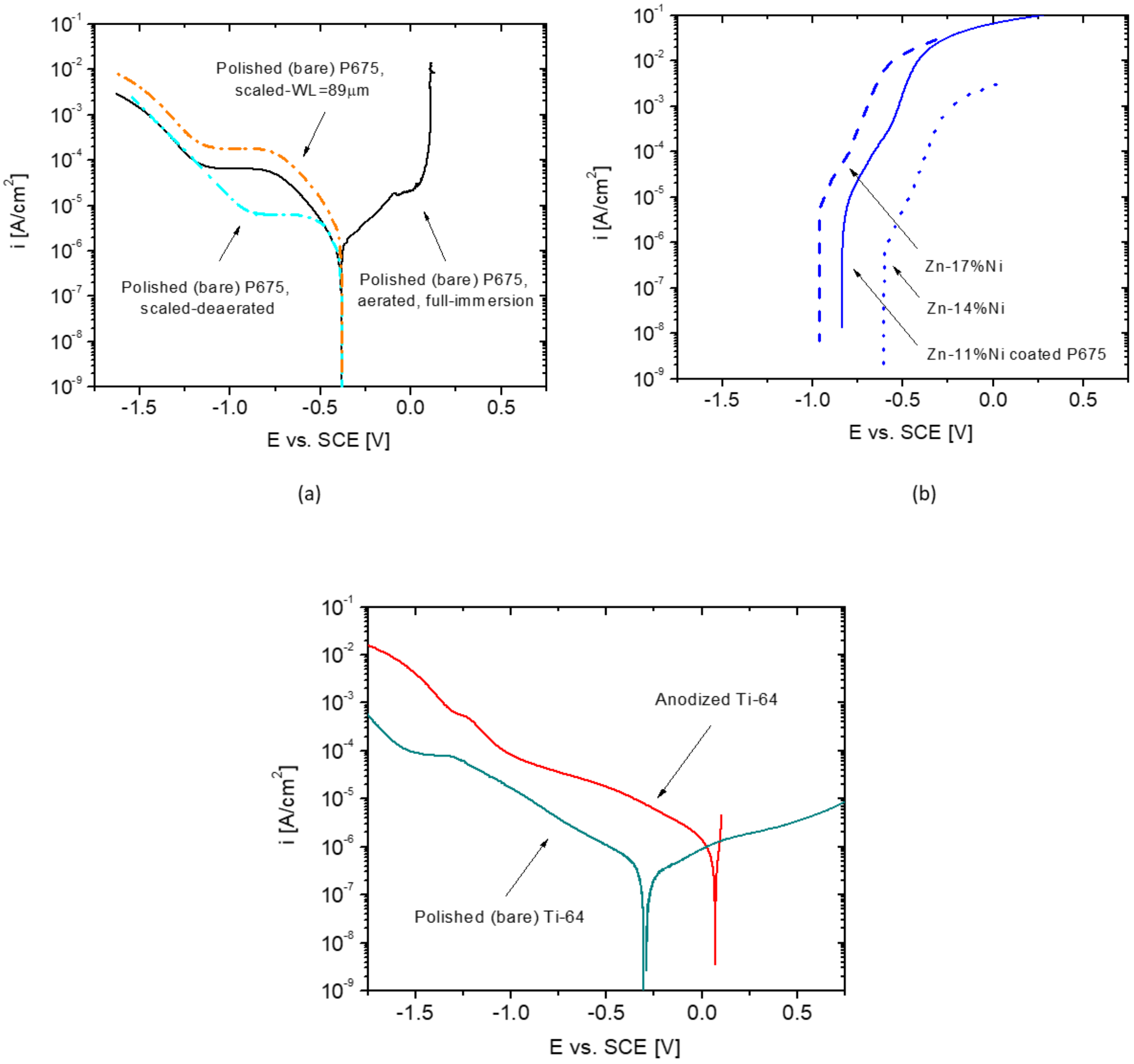

(a)

(b)

(c)

Figure 8.1: Potentiodynamic scans in 0.6M NaCl (anodic) and 0.6M Na_2SO_4 (cathodic); (a) polished (bare) P675, pseudo-deaerated P675, and pseudo-WL=89 μm; (b) Zn-11%Ni, Zn-14%Ni, and Zn-17%Ni; (c) anodized Ti-6Al-4V, and polished (bare) Ti-6Al-4V

Each material surface in the present work was tested in 3 M NaCl environment. Anodic and cathodic scans were again conducted on both the bare P675 and Ti-6Al-4V, in 3 M NaCl and the

1.55 M Na_2SO_4 (equivalent to 3 M NaCl in ORR diffusion limited current density), respectively, to account for variations in the galvanic relations, depending on the overall material selection of the system (Figure 8.2**(a)**). Anodic polarization on bare P675 indicated that the OCP and E_{pit} increased electropositively in comparison to the 0.6 M NaCl solution, to -0.25 V_{SCE} and 0.2 V_{SCE}, respectively, as would be expected from the increase in molarity. The OCP on the identical Zn-11%Ni coated P675 surface decreased with the increased molarity (to -0.897 V_{SCE}), in contrast to the increase in OCP with molarity seen with the bare P675 (Figure 8.2**(b)**).

In 3 M NaCl, the anodized surface treatment on the Ti-6Al-4V surface increased the kinetics of the bare surface to a lesser degree than the 0.6 M NaCl surrogate solution (Figure 8.2**(c)**). However, the higher concentration solution did result in a more electropositive OCP for the anodized surface to 0.167 V_{SCE}. As the cathodic and anodic curves were conducted separately on the bare Ti-6Al-4V surface, a difference in OCP occurred. The average, -0.315 V_{SCE}, was taken as a representative value.

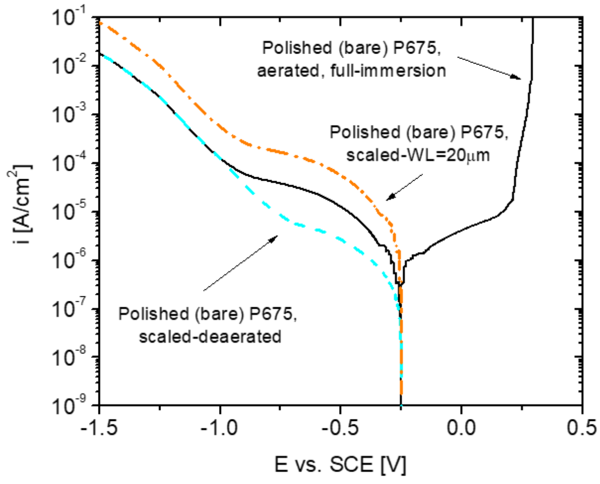

(a)

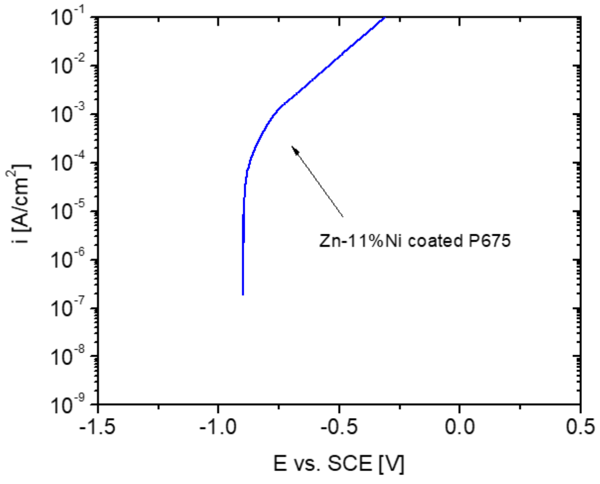

(b)

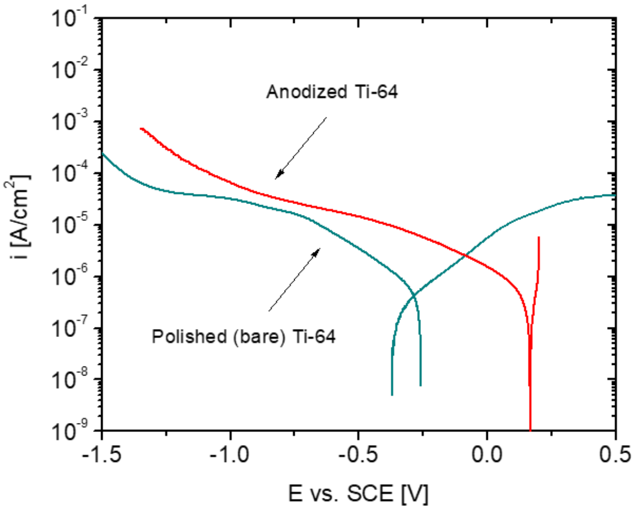

(c)

Figure 8.2: Potentiodynamic scans in 3M NaCl and 1.55M Na_2SO_4; (a) polished (bare) P675, pseudo-deaerated P675, and pseudo-WL=20 µm; (b) Zn-11%Ni coated P675; (c) anodized Ti-6Al-4V, and polished (bare) Ti-6Al-4V

8.4.2. Potential Distribution within the Fastener Hole, in 0.6 M NaCl Conditions

Computational models were first conducted with varying material selection combinations on the fastener, panel surface, and panel within the fastener hole, within an atmospheric thin-film condition of 0.6 M NaCl, relating to RH = 98% environment, described in Table 8.1. As the Ti-6Al-4V surface, both anodized and bare, had an i_{lim} below the potential range in this work (around -1.3 V_{SCE}), the kinetics were not modified in the occluded regions or the thin-film surface conditions.

Table 8.1: Descriptions of the tested scenarios in a 0.6 M NaCl environment, with a continuous conformal WL = 89 μm over the entire panel and fastener, RH = 98%, and LD = 3.5 $\mathbf{g/m^2}$

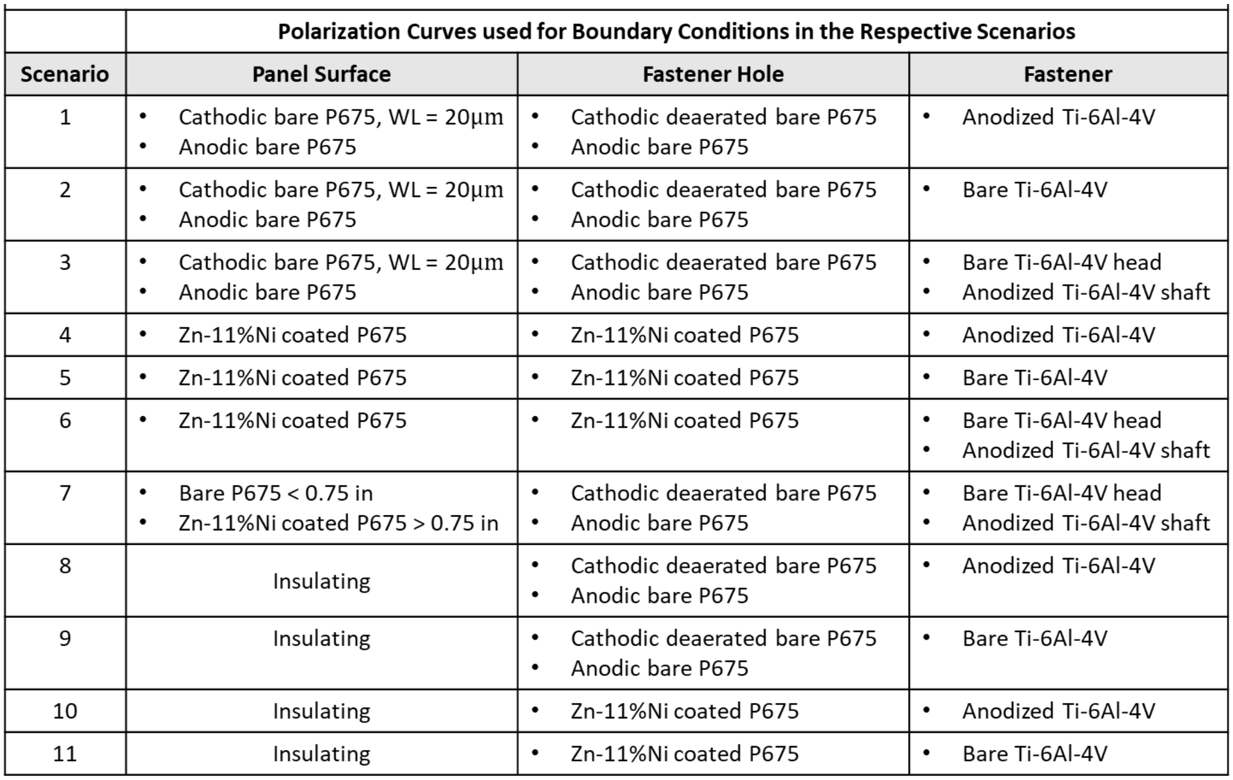

	Polarization Curves used for Boundary Conditions in the Respective Scenarios		
Scenario	**Panel Surface**	**Fastener Hole**	**Fastener**
1	• Cathodic bare P675, WL = 20μm • Anodic bare P675	• Cathodic deaerated bare P675 • Anodic bare P675	• Anodized Ti-6Al-4V
2	• Cathodic bare P675, WL = 20μm • Anodic bare P675	• Cathodic deaerated bare P675 • Anodic bare P675	• Bare Ti-6Al-4V
3	• Cathodic bare P675, WL = 20μm • Anodic bare P675	• Cathodic deaerated bare P675 • Anodic bare P675	• Bare Ti-6Al-4V head • Anodized Ti-6Al-4V shaft
4	• Zn-11%Ni coated P675	• Zn-11%Ni coated P675	• Anodized Ti-6Al-4V
5	• Zn-11%Ni coated P675	• Zn-11%Ni coated P675	• Bare Ti-6Al-4V
6	• Zn-11%Ni coated P675	• Zn-11%Ni coated P675	• Bare Ti-6Al-4V head • Anodized Ti-6Al-4V shaft
7	• Bare P675 < 0.75 in • Zn-11%Ni coated P675 > 0.75 in	• Cathodic deaerated bare P675 • Anodic bare P675	• Bare Ti-6Al-4V head • Anodized Ti-6Al-4V shaft
8	Insulating	• Cathodic deaerated bare P675 • Anodic bare P675	• Anodized Ti-6Al-4V
9	Insulating	• Cathodic deaerated bare P675 • Anodic bare P675	• Bare Ti-6Al-4V
10	Insulating	• Zn-11%Ni coated P675	• Anodized Ti-6Al-4V
11	Insulating	• Zn-11%Ni coated P675	• Bare Ti-6Al-4V

The first material combination represented a conventional worst-case scenario during atmospheric conditions relating to an RH = 98%, in which the entire panel was bare P675, as could occur if the surface topcoat was delaminated or mechanically damaged and the fastener was dry-installed with no sealant applied within the hole. Although the steady-state model could not track the inflow diffusion of O_2 through the solution/air interface and through the solution itself, the boundary conditions were modified to account for these processes, through scaled-deaerated and scaled-WL kinetic scaling, based on values experimentally determined in literature[21,25,35–37,53]. Accelerated cathodic P675 curves in scaled-WL= 89 µm were used as boundary conditions on the surface of the panel, whereas scaled-deaerated P675 boundary conditions were used within the fastener hole. Anodic P675 curves were used on all panel surfaces, and the bolt was anodized Ti-6Al-4V, as a default, consistent with previous work conducted for full-immersion conditions **(**Figure *8.3***(a))** (Chapter 7).

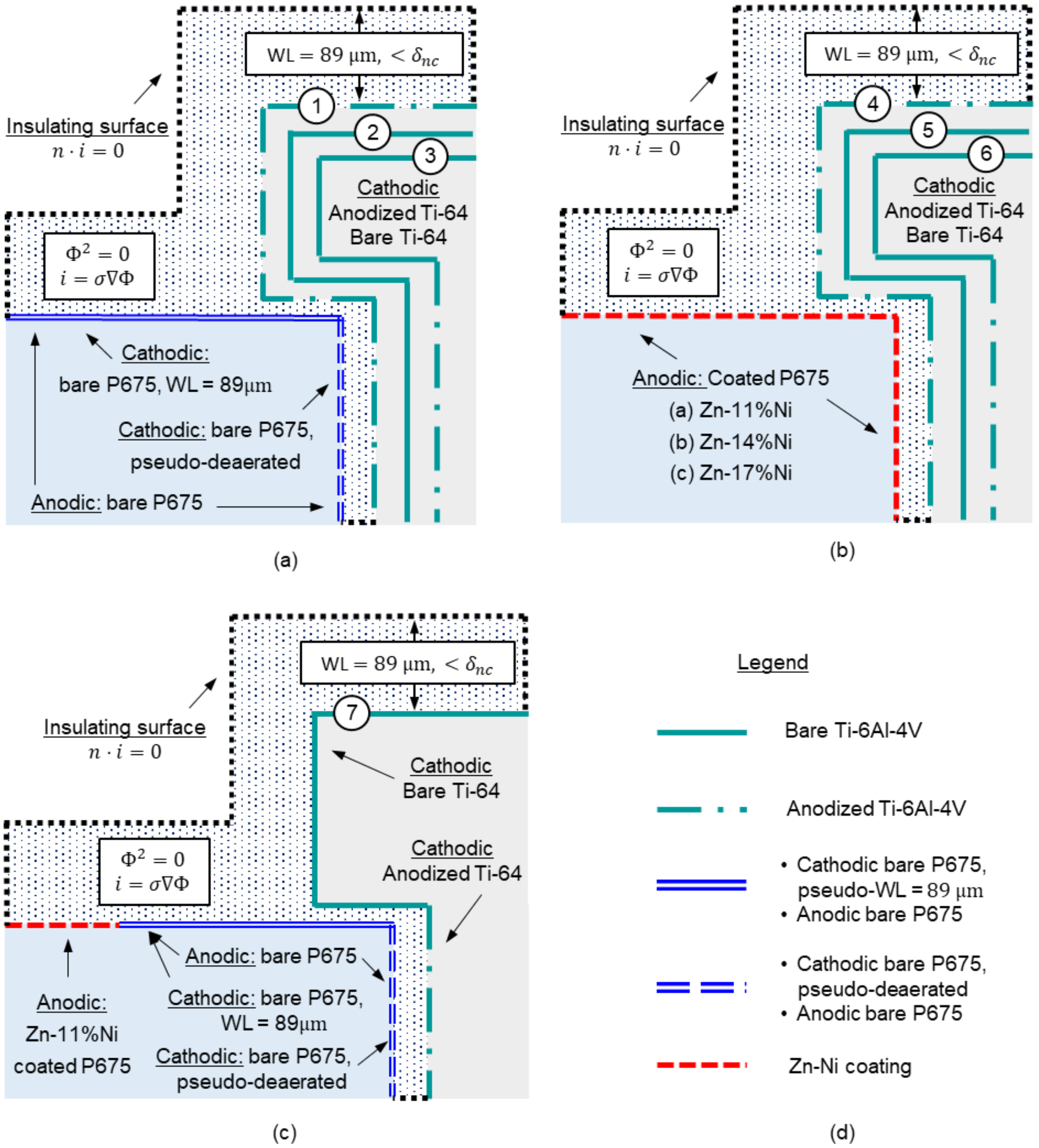

Figure 8.3: Schematics of material selection scenarios tested in a 0.6 M NaCl environment with WL = 89 µm, RH = 98%, and LD = 3.5 g/m². (a) Bare P675 panel and a Ti-6Al-4V fastener varying from scenarios 1) anodized to 2) bare to 3) anodized shaft and bare head. (b)

Zn-Ni coated panel, varying composition from 11% Ni to 17% Ni, and a Ti-6Al-4V fastener varying from scenarios 4) anodized to 5) bare to 6) anodized shaft and bare head. (c) A distant coating of scenario 7 with Zn-11%Ni outside of a 0.75 in radius from the fastener hole, bare P675 within the radius, and a partially anodized Ti-6Al-4V with an anodized shaft and bare head. (d) Legend of boundary conditions across all scenarios.

False-color plots of the electrode potential on the anodic panel for both the surface and within the fastener hole were plotted for the first scenario of boundary conditions. The surface indicated a distribution of potential, via the high ohmic drop in the thin WL, whereas the potential within the fastener hole seemed nearly uniform (Figure *8.4*(**a**)). Looking instead only at the potential within the fastener hole, a small gradient could be seen (1.4 mV) with more-electronegative values near the top of the fastener hole and more-electropositive values near the base. This distribution correlates to the relative 1:1 cathode-to-anode ratio at the base of the fastener hole, which polarizes the fastener hole in that location to more electropositive values. Conversely, near the top of the fastener hole, the active panel has a larger surface area than the fastener surfaces, which leads to a stronger polarization towards the electronegative bare P675 OCP.

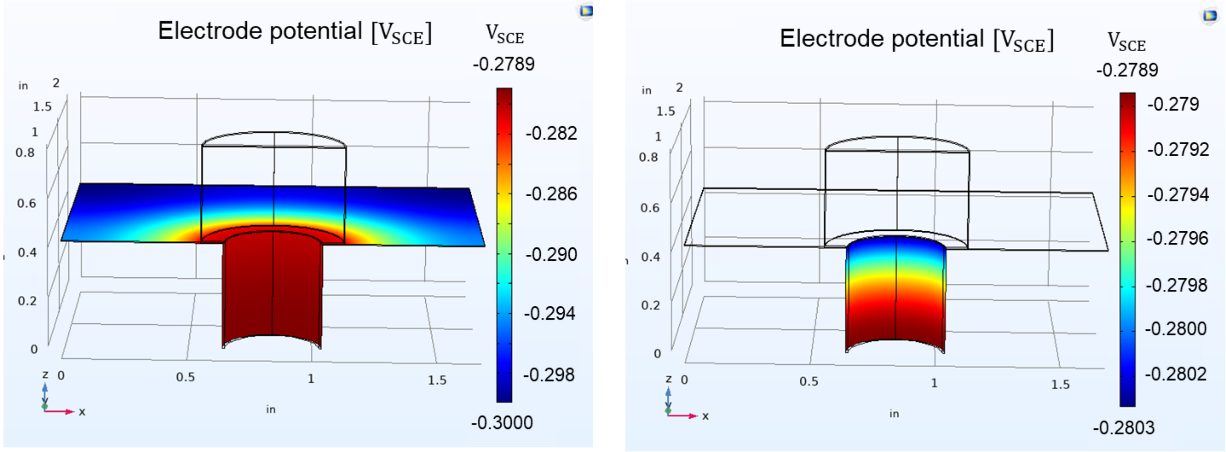

(a)

(b)

Figure 8.4: False-color plot of a bare P675 panel with an anodized Ti-6Al-4V bolt (scenario 1), with the potential distribution (a) over the entire panel and (b) only within the fastener hole, in a 0.6M NaCl environment with WL = 89 μm, RH = 98%, and LD = 3.5 g/m²

As the fastener hole represents the highest-stress region and was the focus of this work, the maximum and minimum potential values within the hole, -0.2789 V_{SCE} and -0.2803 V_{SCE}, respectively, were plotted on a potential number line (Figure 8.5). The width of the line therefore represented the distribution, and correspondingly the ohmic drop, within the fastener hole. Dashed vertical lines represented the OCP of each material for clarity. Each iteration of the boundary conditions and material selections were then labeled according to Table 8.1 and Figure 8.3**(a),** and were plotted along Figure 8.5**.**

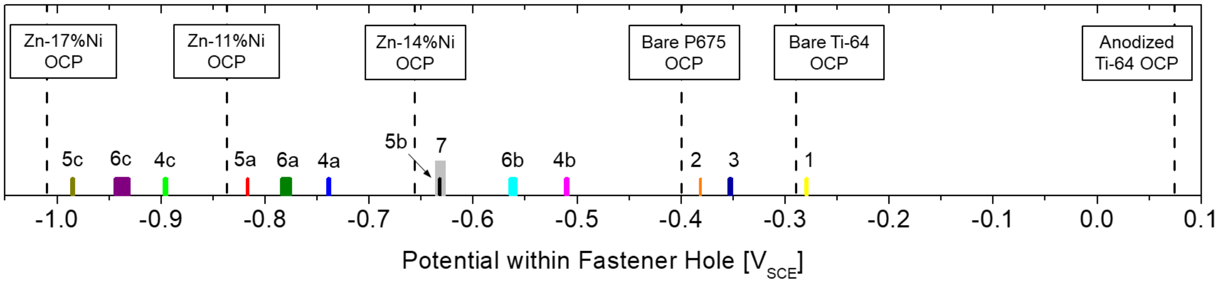

Figure 8.5: Potential distribution within the fastener hole in a 0.6M NaCl environment, WL = 89 μm, RH = 98%, LD = 3.5 g/m², with numeric labels correlating to defined scenarios in Table 8.1. Dashed lines represent the OCP of the tested materials.

The second and third scenarios represented the effects of varying the surface treatment on the fastener to either bare Ti-6Al-4V or a partial-surface treatment, whereas the panel remained constant with bare P675 boundary conditions. The potential within the fastener hole in both scenarios fell between -0.4 V_{SCE} and -0.3 V_{SCE} (Figure 8.3**(a))**.

The next set of scenarios (4 through 6) incorporated a Zn-Ni coating over all bare P675 surfaces, with the fastener surface treatment varied as it was with the previous scenarios (Table 8.1 and Figure 8.3**(b))**. Subset labels of (a), (b), and (c) in Table 8.1 and Figure 8.5 correlated to increasing Ni composition in the coating. The Zn-Ni coating composition had a larger impact on the potential within the fastener hole than the fastener surface treatment (i.e., anodized or bare Ti-6Al-4V). For example, scenarios 4c, 5c, and 6c, correlating to Zn-17%Ni, grouped together at the electronegative side of the potential range, in opposition to the scatter seen in scenarios 4a, 4b, and 4c, correlating to a constant anodized Ti-6Al-4V fastener (Figure 8.5**)**. This grouping trend continued with increasing potentials, for 4a, 5a, 6a, and then finally 4b, 5b, 6b, which directly correlated with the OCPs of the respective Zn-Ni compositions. That is, $\mathrm{OCP}_{\mathrm{Zn-17\%Ni}} < \mathrm{OCP}_{\mathrm{Zn-11\%Ni}} < \mathrm{OCP}_{\mathrm{Zn-14\%Ni}}$, which would correspond to the potentials in the subset of scenarios, $(4\mathrm{c}, 5\mathrm{c}, 6\mathrm{c}) < (4\mathrm{a}, 5\mathrm{a}, 6\mathrm{a}) < (4\mathrm{b}, 5\mathrm{b}, 6\mathrm{b})$. Furthermore, the potentials in scenario 6 were always between scenarios 4 and 5, due to the multi-surface treatment on the fastener combining the polarization of the anodized Ti-6Al-4V (in scenario 4) and the bare Ti-6Al-4V (in scenario 5) (Figure 8.5).

Lastly, a selective plating scenario was investigated, in which the Zn-11%Ni coating was only on the P675 surface outside of a 0.75 in radius from the fastener **(**Figure 8.3**(c))**. All non-coated portions of the panel were bare P675, with the scaled-WL boundary condition applied to the surface and scaled-deaerated conditions applied within the fastener hole. The fastener surface treatment was also non-uniform, with a bare Ti-6Al-4V head and an anodization applied on the shaft. When combining all four materials of interest into the same system, the global anode became the sacrificial Zn-11%Ni coating whereas all other materials contributed cathodic current to the system (Figure 8.5).

8.4.3. Total Current and Current Distributions in 0.6 M NaCl Conditions

To further evaluate the efficacy of each material system, the total anodic currents on the surface of the panel and fastener hole were plotted and are labeled numerically in correspondence with Table 8.1 **(**Figure **8.6).** Note that throughout all scenarios the geometry was not varied, making a comparison of the currents possible, without the need to normalize by the exposed area. Although the majority of all currents were less than 100 µA, the lowest current was scenario 2, which incorporated both bare P675 and bare Ti-6Al-4V boundary conditions in the system. In generally, coupling with the bare Ti-6Al-4V fastener decreased the total currents in the system due to its slower cathodic kinetics relative to anodized Ti-6Al-4V (Figure 8.6).

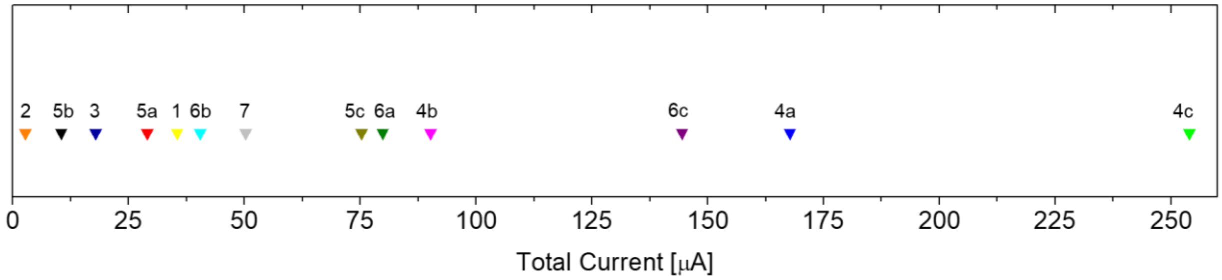

Figure 8.6: Total current in each 0.6 M NaCl system, WL = 89 µm, RH = 98%, LD = 3.5 g/m^2, with numeric labels correlating to defined scenarios in Table 8.1

Three scenarios (6c, 4a, and 4c) had larger currents than the rest. Each of the three scenarios corresponded to cases in which the entire P675 surface was coated in Zn-Ni of 11% Ni or 17% Ni, with either an anodized or partially-anodized Ti-6Al-4V bolt. The Zn-17%Ni coating generally resulted in high currents, as well as all Zn-Ni/anodized Ti-6Al-4V galvanic couples (Figure 8.6).

To determine the rate of mass loss across the surface of the panel, the current density distribution was analyzed. In Figure 8.7**(a)** the current distribution is shown for scenario 4a (a Zn-11%Ni coating over the P675 panel and an anodized Ti-6Al-4V bolt). Assuming uniform dissolution, the mass loss rate of the coating could be calculated through Faraday's law of electrolysis, adapted from a singular material to account for alloys (Eq. 8.3).

$$\frac{m}{t} = \frac{EW \cdot i}{\rho_{alloy} \cdot F} \tag{8.3}$$

where m is the mass loss, t is the time, EW is the equivalent weight, i is the current density, ρ_{alloy} is the density of the alloy, and F is Faraday's constant. The EW can be defined as,

$$EW = \left(\sum \left(\frac{z_i \cdot wt\%_i}{M_{at_i}} \right) \right)^{-1} \tag{8.4}$$

where z_i is the charge of each species, $wt\%$ is the weight percentage of each species within the alloy, and M_{at_i} is the atomic mass of each species. Lastly, ρ_{alloy} can similarly be defined,

$$\rho_{alloy} = \left(\sum \left(\frac{wt\%_i}{\rho_i} \right) \right)^{-1} \tag{8.5}$$

where ρ_i is the density of each species. Material constants to calculate EW and ρ_{alloy} are documented in Table 8.2.

Table 8.2: Material constants for Zn-Ni coating

	Zn	Ni
$M_{at}\ [g/mol]$	65.38	58.6934
$\rho\ [g/cm^3]$	7.14	8.908
z	2	2

As FEM solves for i at each point spatially along the electrode surface, the mass loss rate could then be calculated as a function of position. Specifically, a line of current density was extracted from the data along the surface of the panel (indicated by the black arrow in Figure *8.7*a), from the edge towards the anodized Ti-6Al-4V bolt **(**Figure 8.7**(b))**. The current density and the corresponding mass loss rate were highest near the fastener, due to the ohmic drop limiting the "throwing power" (*i.e.*, coupling distance) of the cathode. The peak mass loss rate of the Zn-11%Ni coating on the surface of the panel was $\sim 0.4\,\frac{\text{mm}}{\text{yr}}$ (Figure 8.7**(b))**.

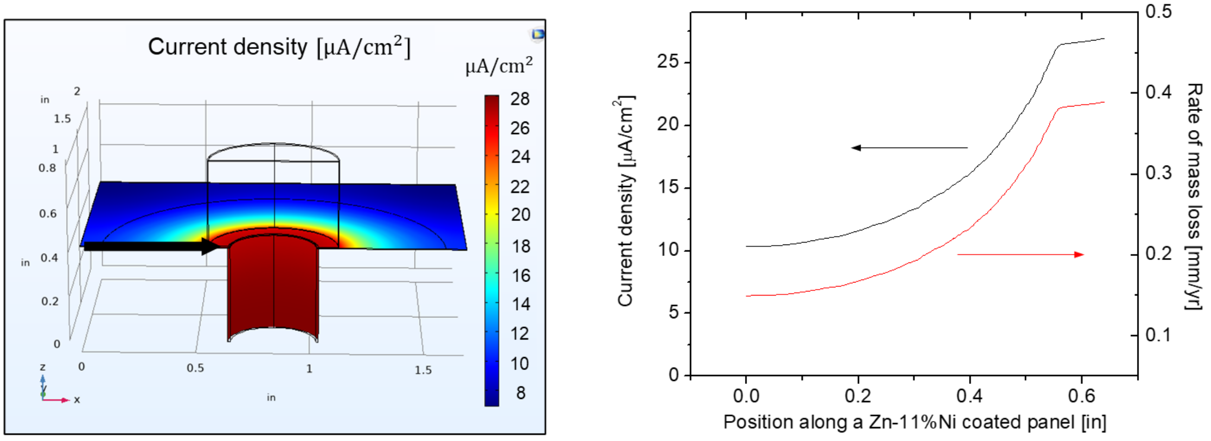

(a)

(b)

Figure 8.7: A Zn-11%Ni coated panel, with a bare P675 fastener hole and an anodized T-6Al-4V fastener; (a) schematic of line graph along the panel and fastener hole, (b) current density and rate of mass loss along the panel and fastener hole, in a 0.6M NaCl environment

8.4.4. Inclusion of a Pit in 0.6 M NaCl Condition

Often, especially at the onset of coating breakdown, there exists an area of active corrosion as the remaining surface is still passive. To consider this more complex scenario, an active pitting bare P675 anodic boundary condition was utilized to simulate a 100 μm radius pit, with the remaining panel surfaces considered passive (inert). The polarization behavior of the actively pitting surface indicated an increase of nearly two orders of magnitude in both cathodic and anodic kinetics relative to the conventionally-scanned anodic bare P675 (Figure *8.8* **(a)**). An anodized Ti-6Al-4V was used as the fastener in the simulation with the active pit, which resulted in a cathode:anode ratio of 1.9×10^4.

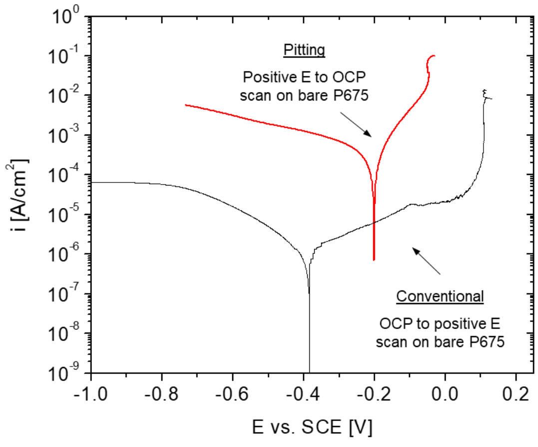

(a)

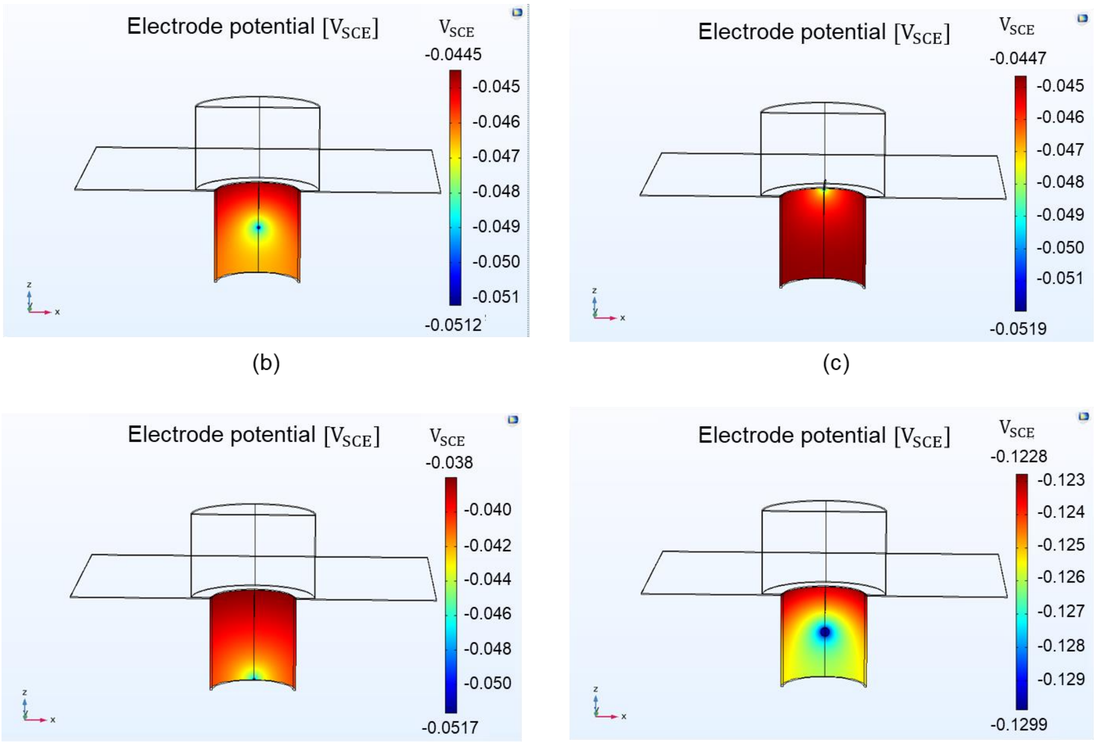

(b) (c)

(d) (e)

Figure 8.8: (a) Pitting and conventional anodic scans on bare P675 in 0.6M NaCl. False-color potential distributions of a bare P675 panel and fastener hole with an anodized Ti-6Al-4V bolt and solution (scenario 1), and 100 µm pit in (b) middle of fastener hole, (c) top of fastener hole, (d) base of fastener hole; (e) 500 µm pit in middle of fastener hole.

The pit was first located in the middle of the fastener hole, and the resulting potential range within the fastener hole was 6.2 mV, with the base of the pit at -0.0512 V_{SCE} (Figure *8.8***(b)**). Furthermore, the distribution of potential radiated out equally from the pit hot spot to more electropositive values. Moving the location of the 100 µm pit to the top or the base of the fastener hole resulted in similar potential ranges of 7.2 mV and 13.7 mV, respectively, whereas the base of the pit remained near -0.051 to -0.052 V_{SCE} (Figure *8.8* (c) and (d)).

For a pit located in the middle of the fastener hole, the radius was increased to 500 µm. The potential range within the fastener hole remained only a few mV (7.1 mV), but the potential at the base of the pit dropped towards the more electronegative OCP of the bare P675 activated kinetics, -0.2 V_{SCE} (Figure *8.8***(e)**). Furthermore, the pit was able to polarize the base of the fastener hole to more electronegative values than the top of the fastener hole, which was closer to the large cathodic surface area of the fastener head.

8.4.5. Potential Distribution within the Fastener Hole in 3 M NaCl Conditions

Utilizing the same overarching model and assumptions, the boundary conditions were modified to represent case in which the evaporation takes place during an RH decrease from 98% to 88%. The loading density (LD) of salt was held constant, which resulted in a 20 µm WL of 3 M NaCl. The identical seven material combinations tested in 0.6 M NaCl were again conducted in the lower RH environment, with the exception of any compositional variation to the Zn-Ni coating (Table 8.3, Figure *8.9* **(a)** through **(c)**).

Table 8.3: Descriptions of the tested scenarios in a 3 M NaCl environment, with a continuous conformal WL = 20 µm over the entire panel and fastener or solution only within the fastener hole

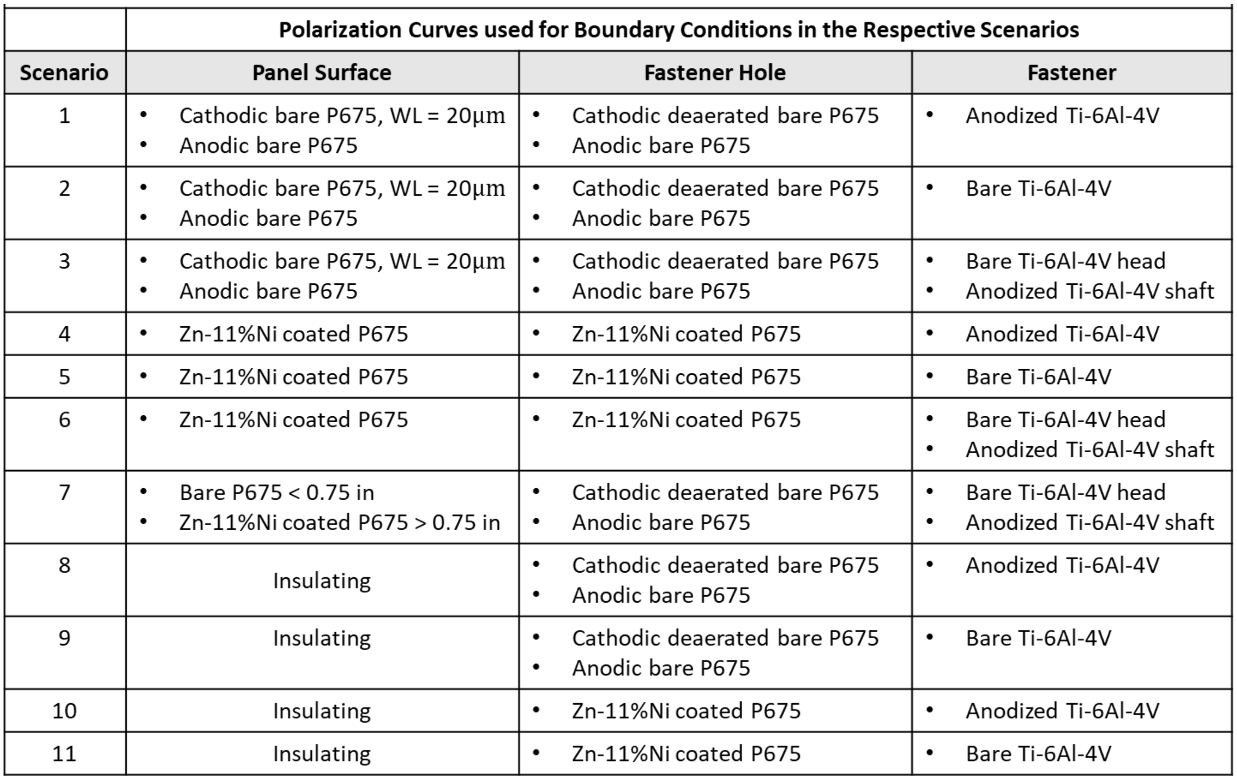

	Polarization Curves used for Boundary Conditions in the Respective Scenarios		
Scenario	**Panel Surface**	**Fastener Hole**	**Fastener**
1	• Cathodic bare P675, WL = 20µm • Anodic bare P675	• Cathodic deaerated bare P675 • Anodic bare P675	• Anodized Ti-6Al-4V
2	• Cathodic bare P675, WL = 20µm • Anodic bare P675	• Cathodic deaerated bare P675 • Anodic bare P675	• Bare Ti-6Al-4V
3	• Cathodic bare P675, WL = 20µm • Anodic bare P675	• Cathodic deaerated bare P675 • Anodic bare P675	• Bare Ti-6Al-4V head • Anodized Ti-6Al-4V shaft
4	• Zn-11%Ni coated P675	• Zn-11%Ni coated P675	• Anodized Ti-6Al-4V
5	• Zn-11%Ni coated P675	• Zn-11%Ni coated P675	• Bare Ti-6Al-4V
6	• Zn-11%Ni coated P675	• Zn-11%Ni coated P675	• Bare Ti-6Al-4V head • Anodized Ti-6Al-4V shaft
7	• Bare P675 < 0.75 in • Zn-11%Ni coated P675 > 0.75 in	• Cathodic deaerated bare P675 • Anodic bare P675	• Bare Ti-6Al-4V head • Anodized Ti-6Al-4V shaft
8	Insulating	• Cathodic deaerated bare P675 • Anodic bare P675	• Anodized Ti-6Al-4V
9	Insulating	• Cathodic deaerated bare P675 • Anodic bare P675	• Bare Ti-6Al-4V
10	Insulating	• Zn-11%Ni coated P675	• Anodized Ti-6Al-4V
11	Insulating	• Zn-11%Ni coated P675	• Bare Ti-6Al-4V

The potential within the fastener hole in the first three scenarios, with bare P675 and varying fastener surface treatments, fell grouped between -0.3 V_{SCE} and -0.1 V_{SCE} (Figure 8.10). Similarly, the following three scenarios (4, 5, and 6) were grouped more tightly and fell very close to the OCP of the Zn-11%Ni coated P675. The distant coating scenario 7, incorporating all four materials of interest, seemed to reach a moderate potential around -0.57 V_{SCE} (Figure 8.10).

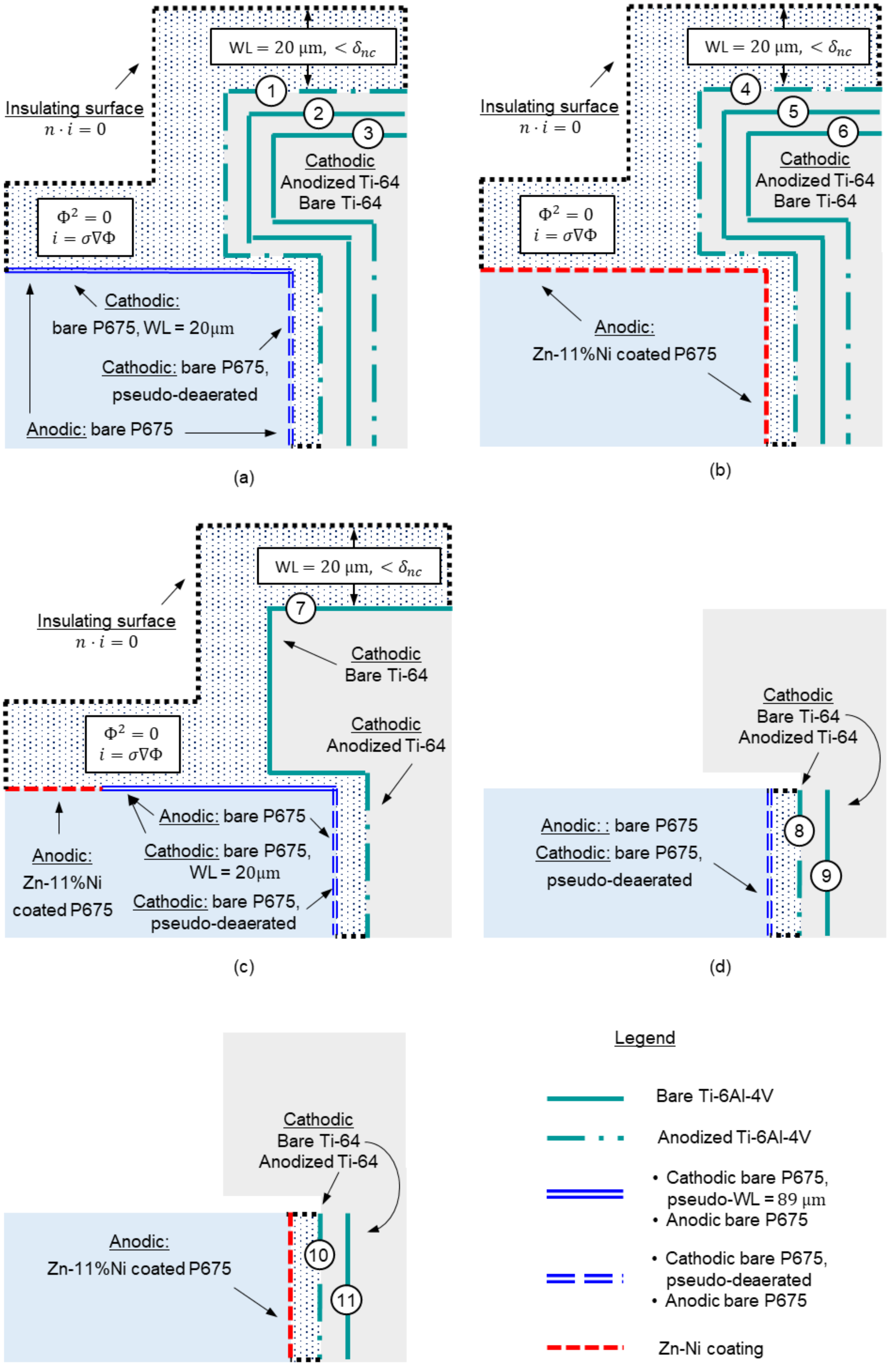

Insulating surface
$n \cdot i = 0$
WL = 20 μm, < δ_{nc}
$\Phi^2 = 0$
$i = \sigma \nabla \Phi$
①
②
③
④
⑤
⑥
⑦
⑧
⑨
⑩
⑪
Cathodic
Anodized Ti-64
Bare Ti-64
Cathodic: bare P675, WL = 20μm
Cathodic: bare P675, pseudo-deaerated
Anodic: bare P675
Anodic: Zn-11%Ni coated P675
Cathodic
Bare Ti-64
Cathodic
Anodized Ti-64
Anodic: : bare P675
Cathodic: bare P675, pseudo-deaerated
Legend
Bare Ti-6Al-4V
Anodized Ti-6Al-4V
• Cathodic bare P675, pseudo-WL = 89 μm
• Anodic bare P675
• Cathodic bare P675, pseudo-deaerated
• Anodic bare P675
Zn-Ni coating

(a) (b) (c) (d) (e) (f)

Figure 8.9: Schematics of material selection scenarios tested in a 3 M NaCl environment with WL $= 20$ μm, RH = 88%, and LD = 3.5 $\mathrm{g/m^2}$. (a) Bare P675 panel and a Ti-6Al-4V fastener varying from scenarios 1) anodized to 2) bare to 3) anodized shaft and bare head; (b) Zn-11%Ni coated panel and a Ti-6Al-4V fastener varying from scenarios 4) anodized to 5) bare to 6) anodized shaft and bare head. (c) A distant coating of scenario 7 with Zn-11%Ni outside of a 0.75 in radius from the fastener hole, bare P675 within the radius, and a partially anodized Ti-6Al-4V with an anodized shaft and bare head. (d) Solution only within the bare P675 fastener hole, with the fastener varying from scenarios 8) anodized to 9) bare. (e) Solution only within the Zn-11%Ni coated P675 fastener hole, with the fastener varying from scenarios 10) anodized to 11) bare. (f) Legend of boundary conditions across all scenarios.

Recall that in all scenarios tested above, the WL was assumed to be a continuous and conformal 20 μm over the entire fastener and panel. Although this assumption may be valid on larger WL, in the range of 20 μm it might be expected to be breaks in the continuity, due to the presence of, for example, dirt particulates, surface roughness of the panel itself, or complete evaporation of the solution on the surface. The resulting discontinuous WL may include discrete droplets of unknown size across the surface of the panel. However, as galvanic coupling between two materials can only occur through electrolyte contact, droplets on the surface not in contact with the fastener would not allow for any galvanic corrosion. The occluded region within the fastener hole is more protected from foreign objects and initial evaporation effects and would therefore be the only consistent connection between the fastener and panel if discontinuous WL over the surface was to occur.

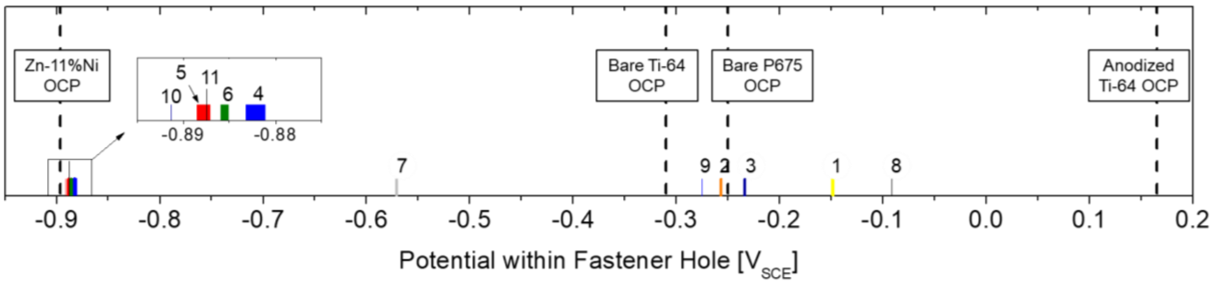

Figure 8.10: Potential distribution within the fastener hole in a 3M NaCl environment, WL = 20 μm, RH = 88%, LD = 3.5 g/m^2, with numeric labels correlating to defined scenarios in Table 2. Dashed lines represent the OCP of the tested materials.

Therefore, four new simulations were conducted with solution only within the fastener hole (scenarios 8, 9, 10, and 11), which corresponded to the WL = 20 μm scenarios of 1, 2, 4, and 5, respectively (Table 8.3, Figure 8.9**(d)** and **(e)**). No cases of partial surface treatment on the fastener or distant coating were considered, as the solution was not in contact with the fastener head nor with the surface of the panel.

The eighth scenario, with bare P675 and an anodized Ti-6Al-4V bolt, resulted in a more electropositive potential than when the solution was continuous over the entire surface, due to the near 1:1 cathode-to-anode ratio of the solution only within the fastener hole polarizing the sample towards the OCP of the anodized Ti-6Al-4V (Figure 8.10). Furthermore, there was no distribution of potential within the fastener hole, and all electrode potentials were of a uniform value. Similarly, the ninth scenario incorporated a bare Ti-6Al-4V bolt and the potential was shifted closer to the bare Ti-6Al-4V OCP (Figure 8.9**(d))**.

The final two scenarios utilizing the Zn-11%Ni coated P675 and different fastener surface treatments again resulted in a strong polarization and grouping of the potentials near the OCP of the Zn-11%Ni (Figure 8.9**(e)**).

8.4.6. Fracture Mechanics in 3 M NaCl Conditions

The crack growth rate dependence on potential was determined in the same way as Chapter 7, at a constant dK/dt = 0 and dK/dt = 4 MPa√m/hr. Results in Figure 8.11 indicate little variation between the different dK/dt values, with the magnitude of crack growth rate with dK/dt = 4 MPa√m/hr slightly higher than that of dK/dt = 0. The electronegative threshold of the low crack growth rate potentials for dK/dt = 0 was around -0.7 V_{SCE}, whereas for dK/dt = 4 MPa√m/hr the threshold was -0.8 V_{SCE}, indicating a wider range of low-cracking potentials, although once outside of the "well", higher magnitudes of crack growth rate were still observed.

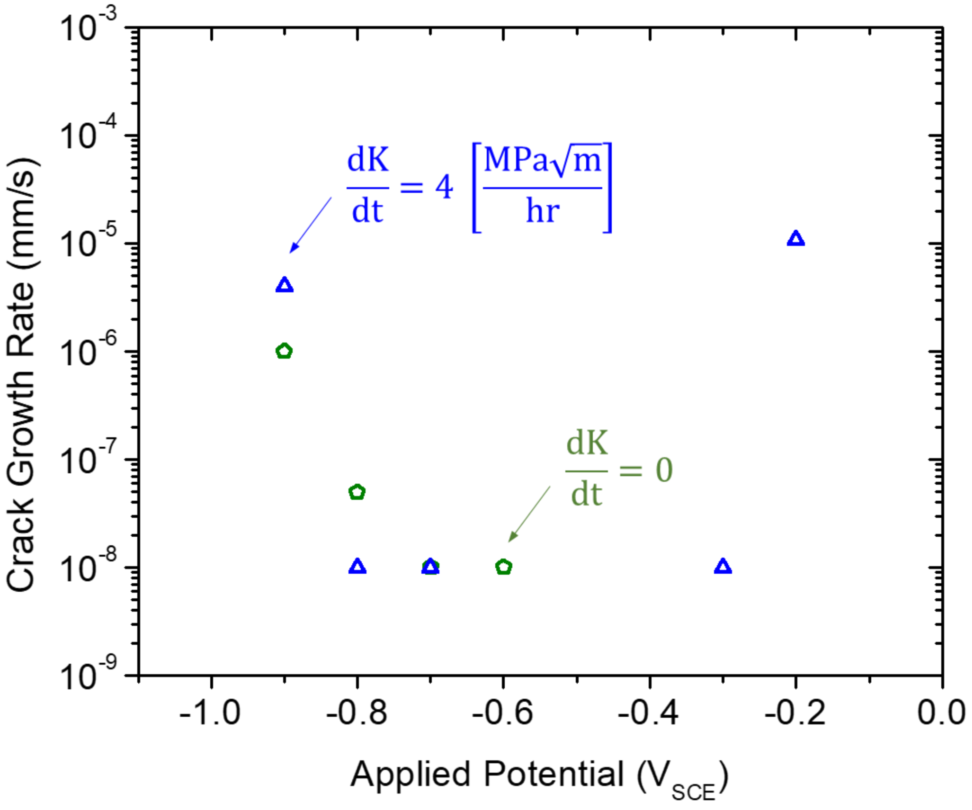

Figure 8.11: Effect of applied loading rate on the crack growth rate at $K_J \approx 50$ MPa√m as a function of applied potential for P675 immersed in 3 M NaCl.

8.5 Discussion

In this work, fracture mechanics and FEM modeling were conducted in a variety of environments, to determine a material combination which would minimize the crack susceptibility of a P675 plate containing a Ti-6Al-4V fastener in an atmospheric chloride exposure. As the cylindrical nature of the fastener hole acts as an additional stress concentrator (up to three times that of the external stress), the potential distribution in that region was the focus of this work[57]. The structural materials of interest included a bare and Zn-Ni coated P675, while the fastener materials were a bare and anodized Ti-6Al-4V bolt. The environments tested included RH = 98% and 88%, with comparisons conducted to the previous full-immersion work (Chapter 7).

8.5.1. Combining the FEM and LEFM Techniques to Develop a Material Selection Framework

Therefore, in the present work, polarization data of current as a function of potential were input as boundary conditions to inform a FEM model. The spatial resolution of the FEM was able to determine the potential distribution at any region, including the high-stress region of the fastener hole, within a given material system and environment. Fracture mechanics in 0.6 M NaCl and 3 M NaCl were able to determine the crack growth rate as a function of potential on the bare P675, the structural panel of interest. The resulting potentials from both techniques were combined and plotted on a singular x-axis, to determine a material selection framework to reduce crack susceptibility from hydrogen embrittlement and anodic dissolution (Figure 8.12). In addition, the current and current densities were calculated, to moderate the corrosion rate as well as the cracking susceptibility.

Considering the case with an 89 μm WL and a 0.6 M NaCl atmospheric environment, six scenarios were found to have resulting potentials, in the fastener hole region of interest, which correlated with the low crack growth regime of -0.3 V_{SCE} to -0.7 V_{SCE} (Figure 8.5). Utilizing a bare or partially-bare Ti-6Al-4V fastener with the bare P675 (scenarios 2 and 3, respectively) resulted in the potential being close to the OCP of the bare P675, which happened to be in the low crack growth rate region (Figure 8.3**(a)**). However, using the bare Ti-6Al-4V fastener with either the Zn-11%Ni or Zn-17%Ni coatings, the combined electropositive polarization of the Ti-6Al-4V and P675 was not strong enough to pull the potentials out of the high crack growth rate region (i.e., below -0.7 V_{SCE}). Only a composition of Zn-14%Ni resulted in potentials within the optimum potential range, that is, scenarios 4b, 5c, and 6c (Figure 8.3(b)). Combining all four present materials, with a distant coating and non-uniform surface treatment of the fastener, also resulted in a potential range within the fastener hole which was approximately 50 mV from the electronegative side of the well (Figure 8.3(c) and Figure 8.5).

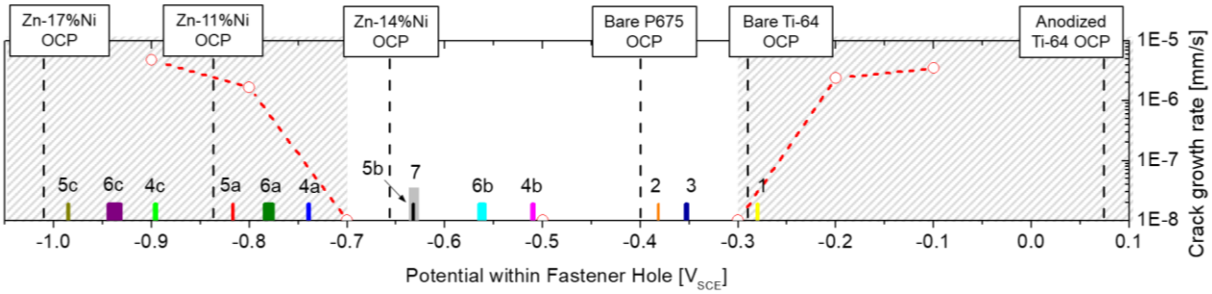

Figure 8.12: Simulated potential ranges within the fastener hole for various material selection scenarios in thin-film conditions (Figure 8.5) with the overlaid crack growth rate vs. potential at a constant dK/dt = 4 MPa$\sqrt{m}$/hr on the secondary x-axis (Chapter 7), all in 0.6 M NaCl

conditions. Dashed grey regions represent the potentials which result in high crack-growth rates.

Interestingly, potentials resulting from scenarios 5b and scenarios 7 fell within the same range, with scenario 7 having a wider distribution, within the fastener hole, although the material combinations were different (Figure 8.5). Scenario 5b only included a Zn-14%Ni coating with an anodized bolt, whereas scenario 7 included a partial coating of Zn-11%Ni, bare P675 over the remainder of the panel, and a partial surface treatment on the shaft of the Ti-6Al-4V bolt. This result indicates that the potential distributions are not exclusive to a singular material combination, and as more materials are tested an infinite number of scenarios could exist with potentials within the low-cracking regime.

In addition to considering the potential within the high-stress region, the total anodic current in the system must also be evaluated to narrow down the material selection process. If the dissolution rate is too high, there will be substantial production of corrosion products from the Zn-Ni coating which could interfere with the component operation. In addition, the high dissolution rate is non-uniform, due to the distribution of current density, leading to the Zn-Ni coating closest to the cathodic fastener to be dissolved at a higher rate than that of the coating near the edge of the panel (Figure 8.7). Of the six scenarios which resulted in low-cracking potentials, three had total currents that fell below 25 μA (scenarios 2, 3, and 5b), while the remaining three had currents between 25 μA and 100 μA (scenarios 4b, 6b, and 7) (Figure 8.6). Therefore, the most optimum material combinations in the RH = 98% environment would be either a completely bare P675 with a bare or partially-bare Ti-6Al-4V (with anodization on the threaded shaft to maintain the wear resistance), or a completely coated Zn-14%Ni surface and fastener hole with a completely bare Ti-6Al-4V bolt.

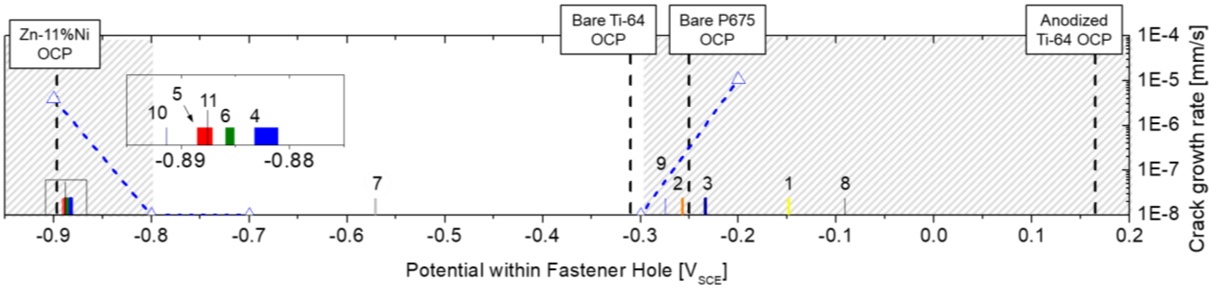

Figure 8.13: Simulated potential ranges within the fastener hole for various material selection scenarios in thin-film conditions (Figure 8.10) with the overlaid crack growth rate vs. potential at a constant dK/dt = 4 MPa√m/hr on the secondary x-axis (Figure 8.11), all in 3 M NaCl conditions. Dashed grey regions represent the potentials which result in high crack-growth rates.

In the same way as the previous analysis, the 3 M NaCl cracking and simulated results were compared through overlaying each graph with a common x-axis of potential (Figure *8.13*). Through this combined approach, it can clearly be seen that of the 10 total scenarios tested (Table 8.3), only one falls within the low crack-growth regime, scenario 7.

Therefore, clearly, there exists certain variables relevant to the system design which can be used to tune the potential within the fastener hole to more electronegative or more electropositive values. Of these tunable features, the Zn-Ni coating stands out, as both the location and composition of the coating were shown to have a strong influence over the resulting potential in the hole (Figure 8.5 and Figure 8.10). Selective plating boasts a near-infinite level of possibilities to control the polarization of the coating on the system. Although in this work, the coating was simulated to be applied outside of a simple radius, which optimized the system to the low-cracking regime in both RH-environments, spatially-selective plating could include a hatch pattern or more complex designs based on the geometry of the panel itself to further optimize the potential. The Ni content of the coating had a strong effect as well, with Zn-14%Ni optimizing both the potential in the low-cracking regime and the current to the lower range of values (Figure 8.5 and Figure 8.6). This effect points to the importance of tight control of the composition during the electroplating.

However, caution must be given to both Zn-Ni plating solutions. In the case of a distant coating in this work, the WL is assumed to be continuous across the panel and fastener, thereby allowing a pathway for ions to connect the sacrificial coating to the cathodic driving force of the Ti-6Al-4V bolt. However, if the WL was discontinuous and solution was only present within the fastener hole, the distant coating would then have no effect on the potential in the hole. The impact on potential would be as though the distant coating scenario 7, in the 3 M NaCl solution, suddenly transitioned to the discontinuous WL scenario 8, which results in an increase of approximately 0.5 V (Figure 8.10). In both scenarios, the shaft of the fastener was an anodized Ti-6Al-4V bolt while the fastener hole panel was bare P675 (Figure 8.9 **(c)** and **(d)**).

In addition, as the coating begins to completely dissolve, accomplishing its goal as a sacrificial anode, the surface area ratios would change with increasing bare P675 and decreasing Zn-Ni areas. The carefully controlled potential would then rise electropositively. For example, if the entire surface and fastener hole were coated with a 15 µm thick Zn-11%Ni and exposed to a constant 98% RH environment (correlating to 0.6 M NaCl solution) for a period of two weeks, the coating closest to the fastener would be expected to completely dissolve based on the high mass loss rate closest to the galvanic couple interface (Figure *8.7*). Therefore, the potential at the start of the two weeks would correlate to scenario 4a, in 0.6 M NaCl, while the potential at the end of the two weeks would correlate to scenario 7, in 0.6 M NaCl (Figure 8.3**(b)** and **(c)**).

Continuous exposure without maintenance or replating on the panel would result in all of the Zn-Ni coating dissolved, which would correlate to scenario 1, in 0.6 M NaCl (Figure *8.3***(a)**). As the potentials rose electropositively, they first achieved and then overshot the low-cracking well, as the potentials found from scenario 4a fell in the electronegative high-crack growth rate regime and the potential found from scenario 1 fell in the electropositive high-crack growth rate regime (Figure 8.5). Therefore, controlling the position of the coating can lead to a wide range of control, but must be maintained and carefully monitored.

Engineering the composition of the Zn-Ni coating is also not straightforward, as the electrochemical behavior does not scale linearly with wt% of Ni (Figure 8.1). With lower Ni content (~11% Ni), a hexagonal close packed (HCP) Zn-rich phase η is precipitated, while at higher Ni content (~17% Ni), a simple cubic β intermediate phase forms[51]. The optimum Ni composition falls in the range of 12% – 15% Ni, in which a body centered cubic (BCC) γ phase is most energetically favorable[41,51]. However, the electrodeposition parameters (such as applied current and electrolyte bath composition) can have a large impact on the resulting Zn-Ni composition[40,58]. In addition, trapped H_2 and microcracks may result in the coating, due to the electrodeposition process[59].

An additional method which was found to engineer the potential within the fastener hole involved control of the extent of the anodization surface treatment on the Ti-6Al-4V fastener. The OCP of the bare Ti-6Al-4V was very similar to that of the bare P675, which naturally constrained the potential in the system to a narrow set of values (Figure *8.1* and Figure *8.2*). However, in the 88% RH environment (equilibrium of 3 M NaCl), the OCP of the bare Ti-6Al-4V became *more active* than the bare P675, indicating that the bare Ti-6Al-4V would preferentially corrode as the anode in the two-material galvanic couple (Figure *8.2*). Therefore, scenarios 2 and 3 in the 3 M NaCl solution may have potentials near the edge of the cracking well, but the bolt would undergo slight anodic dissolution (~3μA) (Figure *8.10*).

Note that although this work found three main methods which were successful in engineering the potential within the fastener hole to the low-crack growth rate regimes, these results were by no means comprehensive of the *only* methods to engineer the potential. Additional approaches not tested in this work could include the Zn-Ni coating thickness, post-heat treatment of the coatings, carbo-nitriding of the P675 panel, or cathodic coatings on the Ti-6Al-4V bolt, which have all been found in literature to modify the electrochemical behavior of the respective material[41,60–64].

8.5.2. Comparison of Crack Growth Rates and Potentials in Varying RH Environments

Initial work was conducted in 0.6 M NaCl in full immersion conditions (Chapter 7). However, full immersion conditions may not be of practical importance for all fastener/panel systems and may lead to results which are too-conservative in nature. Atmospheric conditions are complex with many interdependent parameters, including exposure to ozone, UV, thin-electrolyte films, and concentrated aggressive species, and have been known to result in higher corrosion rates than bulk immersion conditions[34,65–69]. In addition, the RH may vary throughout the time of day and year at a given location, correlating to a dynamic molarity and σ. In the present system, the LD was assumed to be constant with time at a given location, leaving the WL as the last independent parameter to equilibrate the system. Based on an empirical derivation by Chen *et al.*, at a constant LD = 3.5 g/m^2 and varying RH from 98% to 88%, the evaporating WL will decrease from 89 μm to 20 μm [56].

The largest discrepancy between the present atmospheric work and the previous full immersion conditions was the ohmic potential drop in solution. The thin-film conditions indicated that the largest amount of ohmic drop occurred on the surface of the panel, which is in sharp contrast to the full-immersion conditions, which indicated that the majority of ohmic drop occurred within the fastener hole as opposed to the near-uniform surface distribution **(**Figure *8.4***(a))** (Chapter 7).

Although the ohmic drop, correlating to the potential ranges, varied between the full-immersion and atmosphere conditions, two of the three controlling factors in modifying the potential within the fastener hole were the same. That is, incorporating a bare Ti-6Al-4V fastener or a distant coating (correlating to scenarios 2 and 7, respectively, in this work) (Figure *8.5*) (Chapter 7). In addition to the previous work of the entire Ti-6Al-4V fastener having no surface treatment, this work found that the shaft could be anodized to maintain wear resistance as the head of the fastener was bare (scenario 3), which still allowed for the fastener hole to be polarized into the optimum low-cracking regime **(**Figure *8.5*).

Note that although the local cathodic reaction kinetics of bare P675 were input onto the respective surfaces in the computational simulations in all scenarios involving the bare P675, they did not contribute any current unless Zn-Ni was present (Figure *8.3* and Figure ***8.6***). Mixed potential theory dictates that the system is bounded by the OCP of the global anode and cathode, indicating that any potentials outside of that range (such as the local cathodic reactions on P675 in the absence of Zn-Ni) would have no impact. The impact of this requirement can be seen by comparing the results of the first scenario, with bare P675 and an anodized Ti-6Al-4V bolt, after including and neglecting the local cathodic reactions. As the results were identical, it was confirmed that the local cathodic reactions had zero influence over the resulting potentials and currents, in systems of bare P675 coupled with the Ti-6Al-4V. However, the bare P675 cathodic reactions were included for consistency, as they became an important reaction in subsequent scenarios, when the Zn-Ni coating was incorporated. This method was followed for the full-immersion conditions and atmospheric conditions of 98% and 88% RH.

The decrease in RH was also represented through conducting the crack growth rate experiments at 3 M NaCl. Interestingly, when comparing the crack growth rate results conducted in 0.6 M NaCl and 3 M NaCl, the *size* of the cracking well (*i.e.*, potential window) does not change, but the magnitude of crack growth rate when *outside* of the well was increased in the more concentrated molarity scenario. The validity of the crack growth rates in 3 M NaCl at -0.8 V_{SCE} and -0.2 V_{SCE} need to be tested and reconfirmed with further samples. However, the results from these tests are not expected to impact the overarching conclusions or recommendations proposed in this work.

With the decrease in RH, and corresponding increase in concentration of NaCl, the potential distributions within the fastener hole grouped together with less spread over the potential ranges as in the 98% RH, 0.6 M NaCl conditions (Figure *8.5* and Figure *8.10*). This result is most prominently visible between the potential range of -0.85 V_{SCE} and -0.3 V_{SCE}, within which the 0.6 M NaCl simulations indicate nine material selection scenarios with potentials in this range whereas the 3 M NaCl simulations indicates a single material combination. The lack of potential range in the 88% RH conditions was most likely due to the larger spread between each material's respective OCP, with the anodized Ti-6Al-4V increasing electropositively by ~0.1 V and the Zn-11%Ni decreasing electronegatively by ~0.06 V, as well as the increased conductivity.

These highly grouped potentials result in less tuning possibilities of the potential within the fastener hole, with the exception of the distant coating scenario 7, which was able to reach a moderate potential within the low-crack growth rate regime **(**Figure *8.13*). However, accounting for a discontinuous WL, the distant coating possibility was nullified and potentials were polarized into the high-crack growth rates in both the electronegative and electropositive directions, due to the 1:1 cathode:anode ratio of that geometry (Figure *8.13*).

8.5.3. Pitting Considerations

Simulations were conducted to include the complicating possibility of a single pit inside of the fastener hole. In addition to macro-scale fastener hole geometry acting as stress concentrators, micro-scale geometries, such as a hemispherical pit, can also concentrate the stress and act as a preferential nucleation cite to cracks[57,70–73]. Pitting and coating breakdown on bulk surfaces are generally measured with post-analysis techniques, as they are difficult to predict and often do not repeatedly occur in the same location[74,75]. However, to isolate the impact that pitting may have, assumptions had to be made. To illustrate the impact of pitting, a single pit with a 100 μm radius was assumed to exist within the fastener hole (Figure *8.8*).

It was determined that changing the location of the 100 μm radius pit within the fastener hole had negligible influence over the potential values and range, which is a relevant conclusion to future modeling assumptions (Figure *8.8* **(b)** through **(d)**). Modeling techniques, once validated with experimental work, are often used as predictive tools. However, predicting the exact location of a pit is extremely difficult, only attempted by complex stochastic models, due to the many possible nucleation sites, such as the inhomogeneous microstructure of the material, surface roughness occlusions, and local chemistry[74]. Therefore, if the location of the pit does not impact the overarching results, concerning the potential distribution in the present case, then the location can be safely, albeit arbitrarily, assumed.

However, when the size of the pit was increased to a radius of 500 μm, the potential within the fastener hole was pulled to more electronegative values, indicating an increase in parameter importance (Figure *8.8***(e)**). The theoretical maximum size of a pit has been well documented in literature, leading to more-informed simulations of this important geometric parameter[49,50,76,77]. For the 0.6 M NaCl atmospheric environment, the maximum pit model theory would predict a pit radius of approximately 120 µm, assuming 50% salt film saturation[31]. Therefore, under that pit size condition, the potential within the fastener hole would be expected to fall into the high-crack growth rate regime, with the assumed hemispherical-size of the pit acting as an additional stress-concentrator.

8.6 Conclusion

In this work, interdisciplinary techniques of LEFM and FEM were combined to determine a materials selection framework, with the goal of enhancing experimental design and structural maintenance through mitigating crack growth susceptibility. Atmospheric conditions and a fastener/panel geometry were conducted to represent realistic environments and structures. Pyrowear 675® and Ti-6Al-4V were the materials of interest in this work, with variations of a coating and surface treatment on the respective surfaces, to optimize the potential within the fastener hole. The main findings from this work are summarized below:

- A LEFM and FEM combined framework was extended to atmospheric conditions and solutions with increased molarities.
- In the 0.6 M NaCl environment, a total of 13 material combination scenarios was reduced to three, which optimized both the potential within the high-stress region to minimize crack growth and optimized the current, which would limit corrosion degradation.

- In the 3 M NaCl environment, less tuning capabilities were present, but out of 10 material combination scenarios, one scenario which included a distant coating was able to achieve a fastener hole potential which fell in the low crack-growth rate regime.
- The material parameters which were able to engineer the potential within the fastener hole to the low-crack growth rate regime included 1) a bare Ti-6Al-4V surface, as opposed to a wear-resistance anodization, 2) the composition of the surface coating, with Zn-14%Ni optimum, and 3) the location of the surface coating, with selective plating in this work simulated to be 0.75 in away from the fastener.
- Conversely, coating the entire surface of the structural panel with a non-optimized Zn-Ni composition or utilizing an anodized Ti-6Al-4V bolt led to *overpolarization*, both electronegatively (from the Zn-Ni) and electropositively (from the anodization).
- A single pit was included within the fastener hole, and it was determined that the location of the pit had less of an impact on the overall potential than the size of the pit.

8.7 Acknowledgements

This research was financially supported by Rolls Royce Corporation, with specific thanks to Michelle Boehm, Megan Snellenberger, JD Smith, Skylar Conn, Brian Drier, Tim Cummings, Bradford Wiley, Randa Brice, Mike Whitten, and Ann Heeter.

8.8 References

1. Koch, G.H., M.P.H. Brongers, N.G. Thompson, Y.P. Virmani, and J.H. Payer, “Chapter 1: COST OF CORROSION IN THE UNITED STATES,” in Degradation Economics (2005).

2. Koch, G.H., M.P.H. Brongers, J.H. Payer, N.G. Thompson, and P.Y. Virmani, *NACE International* (2002): pp. 1–12, papers2://publication/uuid/4D469A9D-07D6-4543-B217-3A15873793CF.

3. John W. Lincoln, "Corrosion and Fatigue: Safety Issue or Economic Issue," in RTO AVT Workshop: Fatigue in the Presence of Corrosion (Corfu, Greece, 1998).

4. Steiner, P.J., Z.D. Harris, C.V. Moraes, R.G. Kelly, and J.T. Burns, *Corrosion* 77 (2021): pp. 838–852.

5. Cocke, C., R.S. Marshall, C. Sprinkle, A. Goff, R.G. Kelly, and J.T. Burns, *Corrosion* 78 (2022): pp. 152–162.

6. Harrison, T.J., B.R. Crawford, C. Loader, G. Clark, and M. Brandt, *International Journal of Fatigue* 82 (2016): pp. 700–707, http://dx.doi.org/10.1016/j.ijfatigue.2015.09.028.

7. Moayed, M.H., N.J. Laycock, and R.C. Newman, *Corrosion Science* 45 (2003): pp. 1203–1216.

8. Brossia, C.S., and R.G. Kelly, *Corrosion* 54 (1998): pp. 145–154.

9. Turnbull, A., "2009 W.R. Whitney Award Lecture: Local Hydrogen Generation and Its Impact on Environment-Assisted Cracking and Crevice Corrosion," CORROSION SCIENCE SECTION CORROSION (2009), http://meridian.allenpress.com/corrosion/article-pdf/66/5/055001/1538993/1_3430461.pdf.

10. Galvele, J.R., *CORROSION* 55 (1999), http://meridian.allenpress.com/corrosion/article-pdf/55/8/723/1534358/1_3284027.pdf.

11. Marshall, R.S., R. Kelly, A. Goff, and C. Sprinkle, *Corrosion* 75 (2019): pp. 1461–1473.

12. Moran, A., J. Jennings, H. Nee, S. Pearson, B. Clark, and R.S. Lillard, *Corrosion Journal* 75 (2019): pp. 484–498.

13. Rafla, V.N., and J.R. Scully, *Corrosion Journal* 75 (2019): pp. 12–28.

14. Young, P.S., and J.H. Payer, *Corrosion* 71 (2015): pp. 1278–1293.

15. Mcmurtrey, M.D., D. Bae, and J.T. Burns, (2016).

16. Prasad, P.S., and K.S. Ghosh, *Electrocatalysis* (2022), https://link.springer.com/10.1007/s12678-022-00744-4.

17. Shibata, A., I.G. Urrutia, K. Okada, G. Miyamoto, Y. Madi, J. Besson, and K. Tsuzaki, *Materials Science and Engineering: A* 831 (2021): p. 142288, https://doi.org/10.1016/j.msea.2021.142288.

18. Lee, Y., and R.P. Gangloff, *Metallurgical and Materials Transactions A: Physical Metallurgy and Materials Science* 38 A (2007): pp. 2174–2190.

19. Cooper, K.R., and R.G. Kelly, *Corrosion Science* 49 (2007): pp. 2636–2662.

20. Harris, Z.D., and J.T. Burns, *Corrosion and Materials Degradation* 2 (2021): pp. 360–375.

21. Liu, C., V.N. Rafla, J.R. Scully, and R.G. Kelly, "Mathematical Modeling of Potential and Current Distributions for Atmospheric Corrosion of Galvanic Coupling in Airframe Components," in NACE International: CORROSION (2015), pp. 1–11.

22. Helle, H.P.E., G.H.M. Beek, and J.T. Ligtelijn, *Corrosion* 37 (1981): pp. 522–530.

23. Chen, Y., H. Huang, Y. Zhang, G. Bian, C. Wang, and A. Wang, *Materials and Corrosion* 69 (2018): pp. 1649–1657.

24. Snihirova, D., D. Höche, S. Lamaka, Z. Mir, T. Hack, and M.L. Zheludkevich, *Corrosion Science* 157 (2019): pp. 70–78, https://doi.org/10.1016/j.corsci.2019.04.036.

25. Marshall, R.S., R. Kelly, A. Goff, and C. Sprinkle, *Corrosion* 75 (2019): pp. 1461–1473.

26. Charles-Granville, U.-E., R.S. Marshall, C. v. Moraes, C.F. Glover, J.R. Scully, and R.G. Kelly, *Journal of The Electrochemical Society* 169 (2022): p. 031502.

27. Xu, Y., and H.W. Pickering, *Journal of The Electrochemical Society* 140 (1993): pp. 658–668.

28. Mansfeld, F., and E.P. Parry, *Corrosion Science* 13 (1973): pp. 605–621.

29. Oldfield, J.W., *ASTM Special Technical Publication* STP (1988): pp. 5–22.

30. Marshall, R.S., A. Goff, C. Sprinkle, A. Britos, and R. Kelly, *Corrosion* 76 (2020): pp. 476–484.

31. Marshall, R.S., R.M. Katona, M.A. Melia, and R.G. Kelly, *J Electrochem Soc* 169 (2022): p. 021506.

32. Thébault, F., B. Vuillemin, R. Oltra, C. Allely, and K. Ogle, *Corrosion Science* 53 (2011): pp. 201–207.

33. Simillion, H., O. Dolgikh, H. Terryn, and J. Deconinck, *Corrosion Reviews* (2014).

34. Tomashov, N.D., *CORROSION* 20 (1964).

35. Liu, C., J. Srinivasan, and R.G. Kelly, *J Electrochem Soc* 164 (2017): pp. C845–C855, http://jes.ecsdl.org/lookup/doi/10.1149/2.1641713jes.

36. Katona, R., J. Carpenter, A. Knight, R.S. Marshall, B. Nation, E. Schindelholz, R.F. Schaller, and R. Kelly, *J Electrochem Soc* 168 (2021), https://iopscience.iop.org/article/10.1149/1945-7111/abeb29.

37. Charles-Granville, U.-E., C. Liu, J.R. Scully, and R.G. Kelly, *Journal of The Electrochemical Society* 167 (2020): p. 111507.

38. Alexander, C.L., C. Liu, A. Alshanoon, R.M. Katona, R.G. Kelly, J. Carpenter, C. Bryan, and E. Schindelholz, *Journal of The Electrochemical Society* 165 (2018): pp. C869–C877.

39. Steiner, P.J., and J.T. Burns, *Corrosion* 74 (2018): pp. 1117–1131.

40. Fashu, S., and R. Khan, “Recent Work on Electrochemical Deposition of Zn-Ni (-X) Alloys for Corrosion Protection of Steel,” Anti-Corrosion Methods and Materials (Emerald Group Holdings Ltd., 2019).

41. Conde, A., M.A. Arenas, and J.J. de Damborenea, *Corrosion Science* 53 (2011): pp. 1489–1497.

42. Moraes, C. v., R.J. Santucci, J.R. Scully, and R.G. Kelly, *Journal of The Electrochemical Society* 168 (2021): p. 051505.

43. King, A.D., J.S. Lee, and J.R. Scully, *J Electrochem Soc* 163 (2016): pp. 342–356.

44. Thébault, F., B. Vuillemin, R. Oltra, K. Ogle, and C. Allely, *Electrochimica Acta* 53 (2008): pp. 5226–5234.

45. PFAFFENBERGER, E., and P. TARRANTINI, "High Temperature Corrosion Resistant Bearing Steel Development," in 29th Joint Propulsion Conference and Exhibit (Monterey, CA, 1993).

46. McCaffrey, T.J., and D.E. Wert, *ASTM Special Technical Publication* (1993): pp. 137–148.

47. Harris, Z.D., E.M. Dubas, A.S. Popernack, B.P. Somerday, and J.T. Burns, *Theoretical and Applied Fracture Mechanics* 111 (2021).

48. Liu, C., and R.G. Kelly, *Corrosion* 75 (2019): pp. 1087–1099.

49. Katona, R.M., J. Carpenter, E.J. Schindelholz, and R.G. Kelly, *J Electrochem Soc* 166 (2019): pp. C3364–C3375.

50. Katona, R.M., A.W. Knight, E.J. Schindelholz, C.R. Bryan, R.F. Schaller, and R.G. Kelly, *Electrochimica Acta* 370 (2021): p. 137696, https://doi.org/10.1016/j.electacta.2020.137696.

51. Tafreshi, M., S.R. Allahkaram, and H. Farhangi, *Materials Chemistry and Physics* 183 (2016): pp. 263–272, http://dx.doi.org/10.1016/j.matchemphys.2016.08.026.

52. Pryor, M.J., and D.S. Keir, *J Electrochem Soc* 105 (1958): pp. 629–635.

53. Liu, C., P. Khullar, and R.G. Kelly, *Journal of The Electrochemical Society* 166 (2019): pp. 153–161.

54. Liu, C., and R.G. Kelly, *Corrosion Journal* 75 (2019): pp. 1285–1299.

55. Newman, J., and K.E. Thomas-Alyea, *Electrochemical Systems*, Third Edit (Wiley-Interscience, 2004).

56. Chen, Z.Y., F. Cui, and R.G. Kelly, *J Electrochem Soc* 155 (2008): pp. 360–368.

57. Mcmurtrey, M.D., D. Bae, and J.T. Burns, (2016).

58. T.V. Byk, T.V. Gaevskaya, and L.S. Tsybulskaya, *Surface and Coatings Technology* 202 (2008): pp. 5817–5823.

59. Sriraman, K.R., S. Brahimi, J.A. Szpunar, and S. Yue, *Journal of Applied Electrochemistry* 43 (2013): pp. 441–451.

60. Oliveira, M.A.S., A.K. Vieira, and M. Massi, *Diamond and Related Materials* 12 (2003): pp. 2136–2146.

61. Sriraman Kankoduthavanitham Rajagopalan, "Characterization of Electrodeposited Zn-Ni Alloy Coatings as a Replacement for Electrodeposited Zn and and Cd Coatings," McGill University, Montreal, Quebec, Canada, 2012.

62. Rao, V.R., A. Chitharanjan Hegde, and K. Udaya Bhat, *Journal of Electrochemical Science and Engineering* 3 (2013): pp. 137–149.

63. Trivedi, H.K., F. Otto, B. McCoy, R.S. Bhattacharya, and T. Piazza, *ASTM Special Technical Publication* STP 1580 (2015): pp. 465–484.

64. Kvryan, A., C.M. Efaw, K.A. Higginbotham, O.O. Maryon, P.H. Davis, E. Graugnard, H.K. Trivedi, and M.F. Hurley, *Materials* 16 (2019).

65. Liang, D., H.C. Allen, G.S. Frankel, Z.Y. Chen, R.G. Kelly, Y. Wu, and B.E. Wyslouzil, *Journal of The Electrochemical Society* 157 (2010): p. C146.

66. Hangarter, C.M., and S.A. Policastro, *Corrosion* 73 (2017): pp. 268–280.

67. Stratmann, M., and H. Streckel, *Corrosion Science* 30 (1990): pp. 681–696.

68. Stratmann, M., and H. Streckel, *Corrosion Science* 30 (1990): p. 697.

69. Stratmann, M., H. Streckel, K.T. Kim, and S. Crockett, *Corrosion Science* 30 (1990): pp. 715–734.

70. Burns, J.T., J.M. Larsen, and R.P. Gangloff, *Fatigue & Fracture of Engineering Materials & Structures* 34 (2011): pp. 745–773, https://doi.org/10.1111/j.1460-2695.2011.01568.x.

71. Nicolas, A., N.E.C. Co, J.T. Burns, and M.D. Sangid, *Engineering Fracture Mechanics* 220 (2019): p. 106661, https://doi.org/10.1016/j.engfracmech.2019.106661.

72. Co, N.E.C., and J.T. Burns, *International Journal of Fatigue* 150 (2021): p. 106301, https://doi.org/10.1016/j.ijfatigue.2021.106301.

73. Co, N.E.C., and J.T. Burns, *International Journal of Fatigue* 103 (2017): pp. 234–247, http://dx.doi.org/10.1016/j.ijfatigue.2017.05.028.

74. Shibata, T., *Corrosion* 52 (1996): pp. 813–830, http://meridian.allenpress.com/corrosion/article-pdf/52/11/813/1532784/1_3292074.pdf.

75. Budiansky, N.D., L. Organ, J.L. Hudson, and J.R. Scully, *J Electrochem Soc* 152 (2005): pp. B152–B160.

76. Chen, Z.Y., and R.G. Kelly, *J Electrochem Soc* 157 (2009): pp. 69–78.

77. Woldemedhin, M.T., M.E. Shedd, and R.G. Kelly, *J Electrochem Soc* 161 (2014): pp. E3216–E3224.

Chapter 9: Application of Finite Element Modeling to Macro-Galvanic Coupling of AA7050 and SS316: Methodology for Determining the Correct Boundary Conditions

Utibe-Eno Charles-Granville$^{=}$, Rebecca S. Marshall$^{=}$, Carolina V. Moraes$^{=}$, Carol F. Glover,
John R. Scully, Rob G. Kelly

University of Virginia, 395 McCormick Rd, Charlottesville VA 22903

Authorship contributions: U. Charles-Granville (formal analysis, experimental polarization behavior, experimental material preparation, and writing – original draft), R. Skelton Marshall (formal analysis, computational work, experimental polarization behavior, and writing – original draft), C. V. Moraes (formal analysis, computational work, experimental polarization behavior, and writing – original draft), C. F. Glover (SVET experimental measurement), J. R. Scully (technical expertise)

$^{=}$ Equal contribution

9.1 Abstract

The scanning vibrating electrode technique (SVET) was utilized to experimentally validate the applicability of finite element modeling (FEM) in simulating macro-galvanic-induced corrosion of AA7050 coupled to SS316, in environments representative of the boldly exposed surface of an actual fastener couple. The FEM boundary conditions were modified from the SVET

environments in which the AA7050-SS316 couple sample was initially exposed, in order to better represent the steady-state corroding surface of the localized corrosion-prone AA7050. Better agreements between the SVET-derived data and the model in the case of macro-galvanic coupling behavior were achieved for near-neutral conditions, compared to acidic conditions. The current density at the electrode/electrolyte interface was determined with the validated model. In addition, the percent difference between the measured current density at the SVET probe height and that at the electrode surface was observed to scale with the magnitude of current density at the electrode surface, with the largest discrepancy seen at the galvanic couple interface. Plausible reasons for the deviation of the model predictions from the SVET-derived data are discussed.

9.2 Introduction

Precipitation-strengthened Al alloys such as those belonging to the 2XXX and 7XXX series are the preferred materials for the construction of light-weight aerospace vehicles.[1] Despite their superior mechanical properties, these high-strength Al alloys pose a huge challenge in weldability. Because they are precipitation-strengthened, the use of traditional welding techniques to join them often leaves undesirable weld joints with deteriorated properties due to weld porosity and weld cracking during solidification.[2] As an alternative, high-strength, noble fasteners such as stainless steels (SS) are often used in joining the Al alloy (AA) parts in aerospace structures. In natural corrosive environments, macro-galvanic interactions between the more noble fastener and the AA, in addition to the micro-galvanic coupling within the base AA microstructure,[3] can exacerbate localized corrosion of the Al-based structures.[4–11]

Many studies of galvanic corrosion processes on Al alloys have utilized a number of experimental techniques, including the zero resistance ammeter (ZRA) technique, the coupled microelectrode array (CMEA), and the scanning vibrating electrode technique (SVET).[11–20] The

ZRA technique conducted on planar coupled electrodes enables the simultaneous measurements of global galvanic potentials and coupling currents. In this configuration, spatial resolution of localized corrosion processes occurring on the AA cannot be captured; only global current measurements are possible. In this context, the CMEA coupled with the ZRA allows the interrogation of in-situ local electrochemical processes occurring on individual microelectrodes by mapping the local current density distributions as a function of spatial location and time. In the case of AA7XXX, one can monitor the transition of initial anodes to cathodes which could signify dealloying of Al_2CuMg and/or Cu replating.[11,15] That said, some of the limitations of the CMEA are the intricacy of constructing the arrays, the use of surrogate materials as opposed to plate or sheet products used in aerospace construction, as well as the need for controlling specific geometric parameters such as anode-to-cathode ratio and electrode spacing.

The primary benefit of using the SVET to investigate galvanically-induced corrosion is that it enables the spatial and temporal resolution of the electrochemical behavior from the macro-galvanic couple (between SS and AA, in this instance) and localized behavior as a result of the micro-galvanic coupling on the same surface. The evolution of local net anodic and cathodic activity can be mapped, enabling the magnitude of currents to be monitored as a function of time. This distinction between the two types of corrosion occurring in this system cannot be achieved with bulk electrochemical techniques. Although the SVET provides a good representation of the localized corrosion processes occurring *in-situ* on an electrode surface with no perturbation from the test itself, the results should be used with caution.[21] The SVET measures the dominant reaction or net current and detects current based on the potential gradient. It also does not account for local variations in conductivity that may occur at the electrode surface as a result of corrosion processes, and is disrupted by hydrogen bubbles.[22] The SVET measurements are not taken at the electrode surface but at a specific height above the electrode surface, typically ~ 50-150 µm.[17,23–26] As such, the calculated currents are typically an underestimation of the actual values at the electrode surface.[21] One way to bridge this gap is to utilize finite element modeling (FEM) in conjunction with the SVET. If the FEM simulations can be reasonably validated by the SVET at a specified probe height, then one can utilize the FEM to predict current density distributions at the electrode surface as well as quantify the underestimation of the electrode surface current density as a function of SVET probe height.

A number of studies have employed the SVET to validate FEM simulations using the Laplace,[27–29] Laplace and Fick's second law,[25,30,31] and Nernst-Planck[27,30,32,33] as governing equations. The Laplace equation assumes that the solution is homogeneously mixed such that the diffusive and convective transport of species can be ignored, allowing the solution to be treated as an ohmic resistor, which makes the model less complex.[34] The Laplace approach can be supplemented with transport equations for cases in which kinetics of the electrodes are dependent on the concentration of species present in the electrolyte, that either do not considerably carry the current (minor species) or that do not have charge (e.g., O_2). This approach has been widely used to model the mixed charge-transfer and diffusion-controlled kinetics of the oxygen reduction reaction (ORR).[25,30,31]

The Nernst-Planck equation is more robust in considering concentration gradients of all ionic species in the electrolyte, yet computationally demanding in terms of complexity and execution time.[34] Thébault et al.[30] demonstrated that the locally-induced convection from the vibrating probe tip during SVET measurements homogenizes the electrolyte, thus, eliminating any concentration and conductivity gradients. This natural outcome makes the SVET an ideal experimental technique to compare with a Laplacian model.

When solving for the variables that describe corrosion phenomena in FEM with any of the governing equations above, it is common to use a scaffolding approach to determine the correct boundary conditions by starting with simplifying assumptions and working towards a more realistic scenario.[28,35–37] As noted previously, computational results depend highly on the choice of boundary conditions, which are also dependent on a variety of environmental factors.[34]

The aforementioned studies demonstrate the viability of the SVET for modeling galvanic corrosion processes and, to the best of the authors' knowledge, no studies in the available literature have combined these techniques with a focus on AA-SS galvanically-coupled systems.

The objective of this work is to utilize the SVET to validate the FEM-based Laplacian model in predicting macro-galvanic current distributions on an AA7050-SS316 couple in simulated environments representative of near-neutral and acidic corrosive conditions. The geometry of the AA7050-SS316 couple mimics the boldly exposed surface of an actual fastener couple.

As with all models, the choice of the input boundary conditions is crucial to the accuracy and reliability of the model as a predictive tool, especially for conditions that are experimentally difficult or impractical to investigate. Emphasis is made on the choice of boundary conditions as well as the adjustments made in an attempt to correctly represent the conditions being simulated. The sources of the discrepancies observed between the SVET and modeling results are discussed. The results of this study are intended to add to the knowledge base of the applicability of FEM to the simulation of galvanic corrosion phenomena.

9.3 Methods

SVET Measurements

The AA7050-SS316 couple was constructed by inserting a short rod of SS316 onto an AA7050 plate with the dimensions as shown in Figure 9.1(a). The SS316 rod was flush-mounted so that the transverse cross-section produces a circular disk in the plane of the plate. The anode-to-cathode area ratio was ~ 7:1. No intentional crevice gap was created. The structure was encapsulated in epoxy with an internal Ni wire electrical connection. Immediately preceding each experiment, the sample was wet-ground successively from 400 grit to a surface finish of 1200 grit with SiC paper, rinsed with deionized water, and dried with clean compressed air. A Biologic SP™ instrument was utilized for the SVET measurements. The scans were conducted on an area of ~ 7.5 mm x 7.5 mm within the exposed bare area of the couple surface in each case, under freely corroding conditions. For each experiment, the exposed couple surface was fully immersed (i.e., water layer thickness ≥ 1000 μm) in an electrolyte bath containing aqueous 1 mM NaCl electrolyte at the relevant pH. The choice of 1 mM NaCl was made based on the resolution limitations of the SVET as signal-to-noise ratios decrease with increasing solution conductivity.[21] Experiments were conducted at the electrolyte's natural pH of 5.8 and at pH 3 (adjusted with HCl) to simulate normal rainy conditions and acid rain conditions, respectively.

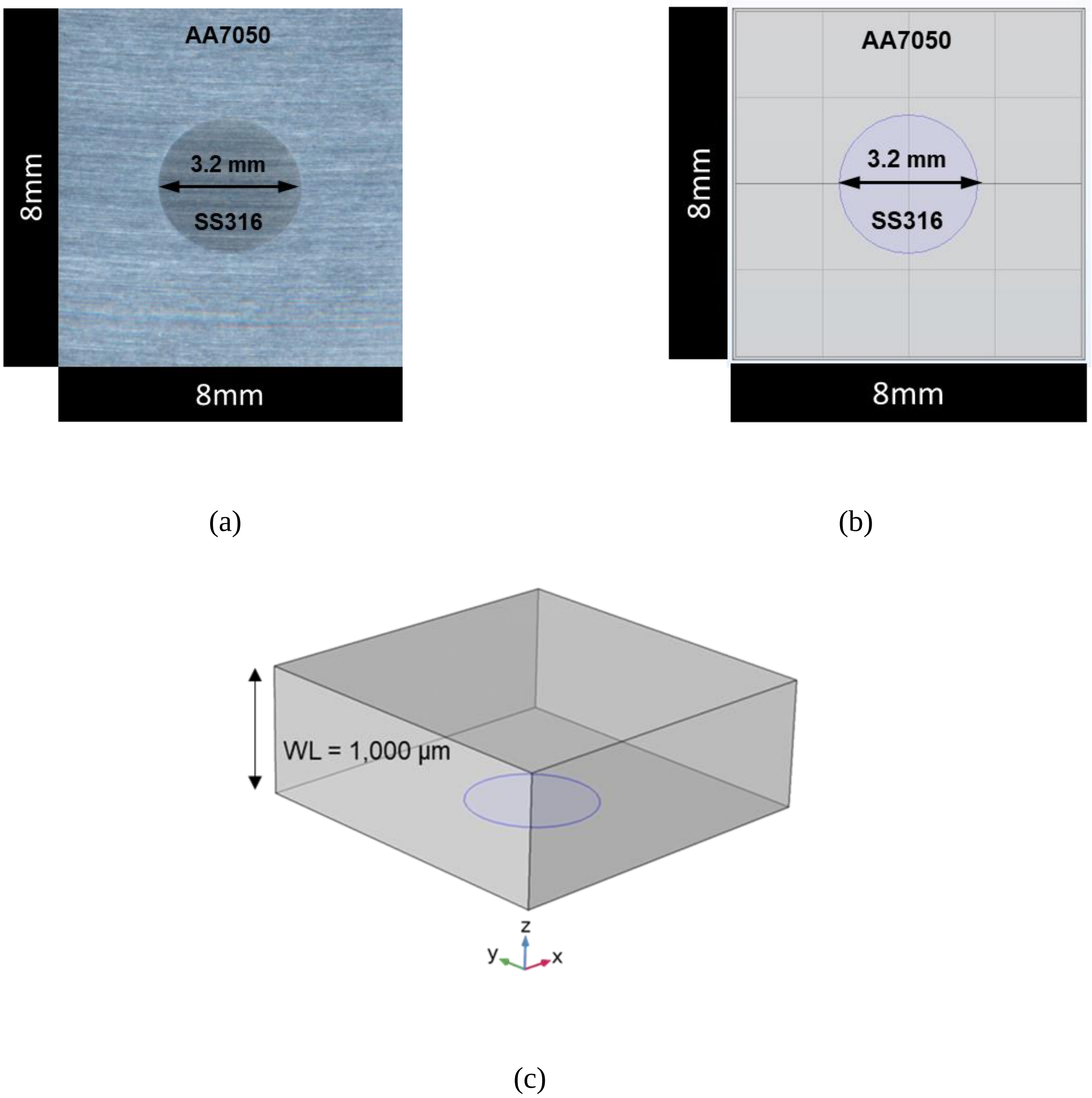

Figure 9.1: Geometry of the AA7050-SS316 couple used for (a) SVET experiments and (b) FEM; (c) xy, yz, and xz boundaries representing the air/solution interface in (b) with z = water layer thickness of 1000 µm.

An additional experiment was conducted on a 200 µm Au point current source that was used to determine the change in the SVET-derived current density as a function of the SVET probe height from the electrode surface. Two current values of 5 µA and 25 µA were applied separately to the Au point current source. The experiments were conducted in 1 mM NaCl at its natural pH of 5.8, for consistency with the galvanic coupling experiment.

The vibrating SVET probe consisted of a platinum probe with a diameter specified by the manufacturer as between 5 and 50 µm. The probe was positioned vertically and scanned at a constant height of 100 µm above the experimental area with a peak-to-peak amplitude of 30 µm and a frequency of 80 Hz. The peak-to-peak SVET voltage signal (V_{pp}) is related to the current flux density along the axis of probe vibration (j_z) by:

$$V_{pp} = j_z \left(\frac{A_{pp}}{\kappa}\right) \tag{9.1}$$

where κ is solution conductivity and A_{pp} is the peak-to-peak amplitude of vibration of the SVET probe, such that a quantity $G = \kappa/A_{pp}$ may be defined as the SVET calibration factor.

SVET calibration was carried out galvanostatically using the point current source technique described above, where a graphite counter electrode was held ~ 8 cm away from the Au point current source, and the setup can be found elsewhere.[38,39] Samples were scanned immediately following immersion and continuously thereafter for a period of 24 h. The total number of measurement points in each scan was ~ 5776, and the time taken for each measurement was ~ 0.12 s, for a full scan duration of ~ 12 min. There was no wait time between measurements. SVET j_z distributions were plotted using Surfer 8™ by Golden Software.

Electrochemical Measurements

Cathodic and anodic potentiodynamic polarization curves were generated on SS316 and AA7050, respectively, to serve as input boundary conditions for the model. Experiments were conducted on separate SS316 and AA7050 specimens in a standard three-electrode flat cell configuration, in the same environments used for the SVET measurements, under quiescent conditions. HCl was used to adjust the pH. Two concentrations of $AlCl_3$, 0.003 mM and 0.3 mM, were added to the cathodic scans while maintaining the total chloride concentration of 1 mM. The pH in both $AlCl_3$ containing solutions was not controlled but was measured to be 5 and 3.6 for the low and high concentrations, respectively. The scans were conducted after a 30-min full immersion exposure at open circuit and at a scan rate of 0.5 mV/s.

Model Description

9.3.1.1. Governing Equation

COMSOL Multiphysics® software (v. 5.6) was used to solve the partial differential equations by the finite element method. Laplace equation (Eq. 9.2) was used to solve for the potential distribution in the electrolyte domain:

$$\nabla^2 \varphi = 0 \tag{9.2}$$

where φ is the electrolyte potential. By using Laplace as the governing equation, the electrolyte is assumed to be well-mixed (i.e., there is a negligible concentration gradient of the ionic species); hence, electrolyte is assumed to behave as a homogeneous ohmic conductor with a constant conductivity. Thus, the electrolyte current density could be solved using Ohm's law:

$$i = \kappa_i \nabla \varphi \tag{9.3}$$

where κ_i corresponds to the conductivity of the solution i. For each case investigated, the conductivities were adjusted according to the solution in which the measurements were performed. Table 9.1 shows the conductivity of the solutions considered in this work, which were calculated using OLI^{TM} Studio Analyzer 10.1 (from OLI Systems, NJ). In all scenarios tested, the conservation of charge (i.e., $I_a = I_c$, with I_a being the total anodic current and I_c being the total cathodic current) was verified.

Table 9.1: Parameters used in the FEM

Parameter	Description	Value
$\mathbf{i_{0,5.8}}$	Pseudo-exchange current density for ORR kinetics in pH 5.8	4 x 10^{-11} (A/cm^2)
$\boldsymbol{b}_{\mathbf{c,5.8}}$	Fitted cathodic Tafel slope in pH 5.8	-0.193 (V) 95%CI (-0.194, -0.191)
$\mathbf{E_{eq,5.8}}$	Equilibrium potential of the cathode in pH 5.8	0.573 (V)
$\mathbf{i_{lim,5.8}}$	Diffusion limited current density in pH 5.8	1.2 x 10^{-5} (A/cm^2)
$\boldsymbol{\kappa}_{\mathbf{5.8}}$	Conductivity in 0.001M NaCl, pH 5.8	0.0188 (S/m)
$\mathbf{i_{0,3}}$	Pseudo-exchange current density for ORR kinetics in pH 3	5 x 10^{-13} (A/cm^2)
$\boldsymbol{b}_{\mathbf{c,3}}$	Fitted cathodic Tafel slope in pH 3	-0.181 (V) 95%CI (-0.182, -0.180)
$\mathbf{E_{eq,3}}$	Equilibrium potential of the cathode in pH 3	0.809 (V)
$\mathbf{i_{lim,3}}$	Diffusion limited current density in pH 3	3 x 10^{-5} (A/cm^2)
$\boldsymbol{\kappa}_{\mathbf{3}}$	Conductivity in 0.001M NaCl, pH 3	0.0767 (S/m)

The assumption of a well-mixed electrolyte to model SVET measurements is reasonable, as the convection induced by the microelectrode vibrations homogenizes the electrolyte, reducing any concentration gradients.[30]

In an additional model, Al^{3+} production and transport were calculated. Fick's second law was used to solve for the concentration distribution through space and time:

$$\nabla^2 c_{Al^{3+}} = 0 \qquad 9.4$$

Note that, even though Al^{3+} is a charged species that can carry current, it was assumed that Na^+, Cl^-, and H^+ were the main species that carried current.

The model was built using a 3D geometry. The dimensions of the sample on which the SVET was performed were used to build the geometry, as shown in Figure 9.1(b).

9.3.1.2. Boundary Conditions

As illustrated by Figure 9.1(c), at the upper (xy), left (yz), and right (xz) boundaries, which represent the air/solution interface (z = water layer thickness), Neumann boundary conditions were applied (i.e., no current flux). At the lower boundary, the electrochemical kinetics of SS316 and AA7050 were defined using different approaches. In the first approach, piecewise interpolations of the full immersion potentiodynamic polarization scans were used as boundary conditions. In a second approach, a limiting current density corresponding to the diffusion-limited oxygen reduction reaction (ORR) current density was imposed. In a third approach, the cathodic kinetics of SS316 were defined using an analytical expression:

$$i = \frac{i_{ct}}{1 + \left|\frac{i_{ct}}{i_{lim}}\right|} \tag{9.5}$$

$$i_{ct} = i_0 \cdot 10^{\frac{E-E_0}{b}} \tag{9.6}$$

where i_{ct} is the charge transfer-controlled portion of the current density, i_{lim} is the ORR limiting current density extracted from the cathodic polarization scans, i_0 is a pseudo-exchange current density, E is the applied potential, E_0 is the reversible potential, and b is a fitted Tafel slope. The pseudo-Tafel parameters were obtained by fitting Eq. 9.6 to the cathodic polarization scans. The values of the parameters are displayed in Table 9.1.

Note that the edges of the sample (x = 0 and 8 mm) were the boundaries of the simulation, which simulates a condition in which the walls of the container in which the SVET was performed were exactly at the edges of the sample (Figure 9.1(b) and (c)). This modeling approach is common in literature, even if the sample is exposed to bulk immersion such as occurs during SVET.[25,27,32,40] However, the dimensions of the container in which the SVET was performed were much larger than the sample's dimensions.

For the case in which Al^{3+} concentration was calculated, Faraday's law was used to calculate the local flux of the Al^{3+} species being produced at the AA7050 electrode ($J_{Al^{3+}}$), with the assumption that the dissolution of the other alloying elements present in AA7050 (e.g., Zn, Mg) are negligible:

$$J_{Al^{3+}} = \frac{i_{local,AA7050}}{nF} \tag{9.7}$$

where n is the number of electrons transferred during the reaction, and F is Faraday's constant. Additionally, for the case in which Al^{3+} was considered, the geometry of the model was altered to match the total volume of the solution in which the SVET measurements were performed. Zero flux boundary conditions were imposed at the interfaces between electrolyte/air and at the walls of the container. Effects of natural convection were not taken into consideration.

9.3.1.3. Error Calculations

When comparing experimental results against each other, such as calculating the conservation of electroneutrality between the experimentally-derived anodic and cathodic currents, or to quantify the difference between computational results, the percent difference was used (Eq. 9.8).

$$\frac{ABS(x_1 - x_2\ )}{ABS\left(\frac{(x_1 + x_2)}{2}\right)} \times 100 \tag{9.8}$$

where ABS represents the absolute value, x_1 represents one experimental/computational datapoint, and x_2 represents another experimental/computational datapoint, respectively. However, when the computational and experimental current densities (or currents) were compared, the percent error was utilized (Eq. 9.9).

$$\frac{ABS(i_{experiment} - i_{computational})}{ABS(i_{experiment})} \times 100 \qquad 9.9$$

In this way, the experimental results acted as a “baseline” with which to compare the computational data.

9.4 Results

9.4.1. *Potentiodynamic Scans*

Cathodic and anodic potentiodynamic scans (PDS) were plotted separately for clarity in Figures 2a and 2b, respectively. Note that only cathodic reactions on the SS316 surface were considered in this work. The anodic passive current density of SS316 was calculated to be approximately three orders of magnitude lower than the cathodic behavior of SS316 within the potential range of interest. This result justifies the assumption that anodic reactions occurring on the SS316 surface in the present system would be negligible.

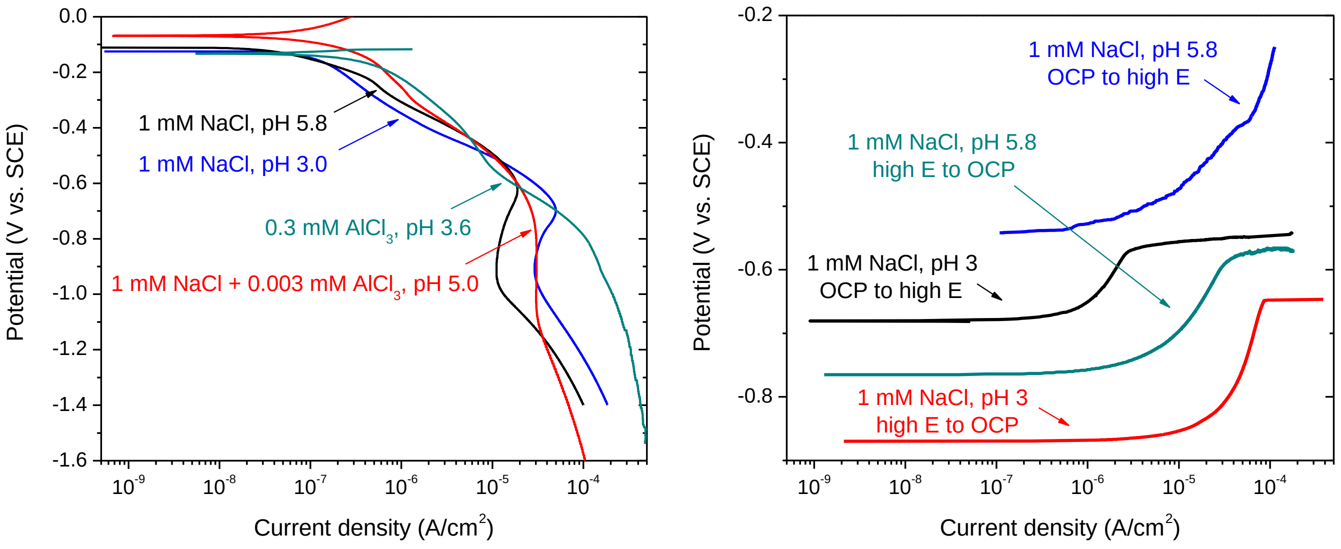

(a) (b)

Figure 9.2: Potentiodynamic polarization scans used as input boundary conditions for the model; (a) cathodic scans on SS316, and (b) anodic scans on AA7050, corrected for ohmic drop.

In the pH 3 environment, cathodic kinetics on SS316 increased by at least two-fold compared to that at pH 5.8, which is consistent with what has been reported in the literature.[41,42] Additionally, it was observed that the cathodic kinetics increased with increasing Al^{3+} concentration while keeping the chloride concentration constant. Decreased amounts of Al^{3+} in solution exhibited a smaller effect, with a diffusion limiting current density visible and approximately equal to that observed in the pH 3 solution, where no additions of $AlCl_3$ were made. Both the change in pH and the addition of Al^{3+} had minimal impact on the open circuit potential (OCP) of the SS316. Concerning the cathodic scans on SS316 without the addition of Al^{3+}, there was a current wave at potentials between the charge-transfer regime and the diffusion limiting regime (Figure 9.2(a)). This cathodic peak was determined to be a transient and will be discussed in a later section.

All anodic curves were manually post-processed to correct for ohmic drop by first calculating the slope of the linear E vs. i plot to determine the ohmic (solution) resistance. The true potential was determined by subtracting the product of the current density and ohmic resistance, that is, the potential due to ohmic drop. To confirm the calculated solution resistance from post-processing, EIS was used to measure the actual resistance between the reference and working electrodes. Impedance at high frequencies performed in the same cell, assuming a Randles circuit, resulted in ohmic resistance values consistent with the manually calculated values as displayed in Table 9.2.

Table 9.2: Ohmic resistance values used for iR correction of anodic polarization curves.

Description of Technique	Description of Solution	R_{ohmic} ($\Omega \cdot cm^2$)
EIS	1 mM NaCl, pH 5.8	5750
Manual correction	1 mM NaCl, pH 5.8, OCP to high E positive scan	7221
Manual correction	1 mM NaCl, pH 5.8, high E to OCP negative scan	5246
EIS	1 mM NaCl, pH 3	3541
Manual correction	1 mM NaCl, pH 3, OCP to high E positive scan	3368
Manual correction	1 mM NaCl, pH 3, high E to OCP negative scan	2467

Conventional anodic polarization of AA7050 typically starts either at, or slightly below, the measured OCP before scanning to more positive potentials. In this study, scans were also conducted starting at a high potential and sweeping towards the OCP. This method captures the anodic kinetics and OCP while the surface is undergoing active localized corrosion, and is evident in the data presented in Figure 9.2(b), where increased anodic kinetics and a suppressed OCP are observed in the ‘high E to OCP’ negative scans, relative to those observed for the positive ‘OCP to high E’ scans. Additionally, independent of scan direction, the OCP of the AA7050 in the pH 3 solution was found to be more negative than that observed in pH 5.8. When considering a steady-state model, the boundary conditions should also reflect steady-state corrosion while neglecting any passive breakdown initiation period that may occur during the initial immersion. Selecting a polarization curve that best describes the steady-state corroding surface requires careful consideration. This aspect of modeling will be discussed later.

9.4.2. SVET Current Density Distributions

Figures 3a and 3b show the SVET-derived current density distribution maps obtained on the AA7050-SS316 couple in 1 mM NaCl at pH 5.8 and pH 3, respectively, after 24 h of immersion.

Under pH 5.8 conditions (Figure 9.3(a)), localized anodic activity was observed in multiple locations on the AA7050 surface, indicative of pitting corrosion. It is noteworthy that these anodically activated regions on the AA7050 surface were not necessarily found to be adjacent to the SS316 cathode. Peak anodic and cathodic j_z values over the couple surface were ~ $\pm$ 10 μA/cm^2. Under pH 3 conditions (Figure 9.3(b)), increased cathodic current density over the SS316 (up to 50 μA/cm^2) facilitated the anodic activation of nearly the entire exposed surface of AA7050, with an anodic j_z maximum of ~ 30 μA/cm^2. The j_z distributions measured above the SS316 were up to five times greater than the values observed over SS316 under pH 5.8 conditions.

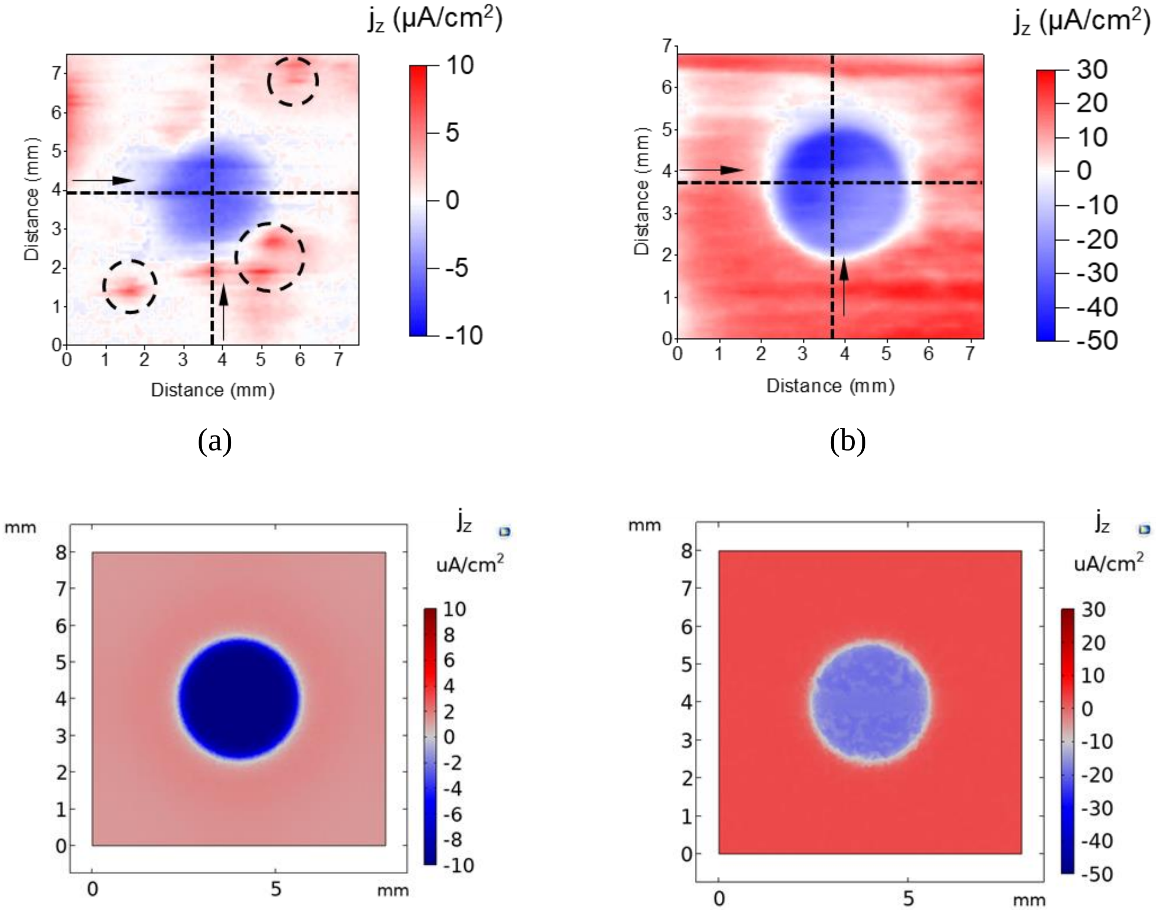

(a) (b)

(c) (d)

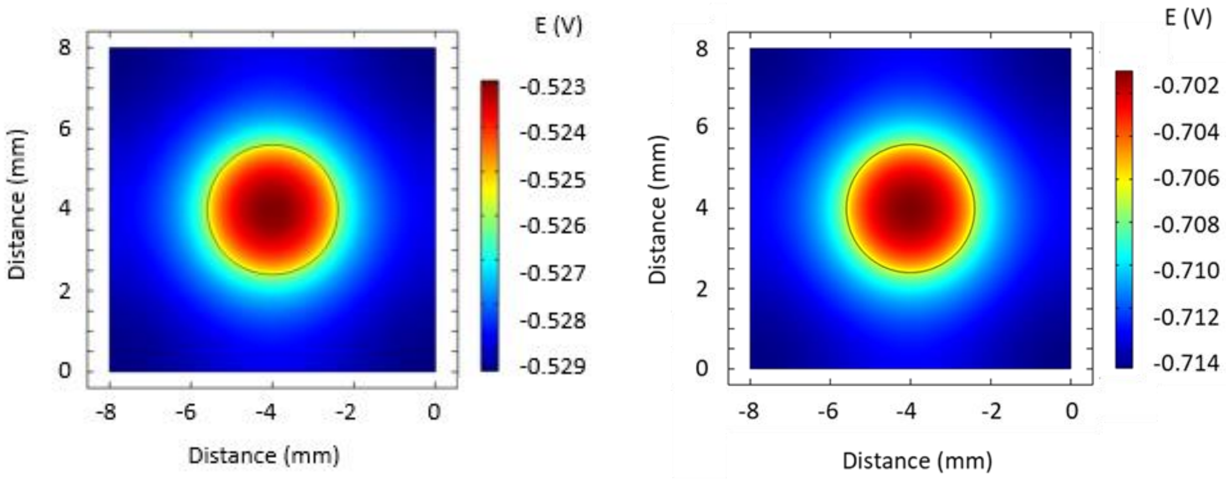

(e) (f)

Figure 9.3: SVET-derived 24 h surface maps (a) and (b), corresponding FEM results (c) and (d) showing current density distributions above a freely-corroding AA7050-SS316 couple immersed in 1 mM NaCl at pH 5.8 and pH 3, respectively. Note that the color bar in each pH scenario is consistent. Current density distributions were taken at a distance of 100 μm above the electrode surface, in each case. Dashed lines in (a) and (b) show the location of vertical and horizontal line profiles taken. Dashed circles in (a) show some regions with localized corrosion activity. Potential distributions (e) and (f) corresponding to FEM current density maps (c) and (d), respectively.

9.4.3. Comparison of the Global Current Density Distributions

Two steady-state finite element models were created, with input from PDS providing the boundary conditions. Each PDS was performed in an identical solution as that used for the SVET measurements. The global current density was calculated for each pH condition and compared with results measured from the SVET (Figures 3c and 3d). At a distance of 100 μm above the surface, the SVET tip measures the electrolyte current density in the normal z-direction by oscillating ± 15 μm to calculate the potential difference. The resulting current density is important to distinguish from that on the electrode surface. Therefore, the z-component of the current density vector 100 µm above the surface was calculated computationally, unless otherwise specified.

To best compare the dynamic experimental data with the steady-state computational results, SVET experiments were conducted for 24 h. Area-averaged integrated current density vs. time plots were used to confirm that the system reached steady-state. Note that the bounds of the color-scale bar from the computational plots are consistent with that of the SVET data and that the pH 3 scenario bounds are not symmetric. Qualitatively, the models at both pH conditions capture the interface between the AA7050 panel and SS316 disk, with the same order of magnitude as was measured via SVET (Figures 3a to 3d). That is, the model also predicted an increase in current density as the solution was changed from pH 5.8 to pH 3.

Figures 3e and 3f show the simulated potential distributions for the pH 5.8 and pH 3 conditions, respectively. For both pH cases, there was a small ohmic drop across the electrodes (6 mV for the pH 5.8 case, and 12 mV for the pH 3 case), and the couple potentials were closer to the non-polarizable AA7050 anode.

9.4.4. Comparison of the Current Density Line Profiles under pH 5.8 Conditions

Line scans taken across the center of the sample, as indicated by the black dashed lines in Figures 3a and 3b, were compared between the SVET data and modeled results to facilitate a more rigorous interrogation of the current density distributions across the galvanic interface. Note that the SVET line scans contain small fluctuations rather than a completely smooth line, indicative of the local reaction transients taking place at the time of the scan or noise due to hydrogen bubbles, as seen in the 2D maps presented in Figures 3a and 3b.

To compare the model with the SVET line scans, three boundary condition scenarios (as displayed in Figure 9.4(a)) were tested in 1 mM NaCl at its natural pH of 5.8:

1. Cathodic SS316 PDS and anodic AA7050 PDS (full PDS)
2. Cathodic SS316 PDS with i_{lim} imposed and anodic AA7050 PDS (PDS + i_{lim})
3. Cathodic SS316 i_{ct} fitting with i_{lim} imposed and anodic AA7050 PDS (i_{ct} + i_{lim})

In all scenarios, the modeled results show the electrolyte current density calculated at a height of 100 µm from the surface for consistency with the SVET-derived data.

For scenario 1 (full PDS), the evaluation largely overestimated both the anodic and cathodic currents when compared to those measured with the SVET (Figure 9.4(b)). Speculating that the overestimation may be due to the current wave between the charge-transfer and diffusion limiting current regime, a new model was created (scenario 2), strictly enforcing that the maximum current density was not greater than the diffusion limiting current density ($i_{lim,\ 5.8}$) reported in Table 9.1 (Figure 9.4(a)). Although neglecting current densities greater than $i_{lim,5.8}$ neglected the HER as well as the cathodic current wave, the couple potential was positive enough such that the HER would not contribute in any way. Utilizing the new cathodic boundary condition (PDS + i_{lim}), the computational line scan of current density decreased to values closer to what was measured with the SVET (Figure 9.4(b)).

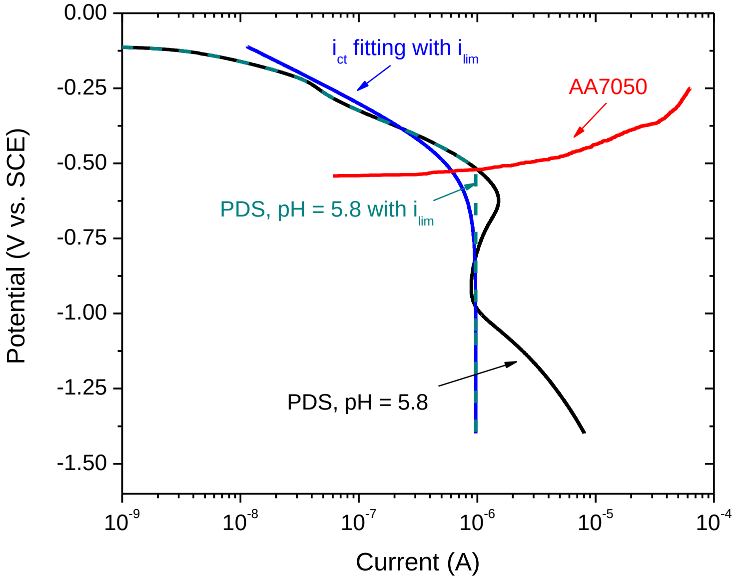

(a)

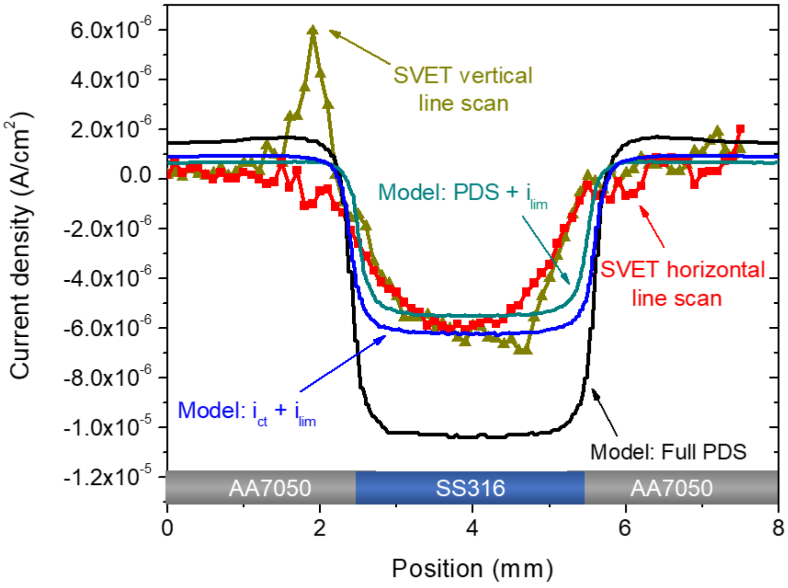

(b)

Figure 9.4. (a) Anodic and cathodic boundary conditions used within the model, scaled to correct for cathode:anode area differences; (b) comparison of the SVET current density line profiles with three computational models for pH 5.8 conditions. The current density line profiles were taken at a distance of 100 µm above the electrode surface, in each case. The notation "full PDS" in (b) indicates the black and red curves in (a) were used as boundary conditions. Correspondingly, "PDS + i_{lim}" in (b) indicates the dashed teal and red curves in (a) were used. Lastly, "i_{ct} + i_{lim}" in (b) indicates the blue and red curves in (a) were used as boundary conditions.

An additional method of selecting model boundary conditions involves the use of charge transfer-controlled kinetic parameters (scenario 3), which were extracted from the measured cathodic PDS (Figure 9.4(a)), and are documented in Table 9.1. These E-log(i) parameters generalize the cathodic behavior in the given environment, increasing the reproducibility of FEM, and were input as new cathodic boundary conditions (i_{ct} + i_{lim}) while the AA7050 anodic boundary condition remained the same. The resulting cathodic current density was increased slightly, while the anodic current remained nearly constant due to the much larger anodic surface area. Both boundary conditions including i_{lim} appeared to accurately capture the peak anodic behavior in the horizontal line scan, as well as the overall cathodic behavior seen in both horizontal and vertical line scans (Figure 9.4(b)).

To determine whether the observed cathodic current wave was a complexation of species, or a transient reaction, a potentiostatic hold was applied to SS316 at a value of -0.62 V vs. SCE for 24 h (Figure 9.5). During the hold, the current density decreased sharply before quickly stabilizing, indicating that a transient reaction may have occurred but would not be sustained nor representative of the long-term cathodic behavior of the SS316. The transient reaction was speculated to be the reduction of the native Fe^{3+} oxide to Fe^{2+}, which is consistent with the system E-pH region on the iron E-pH diagram, calculated using Medusa™ software. It is noted that the native oxide film on the SS316 was not reduced prior to performing the PDS.

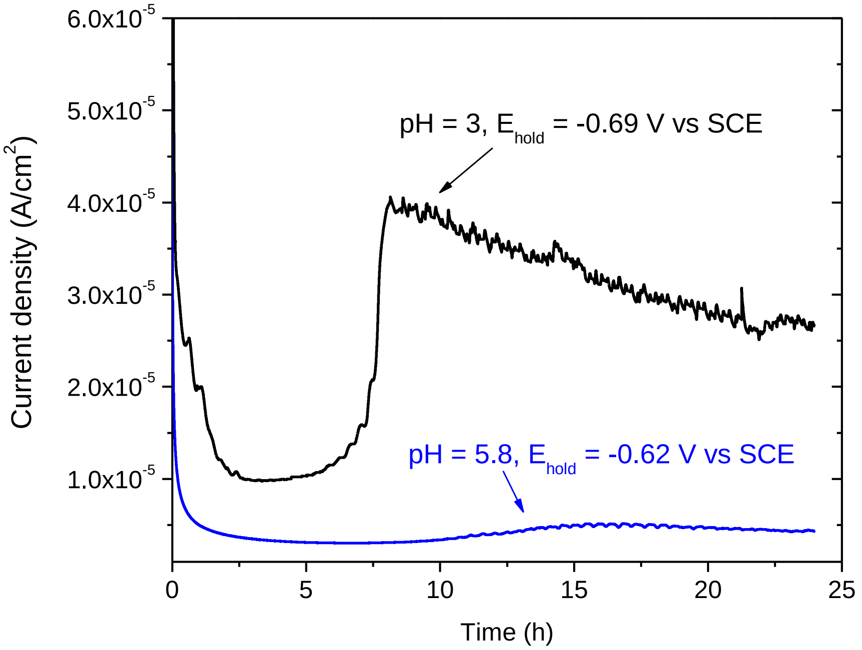

Figure 9.5. 24-h potentiostatic tests on SS316 in 1 mM NaCl at pH 5.8 and pH 3. Potentials were held at the values corresponding to the peak current waves observed on the respective cathodic polarization curves displayed in Figure 9.2(a).

9.4.5. Comparison of the Current Density Line Scans under pH 3 Conditions

A similar approach was employed to model the galvanic coupling between AA7050 and SS316 in the pH 3 solution, with the following boundary conditions tested, as displayed in Figures 6a and 6c:

1. Cathodic SS316 i_{ct} fitting with i_{lim} imposed (1) and anodic AA7050 positive PDS, OCP to high E (2)
2. Cathodic SS316 with 0.003 mM $AlCl_3$ PDS (3) and anodic AA7050 positive PDS, OCP to high E (2)

3. Cathodic SS316 with 0.003 mM AlCl$_3$ PDS (3) and anodic AA7050 negative PDS, high E to OCP (4)

4. Cathodic SS316 with 0.3 mM AlCl$_3$ PDS (5) and anodic AA7050 negative PDS, high E to OCP (4)

Figure 9.6(b) shows current density line profiles calculated by the models and measured by the SVET, both at a distance of 100 μm above the electrode surface. The SVET-derived data were extracted from both the horizontal and vertical centerlines of the sample surface. Additionally, the plot shows an SVET-derived current density line profile where an average value has been applied for the cathodic portion. This corrects the asymmetry observed in the cathodic region and entailed averaging all cathodic current density data points except the first and last three, as they were approximately symmetric. The averaged value was plotted between the original, unaveraged cathodic data points.

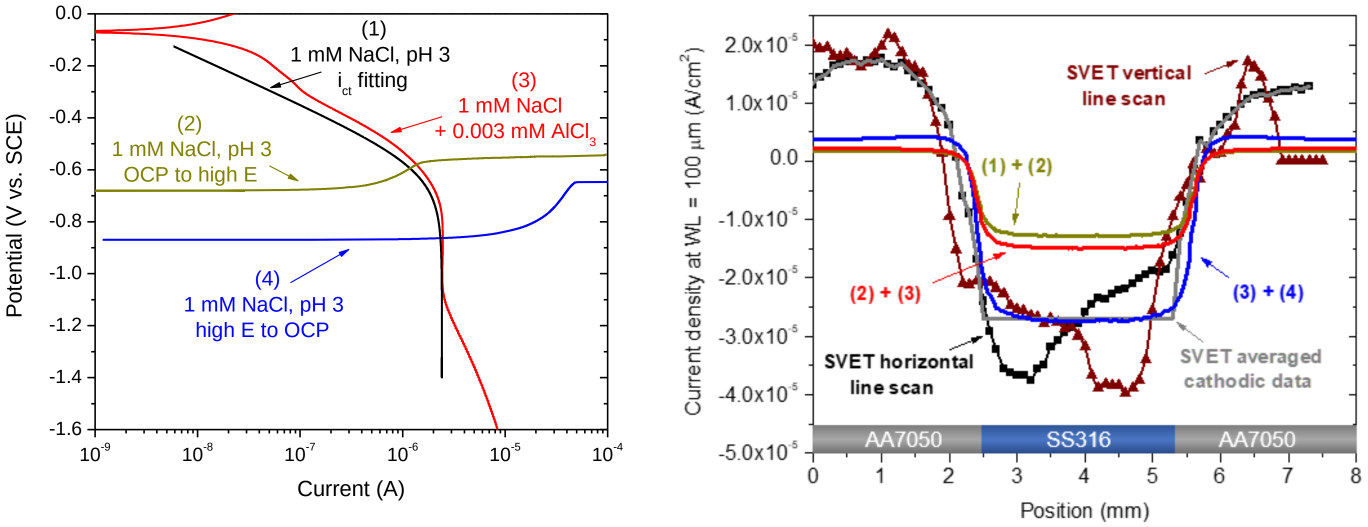

(a) (b)

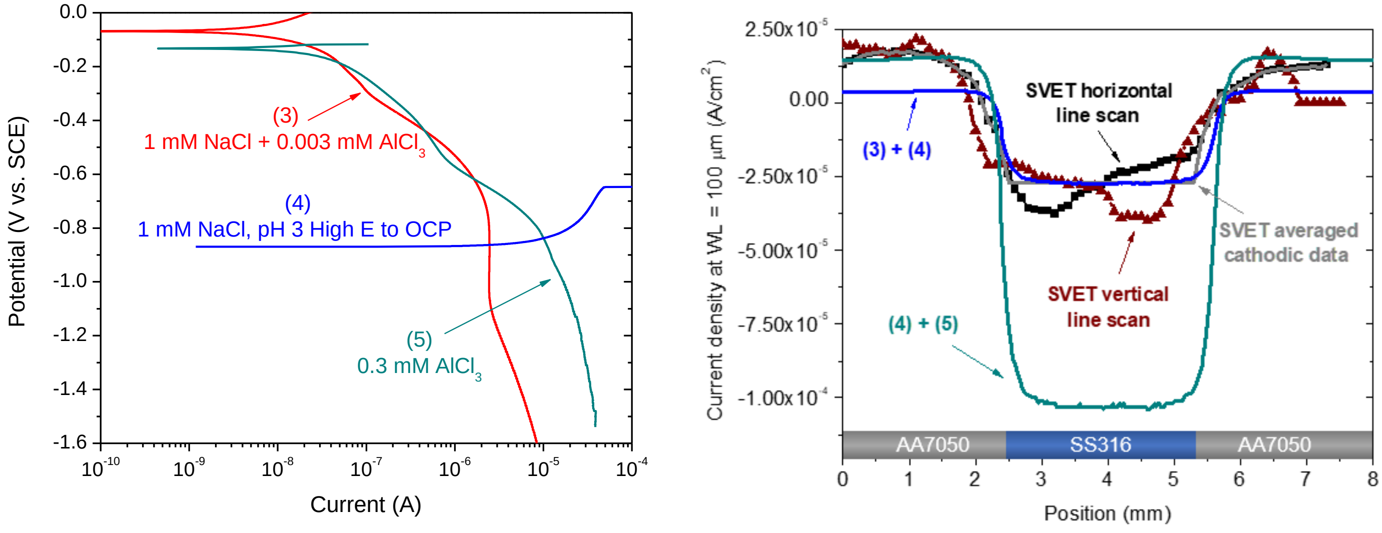

(c) (d)

Figure 9.6: (a) and (c) Anodic and cathodic boundary conditions used within the model, scaled to correct for cathode:anode area differences, and (b) and (d) comparison of the SVET current density line profiles with 4 computational models, for pH 3 conditions. The current density line profiles were taken at a distance of 100 µm above the electrode surface, in each case. Numerical values in (b) and (d) represent the solutions in (a) and (c), with (1) = cathodic analytically-fitted charge transfer-controlled PDS on SS316 in 1 mM NaCl at pH 3, (2) = anodic PDS on AA7050 in 1 mM NaCl at pH 3 scanned in the positive direction from the OCP to high E, (3) = cathodic PDS on SS316 in 1 mM NaCl + 0.003 mM AlCl$_3$, (4) = anodic PDS on AA7050 in 1 mM NaCl at pH 3 scanned in the negative direction from high E to the OCP, (5) = cathodic PDS on SS316 in 0.3 mM AlCl$_3$.

In the first model scenario tested ((1) and (2) in Figure 9.6(a)), the cathodic kinetics on SS316 were implemented using fitted charge transfer-controlled kinetics with a limiting current density ($i_{lim,3}$ = 30 µA/cm^2), as this approach provided better agreement with the SVET-derived data from the experiments performed in the pH 5.8 solution. That is, the coupled SS316 cathode and AA7050 anode within the SVET were assumed to behave exactly as described by the polarization of the individual materials in the same solution and pH but with an imposed limiting current density. The model underestimated both anodic and cathodic current densities (line (1) + (2) in Figure 9.6(b)). The anodic current densities were underestimated by almost one order of magnitude, whereas the cathodic current densities were ca. 30% lower than the averaged cathodic current density. The strikingly different results obtained from the calculations indicated that the boundary conditions implemented at the SS316 and AA7050 surfaces did not represent the kinetics of the coupled alloys after 24 h of exposure in the pH 3 solution. It was rationalized that the electrolyte chemistry after 24 h of exposure evolved due to the higher currents observed in the acidic solution; thus, the behavior of the alloys in the solution in which the SVET sample was initially exposed would not represent the kinetics after the 24 h exposure.

In an attempt to simulate a more representative electrolyte chemistry of the galvanic couple, new cathodic boundary conditions (scenario 2) were generated with a low concentration of Al^{3+} ((3) in Figure 9.6(a)). This modification was incorporated because the presence of Al^{3+} in the electrolyte (stemming from the oxidation of the AA7050 anode) could influence the electrochemical behavior of the SS316 cathode. However, the kinetics of the AA7050 anode were still assumed to behave as the conventional positive polarization of OCP to high E would predict (i.e., with a passive film present). Line (2) + (3) in Figure 9.6(b) shows the current density profile obtained when using this boundary condition, in comparison with the SVET-derived data. Utilizing faster cathodic kinetics in this modified model slightly increased the cathodic current densities; however, it still largely underestimated both the SVET-derived anodic and cathodic current densities.

Scenario 3 simulated a condition in which AA7050 was actively corroding, i.e., little to no passive film present. New anodic polarization scans were performed by starting the scan at a high E and sweeping down to the OCP, as described previously ((4) in Figure 9.6(a)). The results are shown in Figure 9.6(b) (line (3) + (4)). The cathodic current densities calculated from the model correlated well to the averaged SVET-derived cathodic current densities. However, the anodic current densities were still underestimated. The total current density increased by a factor of 1.55, which is consistent with Mixed Potential Theory predictions (Figure 9.6(a)). Due to the smaller area, the current density on the SS316 is higher, so the 55% increase in the cathodic current density results in a higher increase than the anodic current density increase.

One last scenario was tested (scenario 4), in which the anodic kinetics were kept the same as the previous model in scenario 3 (i.e., where negative PDS were conducted from high E to the OCP), but the Al^{3+} concentration was increased on the cathodic boundaries from 0.003 mM $AlCl_3$ to 0.3 mM $AlCl_3$ ((5) in Figure 9.6(c)), to account for the increased dissolution of the AA7050 anode.

Evaluating the PDS data with both Al^{3+} concentrations, the higher Al^{3+} concentration resulted in faster cathodic kinetics (Figure 9.6(c)). This observation also translated to the model. Figure 9.6(d) shows line scans from the models using the two Al^{3+} concentrations as cathodic boundary conditions, in comparison to the SVET-derived data. The high Al^{3+} concentration resulted in anodic current densities that were in agreement with those measured with the SVET. However, the cathodic current densities were largely overestimated by approximately one order of magnitude.

9.4.6. Total Current Comparisons in pH 5.8 and pH 3 Environments

Although it was not possible to simulate the pitting events that occurred under pH 5.8 conditions with the modeling approach used in this work (Figure 9.4(b)), good comparisons were achieved when total currents were considered. Figure 9.7(a) compares the SVET-derived total currents with FEM results for pH 5.8 conditions assuming the horizontal line scan (with no apparent pitting events) was representative of the current distributions over the entire sample. The $i_{ct} + i_{lim}$ fitted kinetics slightly overestimated the total anodic and cathodic currents by 0.13 µA.

However, the same boundary conditions largely underpredicted the experimental data when the total currents derived from the global sample were analyzed (Figure 9.7(c)).

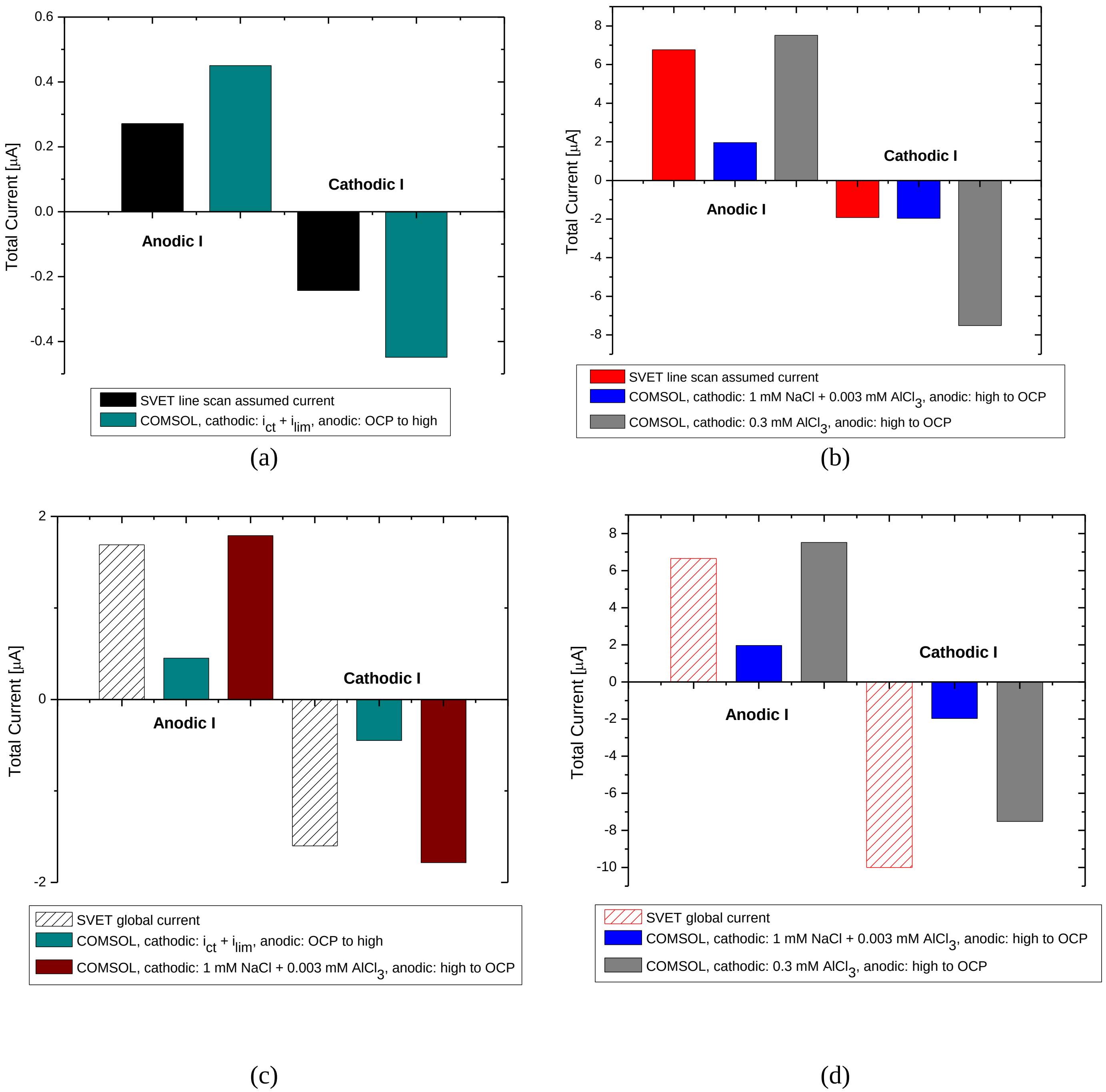

Figure 9.7: Computational and SVET-derived total currents assumed only from the line profiles under (a) pH 5.8 and (b) pH 3 conditions; area-averaged integrated total currents calculated over the entire AA7050-SS316 couple surface under (c) pH 5.8 and (d) pH 3 conditions. Both the computational and SVET-derived total currents in each pH case, were calculated from the current density distributions taken at a distance of 100 µm above the electrode surface.

To better represent the high currents from the localized corrosion, the boundary conditions simulating an actively pitting surface over the entire AA7050 surface (i.e., negative anodic PDS from high E to OCP) with release and transport of a low concentration of Al^{3+} to the bulk solution, including over the SS316 (cathodic scan with the addition of 0.003 mM Al^{3+}) were utilized. A better agreement was attained for total currents, with 3% error between the computational and total anodic currents and 8.5% error between the computational and total cathodic currents (Figure 9.7(c)). Note that the percent difference between the global anodic and cathodic currents from the SVET was 5.5%.

For the pH 3 environment line profiles, the experimental anodic and cathodic current densities could only be replicated with separate models taking into account the two concentrations of Al^{3+} as cathodic boundary conditions (Figure 9.6(d)). When the total current was calculated, assuming that the line scan was representative of the entire system, a similar trend was observed (Figure 9.7(b)). When the low Al^{3+} concentration boundary conditions were used, the *cathodic* currents from the computational results had 7% error relative to the SVET measurements, while the *anodic* current was underestimated by 71%. However, when the higher Al^{3+} concentration boundary conditions were used, the computational *anodic* current had only 11% error when compared with the SVET-derived data, while the computational *cathodic* currents largely overestimated the experimental work by 291% (Figure 9.7(b)).

However, looking instead at the globally calculated SVET currents, there was a reasonable agreement with the high Al^{3+} concentration model (Figure 9.7(d)). That is, the model simulated with the boundary conditions of scenario 4 presented a better agreement with the global SVET currents. The computational anodic currents had 13% error in comparison to the SVET global anodic currents, whereas the computational cathodic currents had 26% error.

9.5 Discussion

9.5.1. Macro Galvanically-Driven Corrosion of AA7050 is Exacerbated in Acidic Conditions

The significant increase in SVET-derived j_z distributions over the surface of the AA7050-SS316 couple when fully immersed in pH 3 solution compared to those observed at pH 5.8 conditions was expected due to the detrimental effect of acidic pH on galvanic corrosion of Al alloys. On the uncoupled AA7050, pH 3 is shown to increase anodic kinetics relative to the case at pH 5.8 (Figure 9.2(b)). This adverse effect of low pH is attributed to the uniform dissolution of the native oxide film in acidic conditions compared to the more localized attack of the protective oxide film in (near) neutral conditions.41–435 Coupling with SS316 exacerbates the attack on AA7050 because of the increased cathodic current available to sustain higher rates of Al dissolution (Figure 9.2(a)). The released Al^{3+} could transport from local anodic sites into the bulk solution, including over the SS316, leading to further increases in cathodic currents (Figure 9.2(a)). This phenomenon of Al^{3+} increasing cathodic kinetics on SS316 has been reported previously, and was determined to mainly impact the HER diffusion kinetics.[41,46] In the present work, this impact on the HER kinetics was evident on the cathodic scan carried out in 0.3 mM $AlCl_3$ (Figure 9.2(a)).

9.5.2. Choice of Computational Boundary Conditions to Best Represent Different Environments

Choosing boundary conditions within the model may seem as straightforward as conducting PDS in a replicate solution of the system of interest. However, this work has shown that there are two potential pitfalls that must be appreciated, 1) the time dependence of the PDS and 2) the effects of localized corrosion.

The PDS time-dependence was apparent during the cathodic scans. Although the model assumed steady-state, the PDS samples were exposed to the solution for 30 min at OCP with an additional 30 min of exposure during the scan, resulting in only 1 h of total exposure time. Therefore, the transient current wave was still observed (Figure 9.2(a)). The decay in current density during the potentiostatic hold (Figure 9.5) confirms that the cathodic current wave was a transient reaction that would not be present during longer times of exposure, such as with the 24 h SVET scan. Neglecting the cathodic current transient (i.e., using PDS + i_{lim}, and i_{ct} + i_{lim} boundary conditions) led to a better comparison between the model and SVET line scans in the pH 5.8 environment (Figure 9.4(b)). Transient reactions may be present during a fast-scan polarization experiment; however, if the goal is to represent a steady-state system such as the SVET after 24 h, then careful evaluation of the PDS must be conducted to determine that no transient reactions are present.

In aggressive environments, such as acidic conditions, it is necessary to ensure that the computational boundary conditions for a steady-state model represent an actively corroding system. In the current system, this was accomplished by modifying both the anodic and cathodic boundary conditions.

As stated previously, an acidic environment breaks down the native passive film of Al alloys. However, the anodic PDS in pH 3 solution that was scanned conventionally from OCP to high E was not able to capture the kinetics of the active system measured with the SVET (Figure 9.6(b)). The reason could either be due to the short exposure time of the PDS when immersed in the acidic condition, thereby not allowing enough time for the passive film to dissolve, or due to the lack of extra polarization provided by the SS316 in the SVET galvanic couple. The latter is justified by the fact that the anodic polarization of AA7050, provided by galvanically coupling with the SS316, is greater in acidic conditions than in near-neutral conditions, as evident by the potential difference between the alloys (i.e., the driving force for galvanic coupling) in Figures 3e and 3f. Performing the anodic polarization scan starting at a high E to OCP artificially ensured that the entire surface was active and uninhibited corrosion could occur (Figure 9.2(b)).

Concerning the cathodic kinetics, it is expected that there would be an increase in the concentration of Al^{3+} due to the relatively high anodic kinetics and the stability of the Al^{3+} species at pH 3.[47] Because it has been observed that Al^{3+} increases the cathodic kinetics on SS316,[41,46] two new cathodic PDS were conducted on SS316 (Figure 9.6(c)). The low Al^{3+} concentration, containing 1 mM NaCl + 0.003 mM $AlCl_3$, was estimated by calculating the total anodic charge from the SVET-derived current density measurements after 24 h, and then using Faraday's law to calculate the total amount of Al^{3+} produced, assuming that the dissolution of the other alloying elements present in AA7050 (e.g., Zn, Mg) to be negligible. The higher concentration of Al^{3+}, 0.3 mM attained with only $AlCl_3$, was determined to be the maximum amount of Al^{3+} possible while keeping the chloride concentration consistent with the other scenarios.

In order to verify if the Al^{3+} concentrations chosen to perform the new boundary conditions were appropriate and to calculate the Al^{3+} concentration at the surface of SS316 and AA7050, the production and transport of Al^{3+} were calculated in the model that simulated the galvanic coupling in the pH 3 solution, using the activated AA7050 PDS. Figure 9.8 shows the simulated Al^{3+} concentration as a function of position and time. At the SS316 surface, the concentration ranged from 0.28 mM to 0.34 mM after 24 h. The method of calculating the Al^{3+} concentration by utilizing the total charge and dividing by the volume of the solution thereby underestimated the Al^{3+} concentration at the surface of SS316. It is noted that the model calculations were performed ignoring the convection caused by the vibration of the SVET probe. The forced convection decreases concentration gradients and homogenizes the solution. Thus, the concentration of the species at the electrode surface is also expected to change.

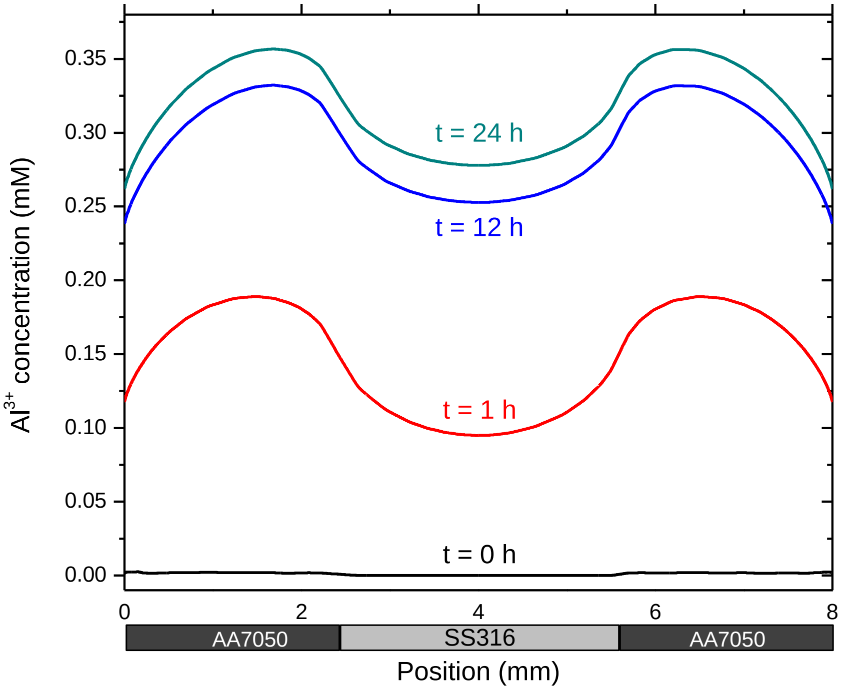

Figure 9.8: Simulated spatial distribution of the Al^{3+} concentration at different times at the centerline of the geometry.

It is also worth noting that the assumption that Na^+, Cl^-, and H^+ are the only species carrying current might not be valid after 24 h as the concentration of Al^{3+} increases to values of the same order of magnitude as Na^+, Cl^-, and H^+. Thus, under this condition, the Nernst-Planck equation approach must be invoked. To maintain electroneutrality, it is likely that an increase in the local Cl^- and OH^- concentration would occur to compensate for the additional positive charge originating from the Al^{3+} production. Additionally, if the supporting electrolyte assumption is no longer valid, then local changes in the conductivity of the solution should be taken into consideration.

9.5.3. Discrepancies Between Model Predictions and SVET Measurements

Both vertical and horizontal SVET-derived line profiles were compared with the model in order to capture a good representation of the localized processes occurring on the AA7050 surface. The simulated galvanic coupling under pH 3 conditions presented higher discrepancies compared to those simulated for pH 5.8 conditions, when using the $i_{ct} + i_{lim}$ boundary conditions (Figures 4b and 6b). Interestingly, the reverse situation was expected because the computational model, with the present homogenous assumptions, should better represent the case of pH 3 in which the oxide film was dissolved globally and more uniform corrosion was occurring, as opposed to the localized corrosion occurring in the pH 5.8 case. Furthermore, the SS316 cathodic current measured potentiostatically at pH 3 varied throughout the 24-h test, indicating that steady-state was not achieved (Figure 9.5), in contrast to the present assumption of a steady-state model. Considering the stability of the current measured by the potentiostatic hold at pH 5.8 and the relatively good comparison with computational results, it is conceivable that the system at pH 3 may not have reached steady-state within 24 h.

When quantifying the difference between the SVET and FEM calculated total currents, the percent error between the anodic and cathodic values was often asymmetric, which can be attributed to an asymmetry in the experimental anodic and cathodic currents. Within the model, the anodic and cathodic currents must be equal to preserve the conservation of charge. However, as visible in Figure 9.7(b), the total anodic and cathodic currents obtained experimentally at pH 3 were not equal, with 111% difference (i.e., 4.8 µA). This situation would therefore be impossible for a singular model to capture, because the computational currents *have to be equal*.

Speculations as to possible causes of the lack of electroneutrality in the experimental measurements are discussed in a later section.

Comparing the globally calculated total current over the entire sample, the experimental difference between anodic and cathodic currents was much lower (41%, 3.5 µA). Using boundary conditions with the high Al^{3+} concentration resulted in the best comparison with the experimental values (Figure 9.7(d)). Notably, the high concentration of Al^{3+} was also predicted to occur based on local flux predictions of the model (Figure 9.8).

It is suggested that another source of the discrepancies observed between the model predictions and the SVET measurements is the inhomogeneities of the anodic and cathodic kinetics of AA7050 and SS316 due to surface heterogeneity and/or changes in local chemistry. Indeed, the analysis of the current density maps in Figures 3a and 3b shows that the distributions are non-uniform. Localized "hot spots" of current density can be seen from the SVET in pH 5.8, where pits grew while the remaining AA7050 surface was either passive or catalytic to cathodic reactions (Figure 9.3(a)). In the pH 3 case, there were regions with significantly decreased anodic activities over the top half of the sample surface (Figure 9.3(b)). These regions with lower current densities might correspond to locations with precipitated corrosion products. Such regions could include locations immediately adjacent to cathodic areas, where the local pH could be considerably higher. As a result, the bulk of the cathodic current that the SS316 supplies may support rapid dissolution of the remaining active areas on the AA7050.

Such localized distributions are not captured in the model, as the polarization scans performed on AA7050 represent averaged kinetics of the intermetallic particles and the matrix weight by their activity and area fractions. Thus, within the model, AA7050 was assumed to be homogeneous with the entire panel actively corroding. On a macroscale, this assumption is generally valid as the local cathodic and anodic regions average out, as noted when comparing the global total currents (Figure 9.7(c) and (d)). One method of manually accounting for the local variations was conducted in the pH 3 horizontal line scan, where the cathodic currents were averaged to provide a better comparison with the homogenous model (Figure 9.6(b)). The peak cathodic current between the modeled scenario 3 and the averaged cathodic kinetics had 1% difference between them (Figure 9.6(b)).

The observations discussed above highlight the experimental complexities of non-steady-state, lack of charge conservation, and inhomogeneities in electrode surface conditions/chemistry. These complexities may shed light on the inability of the model to correctly estimate both the cathodic and anodic current densities with the same boundary conditions. This observation may be important, especially in systems in which the increased electrochemical activity leads to significant changes in the local electrolyte chemistry, which in turn can locally affect the electrochemical behavior of the electrode. That is, one portion of the sample in the pH 3 environment may be undergoing different rates than an adjacent portion, due to local changes in the electrolyte or at the electrode surface, making it difficult to predict computationally. For such cases, transient models that take into account the evolving electrolyte chemistry and its effect on the electrochemical behavior of the alloys can improve the predictability of the computational approach.[37]

9.5.4. Advantages of Combining the SVET and Computational Techniques

The advantages of combining SVET with FEM approaches have been discussed in the literature, and both techniques have been combined to investigate the galvanic coupling behavior between dissimilar alloys.[16,25,27,28,30–33,48] As stated previously, the SVET tip herein measured the potential difference at 85 μm and 115 μm over the entire surface. This potential difference allows for the calculation of the ionic current density (Eq. 9.1), which is assumed to be at an average distance of 100 µm from the sample surface. One important aspect of modeling is the ability to calculate the current density at the electrode/electrolyte interface and also at any point within the electrolyte. Thus, once validated, the models can be used to predict the current density at the electrode/electrolyte interface and better interpret the results obtained with SVET.

Recently, Saeedikhani et al.[25] compared SVET and modeling results performed on a scratched zinc-based coating applied to a steel substrate. Although a good agreement of electrolyte current density above the surface was observed between SVET and FEM, the current density at the electrode/electrolyte was underpredicted, especially within the scribed region. One of the major sources of the discrepancy was due to the geometry of the specimen, as the distance between the SVET probe and the electrode surface almost doubled (from 150 to 270 µm) as it moved from the Zn-coated steel surface to the scribed bare steel. In this work, however, a planar geometry was used to measure the galvanic current densities between AA7050 and SS316. Thus, the SVET probe height from the electrode surface was constant across the sample. Any local variation between the electrolyte current density and the interface current density could then be isolated and attributed to a non-geometric effect.

Figure 9.9(a) shows the calculated electrolyte current densities in the pH 5.8 environment at four heights: z = 0 (at the electrode/electrolyte interface), z = 85 µm, z = 100 µm, z = 115 µm. At the center of the SS316 electrode (x = 4 mm), a difference in current density of ca. 10% was observed between z = 0 and z = 100 µm. The difference in current density from 85 µm to 115 µm above the surface, which were the minimum and maximum distance of the SVET tip, respectively, was calculated. The value was negligible at 0.22 µA/cm^2, in the context of currents discussed in this work, with the peak cathodic current in pH 5.8 being 6 µA/cm^2 (Figure 9.4(b)).

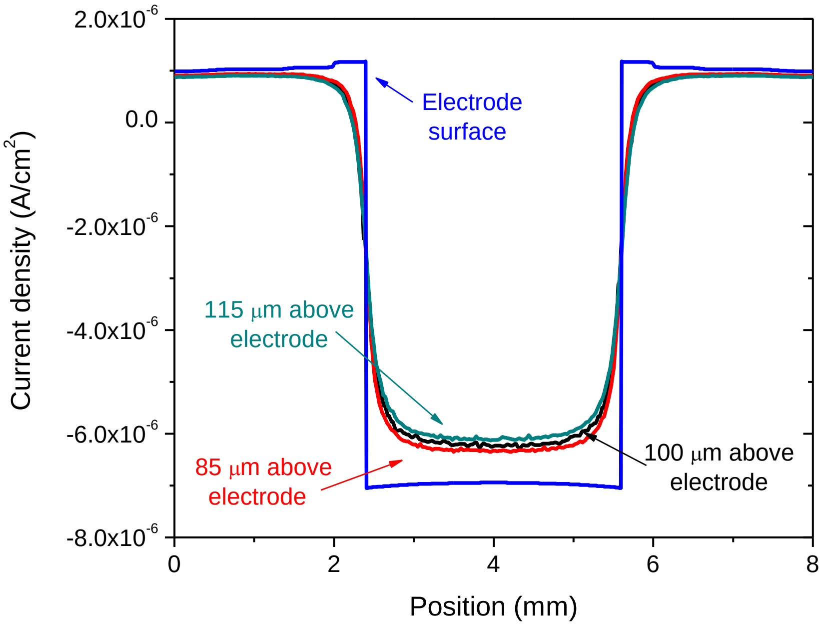

(a)

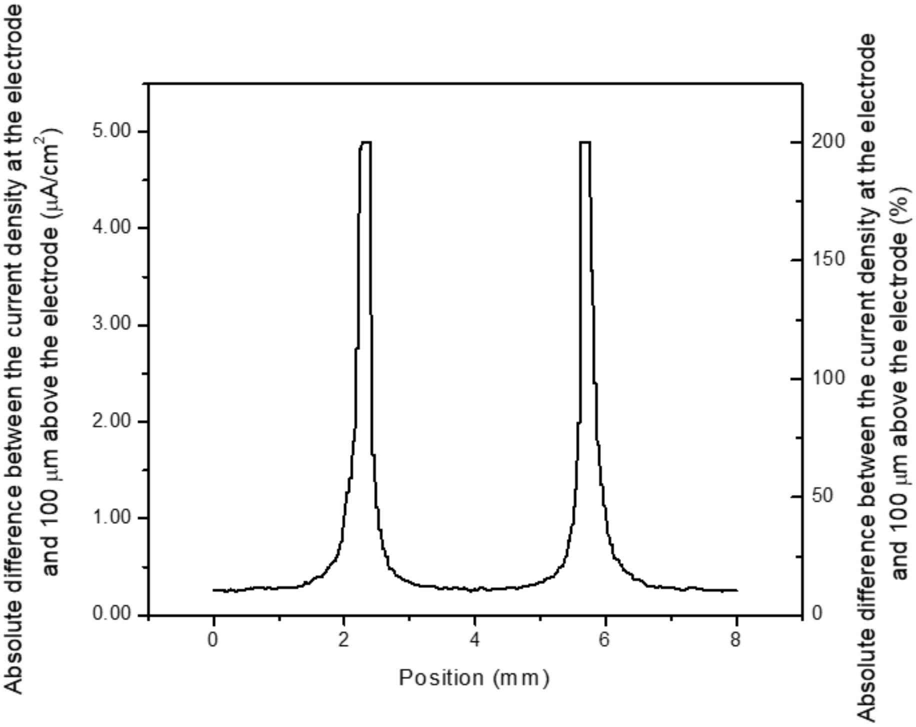

(b)

Figure 9.9: (a) Computationally-derived current densities along horizontal line scan at various distances from the electrode surface; (b) absolute and percent difference between current

density at the electrode surface vs. at 100 µm above the electrode surface, as a function of the x-axis position.

Figure 9.9(b) shows the absolute and percent difference between the current density at the electrode surface and the electrolyte current density calculated at a distance of 100 µm above the surface as a function of position. Near the interface between AA7050 and SS316, there is a significant increase (200%) in the difference between the currents. Conversely, far from the coupled interface, the current densities difference is ca. 10%. The variation in the percent difference can be understood by Figure 9.9(a), in which the current density at the electrode surface follows a step function, with the current densities immediately changing from anodic to cathodic. In contrast, the current density at 100 µm above the surface is a continuous function.

Looking instead at the distance from the electrode surface in the z-direction, the current density magnitude was seen to decrease linearly with a slope of -70 A/m^3 (Figure 9.10(a)). At the position of x = 1 mm above the AA7050 surface, the slope was decreased to -10 A/m^3. The comparison of the two slopes above indicates that lower current densities, as observed above the anodic region, decrease the degree of variation of current density with position from the electrode surface, due to ohmic drop. Indeed, the ratio between the slopes is the same as the ratio between the current densities at the surface of the electrode. Practically, this result indicates that in systems with low overall current densities, the height of the SVET probe tip will not largely impact the results. However, in systems or locations with high current densities, the chosen height of the SVET probe tip can have a substantial effect on the measured results in comparison to the current densities occurring at the electrode surface.

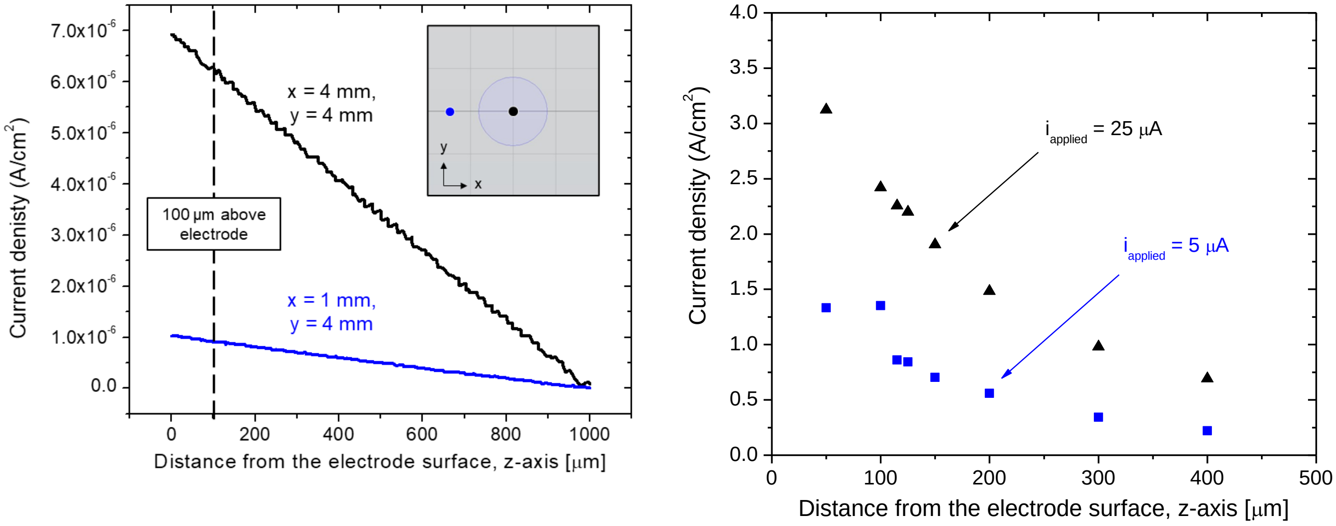

(a) (b)

Figure 9.10: (a) Computationally-derived linear relationship of current density with distance from the electrode surface to the top of the electrolyte, along the z-axis; (b) SVET-derived point source data, with measured current density as a function of SVET probe height, with two applied current values. Inset in (a) represents the x-y view of sample surface, and the points chosen to measure current density along the z-axis.

This result is further demonstrated by the experimental data presented in Figure 9.10(b), where the peak current was measured above a point current source with two applied current values over a range of SVET probe heights. The higher applied current ($i_{applied}$ = 25 µA) resulted in a faster decrease in SVET-derived current density as a function of probe height, i.e., a steeper slope, in comparison to the lower applied current ($i_{applied}$ = 5 µA). These results validate what was observed computationally in Figure 9.10(a). Furthermore, Murer et al.[27] and Demeter et al.[49] also observed this inverse correlation between current density magnitude and probe height, both experimentally and computationally. Therefore, it is recommended that the SVET be conducted at several probe heights, although it does not completelyalleviate issues seen at the galvanic couple interface.

Visualization of the current density vectors in a planar view can improve the understanding of the variations observed between the current density at the electrode surface and at a specified distance within the electrolyte above the anode/cathode interface. Figure 9.11(a) shows the electrolyte current density lines and the magnitude of the electrolyte current density in the z-direction, represented by a color gradient from a “slice” of the geometry in the x-z plane at the center of the geometry, and Figure 9.11(b) shows the ratio between the z-component of the electrolyte current density and the magnitude of the electrolyte current density vector.

Note that the simulation used to determine the current density vectors in Figure 9.11 was conducted in a geometry whose volume was equivalent to the volume of electrolyte used for the SVET experiments. Conventionally, computational works have kept the electrolyte *height* consistent with experimental conditions, but have not considered the effects of keeping the electrolyte *volume* the same.[25,27,32,40] This assumption does not affect the interface current densities, and it is computationally less expensive to mesh a smaller volumed domain. However, when considering current density in the electrolyte (i.e., above the electrode surface) or the concentration of ions, the volume of the electrolyte becomes more important. This distinguishing feature of the large-volume model can be seen by the current density vectors in Figure 9.11(a), in that they continue past the edges of the galvanic couple.

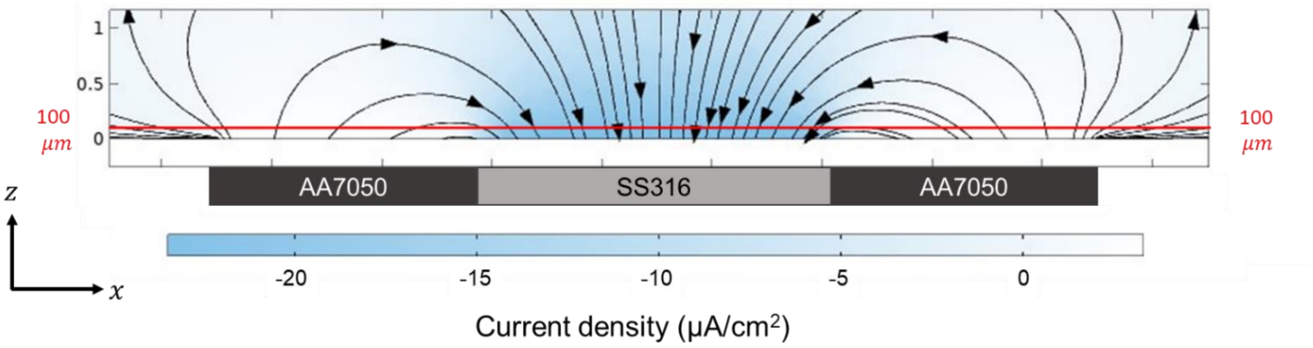

(a)

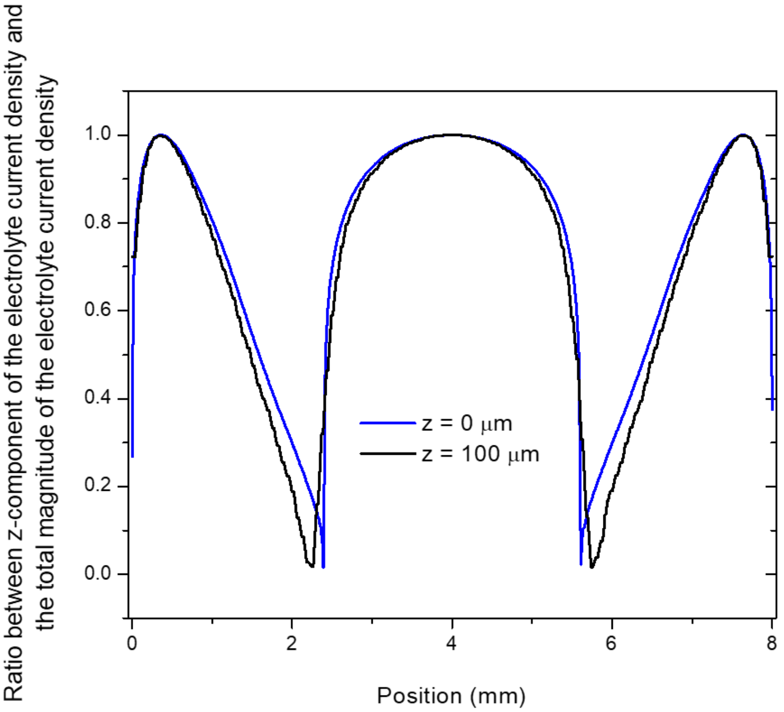

(b)

Figure 9.11. (a) Electrolyte current density lines and the magnitude of the electrolyte current density in the z-direction represented by a color gradient at the x-z plane at the center of the geometry. The red line indicates the distance between the SVET probe and the electrode used in this work; (b) ratio between the z-component of the current density and the magnitude of the current density vector at different electrolyte heights (0 and 100 µm).

As the SVET probe measures the potential difference between two points by oscillating in the z-direction, it is only able to "sense" the z-component of the electrolyte current density. As Figure 9.11(a) indicates, at regions further away from the boundary between the two electrodes (SS316 and AA7050) and from the edges of the AA7050 electrode, most of the magnitude of the current density vectors are composed by the z-component. However, near the boundary between the two electrodes and near the edges of the sample, the magnitude of the z-component of the electrolyte current density vector decreases significantly. As the probe moves closer to the surface, the z-component of the current density vector increases, consistent with the negative slope observation in Figure 9.10. Interestingly, as Figure 9.11(b) shows, the z-component of the current density is small near the edge of the galvanic couple and at the edge of the sample, even at z = 0 μm, indicating an intrinsic limitation of the SVET technique in capturing the current densities at such locations by measuring the potential difference only in the z-direction.

Two important conclusions can be drawn from this analysis. First, increasing the spatial resolution of the SVET by decreasing the step-size in the x- and y-directions would not improve the underestimation of the current density at the electrode surface, as the current density measurement losses are purely based on the limitation of the distance between the probe and the electrode surface and the assumption that all current is in the z-direction. Second, even at locations very close to the surface, part of the current density would not be sensed, because of the direction of the current density vector near the galvanic couple and near the edges of the sample.

9.6 Limitations

9.6.1. Experimental Limitations

As mentioned previously, the choice of 1 mM NaCl used in this work was made based on the resolution limitations of the SVET. In real atmospheric environments, the NaCl concentration would be expected to equilibrate at ~ 600 mM at 98% relative humidity.[11] However, because the SVET signal-to-noise ratios decrease with increasing solution conductivity,[21] experiments conducted in 600 mM NaCl would be too noisy to allow extraction of any meaningful information. Therefore, with reasonable model validation with the SVET at low Cl^- concentrations, predictions could be made with the model for higher Cl^- concentrations scenarios.

Another limitation with the SVET is the frequent mismatch of the area-averaged integrated total anodic and cathodic currents, especially in non-steady state systems, which drift and exhibit transient reactions.[23,50,51] At any instant in time, the total anodic and cathodic currents in reality are equal in magnitude, so that the net current equals zero. A general rule of thumb for the SVET to be able to avoid this situation is that the measurement time be much less than the periodicity of transients or the time frame of drifts. The error depends on the magnitude and area of the current transient relative to the steady-state current and area. Regarding another issue, for the couple geometry utilized in this work, there was a slight overestimation of the total cathodic current, particularly for the pH 3 case, most likely due to edge effects. That is, the SVET misses the anodic activity in the vicinity of the edges of the AA7050 surface but captures the cathodic activity occurring over the entire SS316 surface located at the center of the structure.

9.6.2. Computational Limitations

One shortcoming of the model is readily apparent through its prediction of homogenous current density distributions in Figures 3c and 3d, as opposed to the non-uniform distribution (with distance and time), which occurs experimentally (Figure 9.3(a) and (b)). Additionally, because of the macroscale geometry in this work, the model cannot account for localized corrosion. Localized corrosion is an important form of corrosion that occurs on AA, especially when galvanically coupled with more noble alloys, such as SS, that can polarize the AA to potentials above critical potential thresholds for localized corrosion (e.g., pitting and repassivation potentials). It is acknowledged that in real service conditions, such localized hotspots as observed on the SVET-derived surface map for the pH 5.8 case may be important, as they could act as susceptible sites for fatigue crack nucleation.[52] Furthermore, the model is not able to capture the precipitation of any corrosion products, which may stifle the local anodic and cathodic reactions in some areas and cause a shift of those currents elsewhere. Notice that the white "halo" in the global current distributions is larger in the experimental maps than the computational model would predict (Figures 3b and 3d). As the locations closest to the anode/cathode interface should have the highest currents, it follows that the precipitation of corrosion products would also be greatest in this area, leading to a corresponding decrease in current at longer times. As the present model cannot yet account for the corrosion product formation, the white "halo" is underpredicted. Recent work in the literature have utilized FEM to investigate the effects of corrosion products on micro- and macro-galvanic corrosion.[37,53–55] Understanding the complex precipitation reactions and how they may contribute in stifling localized corrosion, is an area of future work. In addition, sites with copper replating could switch their behavior from anodic to cathodic, which was not accounted for in the present model.

9.7 Conclusion

The scanning vibrating electrode technique (SVET) was utilized to experimentally validate the applicability of finite element modeling (FEM) in simulating macro-galvanic-induced corrosion of AA7050 coupled to SS316. The SVET and FEM both provided local current density distributions, which were then compared. The discrepancy between the two techniques was traced to several sources. However, once the correct boundary conditions were used to validate the model, both techniques were able to enhance each other, thereby providing valuable information otherwise unachievable. In summary, the following findings are highlighted:

- Methods are proposed to generate anodic and cathodic boundary conditions to represent a macro-scaled galvanic couple between AA7050 and SS316, with localized corrosion present. One method of including the accelerated kinetics present during localized corrosion while still assuming a homogenous surface condition was based on performing the anodic scans starting at a high potential and decreasing it to OCP, in order to capture the behavior of a surface without the natural oxide present. Furthermore, the addition of Al^{3+} in the cathodic polarization scans led to better agreement between the total currents calculated with the model and measured with SVET.
- Although the computational model was not able to capture the localized corrosion events (as seen especially in the less aggressive pH 5.8 scenario), the *total anodic currents* in the overall macro-scale geometry, through using boundary conditions generated with the methods above, were found to have less than 13% error when compared with the global SVET currents, in both pH environments.

- The AA7050-SS316 galvanic couple in near-neutral solutions reached steady-state within 24 h, making computational validation through SVET less complicated. Better agreements regarding macro-galvanic couple behavior were achieved in pH 5.8 environment compared to pH 3 environment. However, the FEM method was not able to address corrosion at specific locations on the AA7050 in the pH 5.8 scenario where corrosion was localized.

- Electrolyte current densities measured by vibrating probe methods at a distance of 100 µm from the electrode surface can be significantly different from the actual current density at the electrode surface, and the difference depends on the position above the galvanic coupled surface. It was predicted that there was a 10% difference at locations far away from the galvanic couple interface. At the vicinity between the two electrodes, the difference was as high as 200%, corresponding to ca. 5 µA/cm^2.

- The linear dependence of current density on the SVET probe height from the electrode surface was found to scale directly with the current density magnitude. This result indicated that the underestimation of the SVET-derived data from the current density at the electrode surface is dependent on both the z-position and the spatial location on the galvanic couple and current density magnitude. That is, in systems or positions with high current densities or galvanic coupling currents, choosing the SVET probe tip height from the electrode surface can have a more significant impact on the results as opposed to lower current density systems, due to ohmic drop and the inability of the probe oscillation to capture components of the current that are parallel to the surface.

9.8 Acknowledgements

This work was supported by the Office of Naval Research (ONR) Grant N00014-14-1-0012 (W. Nickerson/A. Rahman), and via contract N00173-19-1-G011 (C. Sanders), as well as by the Department of Defense (DoD) Corrosion Program Office through the USA Air Force Academy via contract FA7000-18-2-0006. In addition, support was also provided by the NASA Virginia Space Grant Consortium through a Graduate Research Fellowship.

9.9 References

1. Davis, J.R., *Corrosion of Aluminum and Aluminum Alloys* (1999).
2. Olson, D., T. Siewert, S. Liu, and G. Edwards, *ASM Handbook Vol 6: Welding, Brazing, and Soldering*, ASM International (New York: ASM International, 1993).
3. Charles-Granville, U.-E., C. Liu, J.R. Scully, and R.G. Kelly, *Journal of The Electrochemical Society* 167 (2020): p. 111507.
4. Matzdorf, C.A., W.C. Nickerson, B.C. Rincon Tronconis, G.S. Frankel, L. Li, and R.G. Buchheit, *Corrosion* 69 (2013): pp. 1240–1246.
5. Feng, Z., and G.S. Frankel, *Corrosion* 70 (2014): pp. 95–106.
6. Marshall, R.S., R. Kelly, A. Goff, and C. Sprinkle, *Corrosion* 75 (2019): pp. 1461–1473.
7. Marshall, R.S., A. Goff, C. Sprinkle, A. Britos, and R. Kelly, *Corrosion* 76 (2020): pp. 476–484.
8. Moran, A., J. Jennings, H. Nee, S. Pearson, B. Clark, and R.S. Lillard, *Corrosion Journal* 75 (2019): pp. 484–498.
9. Rafla, V., A. Davenport, and J.R. Scully, *Corrosion Communications* 71 (2015): pp. 1171–1176.

10. Rafla, V.N., A.D. King, S. Glanvill, A. Davenport, and J.R. Scully, *Corrosion* 74 (2018): pp. 5–23.

11. Rafla, V.N., and J.R. Scully, *Corrosion Journal* 75 (2019): pp. 12–28.

12. Clark, W.J., J.D. Ramsey, R.L. McCreery, and G.S. Frankel, *Journal of The Electrochemical Society* 149 (2002): pp. B179–B185.

13. Feng, Z., G.S. Frankel, W.H. Abbott, and C.A. Matzdorf, *Corrosion* 72 (2016): pp. 342–355.

14. Shi, L., X. Yang, Y. Song, D. Liu, K. Dong, D. Shan, and E.H. Han, *Journal of Materials Science & Technology* 35 (2019): pp. 1886–1893.

15. Rafla, V.N., P. Khullar, R.G. Kelly, and J.R. Scully, *Journal of The Electrochemical Society* 165 (2018): pp. 562–572.

16. Deshpande, K.B., *Corrosion Science* 52 (2010): pp. 2819–2826.

17. Kannan, B., C.F. Glover, H.N. McMurray, G. Williams, and J.R. Scully, *Journal of The Electrochemical Society* 165 (2018): pp. C27–C41.

18. Coelho, L.B., and M.G. Olivier, "The Inhibition Efficiency of Different Species on AA2024/Graphite Galvanic Coupling Models Depicted by SVET," Corrosion Science (2018).

19. Kish, J.R., N. Birbilis, E.M. McNally, C.F. Glover, X. Zhang, J.R. McDermid, and G. Williams, *JOM* 69 (2017): pp. 2335–2344.

20. Glover, C.F., T.W. Cain, and J.R. Scully, *Corrosion Science* 149 (2019): pp. 195–206.

21. Bastos, A.C., M.C. Quevedo, O. V. Karavai, and M.G.S. Ferreira, *J Electrochem Soc* 164 (2017): pp. C973–C990.

22. Fajardo, S., C.F. Glover, G. Williams, and G.S. Frankel, *Electrochimica Acta* 212 (2016): pp. 510–521.

23. Williams, G., and H.N. McMurray, *J Electrochem Soc* 155 (2008): pp. 340–349.

24. Glover, C.F., T.W. Cain, and J.R. Scully, *Corrosion Science* 149 (2019): pp. 195–206.

25. Saeedikhani, M., K.X. Kuah, S. Wijesinghe, S. Vafakhah, and D.J. Blackwood, *Journal of The Electrochemical Society* 168 (2021): p. 081505.

26. Atz Dick, P., G.H. Knörnschild, and L.F.P. Dick, *Corrosion Science* 114 (2017): pp. 28–36.

27. Murer, N., R. Oltra, B. Vuillemin, and O. Néel, *Corrosion Science* 52 (2010): pp. 130–139, http://dx.doi.org/10.1016/j.corsci.2009.08.051.

28. Haque, Z., B.A. Clark, and R.S. Lillard, *Corrosion* 74 (2018): pp. 903–913.

29. Deshpande, K.B., *Corrosion Science* 52 (2010): pp. 3514–3522.

30. Thébault, F., B. Vuillemin, R. Oltra, C. Allely, and K. Ogle, *Electrochimica Acta* 82 (2012): pp. 349–355.

31. Thébault, F., B. Vuillemin, R. Oltra, C. Allely, and K. Ogle, *Corrosion Science* 53 (2011): pp. 201–207.

32. Snihirova, D., D. Höche, S. Lamaka, Z. Mir, T. Hack, and M.L. Zheludkevich, *Corrosion Science* (2019).

33. Dolgikh, O., A. –S Demeter, S. V. Lamaka, M. Taryba, A.C. Bastos, M.C. Quevedo, and J. Deconinck, *Electrochimica Acta* 203 (2016): pp. 379–387.

34. Liu, C., and R.G. Kelly, *CORROSION* (2019).

35. Murer, N., N.A. Missert, and R.G. Buchheit, *Journal of The Electrochemical Society* 159 (2012): pp. C265–C276, http://jes.ecsdl.org/cgi/doi/10.1149/2.102206jes.

36. Wang, H., F. Presuel, and R.G. Kelly, *Electrochimica Acta* 49 (2004): pp. 239–255.

37. Moraes, C. V., R.J. Santucci, J.R. Scully, and R.G. Kelly, *Journal of The Electrochemical Society* 168 (2021): p. 051505.

38. Isaacs, H.S., *Corrosion Science* 28 (1988): pp. 547–558.

39. Böhm, S., H.N. McMurray, S.M. Powell, and D.A. Worsley, *Electrochimica Acta* 45 (2000): pp. 2165–2174.

40. Deshpande, K.B., *Corrosion Science* 52 (2010): pp. 3514–3522.

41. Liu, C., P. Khullar, and R.G. Kelly, *Journal of The Electrochemical Society* 166 (2019): pp. 153–161.

42. Duan, Z., C. Man, C. Dong, Z. Cui, D. Kong, and X. Wang, *Corrosion Science* 167 (2020): p. 108520.

43. Zaid, B., D. Saidi, A. Benzaid, and S. Hadji, *Corrosion Science* 50 (2008): pp. 1841–1847.

44. Huang, I.W., B.L. Hurley, F. Yang, and R.G. Buchheit, *Electrochimica Acta* 199 (2016): pp. 242–253.

45. Yin, L., Y. Jin, C. Leygraf, and J. Pan, *Journal of The Electrochemical Society* 164 (2017): pp. C768–C778.

46. Charles-Granville, U.-E., C. Glover, J.R. Scully, and R. Kelly, *Journal of The Electrochemical Society* (2021).

47. Deltombe, E., and M. Pourbaix, *Corrosion* 14 (1958): pp. 16–20.

48. Saeedikhani, M., and D.J. Blackwood, *Corrosion and Materials Degradation* 1 (2020): pp. 273–281.

49. Demeter, A.S., O. Dolgikh, A.C. Bastos, D. Deconinck, S. Lamaka, V. Topa, and J. Deconinck, *Electrochimica Acta* 127 (2014): pp. 45–52.

50. Coelho, L.B., and M.G. Olivier, “The Inhibition Efficiency of Different Species on AA2024/Graphite Galvanic Coupling Models Depicted by SVET,” Corrosion Science (2018).

51. Bastos, A.C., M.C. Quevedo, and M.G.S. Ferreira, *Corrosion Science* 92 (2015): pp. 309–314.

52. Co, N.E.C., and J.T. Burns, *International Journal of Fatigue* 103 (2017): pp. 234–247, http://dx.doi.org/10.1016/j.ijfatigue.2017.05.028.

53. Ansari, T.Q., J.-L. Luo, and S.-Q. Shi, *Npj Materials Degradation* 3 (2019): pp. 1–12.

54. Saeedikhani, M., N. van den Steen, S. Wijesinghe, S. Vafakhah, H. Terryn, and D.J. Blackwood, *Journal of The Electrochemical Society* 167 (2020): p. 041503.

55. Yin, L., Y. Jin, C. Leygraf, and J. Pan, *Electrochimica Acta* 192 (2016): pp. 310–318.

Chapter 10: Conclusions & Future work

10.1 Conclusions

The general objective of this work was to conduct computational analyses utilizing an experimentally-validated Laplacian model to investigate various geometric and environmental impacts on crevice and pitting corrosion. The practical application would be to aid in the maintenance and design of aerospace structures through the prediction and mitigation strategies proposed in this work.

In the context of galvanic-induced crevice corrosion, the Laplacian model was first validated through ZRA and quantitative cross-sectional metallographic analysis when large external cathodic surface areas were present (Chapter 2). Through using the validated model, computational results were able to capture interactions occurring between dissimilar noble fasteners, which aided in understanding the mechanism of the galvanic-induced crevice corrosion. In addition, experimental analysis determined that substantial corrosion could occur within the fastener hole without indications on the boldly-exposed surface of the panel, highlighting the importance and motivation of understanding conditions within this stress-concentrating occluded area. Therefore, the remaining work focused on corrosion damage within the fastener hole or in pitted (stress-concentrating) areas.

Overall, it was determined that thin (atmospheric) water layer thicknesses (WL), small external scribe dimensions and countersunk fasteners all concentrated large amounts of current into the highly-susceptible creviced regions (Chapters 3 and 4). Two general types of mitigation strategies were proposed, 1) to *prevent* the majority of current from occurring within the fastener hole, through intentionally focusing the current onto the more-visible bulk surfaces, or 2) to lower the overall magnitude of current. These mitigation strategies were found to include the use of a raised fastener, a sol-gel coating applied over the noble fastener, optimizing the surface treatments on the fastener, selective plating of a sacrificial anode over the surface of the more-active panel, large external scribe dimensions, or bulk WL conditions (Chapters 3, 4, 7, and 8).

Specifically, one novel mitigation strategy determined through this work was that only the *exterior* cathodic surfaces need to be coated (or minimized) to decrease the majority of current, as these surface areas were found to provide the main driving force for galvanic-induced crevice corrosion (Chapter 2). A practical application of this method was expressed in Chapter 8, in which the head of the noble fastener was bare Ti-6Al-4V and the shaft was the anodized Ti-6Al-4V. A purely anodized Ti-6Al-4V bolt *overpolarized* the system into high-crack growth rates and high corrosion rates, which could be mitigated by leaving the exterior cathodic surfaces areas bare and still maintaining the anodization for wear resistance on the creviced cathodic surface areas.

To generalize the present work, an open-source machine learning framework was built to predict if the majority of current would occur in a susceptible crevice or bulk region, in the context of a fastener/panel assembly, with the input parameters including the WL and scribe dimensions or the ratio of the creviced:bulk surface areas (Chapter 4).

In addition, to further apply the methodology developed in this work to realistic applications, the influence of cracking kinetics as a function of potential were considered. The computational model in combination with results from fracture mechanics, were able to develop a material selection framework to minimize both high crack growth rates and high corrosion rates (Chapters 7 and 8). The computational model was essential in this framework, as it predicted the potential and current density distributions along the entire panel, which allowed for optimization and focus of the susceptible fastener hole region (Chapters 7 and 8).

The localized corrosion phenomenon of pitting was also under investigation in this work, as it could be considered a micro-galvanic couple in contrast to the macro-galvanic couples described above. The computations aided in simulating a singular pit with varying geometries and dimensions, as isolating these features experimentally is impossible. Although a single pit surrounded by a flat cathodic surface is not realistic, it allows for parameters to be isolated to better understand what features or variables may be controlling the true realistic system. It also represents a worst-case scenario in terms of the depth of pitting damage. It was determined that the anodic surface areas present had more influence over the resulting repassivation of a metastable pit, rather than the specific pit shape (Chapter 5). This conclusion justifies all mathematical and computational assumptions of a hemispherical pit, if the anodic surface area is preserved, despite realistic pits undercutting the surface and being non-hemispherical in nature.

In addition, pit stability thresholds were investigated and compared, with the repassivation potential (E_{rp}) continually estimating more conservative values than that of the pit stability product ($i \cdot x$) (Chapter 5). As both E_{rp} and ($i \cdot x$) should represent the same lower limit of pitting, a novel calculation of E_{rp} was proposed in which values were less conservative than those determined through conventional cyclic potentiodynamic polarization scans yet similar to computational predictions and 1-D pitting scans, and unified with predictions from ($i \cdot x$) (Chapter 6).

Although the geometries between the crevice and pitting samples were very different, their respective impact to environmental factors could be compared. Specifically atmospheric conditions, with thin WL, were shown to aggravate macro-galvanic fastener/panel couples, through forcing large amounts of current into the creviced regions (Chapter 4). However, in the context of pitting, thin WL (assuming no changes to molarity) would instead be *helpful* towards inducing repassivation of the pit, due to the limited cathodic current supply via the ohmic potential drop, which could no longer keep up with the anodic current demand (Chapter 5). This difference is due to the location of the cathodic surface reactions, although in both scenarios the high ohmic potential drop is limiting the galvanic interaction distance (*i.e.,* the throwing power). In the fastener assembly, a decreased interaction distance lowers the total anodic surface area "visible" to the cathode, whereas in the single pit scenario, the decreased throwing power essentially lowers the overall size of the cathode.

However, as expressed previously, a single pit surrounded by a continuous cathodic surface is a highly unlikely scenario, but is possible to study through computational work. To extend the model into more realistic scenarios, interactions between multiple pits must be considered. Therefore, a macro-scale SS316/AA7050 planar galvanic couple was developed, in which numerous pits were experimentally seen to occur on the AA7050 surface. After optimization of the boundary conditions to represent the system of interest, the Laplacian model was able to accurately predict the *total current* in the system and the *average* current density distribution (Chapter 9). An important distinction is that the model was *not* able to capture the local hot-spots of the high current density due to the pitting events, and would never be able to do so with the Laplace equation unless the size and distribution of each pit was known *a priori.*

This concept was highlighted in Chapter 8 as well, in which a single pit was simulated to be within the occluded fastener hole. Although a qualitative example to determine the influence of a pit on the potential within the fastener hole, the size of the pit had to be predefined before the results could be computed. An important conclusion was determined that the *location* of the pit had little influence over the resulting potential, but the *size* (and naturally, the *distribution*) of the pit had a larger influence indicating the importance of this parameter. Therefore, it is not practical to use the Laplace equation to determine local pitting hotspots, and instead an alternative governing equation, which can simulate the local inhomogeneities and accumulation of aggressive species in solution, needs to be considered. However, the Laplace is useful in accurately determining the total current and average current density distribution of an actively pitting surface, when the boundary conditions are correct, which would still be useful in the maintenance and design of structures (Chapter 9).

To conclude, a limitation echoed throughout every chapter in this work was the need for accurate boundary conditions representing the specific solution or environment of interest, to accompany and circumvent the simplifying assumptions of the Laplace equation. Note that this limitation *does not* necessarily mean that Laplacian models require hyper-specific boundary conditions to each simulation. If this were the case, the practical advantages of computational work would be essentially nullified. However, a balance of the boundary conditions is necessary, such as utilizing activated AA7XXX anodic kinetics throughout all SS316/AA7XXX galvanic couples resulted in computational predictions very similar to that of the experimental work, independent of the overall geometry, as shown in Chapters 2 and 9.

10.2 Recommended Future Work

- Utilizing the Laplace equation with the additional transport of *minor* species, to determine if some limitations observed in this work, when using solely the Laplace equation, can be overcome. Specifically in the context of an isolated crevice with no exterior cathodic reactions present.

- Within the model, account for corrosion product formation, which may further limit the mass transport of species within the crevice.
- Continued experimental validation of the Laplace equation in different geometries and environments, such as isolated pitting samples and atmospheric conditions. Specifically, validate the transport of *minor* species and Laplace assumptions through experimentally measuring the pH in a sample which maintains an identical x^2/g crevice scaling factor to that of the fastener/panel assembly.
- Further computationally investigate the influence of atmospheric conditions on localized corrosion, specifically considering the effects of $MgCl_2$ being dominant at low RH and NaCl being dominant at high RH.
- Determining a pit stability threshold which is more relevant for complex non-hemispherical nor 1-D pits, possibly through a dynamic $(i \cdot z)$ or through tracking the evolution of metal cations.
- Experimental cracking validation of the mitigation techniques proposed in Chapters 7 and 8.